

Single-crystal elasticity of Al-rich phases in the Earth's transition zone and lower mantle

Der Bayreuther Graduiertenschule für Mathematik und Naturwissenschaften

zur Erlangung der Würde eines
Doktors der Naturwissenschaften

- Dr. rer. nat. -

Dissertation

vorgelegt von

Martha Giovanna Pamato

aus Cagua (Venezuela)

Bayreuth, 2014

This doctoral thesis was prepared at the Bayerisches Geoinstitut at the University of Bayreuth from November 2010 until July 2014 and was supervised by Prof. Dr. Leonid Dubrovinsky, Dr. Tiziana Boffa Ballaran and Prof. Dr. Daniel J. Frost.

This is a full reprint of the dissertation submitted to obtain the academic degree of Doctor of Natural Sciences (Dr. rer. Nat.) and approved by the Bayreuth Graduate School of Mathematical and Natural Sciences (BayNAT) of the University of Bayreuth.

Date of submission: 30.07.2014

Date of defense: 19.09.2014

Acting director: Prof. Dr. Franz Xaver Schmid

Doctoral committee:

Prof. Dr. Leonid Dubrovinsky (1st reviewer)

Prof. Dr. Steven Jacobsen (2nd reviewer)

Prof. Dr. Daniel Frost (chairman)

Dr. Gerd Steinle-Neumann

*El gran libro, siempre abierto y que tenemos que hacer un esfuerzo para leer,
es el de la Naturaleza,
y los otros libros se toman a partir de él,
y en ellos se encuentran los errores y malas interpretaciones de los hombres.*

Antoni Gaudí

Table of contents

| | |
|---|----|
| Summary | 1 |
| Zusammenfassung | 5 |
| 1. Introduction | 9 |
| 1.1 The dynamic Earth..... | 9 |
| 1.1.1 Subduction of oceanic lithosphere: a source of chemical heterogeneities in the mantle..... | 11 |
| 1.2 Chemical heterogeneities in the mantle: geophysical signatures vs geochemical evidence | 19 |
| 1.3 Seismological observations of the inaccessible Earth | 22 |
| 1.4 Elastic properties of mantle minerals..... | 24 |
| 1.4.1 Elasticity measurements..... | 27 |
| 1.5 Aims of the thesis..... | 29 |
| 2. Methods | 31 |
| 2.1 Synthesis of high quality single crystals | 31 |
| 2.1.1 Starting materials preparation | 31 |
| 2.1.2 Multi anvil apparatus | 32 |
| 2.2 Sample characterization | 34 |
| 2.2.1 Electron microscopy | 34 |
| 2.2.2 X-ray diffraction | 35 |
| 2.3 Elasticity measurements at high pressure, HP, and high temperature, HT | 36 |
| 2.3.1 Externally heated diamond anvil cell..... | 37 |
| 2.3.2 Pressure determination..... | 40 |
| 2.3.2.1 Fluorescence measurements..... | 40 |
| 2.3.2.2 Absolute Pressure Determination | 43 |
| 2.3.3 Single crystal X-ray diffraction | 44 |
| 2.3.3.1 Equations of State | 44 |
| 2.3.3.1.1 F_E-f_E plots..... | 45 |
| 2.3.3.1.1 Thermal equations of state | 46 |
| 2.3.3.2 Four circle diffractometer at BGI | 47 |
| 2.3.3.3 Synchrotron radiation..... | 49 |

| | |
|---|------------|
| 2.3.4 Brillouin Scattering | 49 |
| 2.3.4.1 Brillouin scattering setup at BGI and at APS | 52 |
| 3. Single-crystal elasticity of majoritic garnet at high pressures and temperatures | 55 |
| 3.1 Introduction | 55 |
| 3.2 Experimental methods | 58 |
| 3.2.1 Sample synthesis and characterization | 58 |
| 3.2.2 Simultaneous X-ray diffraction and Brillouin scattering | 62 |
| 3.2.3 Single-crystal data collection and structure refinements | 64 |
| 3.3 Results and discussion | 69 |
| 3.3.1 Elasticity | 69 |
| 3.3.1.1 Absolute pressure determination | 76 |
| 3.3.1.2 <i>P-V</i> Equation of state | 78 |
| 3.3.2 Effect of Fe substitution on the structure and elasticity of majoritic garnet | 80 |
| 3.3.3 Comparison with literature data | 85 |
| 4. Hexagonal $\text{Na}_{0.41}[\text{Na}_{0.125}\text{Mg}_{0.79}\text{Al}_{0.085}]_2[\text{Al}_{0.79}\text{Si}_{0.21}]_6\text{O}_{12}$ (NAL phase): Crystal structure refinement and elasticity | 89 |
| 4.1 Introduction | 89 |
| 4.2 Experimental methods | 91 |
| 4.2.1 Sample synthesis and characterization | 91 |
| 4.2.2 Single-crystal data collection and structure refinements | 94 |
| 4.2.3 Simultaneous X-ray diffraction and Brillouin scattering | 95 |
| 4.2.4 First principles calculations | 97 |
| 4.3 Results and discussion | 97 |
| 4.3.1 Structural model from single-crystal X-ray diffraction | 97 |
| 4.3.2 Atomic vibrations | 100 |
| 4.3.3 Elasticity | 103 |
| 5. High-pressure single-crystal elasticity of the hexagonal $\text{Na}_{0.41}[\text{Na}_{0.125}\text{Mg}_{0.79}\text{Al}_{0.085}]_2[\text{Al}_{0.79}\text{Si}_{0.21}]_6\text{O}_{12}$ (NAL phase) and seismic anisotropy in the deep mantle | 109 |
| 5.1 Introduction | 109 |

| | |
|--|------------|
| 5.2 Experimental methods | 110 |
| 5.3 Results and discussion | 111 |
| 5.3.1 Elasticity | 111 |
| 5.3.2 EoS formalism and absolute pressure determination..... | 115 |
| 5.3.3 Compressibility and Equation of state (Eos) | 118 |
| 5.3.3.1 Axial compressibility..... | 124 |
| 5.3.4 Sound velocities | 125 |
| 5.3.5 Seismic anisotropy..... | 127 |
| | |
| 6. Velocity and density models of the Earth's transition zone and uppermost lower mantel..... | 131 |
| 6.1 Determination of P-V-T Eos of majoritic garnets..... | 133 |
| 6.2 Calculations of elastic properties of majoritic garnets from end member compositions | 137 |
| 6.3 Model of the transition zone and uppermost lower mantle..... | 142 |
| 6.3.1 Pyrolite phase relations | 143 |
| 6.3.2 MORB composition phase relations | 144 |
| 6.3.3 Harzburgite composition phase relations..... | 145 |
| 6.3.4 Calculated acoustic velocities compared with reference models..... | 145 |
| 6.3.5 Density differences at the base of the transition zone/top of the lower mantle..... | 149 |
| 6.3.6 Density and velocity changes at the NAL and CF transition..... | 150 |
| | |
| 7. Conclusions and future perspectives | 155 |
| | |
| Acknowledgments | 161 |
| | |
| References..... | 163 |
| | |
| Appendices..... | 181 |
| | |
| Versicherungen und Erklärungen..... | 185 |

Summary

Understanding the Earth's internal convection process is one of the major frontiers in Earth sciences. The subduction of oceanic lithosphere must produce chemical heterogeneities in the mantle, which may explain some instances of lateral heterogeneity in seismic wave velocities. Seismic observations of the Earth's interior provide the only method to investigate the mantle at the depth and scale required to understand its chemistry and structure and for tracing the chemical anomalies potentially caused by subduction. The velocities of seismic waves through the Earth depend on the elastic properties of the minerals through which they travel. By comparing observations of seismic wave velocities with estimates for what these velocities should be given particular mineral models and mineral elastic properties, it is possible to relate these observations to the chemical and thermal state of the interior.

The P - V - T equation of state and shear (V_s) and longitudinal (V_p) sound velocities of single crystals of minerals that form at conditions compatible with the Earth's transition zone and lower mantle have been determined in this study by combining X-ray diffraction and Brillouin scattering. In particular majoritic-garnet solid solutions and the NAL (new aluminium phase) phase have been studied. The combination of these techniques makes it possible to determine the full elastic tensor of these minerals at high pressures and temperatures which allows us to accurately determine the pressures of these measurements without the use of calibrant materials and to build mineral models that describe the seismic velocity and density of different rock lithologies within the transition zone and lower mantle.

Single-crystal elastic properties of two majoritic garnets ($\text{Mg}_{3.24}\text{Al}_{1.53}\text{Si}_{3.23}\text{O}_{12}$ and $\text{Mg}_{3.01}\text{Fe}_{0.17}\text{Al}_{1.68}\text{Si}_{3.15}\text{O}_{12}$), synthesized at 1900 °C and 17 GPa, were determined as a function of density, temperature and composition under hydrostatic conditions by combining single-crystal Brillouin scattering with X-ray diffraction. Experiments were performed up to ~30 GPa and ~600 K in an externally heated diamond anvil cell. In comparison to studies performed on the pyrope garnet end member, substitution of the majorite component is found to lower both the bulk (K_s) and shear modulus (G) of garnet. The substitution of Fe for Mg affects the compression mechanism and therefore the elastic properties of majoritic garnets. The K_s and G values of both samples are similar at room pressure, however, at pressures of the transition zone, Fe-bearing majoritic garnet (Fe-Mj) becomes more compressible due to

its smaller $(\partial K / \partial P)_T$ value. High pressure crystal structure refinements demonstrate that this behaviour is related to the high-pressure response of the tetrahedral site of the garnet structure, which appears slightly more compressible in Fe-Mj with respect to Mj. This effect is unlikely to be linear with garnet Fe content.

Single-crystals of the $\text{Na}_{0.41}[\text{Na}_{0.125}\text{Mg}_{0.79}\text{Al}_{0.085}]_2[\text{Al}_{0.79}\text{Si}_{0.21}]_6\text{O}_{12}$ (NAL) phase were synthesized at 2260 °C and 20 GPa. The single-crystal structure refinement of NAL, which is consistent with the space group $P6_3/m$, reveals dynamic disorder of Na atoms along channels within the structure, which likely influences transport properties of this phase such as electrical conductivity. The complete elastic tensor was experimentally determined for the first time at ambient conditions and at high pressures by Brillouin scattering spectroscopy. The elastic moduli obtained from the Voigt-Reuss-Hill approximation using the elastic constants determined here are $K_S = 206$ GPa and $G = 129$ GPa, while the isotropic compressional and shear sound velocities are $V_P = 9.9$ km/s and $V_S = 5.8$ km/s. At ~ 1000 km, NAL is expected to transform to the calcium ferrite type aluminum phase (CF). This transformation has been proposed to cause a seismic discontinuity observed at this depth, however, the experimental data imply that the velocity change upon this transformation would be too small to be seismically observed. The NAL phase is elastically anisotropic, displaying 13.9 % compressional and shear wave anisotropy. The anisotropy of NAL decreases as a function of pressure showing 10.9 % compressional (AV_P) and 12.71 % shear wave anisotropy (AV_S) at 19.93 GPa. However, upon transformation to the CF phase a significant change in the seismic wave anisotropy would occur, which could lead to a seismically detectable discontinuity if the crystallographic preferred orientation were favourable.

The elastic properties of majoritic garnets and the NAL phase were used along with literature data to invert the seismic velocities for pyrolite, harzburgite and MORB (mid-ocean ridge basalt) bulk compositions in the depth range between 480 and 780 km. In the transition zone, the mineralogy of these lithologies mostly differs in terms of the proportion and chemistry of garnet. Using the garnet experimental results, elastic properties of majorite and almandine end members were refined using a thermo-elastic model. By refining end member properties using solid solution data instead of the end member data, the compositional range of the refinement remains closer to that over which the model will be employed. This enabled

velocities and densities of garnet compositions in the system Fe-CMAS (CaO-MgO-Al₂O₃-SiO₂) to be calculated at mantle conditions. An extrapolation of this model to mantle temperatures was found to reproduce ultrasonic V_s measurements on complex garnet compositions, although not V_p . A similar model was refined to the NAL experimental data. A thermodynamic model was used to estimate mineral modes and compositions in different lithologies.

Along an adiabat with a potential temperature of 1673 K, the V_s predicted for a pyrolite mantle bulk composition is 0.2 km/s slower than global seismic models between 500 and 660 km. V_p is closer but still lower than PREM although consistent with AK135. Temperatures would have to be approximately 600 K lower at this depth for the V_s model to be in agreement with seismic observations. The low V_s of majoritic garnet is chiefly responsible for this difference. Consequently models for a MORB bulk composition are also over ~0.3 km/s slower in V_s over the same depth interval. A harzburgite model with 80 % by volume of (Mg,Fe)₂SiO₄ phases is very close to seismic observations but is still ~0.1 km/s slower in V_s , a difference which would require temperatures to be lower by 200 K for a perfect match to be obtained. The models for all three lithologies, however, match velocities for the top of the lower mantle. The best explanation for these observations would be that average temperatures in the lower transition zone deviated globally from a normal adiabat. This may reflect the occurrence of large lateral cold anomalies at the base of the transition zone that result from the stagnation of subducting slabs. Additionally, lower temperatures in the harzburgitic layer could stabilize akimotoite at the expenses of garnet. Higher velocities expected for akimotoite would further help to explain the mismatch in calculated and observed V_s .

Subducted MORB material is estimated to be intrinsically denser than pyrolite or harzburgite at the base of the transition zone even at ambient mantle temperatures. However, neither harzburgite nor MORB are denser than pyrolite or global reference model densities at the top of the lower mantle. This may act to focus these subduction related chemical heterogeneities, even at ambient mantle temperatures, at the base of the transition zone. Below 1000 km, however, the phase transformation of NAL to the CF phase likely renders MORB compositions to be as dense as the surrounding mantle.

Zusammenfassung

Das Verständnis des Konvektionsprozesses im Inneren der Erde ist eine der zentralen Probleme in den Geowissenschaften. Die Subduktion ozeanischer Lithosphäre erzeugt chemische Heterogenitäten im Erdmantel, die in einigen Fällen die laterale Heterogenität von seismischen Wellengeschwindigkeiten erklären können. Seismische Beobachtungen des Erdinneren liefern die einzige Methode zur Erforschung des Mantels mit der erforderlichen Auflösung und Tiefe, um seinen Chemismus und seine Struktur zu verstehen und eventuell durch Subduktion verursachte chemische Anomalien zu erkennen. Die Geschwindigkeiten seismischer Wellen durch die Erde hängen von den elastischen Eigenschaften der Minerale ab, die sie durchqueren. Durch den Vergleich der beobachteten seismischen Wellengeschwindigkeiten mit Abschätzungen, die aus Mineralmodellen und mineralelastischen Eigenschaften gewonnen werden, ist es möglich, diese Beobachtungen mit dem chemischen und thermischen Zustand des Erdinneren in Beziehung zu setzen.

Die P - V - T Zustandsgleichung und die Scher- (V_s) und Longitudinal- (V_p) Wellengeschwindigkeiten von Einkristallen der Minerale, die sich unter den Bedingungen der Übergangszone und des unteren Erdmantels der Erde bilden, wurden in der vorliegenden Arbeit durch eine Kombination von Röntgenbeugung und Brillouinspektroskopie bestimmt. Im Detail wurden Majorit-Granat Mischkristalle und die NAL ('neue Aluminium Phase') Phase untersucht. Die Kombination der beiden Untersuchungsmethoden ermöglicht es, den kompletten elastischen Tensor dieser Minerale bei hohen Drücken und Temperaturen zu bestimmen, die Umgebungsdrücke der Messungen ohne den Einsatz von Kalibrierungsmaterialien genau zu bestimmen, und Mineralmodelle zu konstruieren, die die seismische Geschwindigkeit und Dichte verschiedener Gesteinslithologien in der Übergangszone und dem unteren Erdmantel beschreiben.

Die elastischen Eigenschaften von Einkristallen zweier majoritischer Granate ($\text{Mg}_{3.24}\text{Al}_{1.53}\text{Si}_{3.23}\text{O}_{12}$ and $\text{Mg}_{3.01}\text{Fe}_{0.17}\text{Al}_{1.68}\text{Si}_{3.15}\text{O}_{12}$), die bei 1900°C und 17 GPa synthetisiert wurden, wurden als Funktion der Dichte, Temperatur und Zusammensetzung unter hydrostatischen Bedingungen bestimmt, indem Einkristall-Brillouinspektroskopie mit Röntgenbeugung kombiniert wurde. Die Experimente wurden bei bis zu ~ 30 GPa und ~ 600 K in einer extern geheizten Diamantstempelpresse durchgeführt. Im Vergleich zu am Pyrop-

Endglied durchgeführten Untersuchungen führt die Substitution durch die Majorit-Komponente zu einer Erniedrigung des Kompressions- (K_s) und des Schermoduls (G). Die Substitution von Mg durch Fe beeinflusst den Kompressionsmechanismus und daher auch die elastischen Eigenschaften der Majorit-Granate. Die K_s and G Werte beider Proben sind unter Raumdruck ähnlich, bei den Drücken der Übergangszone jedoch wird der Fe-haltige Majorit-Granat (Fe-Mj) durch seinen geringeren $(\partial K / \partial P)_T$ Wert deutlich komprimierbarer. Strukturverfeinerungen der Hochdruckkristalle zeigen, dass dieses Verhalten durch das Hochdruckverhalten des Tetraederplatzes in der granatstruktur verursacht wird, der im Fe-Mj relative zum Mj etwas starker komprimierbar erscheint. Es ist aber unwahrscheinlich, dass dieser Effekt linear mit dem Fe-Gehalt des Granats korreliert ist.

Einkristalle der $\text{Na}_{0.41}[\text{Na}_{0.125}\text{Mg}_{0.79}\text{Al}_{0.085}]_2[\text{Al}_{0.79}\text{Si}_{0.21}]_6\text{O}_{12}$ (NAL) Phase wurden bei 2260 °C and 20 GPa synthetisiert. Die Einkristall-Strukturverfeinerung von NAL, die mit der Raumgruppe $P6_3/m$ konsistent ist, zeigt eine dynamische Unordnung der Na-Atome entlang von Kanälen in der NAL Struktur, die wahrscheinlich einen Einfluss auf die Transporteigenschaften dieser Phase wie z.B. elektrische Leitfähigkeit hat. Der komplette elastische Tensor wurde zum ersten Mal unter Raumbedingungen und hohen Drücken experimentell mit Brillouinspektroskopie bestimmt. Die elastischen Module, die durch eine Voigt-Reuss-Hill Approximierung der elastischen Konstanten erhalten wurden, sind $K_s = 206$ GPa und $G = 129$ GPa, während sich für die Kompressions- und Scherwellengeschwindigkeiten $V_p = 9.9$ km/s und $V_s = 5.8$ km/s ergaben. In ~ 1000 km Tiefe ist die Umwandlung von NAL in eine Aluminium-Phase mit der Calcium-Ferrit-Struktur (CF) zu erwarten. Es wurde vermutet, dass diese Umwandlung die Ursache für eine beobachtete seismische Diskontinuität in dieser Tiefe sein könnte, jedoch die experimentellen Daten deuten darauf hin, dass der Geschwindigkeitsunterschied durch diese Umwandlung zu klein ist, um seismisch detektierbar zu sein. Die NAL Phase ist elastisch anisotrop, mit einer Anisotropie von 13.9% sowohl für Longitudinal- als auch für Scherwellen. Die Anisotropie verringert sich mit zunehmendem Druck auf 10.9% Longitudinal- (AV_p) und 12.71% Scherwellenanisotropie (AV_s) bei 19.93 GPa. Bei der Umwandlung in die CF-Struktur würde jedoch eine signifikante Änderung in der Anisotropie auftreten, die zu einer seismisch detektierbaren Diskontinuität führen könnte, wenn die kristallographischen Vorzugsorientierungen entsprechend günstig vorhanden wären.

Die elastischen Eigenschaften von majoritischen Granaten und der NAL Phase wurden zusammen mit Literaturdaten benutzt, um die seismischen Geschwindigkeiten für typische Zusammensetzungen von Pyrolit, Harzburgit und MORB (mid-ocean ridge basalt) für den Tiefenbereich von 480 bis 780 km zu errechnen. In der Übergangszone unterscheidet sich die Mineralogie dieser Lithologien hauptsächlich im Anteil und Chemismus von Granat. Mithilfe der experimentellen Resultate für die Granate wurden die elastischen Eigenschaften der Majorit- und Almandin-Endglieder durch ein thermo-elastisches Modell verfeinert. Indem die Eigenschaften der Endglieder mithilfe der Mischkristall- anstatt der Endglieddaten verfeinert wurden, blieb der Zusammensetzungsbereich der Verfeinerung näher an dem Bereich, über den das Modell angewendet wird. Das machte es möglich, Geschwindigkeiten und Dichten von Granatzusammensetzungen im System Fe-CMAS ($\text{CaO-MgO-Al}_2\text{O}_3\text{-SiO}_2$) bei Mantelbedingungen zu berechnen.

Eine Extrapolation dieses Modells zu Manteltemperaturen reproduzierte Ultraschallmessungen von Scherwellengeschwindigkeiten V_s in komplex zusammengesetzten Granaten, aber nicht deren Longitudinalwellengeschwindigkeiten V_p . Ein ähnliches Modell wurde auch für die experimentellen Daten der NAL Phase verfeinert. Ein thermodynamisches Modell wurde benutzt, um die Mineralanteile und -zusammensetzungen in den verschiedenen Lithologien abzuschätzen.

Entlang der Adiabate mit einer Potentialtemperatur von 1673 K ist die vorhergesagte V_s für eine Pyrolit-Mantelzusammensetzung 0.2 km/s langsamer als globale seismische Modelle für die Tiefe zwischen 500 and 660 km. V_p ist etwas näher, aber immer noch niedriger als PREM, jedoch konsistent mit AK135. Die Temperaturen müssten danach in dieser Tiefe annähernd 600 K niedriger sein, um das V_s Model in Übereinstimmung mit den seismischen Beobachtungen zu bringen. Die niedrigen V_s des majoritischen Granats sind hauptsächlich für diesen Unterschied verantwortlich. Entsprechend sind auch die Modelle für die MORB-Zusammensetzung mehr als 0.3 km/s langsamer in V_s über das gleiche Tiefenintervall. Ein Harzburgit-Modell mit 80 vol% $(\text{Mg,Fe})_2\text{SiO}_4$ Phasen ist näher an den seismischen Beobachtungen mit nur 0.1 km/s geringerer V_s , würde aber immer noch 200 K niedrigere Temperaturen für einen perfekte Übereinstimmung erfordern. Die Modelle für alle drei Lithologien stimmen jedoch mit den Geschwindigkeiten im oberen unteren Erdmantel überein. Die beste Erklärung für diese Beobachtungen ist, dass die durchschnittlichen Temperaturen in der unteren Übergangszone global von der normalen Adiabate abweichen.

Dieses könnte das Auftreten grosser lateraler und kalter Anomalien an der Basis der Übergangszone widerspiegeln, die durch die Stagnation subduzierter Platten erzeugt werden. Ausserdem würden niedrigere Temperaturen in der Harzburgit-Schicht zur Bildung von Akimotoit auf Kosten von Granat führen. Höhere Geschwindigkeiten, die für Akimotoit erwartet würden, könnten zusätzlich die Diskrepanz zwischen berechneten und beobachteten V_s erklären.

An der Basis der Übergangszone ist das subduzierte MORB Material abgeschätzt sogar bei normaler Umgebungstemperatur des Mantels dichter als Pyrolit und Harzburgit. Weder Harzburgit noch MORB haben jedoch eine höhere Dichte als Pyrolit oder die Dichten der globalen Referenzmodelle im oberen Bereich des unteren Erdmantels. Das kann dazu führen, dass durch Subduktion erzeugte chemische Heterogenitäten, sogar bei normalen Umgebungstemperaturen des Erdmantels, an der Basis der Übergangszone konzentriert auftreten. Unterhalb von 1000 km wird jedoch der Phasenübergang von NAL nach CF Phase dafür sorgen, dass MORB Zusammensetzungen dieselbe Dichte haben wie der umgebende Erdmantel.

1. Introduction

A major challenge in natural sciences is to understand the Earth's internal convection process as it is an apparently unique feature among planets of the solar system that may be essential for sustained habitability. An important consequence of this process is that chemically differentiated material from the surface is recycled into the interior by subduction and mixed within the deep Earth to ultimately form components in the source of later erupted lavas. For many years evidence for this process has come mainly from geochemical studies that examine isotopic anomalies caused by recycling (e.g. Hofmann, 1997). However, these studies provide just circumstantial evidence for the processes of convection. Seismic observations of the Earth's interior provide a far more precise and tangible method for tracing the chemical anomalies caused by subduction in the Earth. These anomalies are likely responsible for the observed lateral heterogeneities in seismic wave velocities (Hellfrich and Wood, 2001; Trampert et al., 2004), but to correctly interpret these observations in terms of chemistry and mantle mineralogy, laboratory data on the elasticity of minerals likely to comprise these mantle rocks are required.

This chapter provides an introduction to our current understanding of the dynamics, structure and mineralogy of the deep Earth with particular emphasis on the structure and mineralogy of subducting slabs and their role as a source of mantle heterogeneities. Geochemical and geophysical evidence for chemical anomalies caused by subduction are briefly summarized.

Also, the relationships between the propagation of sound waves and the elastic properties of the materials through which such waves propagate are introduced together with an overview of the theory of elasticity. The different experimental approaches commonly employed to study the elastic behaviour of minerals at high-pressures and high-temperatures using both single-crystals and mineral aggregates are also presented. Finally the motivation and aims of the present research thesis are described.

1.1 The dynamic Earth

Compared to other bodies in the Solar System, Earth is a “dynamic” planet with volcanic eruptions and earthquakes providing clear evidence for mass transport caused by internal heat loss within our planet. Since the acceptance of the theory of plate tectonics formulated in the last century (Hess, 1962; Wilson, 1962; Morgan, 1968) it became more and more evident that

the geological processes occurring at the Earth's surface are closely linked to much deeper processes. In fact, mantle convection is the driving mechanism for plate tectonics and associated geological activity on the surface of our planet.

At mid-ocean ridges, partial melting of the primitive pyrolite¹ mantle creates new oceanic lithosphere. At convergent plate boundaries, the oceanic lithosphere is subducted and recycled back into the deep mantle, involving different geophysical and geochemical processes. Most of our planet's largest earthquakes and active volcanoes are focussed around subduction zones, where a denser tectonic plate slips beneath less dense overriding lithosphere. As the down going plate encounters higher pressures and temperatures, sediments, oceanic crust, and oceanic mantle undergo metamorphic transformations. Many of these reactions involve the breakdown of hydrous minerals and release substantial amounts of H₂O into the overlying mantle wedge. This water lowers the melting temperature in the overlying mantle leading to large degrees of partial melting. The resulting magma rises upwards eventually producing extensive volcanism and the so-called arc volcanoes such as the 'Ring of Fire' around the Pacific Rim (Figure 1.1-1).

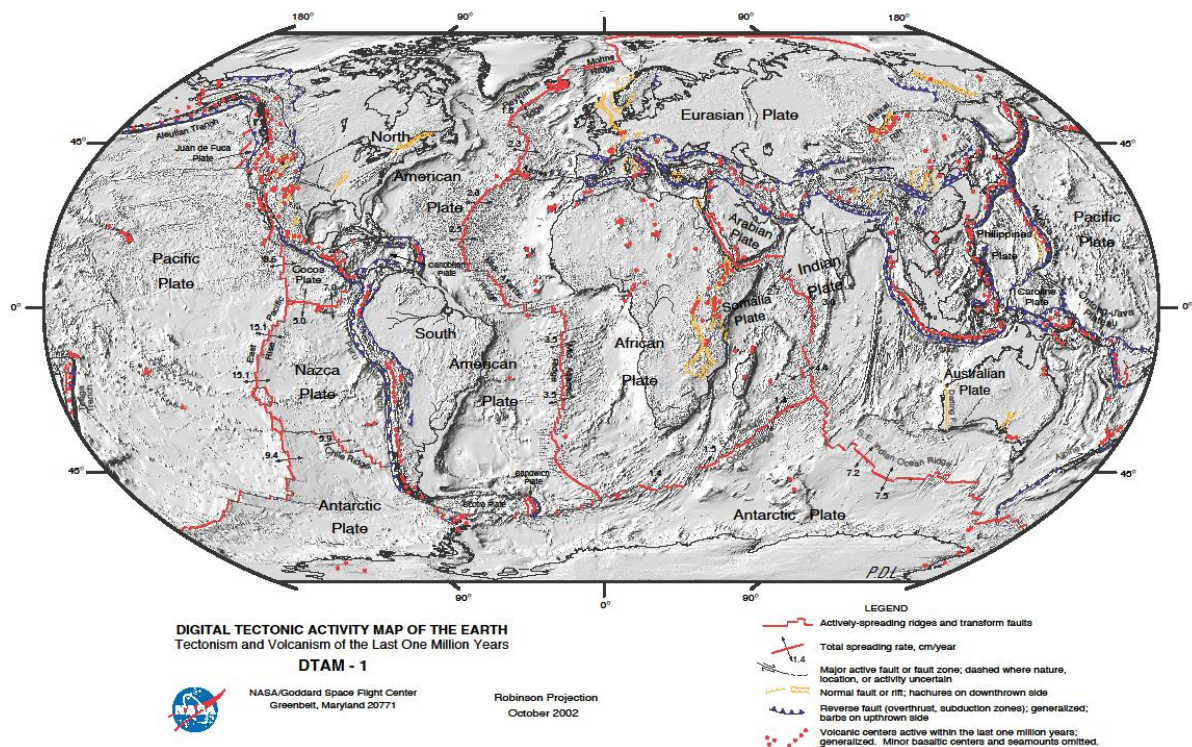


Figure 1.1-1. Earth's plate tectonic map. Source: <http://denali.gsfc.nasa.gov/dtam/>

¹ Pyrolite (pyroxene-olivine-rock) is a synthetic primitive mantle rock conceived by Ringwood (1976) that on fractional melting yields a typical basaltic magma and leaves behind a residual refractory peridotite. A pyrolitic rock can be envisaged as approximately one part basalt and 3-4 parts dunite.

Subduction and subduction-related volcanism are key processes through which geochemical components are recycled between the Earth's crust, lithosphere and mantle. The motion and velocities of lithospheric plates at the Earth's surface are controlled mainly by the buoyancy forces that drive subduction. The depth to which subducted lithosphere penetrates into the mantle is related to the scale of mantle convection and the Earth's evolution over time. Subduction displaces mantle which must then passively upwell forming a gradual return flow of material. This passive upwelling material is also supplemented by thermal plumes of less dense mantle heated at deep thermal boundary layers. Therefore, it is of crucial importance to study the fate of subducted basaltic material in order to understand the physical and chemical evolution of our planet Earth.

1.1.1 Subduction of oceanic lithosphere: a source of chemical heterogeneities in the mantle

Slabs are products of mid ocean ridge melting and are composed of oceanic crust upon variously depleted peridotitic mantle. The crust and mantle are serpentized in the upper portions to varying degree as a result of hydrothermal alteration, with the consequent addition of CO₂ and H₂O. The subducting oceanic slab consists, as suggested by Ringwood (1982), of a lithologically stratified unit of approximately 80 km thickness. Below a potential covering of sediments, this unit is subdivided into a layer of upper mafic crust (mid-ocean ridge basalts or MORBs) of approximately 6 km followed downward by a 24 km layer of residual harzburgite, a 10 km layer of residual lherzolite and a 40 km layer of slightly depleted pyrolite (Figure 1.1-2).

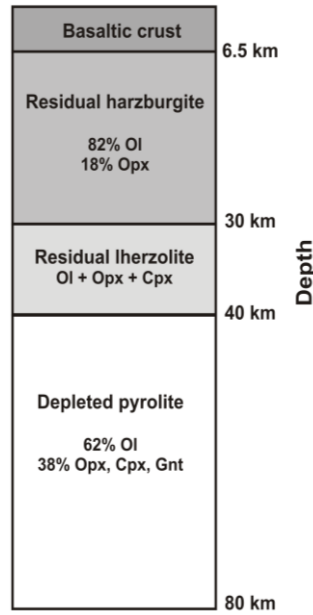


Figure 1.1-2. Schematic representation of an 80 km thick oceanic slab with the different lithologic units developed during partial melting and differentiation at mid-ocean ridges. Ol: Olivine, Cpx: clinopyroxene, Opx: orthopyroxene, Gnt: garnet. Redrawn after Ringwood (1976).

The last three components represent the residues left after different degrees of partial melting of pyrolitic mantle rock and extraction of basalt.

Typical chemical compositions of the lithologies described above are reported in Table 1.1-1.

Table 1.1-1. Chemical compositions of pyrolite, harzburgite and MORB (after Irifune and Tsuchiya, 2007)

| | <i>Pyrolite</i> | <i>Harzburgite</i> | <i>MORB</i> |
|--------------------------------|-----------------|--------------------|-------------|
| SiO ₂ | 44.5 | 43.6 | 50.4 |
| TiO ₂ | 0.2 | - | 0.6 |
| Al ₂ O ₃ | 4.3 | 0.7 | 16.1 |
| Cr ₂ O ₃ | 0.4 | 0.5 | - |
| FeO | 8.6 | 7.8 | 7.7 |
| MgO | 38 | 46.4 | 10.5 |
| CaO | 3.5 | 0.5 | 13.1 |
| Na ₂ O | 0.4 | - | 1.9 |
| K ₂ O | 0.1 | - | 0.1 |

The variation with depth in mineral proportions for pyrolite, harzburgite and MORB (mid-ocean ridge basalt) along a typical adiabatic geotherm (1673 K) are shown in Figure 1.1-3.

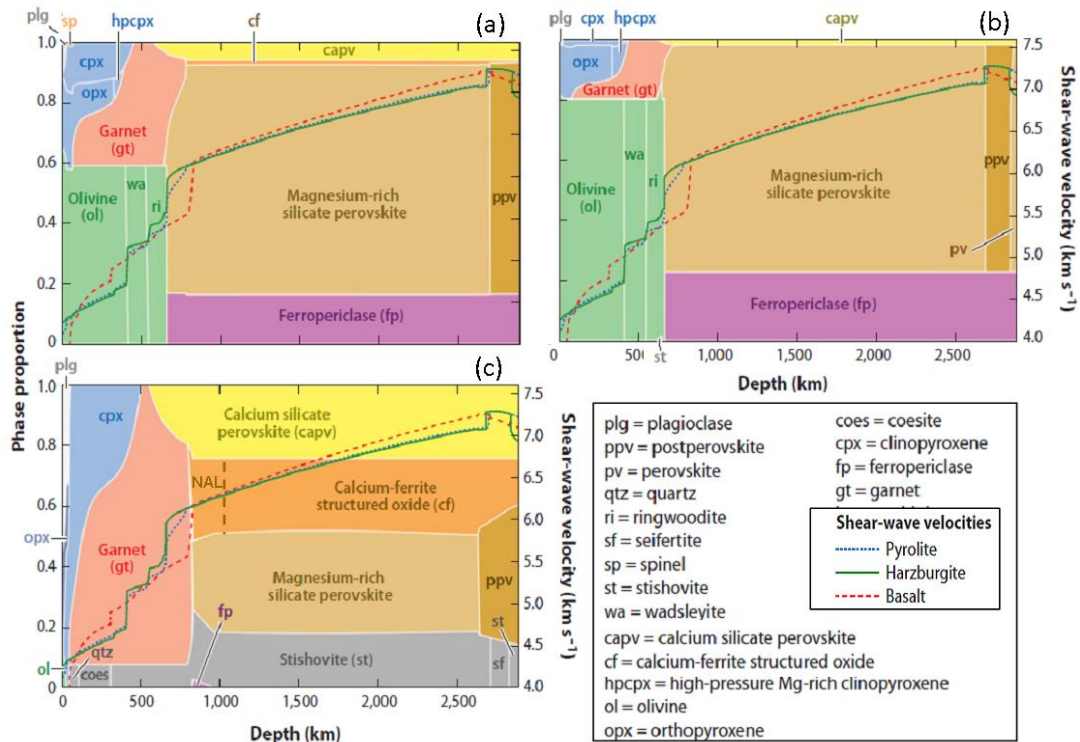


Figure 1.1-3. Phase proportions, expressed in atomic fraction, as a function of depth of (a) pyrolite, (b) harzburgite and (c) basalt. Shear-wave velocities of pyrolite (dotted blue line), harzburgite (solid green line) and basalt (dashed red line) are also reported and repeated in multiple panels as a direct comparison. Modified after Stixrude and Lithgow-Bertelloni (2012).

Figure 1.1-3a illustrates the phase transitions in pyrolite as a function of depth. At a depth of 410 km, $(\text{Mg,Fe})_2\text{SiO}_4$ olivine, or α phase, transforms to the high-pressure polymorph wadsleyite, also referred to as the β phase. This transition is now widely accepted to cause a discontinuity in seismic wave velocity observed globally at this depth. At approximately 17.5 GPa, corresponding to a depth of 520 km, wadsleyite undergoes a phase transition to ringwoodite, also termed γ -phase. This transformation may also cause a weak seismic discontinuity observed at this depth. At approximately 24 GPa, ringwoodite breaks down to an assemblage of $(\text{Mg,Fe})(\text{Si,Al})\text{O}_3$ with the perovskite structure, now called bridgmanite, and $(\text{Mg,Fe})\text{O}$ ferropericase. Such a transition is generally believed to be the main cause of the 660 km discontinuity (Ita and Stixrude, 1992; Frost, 2008). On the Si- and Al-rich side of the pyrolitic compositional diagram, orthopyroxene (opx), clinopyroxene (cpx) and garnet are the stable mineral phases in the upper mantle. With increasing pressure, both opx and cpx components start to dissolve into garnet with substitution of Mg, Fe and Si onto the octahedral site of the garnet normally occupied by Al. The resulting garnet structured phase with pyroxene stoichiometry $(\text{Mg,Fe})_4\text{Si}_4\text{O}_{12}$ is called majorite. At mid-transition zone

conditions of approximately 18 GPa, CaSiO_3 starts to exsolve from garnet, forming calcium silicate perovskite. At depths greater than 660 km, the remaining garnet starts to dissolve into magnesium silicate perovskite. At depths of the lower mantle, a pyrolite phase assemblage comprises magnesium silicate perovskite (Mg-Pv), ferropericlase and calcium silicate perovskite (Ca-Pv). At pressures of 125 GPa and temperatures of 2500 K, conditions close to those of the D'' layer near the core–mantle boundary (CMB), magnesium silicate perovskite transforms to a post perovskite polymorph with a CaIrO_3 structure (Murakami et al., 2004).

Phase proportions in harzburgite are reported in Figure 1.1-3b. Compared to pyrolite, harzburgite rocks contain only small amounts of Ca and Al due to melt extraction. They similarly contain less Fe than pyrolite and consequently have a lower Fe/Mg ratio (see Table 1.1-1). Harzburgite comprises an assemblage of approximately 80% olivine and 20% opx at depths of the uppermost mantle. The olivine transformation sequence in harzburgite is similar to that in pyrolite. However, due to the low Al content, the $(\text{Mg,Fe})\text{SiO}_3$ pyroxene component may not be entirely incorporated into garnet at transition zone conditions, but can, if temperatures are below approximately 1600°C, transform directly to akimotoite, an ilmenite-structured $(\text{Mg,Fe})\text{SiO}_3$ phase which forms at approximately 600 km (Frost, 2008). Akimotoite transforms into $(\text{Mg,Fe})(\text{Al,Si})\text{O}_3$ perovskite at lower pressures than ringwoodite, shifting the perovskite stability field to shallower depths compared to a pyrolite composition. In the lower mantle a harzburgite bulk composition crystallises as approximately 75 wt % perovskite, 23 % ferropericlase and 2 wt % calcium perovskite.

Phase relations for a MORB bulk composition (Figure 1.1-3c) are different from those anticipated in pyrolite and harzburgite compositions. Relative to a pyrolitic composition, a MORB composition is enriched in the major elements that behave more incompatibly during melting at mid-ocean ridges, such as silicon, aluminium, calcium and sodium, and is depleted in compatible elements such as magnesium (see Table 1.1-1). In the mantle transition zone, basaltic compositions are comprised almost entirely of majoritic garnet with additional stishovite (Irifune and Ringwood, 1987, 1993; Hirose et al., 1999; Ono et al., 2001). This assemblage progressively transforms to one comprising Ca-Pv, Mg-Pv, stishovite and an additional aluminium rich phase over a pressure interval of approximately 3 GPa (Irifune and Tsuchiya, 2007). As the transformation into $(\text{Mg,Fe})(\text{Al,Si})\text{O}_3$ perovskite involves only garnet, the perovskite stability is shifted to greater depths with respect to pyrolite. Due to the

lower Mg/Si ratio compared to pyrolite, MORB composition assemblages at lower mantle conditions do not contain ferropericlaase. Several high-pressure phase equilibria studies on minerals of basaltic subducting slabs have shown that additional aluminium-rich phases can form at lower mantle conditions after the breakdown of garnet. One of these Al-rich phases with the general formula $(\text{Na,Ca})(\text{Mg,Fe})_2(\text{Al,Si})_6\text{O}_{12}$ has been proposed to have a hexagonal structure (Akaogi et al., 1999; Miura et al., 2000; Gasparik et al., 2000) and is referred to as NAL (short for new aluminium phase). Other authors have reported the occurrence of an Al-rich phase with the formula $(\text{Na,Mg})(\text{Al,Si})_2\text{O}_4$ with a calcium-ferrite type structure (CF) (Irifune and Ringwood, 1993; Kesson et al., 1994; Hirose et al., 1999, 2005; Ono et al., 2001, 2005). Both NAL and CF are found to coexist up to approximately 50 GPa but NAL disappears above 50 GPa (Perrillat et al., 2006; Ricolleau et al., 2008, 2010). The CF type phase has been observed in MORB composition assemblages up to 130 GPa (Hirose et al., 2005; Ono et al., 2005).

Subducting slabs sink into the mantle because they are negatively buoyant. There are two important sources of slab buoyancy that influence the nature of subduction zones: negative buoyancy forces due to temperature differences with the surrounding mantle and buoyancy anomalies arising from differences in the density of mineral phases between the slab and surrounding mantle- so called “petrological” buoyancy forces. For the main part negative buoyancy originates from the temperature difference between the cold slab and warm mantle material. Slabs are cold when they enter the mantle and warm up only gradually due to the inefficiency of thermal conduction (Figure 1.1-4).

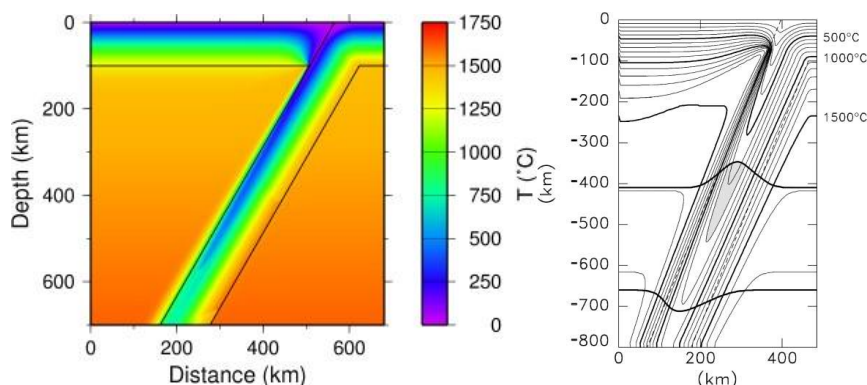


Figure 1.1-4. (Left) Calculated temperature distribution within a subducting slab (Source: Seifert, 2004). (Right) Thermal model of the Izu-Bonin subducting slab. Equilibrium boundaries for the 410 and 660 km discontinuities are displayed using Clapeyron slopes of +2.9 and $-1.9\text{MPa}/^\circ\text{C}$, respectively. The shaded region illustrates a possible metastable region bounded by the 700°C isotherm (see Collier et al., 2001 for more details).

Tectonic plates have a large range of ages, crustal thickness and consequent buoyancies as they enter subduction zones. As a result large variations exist in the evolution of slab thermal structure with depth. Younger plates are generally hotter and have shallow subduction angles and slower subduction velocities. Such slabs will thermally equilibrate more rapidly with the surrounding mantle. Older plates are generally colder and sink more rapidly at steeper angles. As a result lower internal temperatures are maintained to greater depths during subduction (Anderson, 2007). Due to the temperature contrast between a subducting slab and the ambient mantle, phase transformations between low and high-pressure mineral phases can occur at different depths depending on the nature of the corresponding Clausius-Clapeyron slope (Figure 1.1-4). Low temperatures in the mantle component of a slab, for example, result in an upward deflection (due to their positive Clapeyron slopes) of the $\alpha \rightarrow \alpha + \beta \rightarrow \beta$ and the $\beta \rightarrow \beta + \gamma \rightarrow \gamma$ transitions from their nominal depths in the ambient mantle of 410 and 520 km, respectively (Akaogi et al., 1989). Conversely a downward deflection of the $\gamma \rightarrow \text{pv}$ (perovskite) + mw (magnesiowüstite) transformation from its nominal depth of 660 km (see Bina et al., 2001 and references therein) should occur due to the negative Clapeyron slope of this transition. As these transformations cause significant increases in density, then at certain depths there can be a lateral concurrence of phase assemblages of differing densities resulting in “petrological” buoyancy forces (Bina et al., 2001). In addition, due to the low temperature conditions in the subducting lithosphere, chemical reactions may be kinetically inhibited, leading to the metastable persistence of low-pressure minerals into the stability fields of high-pressure phases (Rubie and Ross, 1994; Tetzlaff and Schmelting, 2000; van Mierlo et al., 2013). The resulting spatial variations in mineralogy will further supplement petrological buoyancy forces that ultimately control the rate and style of downward convection.

The buoyancy forces, thermal and petrological, described above, have important effects on the physical behaviour of subducting slabs. As noted by Ringwood (1976), when differentiated oceanic lithospheric plates sink into the mantle, phase transformations in the respective mafic, harzburgite and lherzolite layers will occur at different depths because of the different chemical compositions. The depths and extent to which the different layers sink may be controlled by the sequence and properties of the phase transformations that take place. Consequently, some of the phase transformations associated with larger density changes, such as the $\gamma \rightarrow \text{pv} + \text{mw}$ transformation, may act as a chemical filter, leading to significant degrees of lateral and vertical chemical heterogeneity in the mantle (Ringwood, 1976). In order to constrain the balance of forces that control the fate of subducting slabs in

the deep mantle, a comprehensive analysis of the density structure which takes into account the effects of all important phase transformations in the slab-mantle system is necessary (Ganguli et al., 2009).

In the past decades, numerous studies have focused on the fate of basaltic crust in the deep mantle. For instance, Hoffmann and White (1982) anticipated that the basaltic crust of a slab has a greater density than the mantle throughout its entire depth, and consequently it should separate from the associated lithosphere and sink, possibly all the way to the core-mantle boundary, and potentially forming an accumulation of subducted crustal material. Anderson (1989) on the other hand suggested that the basaltic crust becomes less dense than the pyrolytic mantle at the 660 km discontinuity, being thus trapped during subduction to form a “perched eclogite layer”. This was later supported by Irifune and Ringwood (1993), who presented high-pressure experimental work on the behaviour of MORB up to 27 GPa. Later, Hirose et al. (1999) found that basaltic oceanic crust is no longer buoyant when it transforms to a perovskite lithology at about 720 km, and therefore would gravitationally sink into the lower mantle. Numerous other experimental studies have focused on the fate of MORB at the 660 km discontinuity region (e.g. Litasov et al., 2004; Litasov and Ohtani, 2005; Ricolleau et al., 2010). Some studies indicate that subducting slabs may become buoyant in the lower mantle at depths below 1500-2000 km (Kesson et al., 1998; Ono et al., 2001) whereas, recent works suggest that MORB remains denser than the average mantle and can ultimately reach the core-mantle boundary (Ono et al., 2005; Hirose et al., 2005; Ricolleau et al., 2010). Using results from *in situ* determinations of mineral transformations in basalt, Litasov et al. (2004) concluded that there is no density cross-over between the basaltic component of a cold slab and surrounding mantle at 660 km depth. Consequently these authors suggested that the basaltic component should penetrate into the lower mantle without gravitational separation from the peridotite body of the slab.

In spite of the different high-pressure experimental studies, the behaviour of the subducting slabs in the deep mantle remains unclear. Most of the recent data reported above determined the phase relations, mineral chemistry and densities of basaltic compositions by combining *in situ* X-ray diffraction measurements and chemical analysis. The densities of the individual high-pressure phases are calculated at given pressures and temperatures using thermal Equations of State (EoS) along an appropriate geotherm (e.g. Irifune and Tsuchiya, 2007; Ricolleau et al., 2010). The density changes in the bulk compositions are then calculated

using the proportions of the individual phases at different pressures along a geotherm (Figure 1.1-5).

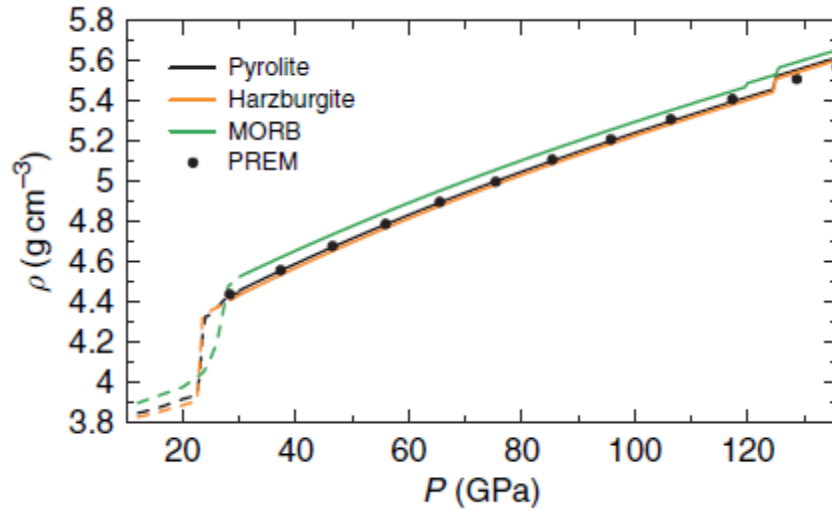


Figure 1.1-5. Bulk density variations of pyrolite, harzburgite, and MORB calculated based on the P - V - T Equations of State (EoS) of the different constituent mineral phases and their respective proportions reported in Irifune and Tsuchiya (2007). Broken lines are results from Irifune (1993) performed at pressures below 30 GPa. Dots represent the PREM (Primary Reference Earth Model) from Dziewonski and Anderson (1981). Source: Irifune and Tsuchiya (2007).

The results of in situ X-ray diffraction measurements depend largely on the choice of pressure standards. The problem of pressure scale becomes, therefore, a major issue in such experiments. In fact, the pressure at which these measurements apply has a large uncertainty as it is determined from X-ray unit cell measurements of calibrant materials. The P - V - T EoS of a pressure standard is usually derived on the basis of a conversion of dynamic shock Hugoniot data to isothermal compression data. Consequently the material properties are not studied under the conditions where they are to be used as a calibrant but must be extrapolated. The resulting uncertainties in the pressure measurement may be quite large. Platinum (Pt) and gold (Au) are widely used as internal pressure standards in situ X-ray diffraction measurements at high pressure because of their intense diffraction peaks, low chemical reactivity, and high crystal symmetry (Irifune and Tsuchiya, 2007). An estimate of the real uncertainties can be obtained simply by extrapolating different EoS reported for gold in the literature (Irifune and Tsuchiya, 2007) which result in pressure estimates from the same unit cell dimensions that differ by over 2 GPa (equivalent to approximately 60 km) at pressures >20 GPa (see for example Irifune and Tsuchiya, 2007; Fei et al., 2007) and at a

temperature of 2300 K. Large uncertainties on the pressure values will cause inaccuracy in the equations of state (EoS) and consequently in density calculations. Aside from affecting density determinations, the lack of an absolute primary pressure scale is a major problem for interpreting observations of mantle seismic discontinuities.

1.2 Chemical heterogeneities in the mantle: geophysical signatures vs geochemical evidence

The fate of slabs at the 660 km discontinuity has been a highly debated subject of recent years also from the geophysical and geochemical point of view. Global tomography studies (e.g. Kárason and van der Hilst, 2000) showing the different styles of subduction across the upper mantle and transition zone indicate that some slabs penetrate the 660 km boundary and sink into the lower mantle, whereas others slabs appear to be deflected at the boundary, supporting the concept that they encounter significant resistance to entering the lower mantle (Figure 1.2-1).

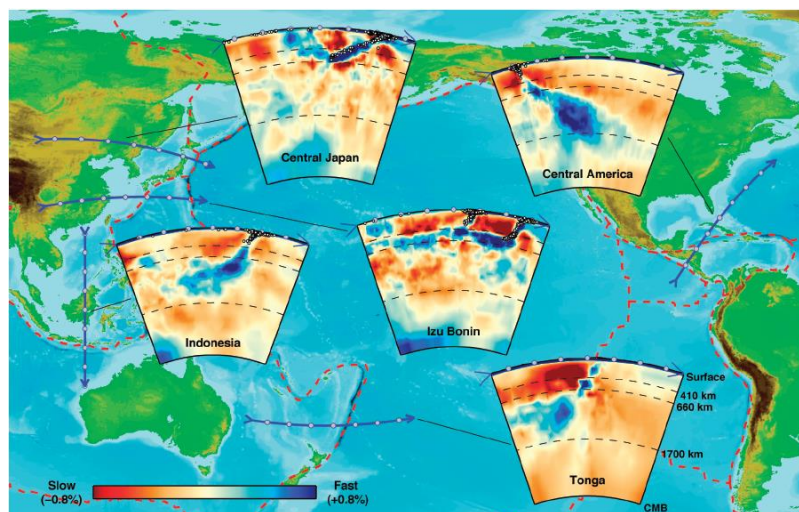


Figure 1.2-1. Slab structure illustrated by vertical mantle sections across several subduction zones in the Western Pacific and Central America. Source: Bass and Parise (2008). See Karason and van der Hilst (2000) for further details.

Whether the subducting slabs deflect and flatten at 660 km or penetrate into the lower mantle is a major seismological and geochemical debate since it can reinforce or weaken the hypothesis of whole mantle versus layered convection through Earth's history (e.g., Hofmann, 1997; Van der Hilst et al., 1998; Hellfrich and Wood, 2001).

Although the major element composition of the upper mantle appears to have remained uniform over time, trace element and isotopic studies imply the presence of significant heterogeneities in the basalt source region (see e.g. Frost, 2008). Geochemical analyses of the basaltic products of mantle melting are frequently used to infer that mantle convection is layered, with the deeper mantle largely isolated from the upper mantle. However, tomographic images of cold slabs in the lower mantle and the occurrence of small-scale heterogeneities in the lower mantle indicate that subducted material penetrates the deep mantle (Figure 1.2-2), implying whole mantle convection (Hellfrich and Wood, 2001).

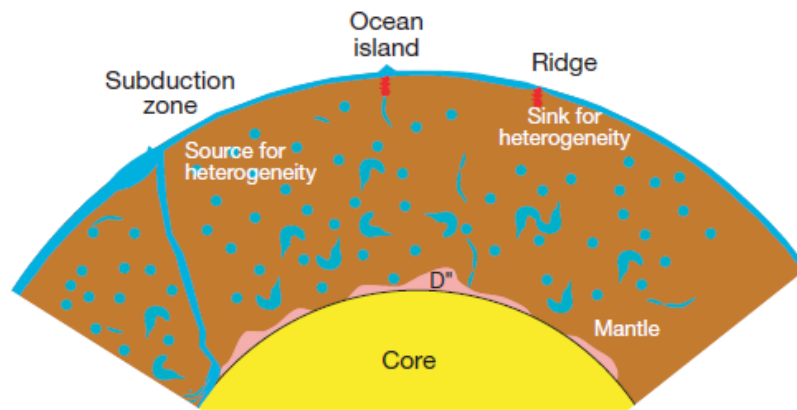


Figure 1.2-2. 2D section of the inner Earth showing the model proposed by Hellfrich and Wood (2001) of a chemically unstratified mantle. The subduction of oceanic lithosphere introduces heterogeneity into the mantle. Mixing by convective stirring of the mantle disaggregates the subducted lithosphere but does not lead to homogenization due to the long time scales required for chemical diffusion. This produces isolated heterogeneities that can scatter seismic waves. Melting at mid-ocean ridges and at ocean islands produces basalts which are a mixture of melts from the two types of mantle material.

Recent advances in seismological observations suggest that compositional heterogeneity in the deep mantle is ubiquitous, and is particularly strong beneath 2000 km depth (e.g. Van der Hilst, 2004 and references therein). Due to the extremely long time scale required for the chemical equilibration of subducted crustal heterogeneities in the lower mantle (Holzapfel et al., 2005), it has also been proposed that the bulk of the mantle might be a mechanical mixture between a depleted mantle residue and subducted crustal components (Xu et al., 2008). As a result, seismic velocities may reflect the average velocities arising from this mixture of different mineral assemblages (Xu et al., 2008). In addition, it is possible that due to the stagnation of subducting material (i.e. in the transition zone, as suggested by van Mierlo et al., 2013), chemically distinct material may accumulate at specific depths in the mantle.

Hence, it is important to identify the factors that influence lateral heterogeneity in density and seismic velocities. In particular, it is essential to understand whether seismic heterogeneities are thermal or chemical in origin. For many years it was thought differences in velocity particularly in the lower mantle were due to differences in temperature alone, with low seismic velocities attributed to elevated temperatures. By assuming seismically slow material was hot and buoyant, the observations could be combined with geodynamic modelling to understand the regional operation of mantle flow (Bass and Parise, 2008). However, such direct scaling is unwarranted as shear wave speeds and temperature are not sufficiently correlated (van der Hilst, 2004). Also, at the high pressures of the deep mantle there is little thermal expansion, and so the chemical contribution to buoyancy can easily exceed the thermal effect. It is increasingly clear that such heterogeneities are more likely due to a combination of chemical, thermal, and phase-change effects (Trampert et al., 2004). Trampert et al. (2004) argue that the traditional view that slow wave speed implies high temperatures (and thus positively buoyant material) is not always correct and that in the deep mantle lower mantle slow wave speeds may be due to the higher intrinsic density of negatively buoyant material (Figure 1.2-3).

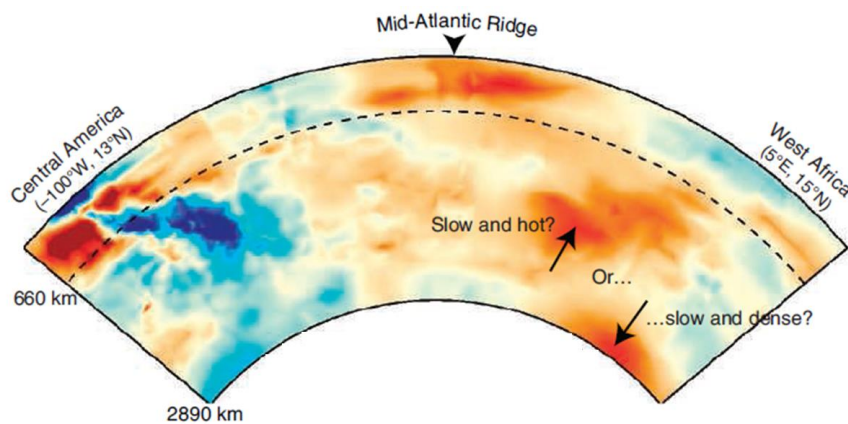


Figure 1.2-3. Primary wave speed variations in the mantle between Central America and Africa, from Earth's surface to the core-mantle boundary (~2890 km depth). The blue structure on the left depicts the slab of subducted lithosphere of the former Farallon tectonic plate, which dips very deep into the mantle, whereas the red structures on the right mark the low wave speeds deep beneath West Africa. Source: van der Hilst (2004).

To correctly interpret the available observations in terms of chemistry and mantle mineralogy, high-pressure experimental data on the elasticity of minerals likely to comprise these anomalies are therefore essential.

1.3 Seismological observations of the inaccessible Earth

As most mantle rock samples come from depths of less than 200 km, seismic observations provide the primary tool for understanding the chemistry and structure of the otherwise inaccessible Earth's interior. The major divisions of the Earth i.e. crust, mantle and core, in addition to mantle and core subdivisions e.g. upper mantle and transition zone, are defined from seismology, as revealed by the one-dimensional models such as the preliminary reference Earth model, PREM (Figure 1.3-1).

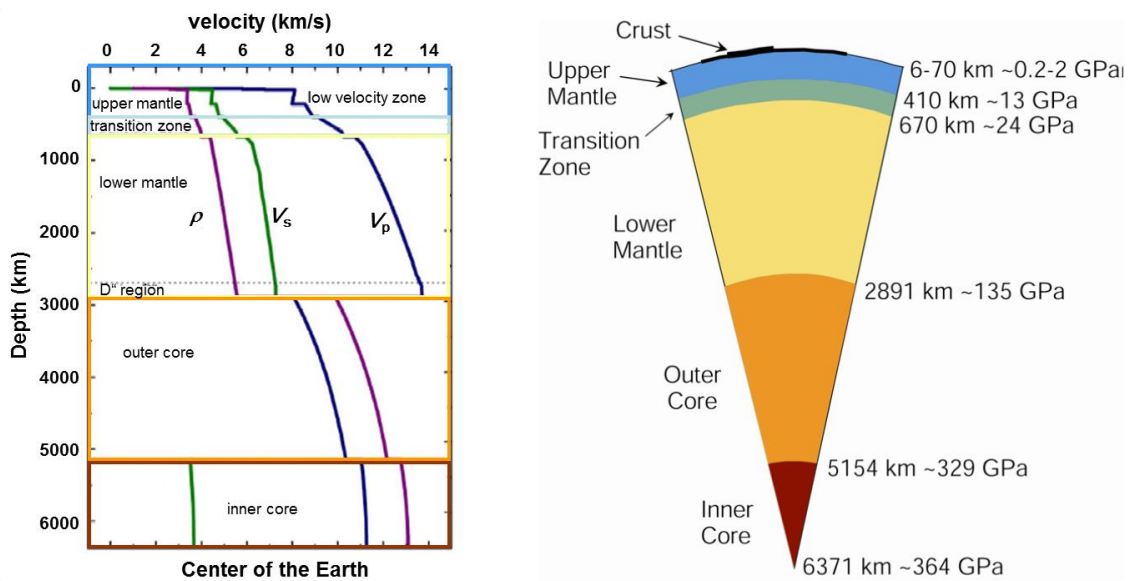


Figure 1.3-1. Concentric internal subdivision of the Earth into crust, upper mantle, transition zone, lower mantle and outer and inner core as defined by the preliminary reference Earth model, PREM (Dziewonski and Anderson, 1981).

When earthquakes occur, two types of acoustic waves are generated that propagate through the deep Earth: the primary, or compressional, P-waves, which are faster and vibrate material parallel to the direction in which the wave propagates, and the secondary, or shear, S-waves, which are slower and vibrate material perpendicular to the direction in which the wave propagates. Seismological studies of these wave arrival times at different places on the globe reveal the velocity variation of P-waves and S-waves with depth (Bass and Parise, 2008). The crust, extending to an average depth of 6 km beneath ocean basins and 70 km beneath continents, is separated from the mantle by the Mohorovičić seismic discontinuity (the Moho). The Earth's mantle, defined in terms of major seismic discontinuities occurring near 410 and 660 km, is divided into an upper mantle, a transition zone, and a lower mantle. In the

transition zone, the part between the major seismic discontinuities at 410 km and 660 km depth, velocity gradients are high. In the lower mantle, considered as starting at the 660 km discontinuity, seismic velocities vary smoothly and gradually with depth. Beneath the mantle is the liquid outer core, where P wave speeds drop dramatically and S-waves do not propagate, followed by the solid inner core where seismic velocities recover but are still depressed compared to the silicate mantle.

Seismic reference models such as the Preliminary Reference Earth Model (Dziewonski and Anderson, 1981) and the AK135 (Kennet et al., 1995) provide a radially symmetric velocity depth profile of the Earth based on the inversion of body wave travel time data and normal mode periods. In these models velocities in the Earth's interior are refined to a set of polynomial functions that operate over a specified depth interval, with the assumption that mantle discontinuities occur at fixed depths. A different procedure, proposed by Cammarano et al. (2005), consists of fitting the same global seismic data to models calculated for actual mineral assemblages, assuming a particular bulk composition and temperature gradient.

Seismic models are used to examine petrological models representing the mineral assemblages as a function of depth. The main approach consists in assuming a mantle bulk composition, determining the mineralogy as a function of depth and then calculating the sound velocities for this assemblage using mineral-physics data. The difference between the observed seismic properties and those calculated for the assumed mineral assemblage (Frost, 2008) gives a measure of the goodness of the model. Different methods have been used to estimate the upper-mantle composition. One method employs analyses of xenoliths that appear to have been unaffected by melting. Others assume that certain elements in the mantle have chondritic ratios. In 1976, Ringwood proposed a mantle composition, named pyrolite, constructed by mixing a basalt composition with a corresponding mantle-melt residue. Differences in major-element concentrations between most of the proposed upper-mantle compositions seem relatively minor (Walter, 2004) and most of the compositions result in olivine contents in the range 49-62%, with pyrolite falling in the middle (56%).

Seismic waves velocities through the Earth depend on the elastic properties of the minerals through which they travel in the interior. In the special case of an elastically isotropic material, average compressional V_p and shear V_s wave velocities can be computed from the shear G and (adiabatic) bulk modulus K_s and the density ρ (e.g. Poirier, 2000; Karki et al., 2001) according to the following identities:

$$V_p = \sqrt{\frac{K_s + (4/3)G}{\rho}}, \quad (1.1)$$

$$V_s = \sqrt{\frac{G}{\rho}} \quad (1.2)$$

The shear modulus, or rigidity describes the response of a material to shear stress, whereas, the bulk modulus or incompressibility measures the resistance of a material against a change of volume. By comparing the elastic properties of relevant mantle minerals with seismic properties it is possible to constrain the chemical and thermal state of the interior of the Earth.

1.4 Elastic properties of mantle minerals

Hooke's law, "*Ut tensio, sic vis*" literally translated "As the extension, so the force", establishes that for any elastic material undergoing small distortions due to stress, there is a simple linear relationship between stress and strain. In the case of a crystal of arbitrary symmetry, Hooke's law can be generalized as follows (e.g. Nye, 1985):

$$\sigma_{ij} = c_{ijkl} \varepsilon_{kl} \quad (1.3)$$

where σ_{ij} is the stress tensor, ε_{kl} is the strain tensor, and c_{ijkl} are the elastic stiffness constants (Nye, 1985). Note that the Einstein summation is assumed. The relation between elastic strain and stress can also be expressed as:

$$\varepsilon_{ij} = s_{ijkl} \sigma_{kl} \quad (1.4)$$

where s_{ijkl} are the elastic compliances. Both stress and strain are second rank tensors, where the first subscript gives the direction of force or displacement and the second subscript refers to the normal to the face on which the force acts or deformation occurs. The elastic stiffness tensor is a fourth rank tensor containing 81 components (Nye, 1985). Since static equilibrium is required (no translation or rotation) both stress and strain tensors are symmetric, so the 81 independent components of the elastic stiffness tensor are reduced to 36. Further, the change in energy per unit volume of a body resulting from a set of strains ε_{ij} is given by the sum

$\frac{1}{2} \sum_{ijkl} c_{ijkl} \varepsilon_{ij} \varepsilon_{kl}$ over all the strain components and tensor components (Angel et al., 2009). The

energy for a given set of strains must be independent of the order in which the strains ε_{ij} and

ε_{kl} are considered in the summation; this requires that the terms $c_{ijkl}\varepsilon_{ij}\varepsilon_{kl}$ and $c_{klij}\varepsilon_{kl}\varepsilon_{ij}$ must be equal. This can only be achieved if $c_{ijkl} = c_{klij}$ for all of the tensor components. The same is true also for the compliance tensor. In this way, the number of independent components is reduced from 36 to 21, and this number is further reduced by crystal symmetry (Nye, 1985). The described symmetry requirements allow for expressing the elastic tensor components in a simplified Voigt (Voigt, 1928) notation, where the four indices are replaced according to the following conventions: 11 = 1, 22 = 2, 33 = 3, 23 = 4, 31 = 5, 12 = 6.

In general, single-crystals are elastically anisotropic regardless of the symmetry. As a result, elastic wave velocities depend on the direction of propagation. The single-crystal elastic percentage anisotropy A can be described as follows:

$$A = 200 \times \left[\frac{(V_{i\max} - V_{i\min})}{(V_{i\max} + V_{i\min})} \right] \quad (1.5)$$

where $V_{i\max}$ and $V_{i\min}$ correspond to maximum and minimum velocities which are found by exploring a hemisphere of all possible propagation directions (Mainprice, 2007). The subscript I can be replaced by “p” for the compressional or “s” for the shear wave anisotropy. For the P-wave velocities the anisotropy is defined by the maximum and minimum velocities in two different propagation directions, for example, the maximum A is given by the maximum and minimum V_p in a hemisphere. For S-waves in an anisotropic medium there are two orthogonally polarized S-waves with different velocities for each propagation direction. Consequently, A can be defined for each direction (Mainprice, 2007).

In a polycrystalline material, each individual grain is usually anisotropic and randomly aligned within the bulk material. The elastic behavior of a polycrystalline material is described by its bulk modulus, K , and shear modulus, G as follows:

$$K = \frac{1}{3}(C_{11} + 2C_{12}) \quad (1.6)$$

$$G = C_{44} = \frac{1}{2}(C_{11} - 2C_{12}) \quad (1.7)$$

Note that the elastic constants C_{11} , C_{12} , and C_{44} are isotropic cases, and are not the same as the single-crystal elastic constants associated with individual grains. Experimental methods determining K and G of polycrystalline materials often employ single crystal samples of the same material. An aggregate average over the single crystal elastic constants can be

calculated to obtain isotropic values for the polycrystalline sample. The average value lies between two limits named the Reuss and Voigt bounds. The arithmetic average of the two bounds, (Voigt-Reuss-Hill average) is frequently used (Hill, 1952). The Reuss bound (Reuss, 1929), is calculated assuming that the stress is uniform in the aggregate and that the strain is the total sum of all the strains of the individual grains in series. The effective isotropic compliances are derived in terms of single-crystal compliances (s_{ij}) averaged over all orientations, where the bulk and shear moduli are expressed as follows (Watt et al., 1976):

$$K_R = [3(a + 2b)]^{-1} \quad (1.8)$$

$$G_R = 5/(4a - 4b) + 3c) \quad (1.9)$$

$$\text{where } a = \frac{1}{3}(s_{11} + s_{22} + s_{33}), \quad b = \frac{1}{3}(s_{12} + s_{23} + s_{31}), \quad c = \frac{1}{3}(s_{44} + s_{55} + s_{66}) \quad (1.10)$$

The Voigt bound (Voigt, 1928), is calculated assuming that the strain is uniform and that the stress is supported by the individual grain in parallel. The bulk and shear moduli are expressed as follows:

$$K_V = \frac{1}{3}(A + 2B) \quad (1.11)$$

$$G_V = \frac{1}{5}(A - B + 3C) \quad (1.12)$$

$$\text{where } A = \frac{1}{3}(C_{11} + C_{22} + C_{33}), \quad B = \frac{1}{3}(C_{12} + C_{23} + C_{31}) \quad \text{and} \quad C = \frac{1}{3}(C_{44} + C_{55} + C_{66}) \quad (1.13)$$

There are numerous descriptions of the derivations of the expressions for Voigt and Reuss limits of K and G for different symmetries (Meister and Peselnick, 1966; Ledbetter, 1973; Watt et al., 1976; Watt, 1979; 1980; 1986; Watt and Peselnick, 1980). The specific formulations used in this thesis for cubic and hexagonal symmetries are given by Ledbetter (1973) and Watt and Peselnick (1980).

The Earth is composed of multi-phase mineral assemblages (rocks), with adjacent grains having different elastic properties. In order to link experimentally determined single-crystal elastic properties of mantle minerals to the large-scale elastic properties sampled by seismology, averaging schemes are required. In particular, once the elastic properties of each

individual mineral phase are determined as a function of pressure and temperature, they must be combined to determine the seismic velocity of a multiphase assemblage.

The volume fraction of the individual minerals in an assemblage can be defined as follows:

$$v_i = n_i \frac{V_i}{V} \quad (1.14)$$

where V_i and n_i are the molar volume and the molar fractions of the i th individual phase, and V is the total molar volume of the assemblage:

$$V = \sum_i n_i V_i \quad (1.15)$$

From this, the density of the mineral phase assemblage can be determined:

$$\rho = \sum_i v_i \rho_i = \frac{1}{V} \sum_i v_i \mu_i \quad (1.16)$$

where ρ_i and μ_i are the density and the molar mass of the i th individual phase.

The bulk and shear moduli of a multiphase rock, depend on the specific distribution and orientation of the constituent minerals. As noted above, there are several schemes for averaging the elastic moduli, but there is no analytical solution of the problem in contrast to the analysis of single crystals elasticity. The Voigt average, assuming constant strain across all phases, is defined as:

$$X_V = \sum_i v_i X_i \quad (1.17)$$

where X_i is the bulk or shear modulus for the i th phase. The Reuss average, assuming constant stress across all phases, is defined as:

$$X_R = \left(\sum_i \frac{v_i}{X_i} \right)^{-1} \quad (1.18)$$

The Voigt-Reuss-Hill average is the arithmetic mean of Voigt and Reuss bounds:

$$X_{VRH} = \frac{1}{2} (X_V + X_R) \quad (1.19)$$

Finally, once the elastic moduli of the multiphase assemblage are computed the compressional and shear wave velocities can be determined. Further details regarding this thematic can be found in Cottaar et al. (2014).

1.4.1 Elasticity measurements

As noted above, by comparing the elastic properties of relevant mantle minerals with seismic properties it is possible to constrain the chemical and thermal state of the interior. However, an important limitation of this approach is the lack of knowledge of mineral elastic properties at the extreme conditions of the Earth's mantle (i.e. up to 130 GPa and 2800 K).

Different experimental approaches for measuring elastic properties, including ultrasonic interferometry, Brillouin spectroscopy, impulsive stimulated scattering (ISS), resonant ultrasound spectroscopy (RUS), or synchrotron based techniques such as inelastic X-ray scattering and nuclear resonance inelastic scattering, have been developed and used to investigate the elastic behaviour of materials under ambient and not ambient conditions (see reviews by Li and Lieberman, 2007; Bass, 2007; Angel et al., 2009). In addition to physical measurements, atomic scale first-principles methods can be used to predict elastic properties of crystals (see review by Karki et al., 2001).

Although mineral-physics has examined such properties for over 40 years, the majority of measurements have been performed at room temperature and high pressure. Very few measurements have been performed on silicate minerals at simultaneously high pressures and temperatures, and those that have (i.e. Irifune et al., 2008), examined only the average properties of monomineralic polycrystalline aggregates. Aggregate properties overlook the intrinsic elastic anisotropy of most minerals, which is reflected in seismic anisotropy in the Earth. Many regions of the mantle in fact display pronounced seismic anisotropy, with seismic waves having differing speeds when propagating in different directions. To correctly interpret the seismic anisotropy requires knowledge of the complete set of individual elastic moduli for each mineral phase involved, rather than bulk elastic moduli.

Recent developments of externally heated diamond anvil cells with large optical access in combination with Brillouin scattering and X-ray diffraction (Sinogeikin et al., 2006; Trots et al., 2013) provide new possibilities to studying the full elastic tensor as well as density of single crystals at pressures and temperatures comparable with the conditions of the Earth's interior. Brillouin scattering on single-crystals has become the technique of choice as it allows the determination not only of the full elastic tensor of low symmetry materials but also their anisotropic behaviour. Such experiments, although more challenging and time consuming than those performed with powdered samples, give better constraints on the effect

of temperature and chemical substitution on the elastic behaviour of minerals. In addition, single-crystal X-ray diffraction data collections allow unequivocal crystal structure determination of high-pressure phases at conditions compatible to the Earth's mantle. Crystallographic studies in combination with measurements of sound velocities can reveal information on the nature of interatomic forces and compression mechanisms controlling mineral elasticity. Such studies under deep-Earth conditions have been limited so far to polycrystalline or powder samples, which give less-accurate results than single crystals (see Duffy, 2014).

1.5 Aims of this thesis

The principal aim of this project is to determine the P - V - T equation of state and V_s and V_p sound velocities of single crystals of minerals that form from subducted MORB crust at conditions compatible with the Earth's transition zone and lower mantle. In particular garnets along the pyrope-majorite substitution trend ($\text{Mg}_3\text{Al}_2\text{Si}_3\text{O}_{12}$ - $\text{Mg}_4\text{Si}_4\text{O}_{12}$), the NAL phase and CF type phase have been studied. Garnet is the dominant constituent of the crustal basaltic composition component of a subducting slab throughout much of the upper mantle and transition zone. Both CF and NAL phases will be major contributors to the bulk elastic properties in the lower mantle. The elastic constant tensors and the seismic properties of the NAL phase, which has a relatively low symmetry, require several crystal orientations for the complete experimental determination of the elastic constants tensor.

Single crystal elastic properties were determined using Brillouin scattering in conjunction with X-ray diffraction. Using these techniques the complete elastic tensor in addition to the density of the single crystals could be studied in the diamond anvil cell up to the high pressures of Earth's lower mantle. As both densities and velocities were measured simultaneously, pressure could be determined absolutely in each measurement, independent of calibrant materials or extrapolated equations of state.

Critical to the success of the project were developments in synthesis techniques employed in the large volume press that enabled large gem quality single crystals of high-pressure phases to be fabricated that were of suitable quality for both Brillouin and X-ray measurements. In addition, an externally heated diamond anvil cell (DAC) was designed for single-crystal Brillouin and X-ray measurements at high-pressure and high-temperatures.

Simultaneous measurements of density and sound velocities provide a complete description of the anisotropic elastic constants of these major mantle phases as a function of absolute pressure, temperature and composition. These data not only allow constraints to be placed on the seismic signature of chemical variations in the Earth's transition zone and lower mantle, but are also essential for determining the buoyancy of subducting slabs in the mantle and identifying levels in the mantle where slabs are likely to accumulate and create long-term chemical heterogeneity.

Finally, by combining these measurements with thermodynamic and phase equilibria data on mineral phases a joint petrological and mineral physics model is developed and compared with global seismic models.

2. Methods

2.1 Synthesis of high quality single crystals

A major obstacle to elasticity studies on high pressure minerals is the synthesis of large (at least 50 μm), high-quality single crystals. Both single crystal X-ray diffraction and Brillouin spectroscopy analyses in fact require extremely high-quality crystals without twins, significant stacking faults, inclusions or cracks. To be suitable for such measurements, crystals also need to be of appropriate size. Single-crystals with at least one dimension of approximately 100 μm provide optimal quality high-pressure data for both Brillouin scattering and X-ray diffraction. However, as crystals for Brillouin measurements need to be polished into plates with parallel faces, the initial unpolished crystals need to be even larger (see Section 2.3.4).

The first step in this project was, therefore, the development of a methodology for synthesizing large single-crystals at the conditions of the Earth's transition zone and lower mantle. The growth of high quality single- crystals of mantle minerals of more than 50-70 μm is extremely challenging and has been one of the major barriers to the study of single crystal elastic properties in the past. To enhance crystal growth, a flux is required to promote melting of the silicate assemblage and allow crystal growth in the presence of a melt (Ito and Weidner, 1986; Keppler et al., 2003; Shatskiy et al., 2007). Heating and cooling cycles can help to minimize the number of nucleating crystals causing fewer but larger crystals to grow (Dobson and Jacobsen, 2004). A critical balance between temperature, pressure and flux proportion has to be found for each mineral. Specific details on these issues are provided in the subsequent chapters.

2.1.1 Starting material preparation

For the synthesis of the high-pressure phases investigated in this study, the starting compositions were prepared by mixing oxides, hydroxide as well as carbonates in different proportions. The reagents were first dried at 1000 $^{\circ}\text{C}$ (for oxides) and at 120 $^{\circ}\text{C}$ (for hydroxides and carbonates) for 1 hour, then weighed in the required proportions (exact compositions are given in the following chapters) and finally mixed. When needed, the mixtures were placed in a Pt crucible, and decarbonated at 1000 $^{\circ}\text{C}$ for 6 hours. The mixtures

were ground under ethanol in an agate mortar for about 1 hour and then dried under an infra-red lamp. In some cases, a glass was prepared by melting the mixtures in air at 1600 °C for twenty minutes and then rapidly quenched in icy water, to ensure the homogenization of the starting material. Hydroxides if needed were added subsequently to the glasses. Finally, the starting mixtures were transferred to glass containers and stored in a desiccator.

2.1.2 Multi anvil apparatus

The high pressure phases were synthesized by performing high pressure (HP) and high temperature (HT) experiments with 500, 1200 and 5000 tonne multianvil presses at the Bayerisches Geoinstitut (BGI). The multianvil apparatus consists of a hydraulic press generating a uniaxial force, which is applied onto a set of 6 steel anvils also referred to as the first stage anvils. The first stage anvils form a cubic volume in which is placed a set of eight corner-truncated tungsten carbide cubes (second stage anvils). These truncated cubes create an octahedral high-pressure chamber, in which is placed the pressure cell containing the sample. Pyrophyllite gaskets are placed between the anvils to support the truncations and seal the high-pressure region. By varying the force exerted by the hydraulic press, the truncation edge length (TEL) of the second stage anvils and the octahedral edge length (OEL) of the pressure medium, different pressures can be achieved. Details concerning this technique and its applications can be found in Kawai and Endo (1970), Keppler and Frost (2005), Ito (2007), and Liebermann (2011).

The phases investigated in this thesis are stable at different pressure and temperature conditions, ranging from the upper mantle and transition zone (garnets) up to the lower mantle (NAL and CF). Therefore, the multianvil experiments were performed in the pressure and temperature range of 6-26 GPa and 1200-2260°C. Experiments conducted at 6 GPa, employed an 18 mm edge length Cr₂O₃-doped (5 wt%) MgO octahedron as a pressure medium with tungsten carbide cubes of 32 mm edge length and 11 mm truncation edge length (18/11 assembly). The powdered starting materials were loaded into platinum (Pt) capsules made of 2 mm outer diameter Pt tubing and had initial lengths of approximately 3.5 mm. Capsules were also fabricated from a 2 mm diameter Pt rod which was cut into sections and spark eroded on one surface producing different holes of approximately 0.6 mm depth and 0.25 mm in diameter. Each capsule contained 4 chambers where different starting mixtures were loaded. The capsule was enclosed in an MgO sleeve and two MgO spacers

were placed at the top and bottom of the MgO sleeve. Depending on the target pressure and temperature of the experiment, either a stepped graphite or LaCrO_3 resistance heater was employed. The temperature was monitored by means of Type D (W3\%Re/W25\%Re) thermocouple wires (0.25 mm thick) inserted, within a 4-hole alumina tube ($d=1.6$ mm, 4.35 mm in length), axially into the octahedral assembly. For pressures above 10 GPa the ZrO_2 sleeve was shortened and at the top and bottom two softer MgO rings were placed to compensate for the incompressibility of ZrO_2 within the MgO pressure media.

For pressures from 20 to 24 GPa a 10/4 assembly was employed. A cylindrical LaCrO_3 furnace was used, which was surrounded by an insulating ZrO_2 sleeve, to prevent excessive heat transport to the WC anvils. The capsule, with 1.2 mm diameter, was placed at the centre of the assembly and was separated from the furnace by an insulating MgO sleeve and MgO spacers filled the space at top and bottom of the sample. The temperature was measured using type D thermocouple wires (0.13 mm thick). The thermocouple within a 4-hole alumina tube ($d=1.2$ mm, 2.6 mm in length) was inserted axially into the octahedral assembly, with the hot junction in contact with the capsule. Thermocouple wire coils were used in order to protect the thermocouple as it passes through the gaskets.

At pressures of 26 GPa a 7/3 type assembly was used and a cross section of the assembly employed in these experiments is shown in Figure 2.1-1.

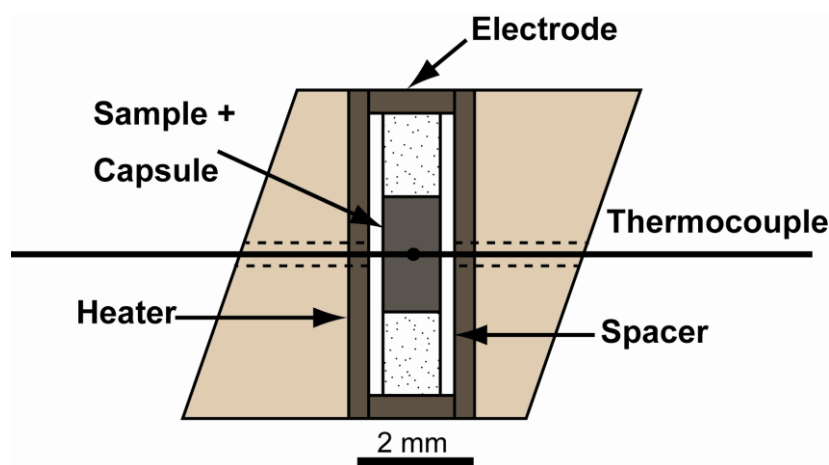


Figure 2.1-1. Schematic section through the octahedral pressure medium employed in the 7/3 assembly.

In this type of assembly, due to the reduced space, the LaCrO_3 furnace was placed directly into the octahedron and no insulating ZrO_2 sleeves were used. Type D thermocouple wires (0.07 mm thick) were inserted longitudinally, through the wall of the heater, with the hot

junction at the midpoint of the furnace. Small coils made of the same thermocouple wire protected the wires as they passed through the gaskets. Two platinum capsules containing each a different starting material, were used. The capsules (1 mm diameter) inside an insulating MgO sleeve were placed on top and bottom of the thermocouple junction. MgO spacers filled the space at the top and bottom of the sample. LaCrO₃ lids were located at the top and bottom of the heater in order to ensure good electrical contact with the anvils.

The pressure calibration curves for the assemblies used in this study are described in Frost et al. (2004) and Keppler and Frost (2005). For all multi-anvil experiments performed for this project, the samples were first compressed up to the desired pressure and then heated to the desired temperature. After heating at high pressure, the experiments were quenched isobarically by shutting off the power and the samples were recovered after slow decompression over 15 or 18 hours.

2.2 Sample characterization

After each multianvil experiment the capsules were recovered from the pressure cell, embedded in epoxy resin and polished. The experimental runs were then analyzed using scanning electron microscopy (SEM), electron microprobe analysis (EMPA) and X-ray diffraction to characterize the synthesized samples. The charges were coated with layers of carbon (up to 10 nm) to prevent charging on the surface when analyzing with SEM or EMPA.

2.2.1 Electron microscopy

In the present study, the run products were first characterized using *scanning electron microscopy*, which is a suitable technique for imaging and identifying high-pressure phases, and for determining semi-quantitatively the mineral compositions. In this technique a focused electron beam, generated from an electron gun, is scanned over a polished sample. Depending on the interaction between the electron beam and the sample, different signals can be generated. Backscattered electrons (BSE) for instance are produced by elastic interactions between the electrons and the atoms of the sample. In particular, these are electrons that are scattered once or several times off the atoms of the sample and have re-exited its surface. The intensity of the BSE is strongly dependent on the average atomic number of the target sample, providing an image of the sample with brightness that is a function of atomic mass. Moreover, when the electron beam collides with the sample, electrons from the inner shells

are ejected. Consequently, electrons from the outer shell fill the vacancy created by the inner shell electrons generating characteristic X-ray. The emitted X-rays, which have characteristic energies of each element present in the sample, can be simultaneously collected in energy dispersive (ED) mode allowing a rapid qualitative chemical analysis.

A GEMINI LEO (now Zeiss) 1530 scanning electron microscope operating at 20 kV was used for the analyses in a backscattered electron (BSE) imaging mode. A working distance of 13-14 mm was normally applied and preliminary phase identification was performed by means of EDS (energy dispersive spectroscopy) analysis using a Si(Li) detector (Oxford INCA).

Electron microprobe analyses were conducted in order to obtain precise quantitative analyses of the synthesized crystalline phases. Similarly to the SEM, an electron beam, produced by a tungsten filament, is focused and accelerated toward the sample being analyzed. When the high-energy electrons collide with the target material, characteristic X-rays are emitted. These characteristic X-rays can be analyzed either by an energy dispersive spectrometer (EDS) or by a crystal spectrometer (wavelength dispersive mode). For precise quantitative analyses the wavelength dispersive mode (WDS) was employed. In this mode, characteristic X-rays from the sample are selected based on their wavelength using the Bragg reflections from crystals with known d spacings. To select the different wavelengths, the electron microprobe is equipped with different crystal spectrometers (e.g. synthetic LiF, PET or TAP crystals) each with a specific d spacing. The intensity and position of each spectral line are then compared with those emitted by standards with known composition, allowing a precise quantitative analysis by comparison. Details concerning the electron microscopy techniques can be found for example in Reed (2005).

The element concentrations were measured with a JEOL JXA-8200 electron microprobe (EMPA), operating at 15 kV and 15 or 5 nA, depending on the phases being analyzed. The electron beam size was approximately 1-2 μm in diameter and the peak counting times were 20 s. Enstatite or diopside, spinel, forsterite, albite and metallic iron were used as standards for determining the concentrations of Si, Al, Mg, Na and Fe respectively.

2.2.2 X-ray diffraction

X-ray diffraction is a standard method for identifying crystalline samples, determining their unit-cell lattice parameters and also for determining the crystal structure. In high pressure

research, X-ray diffraction is commonly used to determine the density, compressibility or bulk modulus, and the thermal expansion, which are fundamental properties for the interpretation of seismic observations of the Earth's interior.

Initial X-ray diffraction measurements were used in this study to select high quality single-crystals of majoritic garnet and the NAL phase for further high pressure diffraction and Brillouin scattering measurements (Section 2.3.3 and 2.3.4). The crystals were selected according to their reflection intensity and sharpness of the peak profiles. For testing the crystals, a four-circle Huber diffractometer, equipped with MoK α radiation was employed, at operating conditions of 50 kV and 40 mA.

For single-crystal X-ray structural analyses, suitable crystals were selected from the run products, and mounted on glass fibers. Intensity data collections were performed on an Xcalibur diffractometer (operating at 50 kV and 40 mA and equipped with a CCD detector) using MoK α radiation (graphite monochromator). Details of the data collection and structure refinements strategy for each phase will be described in the following chapters.

2.3 Elasticity measurements at high pressure, HP, and high temperature, HT.

The novelty of this project resides in the use of single-crystals to determine the elastic properties of mantle minerals at HP and HT. Recent developments of externally heated diamond anvil cells with large optical access (Kantor et al., 2012) allow measurements of unit cell volume (density) by X-ray diffraction and acoustic velocities by Brillouin scattering (Sinogeikin et al., 2006; Trots et al., 2013). The combination of these techniques provides new possibilities to study the full elastic tensor of minerals at high pressures and temperatures compatible with conditions in the Earth's interior (Sinogeikin et al., 2006; Mao et al., 2012; Lu et al., 2013). Moreover, measuring simultaneously density and sound velocities for the same sample at the same conditions allows accurate determination of the absolute pressure without having to rely on a secondary pressure scale (Trots et al., 2013).

The following part of this chapter provides a description of the techniques employed for single-crystal elasticity measurements. Firstly, we report the principles of operations and the type of diamond anvil cell employed in this study, we then discuss the absolute pressure determination resulting from simultaneous measurements of sound velocities and density.

Finally we describe the X-ray diffraction and Brillouin scattering systems employed at BGI and at the 13-BM-D beamline of the GSECARS sector at the Advanced Photon Source (APS), Argonne National Laboratory that allow measurements of X-ray diffraction in combination with Brillouin scattering in the same experimental setup.

2.3.1 Externally heated diamond anvil cell

High-pressure measurements were performed using a Diamond Anvil Cell (DAC). The sample, together with a pressure calibrant, is placed in a pressure chamber created between the flat parallel faces (culets) of two opposite diamond anvils and the hole drilled in the middle of an indented metal foil (gasket). The pressure chamber is filled with a pressure transmitting medium, a fluid or gas, which exerts a hydrostatic pressure on the sample (Figure 2.3-1).

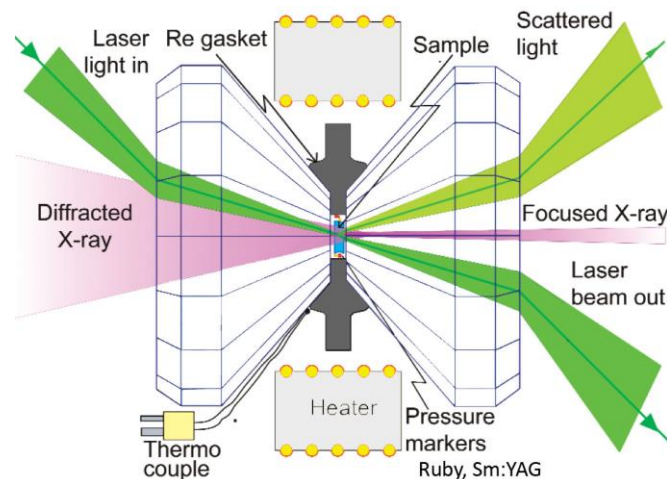


Figure 2.3-1. Schematic of an externally heated DAC suitable for X-ray diffraction and Brillouin scattering. Modified after Sinogeikin et al. (2006)

The pressure is generated by forcing the two diamonds together through screws/bolts. For a successful operation of the DAC at high pressure, the two diamonds must remain coaxial and perfectly aligned against each other. Further details about principles of cell operation can be found in Miletich et al. (2000).

In the experiments a piston cylinder type DAC with a wide conical opening on both sides of the cell was used (Kantor et al., 2012). In such a DAC, one diamond anvil is attached to a piston moving inside a perfectly matching cylinder carrying the other anvil. Low birefringence and low fluorescence Boehler-Almax diamonds were employed in combination

with tungsten carbide seats, providing a large angular access of 90° to the sample (Figure 2.3-2).

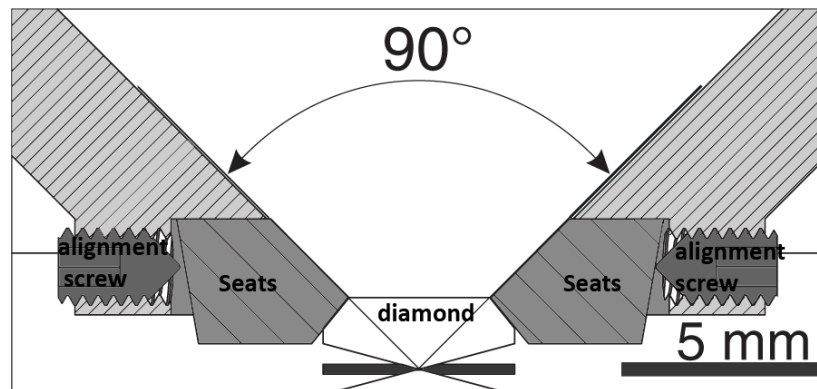


Figure 2.3-2. *90 degrees X-ray and optical opening in the piston cylinder cell achieved using specially designed Boehler-Almax anvils and tungsten carbide supporting plate. Modified after Kantor et al. (2012).*

The wide opening angle is crucial for both powder and single-crystal angle-dispersive X-ray diffraction, as it increases the number of available Bragg diffraction peaks. Moreover, such an opening angle is essential for Brillouin scattering measurements (section 2.3.4) as it can prevent for instance the shadowing of the scattered light cone by parts of the DACs, which can affect the sound velocities (Sinogeikin and Bass, 2000).

There are two main methods of sample heating in a DAC; laser and external electrical resistive heating. The laser heating technique covers a wide temperature range from above 1200 up to 5000 K. However, the major disadvantage of such a technique is that strong thermal gradients occur due to very localized spot heating within the pressure chamber. Large thermal gradients can create thermal stresses in the DAC. Additionally, combining a laser heating system simultaneously with single crystal X-ray diffraction during the whole measurement time, which can be as long as several hours, is very challenging. For these reasons, electrical heating is an optimal complementary technique to the laser heating method and is the technique employed for the purposes of this project. Externally heated DACs allow temperatures up to approximately 1000 K to be reached (Dubrovinskaia and Dubrovinsky, 2003). Using electrical heaters, the temperature is distributed quite homogeneously inside the gasket hole and stresses are practically absent if a gas pressure medium is employed. Temperatures can be determined accurately using a thermocouple, and can be maintained at a constant value for several hours. However, the thermocouple has to be carefully placed close

to the sample in order to measure the correct temperature inside the DAC. Accurate temperature measurements require, however, a calibration of the thermocouple whose reading clearly depends on where it is placed relative to the furnace and sample (see Boffa Ballaran et al., 2013). Also, special care has to be taken with external heating as oxidation and graphitization of diamond, as well as oxidation of the gaskets can occur (Dubrovinskaia and Dubrovinsky, 2003).

Taking into account all the considerations outline above for electrical heating, and the geometry of the seats and diamonds, we designed an external resistive heater suitable for piston cylinder type cells employed in this study. The heater is fabricated from a ceramic cylinder ring with an internal diameter of 18 mm and external diameter of 20 mm and height of 5 mm (Figure 2.3-3). Grooves are made from both sides of the ceramic ring in order to accommodate the platinum (Pt) wire of 0.4 or 0.5 mm in diameter. The Pt wire is then coiled around the cylinder to form loops as shown in Figure 2.3-3. The wire is deepened into the grooves of the ring in order to provide electrical insulation when the heater is mounted in the cell in contact with the metal base of the plate. The heater is placed in the piston part of the cell around one of the backing plates concentrically so that there is no contact between the heater Pt wire and the metal parts of the DAC or the electrically conductive backing plates. The additional protection from electrical contact is achieved by high temperature resistant cement. We use S type thermocouple wires, inserted through the drilled hole of 0.5 mm. The thermocouple and end wires of the heater are insulated with pyrophyllite tubing.

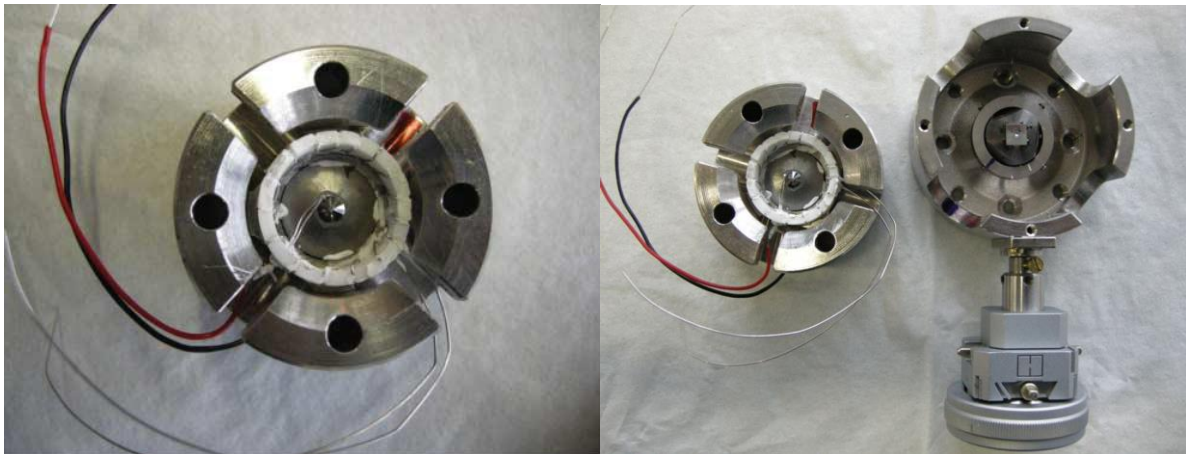


Figure 2.3-3. Electrical heater designed and developed for the piston cylinder DAC. A close up of the heater, placed in the piston part of the cell, together with the thermocouple is shown on the left hand side. The piston with the heater and the cylinder part with a rhenium gasket glued are shown on the right side of the Figure. The DAC is then mounted on a Huber goniometric head (right) for the X ray diffraction and Brillouin scattering measurements.

2.3.2 Pressure determination

One of the major sources of uncertainty in high-pressure experiments is the pressure determination in the DAC. In fact, a direct calculation of the pressure versus the applied load as in piston-cylinder or multi-anvil devices is not possible, as the distribution of the load over the anvils is unknown and part of the load given by turning the screws is lost to internal friction and gasket deformation (Miletich et al., 2000; Boffa Ballaran et al., 2013). Therefore, internal standard materials for which the physical properties change with pressure are employed and loaded together with the sample in the pressure chamber. Different pressure standards, however, usually do not yield identical pressures at the same experimental conditions, leading to considerable uncertainty in determination of the pressure dependence of physical properties, and particularly derivative properties such as bulk modulus.

2.3.2.1 Fluorescence measurements

The most common method for determining the pressure inside the DAC is to use the laser-induced fluorescence technique applied to luminescence sensors, for instance, by measuring the fluorescence shift of optical pressure gauges such as ruby (Cr^{3+} doped $\alpha\text{-Al}_2\text{O}_3$).

Fluorescence is the emission of light after irradiation of a sample. In this process, the system is transferred first to an excited state upon irradiation with a light of frequency ν_1 . A subsequent transition to a second excited state occurs without emission of light. Finally the system decays to the ground state with the emission of light with frequency ν_2 . The essential instrumentation suitable for fluorescence measurements is shown in Figure 2.3-4. It consists of a laser-light source, which excites the fluorescent radiation, an optics system for collection of the incident laser light and the fluorescent light, and a spectrometer for the spectral analysis of the fluorescence signal. More details can be found in Miletich et al. (2000).

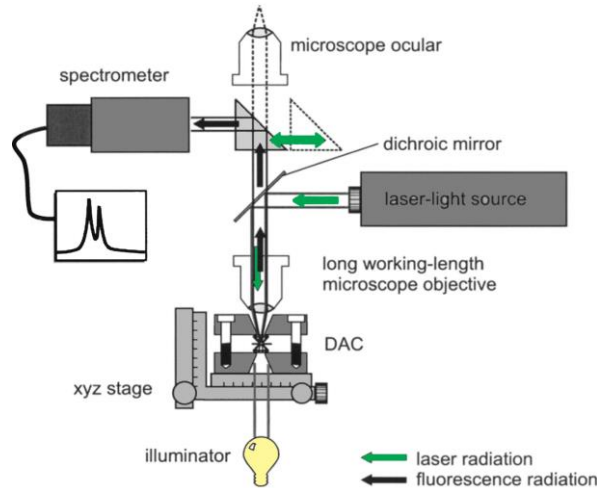


Figure 2.3-4. Schematic diagram of a fluorescence pressure calibration system. Modified after Miletich et al. (2000).

The pressure determination requires the measurements of the fluorescence spectrum from a reference sample at ambient pressure (1 bar) and comparison with the spectrum of the equivalent material within the sample chamber at high pressure.

The fluorescence signal of ruby is characterized by an intense doublet with sharp bands centered at 694.2 (R₁ line) and 692.8 nm (R₂ line) at 1 bar, which, exhibit a shift toward higher wavelengths as the applied pressure increases (Piermarini et al., 1975; Mao et al., 1986). Pressures inside the pressure chamber can be then calculated using the quasi-hydrostatic ruby gauge of Mao et al. (1986) according to the following formula:

$$P = A/B \left\{ \left[1 + (\Delta\lambda / \lambda_0) \right]^B - 1 \right\} \quad (2.1)$$

where P is pressure in megabars, λ is the wavelength of the ruby R line, $A = 19.04$ and $B = 7.665$.

Pressures may also be calculated according to a similar calibration of the scale made by Jacobsen et al. (2008). This pressure scale is adjusted for the softer helium medium and is based on the shift of the ruby R1 line, calibrated against the primary MgO scale of Zha et al. (2000). The formula for calculating the pressure is the same as the one reported above for Mao et al. (1986), with the difference that $B = 10.32(7)$.

Sm:YAG, whose fluorescence and density of single crystal has been calibrated against an absolute pressure determination (Trots et al., 2013), was also used as a pressure calibrant to determine the pressure in this study. Similarly to ruby, the pressure-induced shifts of the

fluorescence lines Y1 and Y2 of Sm:YAG are described as $P = A/B \left\{ [1 + (\Delta\lambda / \lambda_0)]^B - 1 \right\}$ with $A = 2089.91(23.04)$, $B = -4.43(1.07)$ for Y1, and $A = 2578.22(48.70)$, $B = -15.38(1.62)$ for Y2 bands, where $\Delta\lambda = \lambda - \lambda_0$, λ and λ_0 are wavelengths in nanometer at pressure and ambient conditions. The pressure induced shifts of the fluorescence lines of Sm:YAG and ruby are shown in Figure 2.3-5.

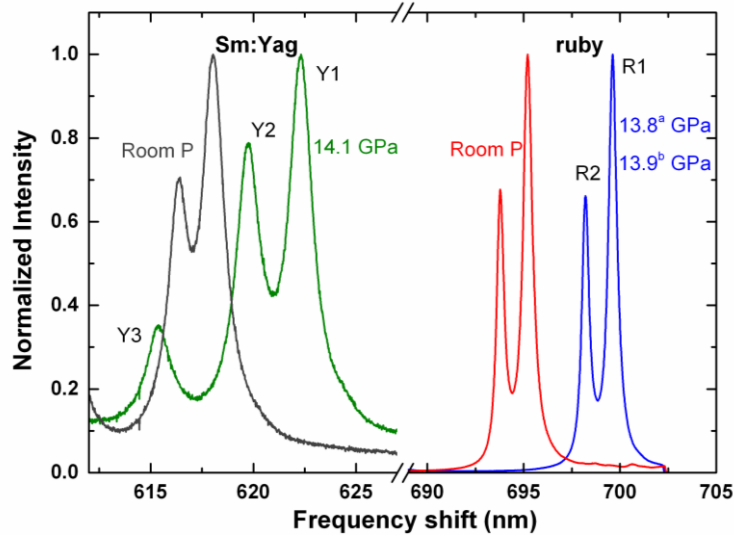


Figure 2.3-5. Sm:YAG and ruby fluorescence spectra at different pressures in helium pressure transmitting medium. The shifts of the of the Sm:YAG Y1 line and the ruby R1 line are used to calculate pressure by using the Sm:YAG calibration of Trots et al. (2013) and the ruby pressure calibration of (a) Mao et al. (1986) and (b) Jacobsen et al. (2008).

Sm:YAG is also suitable for determining pressure at elevated temperatures, since its fluorescence shift is insensitive to temperature changes. In this study, we have combined the fluorescence shifts of Sm:YAG which is independent of temperature with the fluorescence shift of ruby chips which are strongly temperature dependent, to better constrain the temperature inside the pressure chamber without relying uniquely on the thermocouple. In fact, by loading chips of these two calibrants in the DAC, one can determine pressure independently from temperature using the fluorescence of YAG and determine temperature using the fluorescence of ruby (Rekhi et al., 1999) by fixing the pressure value obtained from the YAG fluorescence measurement. The temperature induced shift of ruby, from 100-600 °C, was calibrated up to 15 GPa by Rekhi et al. (1999) and can be calculated as follow:

$$P = \frac{a}{b} \frac{100R}{\lambda_0 + m(T - 298)^b - 1} \quad (2.2)$$

Where P is the pressure in GPa, T is the temperature in Kelvin, λ_0 is the initial wavelength of the ruby line; $a/\text{GPa} = 19.99$ and $b_0 = 6.75$; $R = (R_1 + R_2)/2$ for high temperatures and $b = b_0 + b_1(T - 298) + b_2(T - 298)^2$.

Fluorescence spectra were collected at BGI using a Dilor XY spectrometer in a backscattering geometry operating with a 514 nm Ar⁺ ion laser equipped with a cryogenic solid-state detector. Measurements were performed with 150 mW laser power. Reference fluorescence spectra of Sm:YAG and ruby at ambient pressure were collected before and after each high-pressure measurements. For experiments at APS, the pressure was monitored using an Acton standard series spectrograph from Princeton Instruments operating with a Nd:YVO₄ solid-state laser (532 nm) with 400 mW laser power.

The materials such as ruby described above are secondary standards as they are calibrated using shock data on a series of metals. Consequently, the uncertainties of the pressure measurement can be quite large. Large uncertainties on the pressure values are one of the major causes of inaccuracy of equations of state (EoS) and in particular on pressure derivatives of elastic moduli.

2.3.2.2 Absolute Pressure Determination

In this study, measuring simultaneously density and sound velocities for the same sample at the same conditions provides the advantage of being able to determine accurately the absolute pressure without having to rely on a secondary pressure scale. Absolute pressure can be determined according to the relationship:

$$P = - \int_{V_0}^V \frac{K_T(V)}{V} dV \quad (2.3)$$

where the isothermal bulk modulus K_T is derived from the adiabatic bulk modulus K_S according to:

$$K_S = K_T(1 + \alpha\gamma T) = K_T + \gamma^2 \rho C_V T \quad (2.4)$$

(where α is the thermal expansion and γ is the Grüneisen parameter), calculated from elastic constants obtained from Brillouin spectroscopy, V is the unit-cell volume determined by means of X-ray diffraction and C_V is the isochoric heat capacity.

2.3.3 Single crystal X-ray diffraction

High-pressure single-crystal X-ray diffraction experiments provide direct measurements of the unit-cell parameters and volume of the samples. Further details can be found in Hazen and Downs (2000). From these measurements, the isothermal equation of state (EoS) (i.e. the behaviour of a solid under compression, at constant T) as well as the density and the orientation matrix of single crystals can be accurately determined. Knowing the density and orientation matrix of the crystals at each pressure point is fundamental for deriving the elastic properties and sound wave velocities from Brillouin spectroscopy.

2.3.3.1 Equations of State

In general, the equation of state (EoS) is a thermodynamic equation describing the state of matter under a given set of physical conditions. Measured equations of state are usually parameterized in terms of the value of the bulk modulus and its pressure derivatives, which is characterized by the following parameters: the bulk modulus, defined as:

$$K_0 = -1/\beta_V, \quad K_0' = -V_0 \left(\frac{\partial P}{\partial V} \right)_{P=0} \quad (2.5)$$

and its pressure derivatives:

$$K_0'' = \left(\frac{\partial K}{\partial P} \right)_{P=0} \quad \text{and} \quad K_0''' = \left(\frac{\partial^2 K}{\partial P^2} \right)_{P=0} \quad (2.6)$$

The parameters K_0 , K_0' and K_0'' correspond to the zero-pressure parameters.

The isothermal equation most commonly used to fit P - V data in geosciences is the Birch-Murnaghan equation. This equation of state is based upon the assumption that the strain energy (F) of a solid under compression can be expressed as a Taylor series in the finite strain f (Birch, 1947). The finite strain is defined by the change in distance between two neighboring points during deformation. There are different definitions of f that leads to a different relationship between P and V (Angel, 2000). The Birch-Murnaghan EoS is based upon the Eulerian strain ($f_E = [(V_0/V)^{2/3} - 1]/2$) and its fourth order expression is the following:

$$P = 3K_0 f_E (1 + 2f_E)^{5/2} \left(1 + \frac{3}{2}(K_0' - 4)f_E + \frac{3}{2} \left(K_0 K_0'' + (K_0' - 4)(K_0' - 3) + \frac{35}{9} \right) f_E^2 \right) \quad (2.7)$$

If this equation is truncated to second order in the energy, the coefficient of f_E must equal zero, which requires that the first pressure derivative K' is fixed to 4. The third-order truncation (the coefficient of f_E^2 is set to 0) yields a three-parameter (V_0, K_0, K') EoS with an implied value of K'' :

$$K'' = \frac{-1}{K_0} \left[(3 - K')(4 - K') + \frac{35}{9} \right] \quad (2.8)$$

Further information about the theory of Equation of State is reported in Angel (2000) and Boffa Ballaran (2010)

2.3.3.1.1 F_E - f_E plots

A direct indication of the compressional behaviour and useful visual evaluation of the quality of an EoS fit is provided by the by the so-called F_E - f_E plot (Angel, 2000). Such plots can be applied to any isothermal EoS based upon finite strain. For the Birch-Murnaghan EoS, F_E is the normalized stress defined as:

$$F_E = P / \left[3f_E(1 + 2f_E)^{5/2} \right] \quad (2.9)$$

and f_E is finite strain defined as

$$f_E = \left[(V_0 / V)^{2/3} - 1 \right] / 2 \quad (2.10)$$

The uncertainties in f_E and F_E are calculated by propagation of the experimental uncertainties in compression ($\eta = V / V_0$) and pressure, according to Heinz and Jealonz (1984), as follow:

$$\sigma_f = \frac{1}{3} \eta^{-5/3} \sigma_\eta \text{ and } \sigma_F = F_E \sqrt{(\sigma_P / P)^2 + (\sigma')^2}, \quad (2.11)$$

where

$$\sigma' = (7\eta^{-2/3} - 5) \sigma_\eta / (3(1 - \eta^{-2/3})\eta) \quad (2.12)$$

and

$$\sigma_\eta = \sqrt{(1/V_0)^2 \sigma^2(V) + (V/V_0^2)^2 \sigma^2(V_0)^2}, \quad (2.13)$$

which was obtained from:

$$\sigma^2(f) = \sum (\partial f / \partial x_i)^2 \sigma^2 x_i \quad (2.14)$$

If the data lie on a horizontal line of constant F , the data can be fitted with a 2nd-order truncation of the Birch-Murnaghan EoS with $K' = 4$. If the data in the F_E - f_E plots lie on an inclined straight line, the data will be adequately described by a 3rd-order truncation of the EoS with a value of K_0 greater than 4. The K_0 value is given by the intersection of the line with the F_E axis whereas the K' value is given by the slope of the line $(3K_0(K'-4)/2)$. In some cases the data fall on a parabolic curve in the F_E - f_E plot indicating that the data are described by a 4th-order truncation of the EoS.

2.3.3.1.2 Thermal equations of state

There are different EoS which can be used to evaluate high-temperature and high-pressure data. A relatively simple approach but sufficient for fitting most of the P - V - T data collected up to 1000 K is to use a high-temperature form of the 3rd-order Birch-Murnaghan EoS, where isothermal compression curves are considered in the fitting. The parameters V_0 and K_0 and K_0' are the material properties at $P = 0$ but at elevated temperature T . The high-temperature values for the volume and bulk modulus are given by:

$$V(T) = V_0(T_0) \exp \int_{T_0}^T \alpha(T) dT \quad (2.15)$$

$$K(T) = K_0(T_0) + \left(\frac{\partial K}{\partial T} \right)_P (T - T_0) \quad (2.16)$$

where T_0 is the reference temperature (usually 298 K). The ambient-pressure thermal expansion $\alpha(T) = a + bT$ as well as the bulk modulus are considered to vary linearly with T . Given the uncertainties on most of the P - V - T data, it is usually assumed that K' does not vary with T (Duffy and Wang, 1998) and its value is fixed to 4. However, if the data are particularly accurate, it is possible to use a variable K' associated with each isothermal EoS (Boffa Ballaran, 2010). The derivations of thermal EoS that are appropriate for higher-temperature datasets are given by Duffy and Wang (1998) and Poirier (2000).

2.3.3.2 Four circle diffractometer at BGI

The unit-cell parameters of single crystals were determined at different pressures using a four-circle Huber diffractometer (with MoK α radiation) equipped with an ultrahigh-intensity rotating anode FR-E⁺ SuperBright from Rigaku, operating at 45 kV and 55 mA (Figure 2.3-6). The diffractometer is also equipped with a focusing optics system that consists of an optic housing assembly with two focusing parabolic-curved mirrors in a “side-by-side” Kirkpatrick-Baez scheme. The X-ray counting system consists of a YAP: Ce scintillator coupled to a photomultiplier, amplifier and two discriminators.

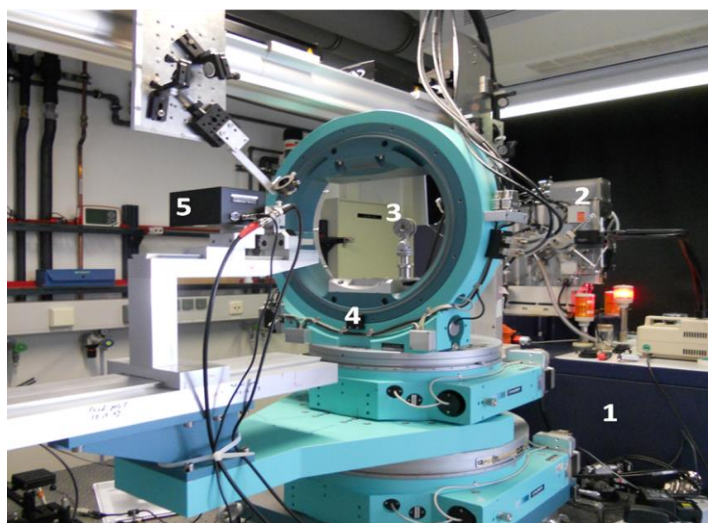


Figure 2.3-6. Single crystal X-ray diffraction and Brillouin spectroscopy laboratory at the Bayerisches Geoinstitut. (1) Ultrahigh-intensity rotating anode FR-E⁺ SuperBright from Rigaku, (2) VariMax Focusing optics, (3) Almax-Boehler DAC mounted on the four circle Huber diffractometer (4) and (5) X-ray counting system (YAP:Ce scintillator coupled to photomultiplier, amplifier and two discriminators).

The high brightness of the rotating anode results in an intensity gain of approximately 80 times with respect to a conventional X-ray tube (Figure 2.3-7) allowing the measurement of accurate lattice parameters of the crystals of very small dimensions investigated in this study.

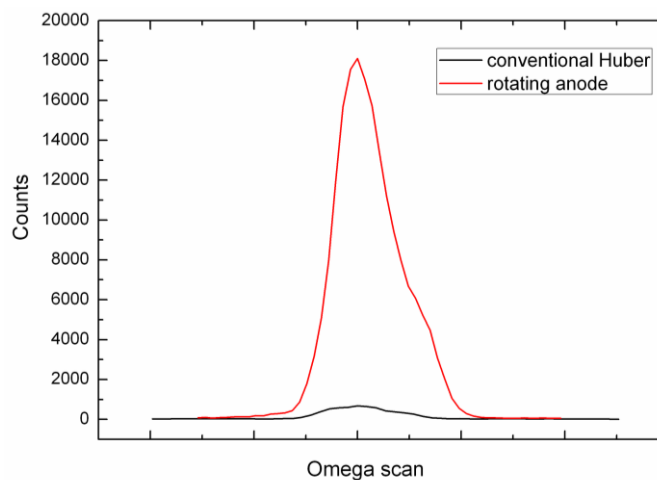


Figure 2.3-7. Omega scan profile of a (400) reflection of pyrope measured with a conventional X-ray tube (black) and with a rotating anode (red). With a conventional source the maximum intensity is 3160 counts, whereas with the rotating anode the intensity gains 62812 counts.

For each sample, the lattice parameters were determined using eight-position centering of at least 10-15 Bragg reflections at each pressure, according to the procedure of King and Finger (1979). The setting angles of a single reflection always deviate from the “true” angles as a result of a number of experimental aberrations (Angel et al., 2000). These aberrations may include offsets of the crystal from the center of the goniometer, absorption by the crystal and a number of diffractometer aberrations (incorrect zero position). The elimination of such positional offsets can be overcome by applying eight-position centering (Miletich et al., 2005). The procedure consists of centering a single reflection at the 8 equivalent positions on the diffractometer. This involves measurements of well resolved profiles across the Bragg intensities in various directions in the reciprocal space through a sequence of ω , $\omega/2\theta$, and χ scans. Centering procedures and vector-least squares refinement of the unit-cell constants are then performed using the SINGLE software (Angel and Finger, 2011), according to the protocols of Ralph and Finger (1982) providing lattice parameters and unit cell volumes to a precision of 10^{-4} to 10^{-5} (Angel et al., 2000). Detailed data analysis and the accurate refinement of lattice parameters were performed using the software package WinIntegrStp 3.7 (Angel, 2003), which allows integration of the single-crystal intensity data by fitting of individual diffraction profiles by pseudo-Voigt functions. The total integrated intensity, the positions of individual reflections and their full-width-at-half-maxima (FWHM) were refined, as well as the intensity ratio between the $\text{MoK}\alpha_1$ and $\text{MoK}\alpha_2$ contributions to each profile.

2.3.3.3 Synchrotron radiation

X-ray diffraction experiments were also carried out at the bending magnet sector 13-BM-D of GeoSoilEnviroConsortium for Advanced Radiation Sources (GSECARS) at the advanced photon source (APS). A detailed description of the 13-BM-D station can be found in Schen et al. (2005). A monochromatic X-ray beam of 0.3344 Å wavelength was employed together with a PerkinElmer amorphous silicon based Flat Panel detector. The detector geometry parameters were calibrated with a CeO₂ or LaB₆ National Institute of Standards and Technology diffraction standards. In order to obtain the density and the orientation matrix of single crystals, the DAC was rotated around the axis perpendicular to the incident X-ray beam by 50° or 70°. Step scans of 1° were collected with typical exposures of 5 s/scan. The program packages GSE_ADA and Reciprocal_Space_Viewer developed at GSECARS were used to calculate crystal orientations and volumes from the diffraction data.

2.3.4 Brillouin Scattering

Brillouin scattering is a widely used technique to determine the full elastic tensor and sound wave velocities of mantle minerals. It is an optical method, requiring transparent or translucent samples larger than the focused laser beam (eg. 50 x 50 x 10 μm³ crystal dimensions). Due to the optical access and acceptable sample size, Brillouin scattering experiments can be readily performed on samples within a diamond anvil cell to obtain high pressure and high temperature data. Brillouin scattering is a light scattering technique, in which light interacts with a sample and exchanges energy and momentum with the material. In some interactions the laser light excites new lattice vibrations (phonons), with energy being transferred from the light to the vibration. In this case, the light scattered by the sample has a lower energy than the incident radiation, which is known as a Stokes event. On the other hand, the energy can be transferred from the acoustic mode to the incident light, resulting in an increase in frequency of the scattered light in a so-called anti-Stokes event. A representation of these processes is shown in Figure 2.3-8. The theory behind the Brillouin scattering effect is described in detail in Cummins and Schoen (1972).

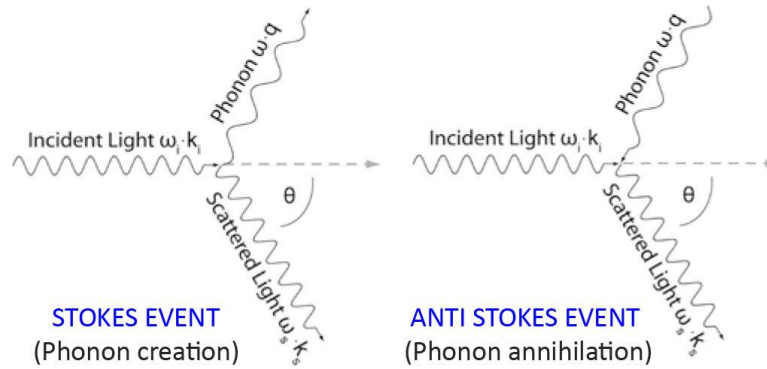


Figure 2.3-8. Inelastic interactions between the incident light and the vibrational modes in a crystal. In a Stokes event the energy is transferred to the phonon, and the energy of the scattered light is reduced. In an anti-Stokes event, the energy is transferred from the phonon to the radiation, which results in an increase in energy of the scattered light. In the figure, ω represents the circular frequency, k the photon wave vector, q the phonon wave vector and θ the scattering angle. Modified after Angel et al. (2009).

By measuring the changes in energy of the scattered light, one can obtain information on the atomic vibrations. In Brillouin scattering, acoustic vibrations (phonons), which result from the thermal motion of atoms in a material, inelastically scatter the laser light as it passes through the crystal. This interaction causes a Doppler shift of the scattered light (the Brillouin shift) with both positive and negative frequency shifts. The Doppler shift of the light scattered from the sample is then analyzed using a Scanning Fabry-Perot interferometer (Figure 2.3-9)

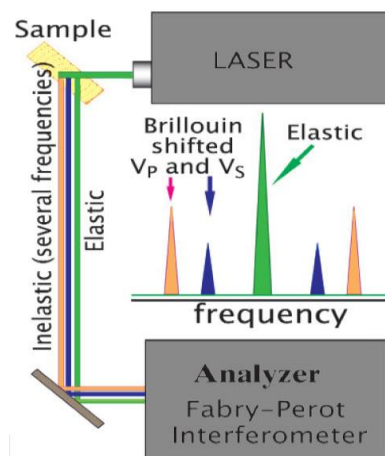


Figure 2.3-9. Schematic representation of a Brillouin scattering experiment. The laser light is focused on the sample and is scattered inelastically by thermally generated acoustic phonons. The scattered light is analyzed by a Fabry-Perot interferometer. Modified after Bass et al. (2008).

Brillouin scattering frequency shifts are a function of the scattering geometry (angle between the incident beam and scattering direction), the phonon velocities in the crystal along the particular crystallographic orientation and the refractive index of the material. The relationship between these parameters can be described as:

$$V_i = \frac{\Delta\omega_i \lambda}{2n \sin(\theta/2)} \quad (2.17)$$

where V_i is the velocity of one of the acoustic waves (longitudinal V_P , horizontally polarized shear wave, V_{SH} and is the vertically polarized shear wave, V_{SV}), $\Delta\omega_i$ is the Brillouin shift, λ is the wavelength of the incident light, n is the refractive index, θ is the scattering angle inside the sample.

The dependence of Brillouin scattering on the refractive index of the media across which the light passes introduces complications when measuring in the DAC, as the light has to pass through a number of materials such as the diamonds and the pressure medium, each having very different refractive indices. The basic experimental strategy for carrying out a high-pressure Brillouin measurement using the diamond cell is described by Whitfield et al. (1976). By assuming the so called forward platelet-symmetric scattering geometry (Whitfield et al., 1976), where the incident and scattered ray paths are symmetrical and the crystal surfaces are perfectly parallel with those of the diamond anvils (Figure 2.3-10), the velocities can be measured independently of the refractive indexes of the sample and surrounding materials.

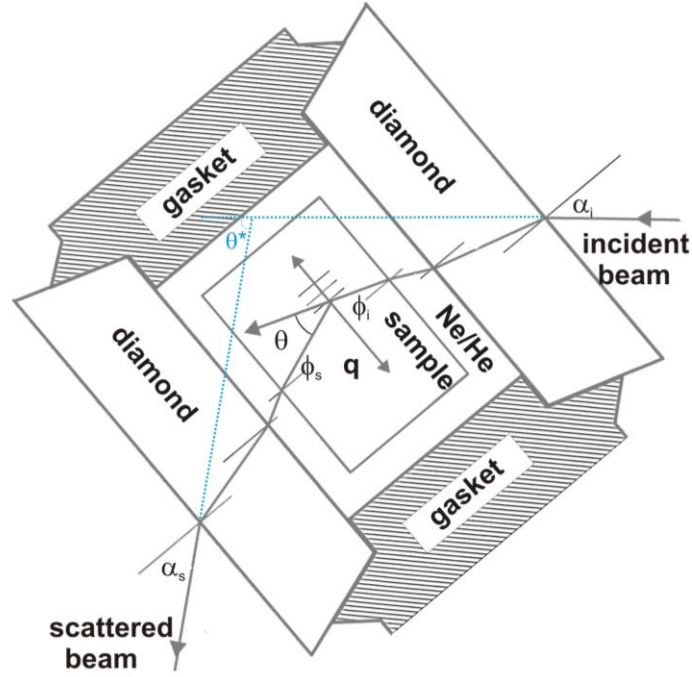


Figure 2.3-10. Platelet-symmetric scattering geometry showing the sample with two flat parallel faces oriented symmetrically with respect to the incident and scattered light. α and ϕ are the angles between the incident (i) and scattered (s) beams and sample face normal, q is the phonon direction, θ is the scattering angle inside the sample and θ^* is the external scattering angle (Modified after Sinogeikin and Bass, 2000).

By assuming such a geometry, the refractive indices of materials along the incident and scattered beam paths cancel out and the phonon velocity is merely proportional to the Brillouin shift:

$$V_i = \frac{\Delta\omega_i \lambda}{2 \sin(\theta^*/2)} \quad (2.18)$$

Where $\Delta\omega_i$ is the Doppler shift, λ is the incident laser wavelength and θ^* is the external scattering angle. In the DAC a scattering geometry of $\theta = 90^\circ$ is generally employed.

2.3.4.1 Brillouin scattering setup at BGI and at APS

Brillouin spectrometers usually employ a horizontal scattering plane (plane containing the incident and scattered light directions), where the incident laser and signal collection paths are parallel to the plane of the optics table (Sinogeikin et al., 2006). When combining X-ray diffraction and Brillouin spectroscopy, the position and orientation of the DAC is fixed by the path and focus of the X-ray beam. Therefore, the Brillouin system has to be flexible with respect to the sample so it can both deliver a focused laser beam to and collect a Brillouin

signal from the predefined spot. For this, both Brillouin systems at BGI and the BM-13-D APS beamline employ a vertical scattering plane (Figures 2.3-11 and 2.3-12).

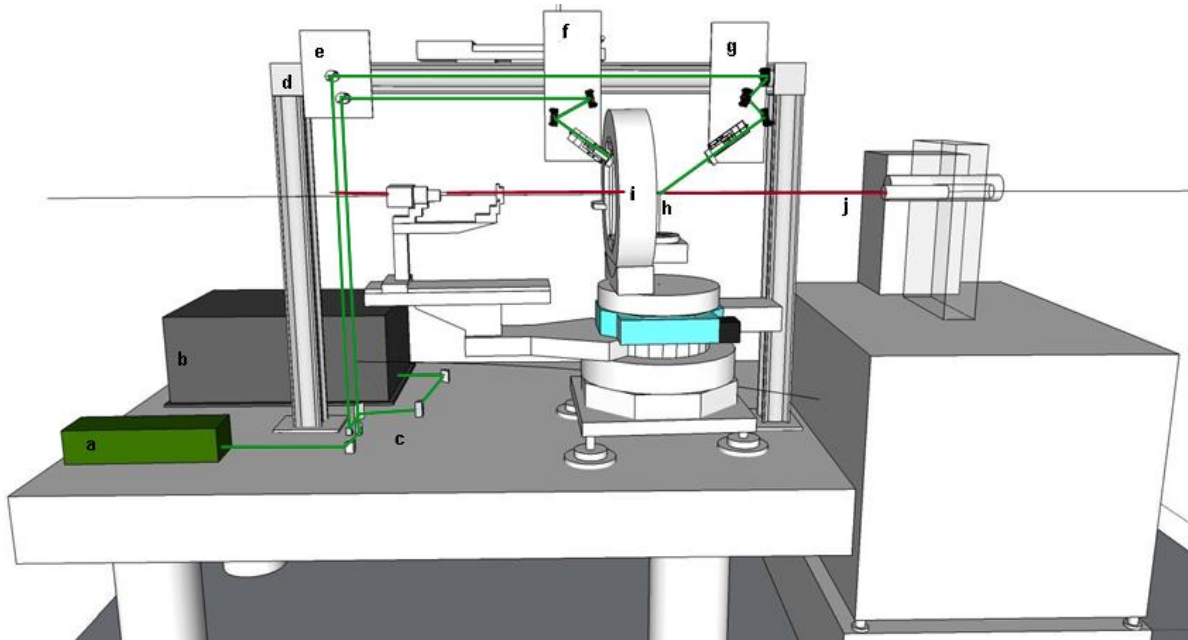


Figure 2.3-11. Schematic view of the Brillouin spectroscopy and X-ray diffraction systems at BGI. a) laser, b) interferometer, c) horizontal optical elements, d) arm for vertical optical assembly, e) periscope plate, f) focusing optical assembly, g) collecting optical assembly, h) sample position, i) diffractometer, j) X-ray beam.

Both systems comprise a Coherent Verdi V2 solid-state Nd:YVO₄ laser with a 532 nm single wavelength output. The heart of the Brillouin spectrometer is a six-pass Sandercock-type piezoelectrically scanning tandem Fabry-Pérot interferometer equipped with a Hamamatsu 464 S photomultiplier. This is an extremely high-resolution megahertz to gigahertz range interferometer that is intended primarily for the study of Brillouin spectra with a typical frequency shift of 1 cm⁻¹. The construction and operation of the interferometer is described in detail in Sandercock (1982). Focusing-collecting optics with 7 cm, at BGI and 5 cm, at BM-13-D, focal lengths are used to focus the laser beam on to the sample position and to collect the scattered inelastic signal. Measurements using the DAC are performed in a forward platelet symmetric geometry with an angle of 80° at BGI and 50° at BM-13-D between the incident and scattered beams.

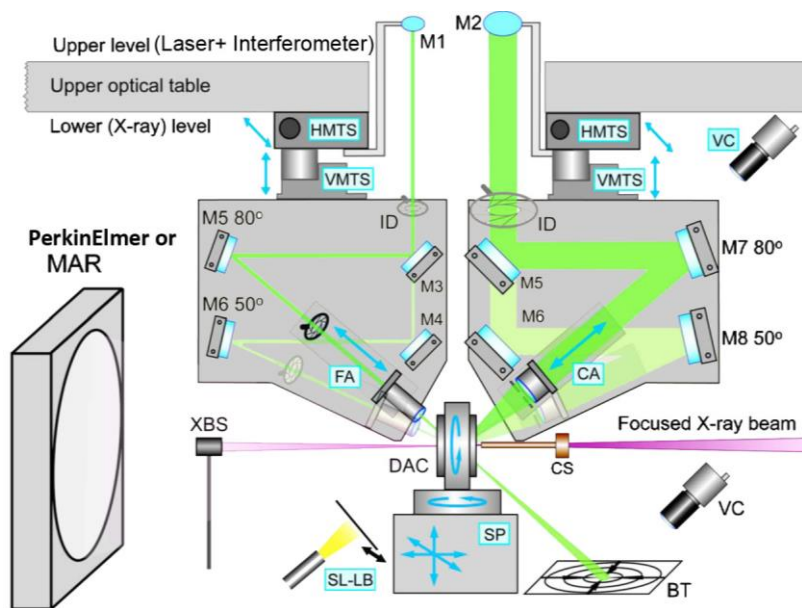


Figure 2.3-12. Schematic view of the Brillouin spectroscopy and X-ray diffraction systems at APS at the 13-BM-D sector. The system is subdivided in two levels. The upper level is composed of the laser and the Brillouin spectrometer. The lower level shown here in detail is composed of the following components: motorized translation components HMT (horizontal motorized translation stage) VMTS, vertical motorized translation stage; FA, motorized laser focusing assembly; CA, motorized signal collecting assembly; SP, sample positioning and orientation assembly; SL-LB, sample light/light block. VC, video camera; BT, beam target. X-ray components: MAR, MAR345 imaging plate or PerkinElmer Flat Panel Detector; XBS, X-ray beam stop; CS, cleanup slit. Modified after Sinogeikin et al. (2006)

The major difference between the two systems is that at APS, the Brillouin system is subdivided in two parts (Figure 2.3-12): the upper horizontal tier containing the main components of the Brillouin system and the vertical collecting and focusing plates. The vertical plates are mounted on symmetric aluminum platforms that are attached to two heavy-duty translation stages, so that the focusing and collecting optics of the Brillouin system can move easily. When X-ray measurements are performed, the Brillouin optics are translated sideward (at BGI) and upward (at APS) to avoid collisions between parts of the Brillouin and X-ray systems. The systems at BGI and APS are designed in a way that during the movements of the optics all the angular relations in the system are preserved. A detailed description of the setups at BGI and APS is given in Trots et al. (2013) and in Sinogeikin et al. (2006), respectively.

3. Single-crystal elasticity of majoritic garnet at high pressures and temperatures

3.1 Introduction

Seismic studies provide essential information for constraining the thermal and chemical state of the Earth's interior. To correctly interpret seismic observations in terms of chemistry and mantle mineralogy, however, requires laboratory data on the elasticity of minerals under the conditions at which they exist in the mantle. In this context, garnet minerals are very important since they form major components of both mafic and ultramafic rocks in the upper mantle and transition zone, and are in fact the main mineral host for the mantle's complement of Al_2O_3 and CaO throughout these regions. The density change associated with the transformation of subducted basaltic rocks to garnet-bearing eclogitic rocks is, for example, considered to significantly enhance the negative buoyancy of slabs. As garnets dominate the mineralogy of subducted mafic rocks throughout much of the upper mantle and transition zone they have a major influence on the physical properties of what is likely to be the main source of chemical heterogeneity in the mantle.

In general, most garnets from the Earth's crust crystallize in the cubic space group *Ia-3d* forming a series of complex solid solutions that are described using the crystal-structural formula $^{\text{VII}}\text{X}_3^{\text{VI}}\text{Y}_2^{\text{IV}}\text{Z}_3\text{O}_{12}$. The garnet structure is formed by a three-dimensional network of alternating corner-shared ZO_4 tetrahedra and YO_6 octahedra, with the X cations occupying 8-fold coordinated dodecahedral sites. Usually X is a large cation such as Mg, Ca, Fe^{2+} , or Mn, Y is medium size cation such as Al, Fe^{3+} , or Cr and the Z site is mainly occupied by Si.

It was first reported by Ringwood (1967) that aluminous enstatite with 10 mol % Al_2O_3 transforms into a garnet-structured high-pressure phase $\text{M}_4\text{Si}_4\text{O}_{12}$ (where M = Mg, Fe, Ca, Na, Al) at pressures corresponding to the Earth's transition zone. In particular, with increasing pressure both orthopyroxene and clinopyroxene dissolve into garnet forming extensive solid solutions in the transition zone. The Al-free garnet end-member is referred to as majorite ($\text{Mg}_4\text{Si}_4\text{O}_{12}$). It crystallises with tetragonal symmetry due to a slight distortion from cubic symmetry as a consequence of ordering of Mg and Si on the octahedral sites. Majorite is stable at pressures between 16 and 23 GPa and temperatures above 1600 °C

(Angel et al., 1989; Kato and Kumazawa, 1985; Ohtani et al., 1991; Wang et al., 1993). Among the garnet minerals, the high-pressure structured majoritic garnets along the solid solution between majorite (Mj) and pyrope (Py) $\text{Mg}_3\text{Al}_2\text{Si}_3\text{O}_{12}$, are stable throughout the entire transition zone (410–660 km depth). They constitute approximately 40% by volume of peridotitic compositions and up to 70% for basaltic or eclogitic compositions (Anderson and Bass, 1986; Irifune and Ringwood, 1987; Weidner and Ito, 1987; Duffy and Anderson, 1989; Ita and Stixrude, 1992).

Several studies have investigated the elastic properties of Py–Mj garnets at room pressure and temperature (Yagi et al., 1987; Bass and Kanzaki, 1990; O'Neill et al., 1991). Moreover elastic moduli measurements also have been performed at high pressure and room temperature (Rigden et al., 1994; Gwanmesia et al., 1998; Chen et al., 1999; Wang and Ji, 2001; Conrad et al., 1999; Sinogeikin and Bass, 2000, 2002a; Murakami et al., 2008) or at high temperature and room pressure (Sinogeikin and Bass, 2002b) (Figure 3.1-1).

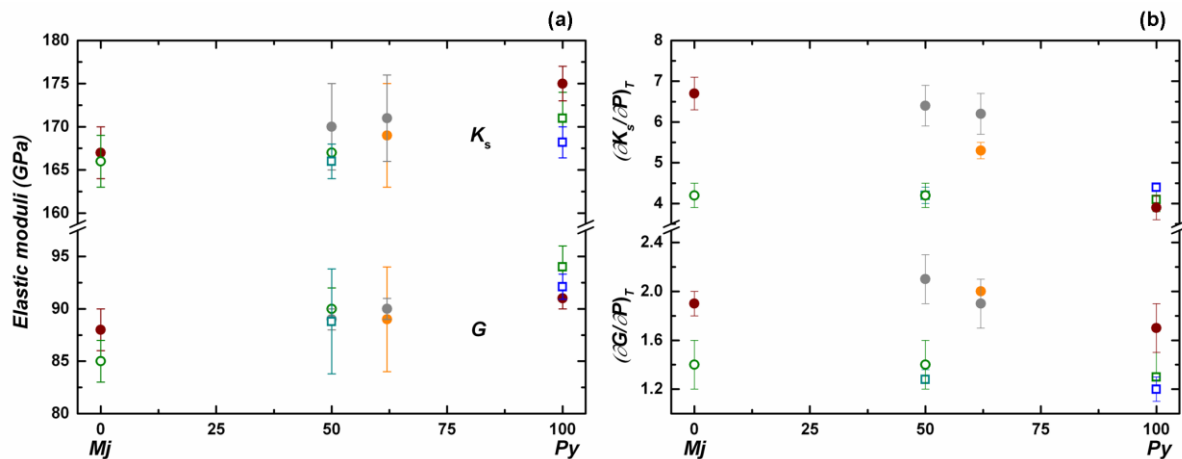


Figure 3.1-1. (a) Bulk (K_s) and shear (G) moduli data and (b) their pressure derivatives along the pyrope-majorite solid solution reported in the literature. Open squares show results of single-crystal Brillouin scattering (Sinogeikin and Bass, 2000; Murakami et al., 2008; Lu et al., 2013) whereas open circles correspond to Brillouin scattering measurements on polycrystalline samples (Sinogeikin and Bass, 2002a). Filled circles correspond to ultrasonic results (Rigden et al., 1994; Gwanmesia et al., 1998, 2006; Liu et al., 2000). Note that data from Murakami et al. (2008) and Lu et al. (2013) correspond to Fe-bearing majoritic garnet and pyrope respectively.

However, the majority of these studies have been performed on powdered samples which were loaded in a mixture of methanol:ethanol:water. This mixture is known to solidify at

pressure above 10-11 GPa (Angel et al., 2007) and therefore provides quite inhomogeneous stresses in the DAC above this pressure.

Recent improvements in ultrasonic techniques coupled with synchrotron radiation have allowed sound velocity measurements on polycrystalline samples along the Py–Mj solid solution to be performed at simultaneous high P and T (Irifune et al., 2008; Gwanmesia et al., 2009). Only one study, however, reports the single-crystal elasticity of an iron-bearing pyrope obtained simultaneously at high-pressures (up to 20 GPa) and high-temperature (750 K) using Brillouin spectroscopy and X-ray diffraction employing Ne as a quasi-hydrostatic pressure medium (Lu et al., 2013).

Although the bulk and shear moduli values are in reasonable agreement among all these studies (Fig. 3.1-1), large discrepancies in elastic moduli pressure derivatives, ranging from 3.2 to 6.7 and from 1.3 to 2.1 for $(\partial K / \partial P)_T$ and $(\partial G / \partial P)_T$, respectively, can be observed. Consequently, interpretations of the seismic results for the transition zone remain still difficult and unclear, since differences in the pressure derivatives of elastic moduli affect not only absolute velocities, but also density at high pressure. Reasons for such discrepancies may reside not only on the different type of material used (i.e. powdered vs single crystals samples), but also on the different pressure calibrants and pressure media chosen for the different experiments.

The aim of this study is, therefore, to constrain the elastic properties of majoritic garnet as a function of density, temperature and composition under hydrostatic conditions by combining single-crystal Brillouin scattering with X-ray diffraction. The simultaneous measurement of elastic properties and density also will be used to obtain absolute values of the experimental pressure (see Section 2.3.2.2) avoiding in this way any systematic errors that are introduced through the use of pressure calibrations. In addition, structural refinements of single-crystal X-ray diffraction data collected at room and at high-pressures and temperatures can provide insights into the interatomic forces and compression mechanisms controlling mineral elasticity. The results of this study not only allow better petrological and compositional models for the Earth's transition zone to be developed but also enable constraints to be placed on the buoyancy and seismic appearance of subducting slabs in the mantle. A detailed analysis of the density and acoustic wave velocities of majoritic garnet bearing rocks at high pressures and temperatures can be found in Chapter 6, where implications for the seismic

appearance of different rock types in the transition zone and lower mantle and their buoyancies are discussed.

3.2 Experimental methods

3.2.1 Sample synthesis and characterization

To obtain high quality single crystals of majoritic garnet of at least 70 μm is challenging, since the run-products of high-pressure and temperature syntheses generally consist of fine-grained materials. To obtain larger crystals it is necessary to add a flux, such as H_2O , during synthesis to lower the melting temperature and allow larger crystals to grown from the surrounding melt. In order to explore such methods, the garnet mineral pyrope was first investigated, given that the pressure conditions at which this mineral is stable are more readily obtained than those of majoritic garnet. Five different starting compositions were prepared, the first consisting of an anhydrous glass having pyrope composition; the second consisting of a mixture of $\text{Al}(\text{OH})_3$, SiO_2 and $\text{Mg}(\text{OH})_2$ in different proportions resulting in a total of 21.12 wt. % of H_2O (mixture A), the third consisting of a mixture of Al_2O_3 , SiO_2 and $\text{Mg}(\text{OH})_2$ in different proportions resulting in a total of 11.81 wt. % of H_2O (mixture C). Two additional pyrope compositions (mixtures B and D) were obtained by mixing the pyrope glass with either mixture A or C in different proportions (Table 3.2-1).

Table 3.2-1. Starting materials in wt.% of oxides

| | pyrope glass | mixture A * | mixture C ⁺ | enstatite glass | Fe- Majorite | Mixtures B, D, A', B', C', D' |
|--------------------------------------|-----------------|----------------|---------------------------|--------------------|-----------------|--|
| Al_2O_3 | 25.29 | 19.95 | 22.3 | - | 12.91 | B: 25% pyrope glass- 75% mixture A (15.95 wt. % H_2O) |
| MgO | 44.71 | 23.66 | 26.45 | 40.15 | 26.96 | D: 75% pyrope glass- 25% mixture C (2.95 wt. % H_2O) |
| SiO_2 | 29.99 | 35.27 | 39.43 | 59.85 | 42.8 | A': 50% enstatite glass - 50% mixture A (10.56 wt. % H_2O) |
| Fe_2O_3 [#] | - | - | - | - | 5.28 | B': 50% enstatite glass - 50% mixture B (7.92 wt. % H_2O) |
| H_2O | - | 21.12 | 11.81 | - | 12.04 | C': 50% enstatite glass - 50% mixture C (5.91 wt. % H_2O) |
| Sum | 100 | 100 | 100 | 100 | 99.99 | D': 50% enstatite glass - 50% mixture D (1.48 wt. % H_2O) |

* using $\text{Mg}(\text{OH})_2$ and $\text{Al}(\text{OH})_3$, ⁺ using $\text{Mg}(\text{OH})_2$, [#] reduced in CO-CO_2 furnace

The powdered samples were loaded into platinum capsules sealed subsequently by arc welding in order to prevent loss of water. Capsules were made of 2 mm outer diameter

platinum tubing and had initial lengths of approximately 3.5 mm. High pressure experiments were carried out using a 1200t Kawai type or 500t Walker-type (experiments V706 and V707) multi anvil apparatus at the Bayerisches Geoinstitut (BGI). All the experiments were conducted at 6 GPa, employing an 18/11 assembly (Section 2.1.2). A stepped graphite heater was employed for all the experiments except for one (S5207) for which LaCrO₃ heater was used instead. The temperature was monitored by means of Type D (W3%Re/W25%Re) thermocouple. In total, five high pressure-high temperature experiments were performed. The experimental conditions, analytical methods and run products of the experiments performed, are summarized in Table 3.2-2.

Table 3.2-2. Experimental conditions used during the synthesis of pyrope

| Run n° | Starting composition | P (GPa) | T (°C) | t (min) | Run products |
|--------------------|------------------------|---------|----------------------|---------|--------------|
| S5207* | pyrope glass | 6 | 1550 | 5 | pyrope |
| S5209 ⁺ | mixture A ₁ | 6 | 1500 | 40 | quench |
| S5221 ⁺ | mixture D | 6 | from 1500 to 1200 | 60 | pyrope |
| V706 ⁺ | mixture A, B, C, D | 6 | 1500 | 30 | pyrope + liq |
| V707 ⁺ | mixture A, B, C, D | 6 | 1300 | 30 | pyrope + liq |

*LaCrO₃ heater was not stable, ⁺graphite heater.

For all multi-anvil experiments performed for this project, the samples were first pressurized up to the desired value and then heated to the desired temperature. For experiment S5221 (Table 3.2-2) the sample was first heated up to 1500 °C and then slowly cooled to 1200 °C. Heating durations ranged from 5 to 60 minutes. After heating at high pressure, the experiments were quenched by shutting off the power and the samples were recovered after slow decompression of 15 hours. The run products of experiments S5207, S5209 and S5221 consisted only of small crystals of pyrope (Fig. 3.2-1).

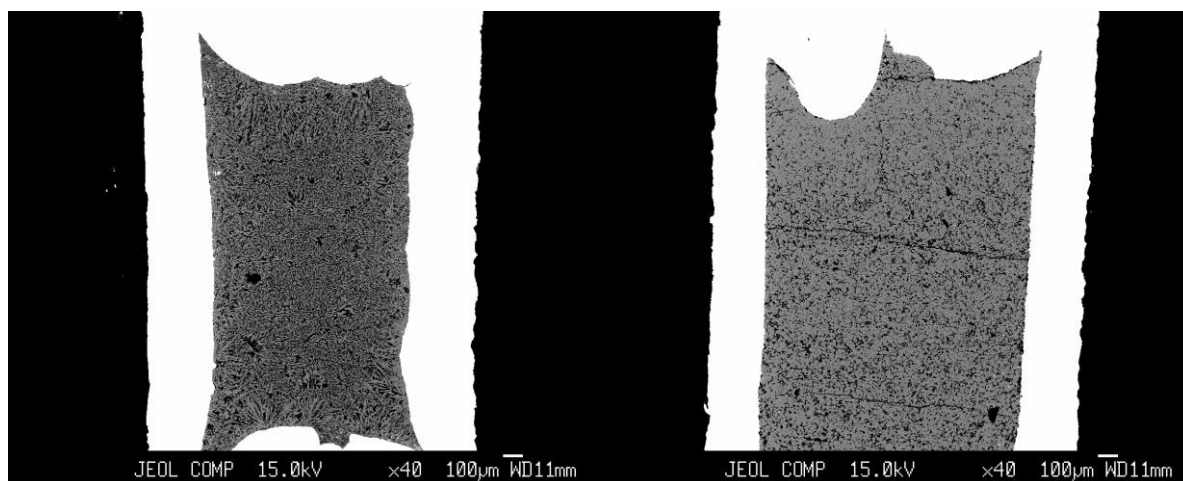


Figure 3.2-1. Backscattered electron image of S5209 (left) and S5221 (right). In both cases only small crystals of pyrope were obtained due to the addition of too much (left-100 % melt) and too little flux (right).

For two experiments (V706 and V707, Table 3.2-1) capsules were fabricated from a 2 mm diameter platinum rod, cut into sections and spark eroded with holes of approximately 0.6 mm deep and 0.25 mm in diameter. Four chambers were created in each capsule and they were loaded with different starting mixtures (A, B, C, D) with different H₂O contents (see Figure 3.2-2). In this way it was possible to directly observe which among the different starting materials crystallised with large single crystals for a given synthesis condition.

As shown in Figure 3.2-2, the starting compositions (mixture A and mixture B) that contained the largest amount of water, resulted in large single-crystals of pyrope (up to ~150 µm in length).



Figure 3.2-2. Backscattered electron image of two experiments performed at 6 GPa and 1500 °C (V706, left) and at 1300 °C (V707, right). From each experiment from left to right the sample chambers were refilled with A, B, C and D starting mixtures (see Table 3.2-1), therefore the water content increases from right to left.

The same approach, i.e. using capsules containing different sample chambers loaded with starting materials with different amounts of water, was then used to synthesise large crystals of majoritic garnet in the compositional range between MgSiO_3 majorite and $\text{Mg}_3\text{Al}_2\text{Si}_3\text{O}_{12}$ pyrope. To this end, four different majoritic garnet compositions were prepared by mixing an enstatite glass with the different pyrope mixtures A, B, C and D in a 50/50 proportion (see Table 3.2-1). By using hydroxides instead of oxides, it was possible to accurately control the amount of water present in the starting composition and, thus, determine the best conditions for enhancing crystal growth.

The powdered samples containing different H_2O contents (mixture A', B', C', D') were loaded into a multi-chamber capsule fabricated from a 2mm diameter rhenium rod.

An iron bearing majoritic garnet composition was also prepared. The starting material was designed by mixing an oxide mixture starting from the chemical composition reported in Murakami et al. (2008), adding water in the form of $\text{Mg}(\text{OH})_2$ as a flux (Table 3.2-1). The mixture of Al_2O_3 , SiO_2 and Fe_2O_3 was melted in air at 1600 °C for twenty minutes and then rapidly quenched in icy water. This glass was then reduced in a 1-atmosphere furnace, at 1000 °C and at an oxygen fugacity ($f\text{O}_2$) of 2 logs units below the quartz-fayalite-magnetite oxygen buffer for approximately 12 hours. This process was performed twice in order to ensure a complete reduction of the mixture. $\text{Mg}(\text{OH})_2$ was then added to the glass to obtain hydrous conditions. The starting material was then loaded into a double capsule consisting of a 1.6 mm diameter Re inner capsule and an outer capsule made of a 2 mm diameter platinum tube sealed from both sides.

High-pressure experiments aimed at producing majoritic garnets were carried out using a 5000t multi-anvil apparatus at BGI. An 18/11 assembly was employed as a pressure medium with tungsten carbide cubes of 52 mm edge length. The pressure calibrations for the assembly used in this study are reported in Keppler and Frost (2005). The samples were first pressurized up to 17 GPa followed by heating at 1900 °C for 5 minutes. After heating at high pressure, the experiments were quenched by shutting off the power and the sample was recovered after decompressing for 18 hours. After the experiments, the capsules were dispersed in resin and polished for electron microprobe analysis. Single-crystals of majoritic garnet (up to ~200 μm in length) were obtained from the starting composition (mixture A') that contained the largest amount of water (Figure 3.2-3).

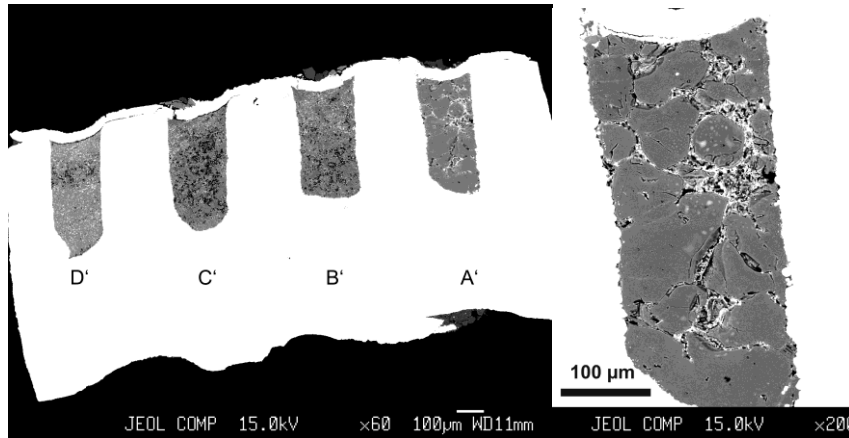


Figure 3.2-3. Backscattered electron image of the experimental run (z946) performed at 17 GPa and 1900 °C. **(left)** Capsule chambers filled with starting materials containing increasing amounts of H₂O from left to right; **(right)** electron image of the run product obtained from mixture A' (10.56 wt. % H₂O) consisting of large single crystals of majoritic garnet.

A similar experiment was then repeated (H3882) at the same conditions employing only mixture A'. The chemical analysis obtained following the procedure described in Section 2.2.1 resulted in the following composition: 32.0 (6) % MgO, 47.5 (9) % SiO₂, 19 (2) % Al₂O₃ (in wt), for majoritic garnet (hereafter named Mj) sample (Z946A' and H3882) and 29.5(5) % MgO, 46 (1) % SiO₂, 3.3 (5) % FeO, 21(2) % Al₂O₃ (in wt) for the iron bearing sample (hereafter named Fe-Mj) (Z1038), with recalculated chemical formula Mg_{3.24}Al_{1.53}Si_{3.23}O₁₂ and Mg_{3.01}Fe_{0.17}Al_{1.68}Si_{3.15}O₁₂ respectively.

The synthesized majoritic garnets were confirmed to contain negligible amounts of H₂O. FTIR analyses² were performed on crystals from run H3882 and show OH absorption bands consistent with approximately 20 ppm wt H₂O. The quantitative analyses were performed following the calibration of Paterson (1982).

3.2.2 Simultaneous X-ray diffraction and Brillouin scattering

The *P-V-T* equations of state and the compressional, V_p , and shear sound velocities, V_s , of two single-crystals of majoritic garnet (Mj and Fe-Mj) were simultaneously determined by means of Brillouin spectroscopy and X-ray diffraction. High quality single-crystals were selected based on their sharp diffraction profile and were double side polished up to 10-18

² FTIR measurements were performed in Clermont Ferrand, at the Laboratoire de Magma et Volcans (LMV) by Dr. Davide Novella and Dr. Nathalie Bolfan-Casanova

μm in thickness before being loaded (Figure 3.2-4) in piston cylinder diamond anvil cells (Kantor et al., 2012).

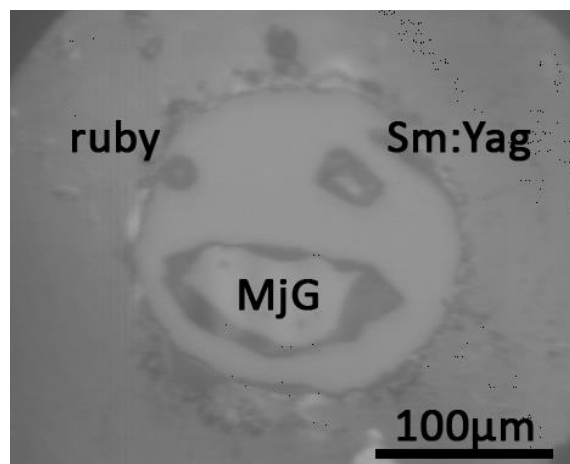


Figure 3.2-4. Image of the DAC after performing the gas loading ($P_1=0.7$ GPa) showing a crystal of majoritic garnet (Z946A', $98\times63\times15$ μm^3 in size) together with Sm:YAG and ruby loaded in Ne pressure medium.

Boehler-Almax diamonds were employed with 400-350 μm culets in combination with tungsten carbide seats. Rhenium gaskets of 200 μm in thickness were pre-indented to 40-55 μm and cylindrical holes of 250 μm were drilled using a spark erosion machine. Single-crystals of Sm:YAG as well as ruby chips were used as pressure calibrants. By combining the fluorescence shifts of Sm:YAG with the fluorescence shift of ruby it was possible to better constrain the temperature inside the pressure chamber without relying uniquely on the thermocouple (see Section 2.3.2.1). The pressure inside the cell was monitored before and after each Brillouin and X-ray measurement using an Acton standard series spectrograph from Princeton Instruments, employing the same laser and the same geometry as in the Brillouin experiment. An external resistive heater (see Section 2.3.1) was placed around the diamonds for achieving high temperatures. An S-type thermocouple located near the diamond surface was used to monitor the temperature inside the cell. A neon gas, as hydrostatic pressure medium, was loaded into the sample chamber using the high pressure gas loading devices at the Bayerisches Geoinstitut (Kurnosov et al., 2008) as well as at GSECARS (Rivers et al., 2008).

Simultaneous acquisition of density and sound velocities at room pressure was performed at the Bayerisches Geoinstitut (see Section 2.3.3.1 and 2.3.4.1). The lattice parameters were determined using the eight-position centring of 15 Bragg reflections ($25<2\theta<40$ degrees) according to the procedure of King and Finger (1979). The resulting unit cell volumes are

1506.6 (5) Å³ and 1506.8 (1) Å³ for Mj and Fe-Mj respectively. Typical half-widths of the ω profiles of different reflections varied between 0.060° and 0.100°. Brillouin scattering measurements were performed in a 80° symmetric/platelet scattering geometry with plate spacing of 4 mm using a coherent Verdi V2 solid state Nd:YVO₄ frequency doubled laser ($\lambda = 532.0$ nm) at the power of ~ 150-200 mW. In addition, for the Fe bearing majoritic sample, room pressure Brillouin scattering measurements were performed³ at the GeoForschungsZentrum (GFZ) in Potsdam as well as at PETRA III in Hamburg, employing a 59.97 and 49.17 degree forward symmetric scattering geometry with plate spacing of 6 mm and 8 mm respectively. A coherent Verdi V2 solid state Nd:YVO₄ frequency doubled laser ($\lambda = 532.0$ nm) was used.

Simultaneous measurements of sound velocities and density at different pressures and temperatures were performed at the BM-13-D (GSECARS) beamline at the Advance Photon Source (see Section 2.3.4.1). The samples were measured first upon compression up to approximately 20 and 21 GPa at room temperature and then heated to 558 K (Mj) and 470 K (Fe-Mj). During heating the pressure increased to 30 GPa, therefore Brillouin spectra and density were measured along an isotherm (at high temperature) upon decompression. X-ray diffraction measurements were performed using a Perkin Elmer detector, collecting step scans in an omega range of 50° or 70° with a step size of 1° and 5 s/step exposure time. Brillouin scattering measurements were performed with a six-pass Sandercock-type tandem Fabry-Pérot interferometer using a coherent Verdi V2 solid state Nd:YVO₄ frequency doubled laser ($\lambda = 532.0$ nm) as a light source. Measurements were performed in a 50° symmetric/platelet scattering geometry with plate spacing of 6.5-7 mm. Brillouin spectra of majoritic garnet were collected with a laser power of 400 mW. Sound velocities were determined from the frequency shift using the relationship reported in Section 2.3.4.

3.2.3 Single-crystal data collection and structure refinements

Two single crystals, one of Mj (84x70x100 μm^3) and one of Fe-Mj (100x70x30 μm^3) optically free of defects were selected from the run products H3882 and Z1038, respectively and mounted on a glass fiber. Intensity data collections were performed on an Xcalibur diffractometer (operated at 50 kV and 40 mA and equipped with a CCD detector) using MoK α radiation (graphite monochromator). Several ω scans were chosen to obtain coverage

³ Brillouin measurements in Potsdam and Hamburg were performed by Dr. Sergio Speziale as part of collaboration.

of the full reciprocal sphere up to $2\theta_{\max} = 72^\circ$, with an exposure time of 60 s/frame and a crystal detector distance of 45 mm. Lorentz and polarization factors together with an analytical absorption correction based on the crystal shape were employed for the correction of the reflection intensities using the CrysAlis package (Oxford Diffraction, 2006). Data collections at high pressures and at high-pressure and temperature were performed at the BM-13-D (GSECARS) at the Advance Photon Source as described in the section above. The program packages GSE_ADA and Reciprocal_Space_Viewer and XPREP developed at GSECARS were used to calculate crystal orientations, volumes and intensities from the diffraction data.

The measured reflections for each data collection were consistent with the cubic space group $Ia\bar{3}d$. Structure refinements were performed based on F^2 using the SHELX97 program package (Sheldrick, 2008) in the WingX System (Farrugia, 1999) starting from the atomic structural parameters of pyrope reported by Zhang et al. (1998). Atomic scattering factors for Si, Al, Mg, Fe and O were used and all atoms were refined anisotropically in the model used for the data collected in air and isotropically for the data collected from the crystals in the DACs. Given the negligible difference in the scattering factors between Mg, Al and Si, the site occupancies at the Y site were constrained according to the chemical analysis as follows: 0.109 Si + 0.750 Al + 0.160 Mg for Mj and 0.070 Si + 0.840 Al + 0.090 Mg for Fe-Mj. The X sites were considered fully occupied by Mg in Mj, whereas the occupancies of Mg and Fe were refined in Fe-Mj, whereas the Z site was considered fully occupied by Si in both samples. Details for all data collections and structural refinements are reported in Table 3.2-3.

Table 3.2-3. Structural refinement details and unit cell parameter of majoritic garnet

| <i>majoritic garnet</i> | | | | | |
|------------------------------------|-----------------------|-----------------------|-----------------------|-----------------------|-----------------------|
| <i>P</i> (GPa) | 0 | 12.15 | 15.50 | 15.72 (558 K) | 19.62 |
| Measured reflections | 2950 | 340 | 340 | 278 | 223 |
| Unique reflections | 297 | 74 | 74 | 67 | 56 |
| Fo > 4sig(Fo) | 276 | 74 | 74 | 67 | 55 |
| Rint | 2.60% | 6.81% | 6.13% | 7.50% | 6.73% |
| Rw for Fo > 4sig(Fo) | 3.30% | 3.00% | 3.39% | 3.84% | 3.50% |
| Rall | 3.82% | 3.00% | 3.39% | 3.84% | 3.57% |
| wR2 | 6.68% | 6.50% | 7.23% | 8.62% | 8.10% |
| GooF | 1.152 | 1.118 | 1.161 | 1.198 | 1.266 |
| No. parameters | 17 | 9 | 9 | 9 | 9 |
| Space group | <i>Ia-3d</i> | <i>Ia-3d</i> | <i>Ia-3d</i> | <i>Ia-3d</i> | <i>Ia-3d</i> |
| Z | 8 | 8 | 8 | 8 | 8 |
| F(000) | 1594 | 1600 | 1600 | 1600 | 1600 |
| Absorption coefficient | 1.21 mm ⁻¹ | 1.29 mm ⁻¹ | 1.30 mm ⁻¹ | 1.30 mm ⁻¹ | 1.33 mm ⁻¹ |
| Unit-cell parameters | | | | | |
| <i>a</i> (Å) | 11.4658(4) | 11.2261(1) | 11.1697(1) | 11.1749(1) | 11.1081(1) |
| <i>V</i> (Å ³) | 1507.35(9) | 1414.77(2) | 1393.56(2) | 1395.50(2) | 1370.63(2) |
| <i>Fe-bearing majoritic garnet</i> | | | | | |
| <i>P</i> (GPa) | 0 | 12.07 | 17.96 | 21.1 | |
| Measured reflections | 1690 | 374 | 360 | 398 | |
| Unique reflections | 293 | 71 | 66 | 68 | |
| Fo > 4sig(Fo) | 258 | 68 | 63 | 67 | |
| Rint | 3.05% | 6.59% | 6.33% | 7.10% | |
| Rw for Fo > 4sig(Fo) | 3.56% | 2.35% | 2.23% | 2.35% | |
| Rall | 4.56% | 2.48% | 2.24% | 2.60% | |
| wR2 | 7.37% | 6.17% | 5.57% | 5.51% | |
| GooF | 1.107 | 1.155 | 1.156 | 1.075 | |
| No. parameters | 19 | 9 | 9 | 9 | |
| Space group | <i>Ia-3d</i> | <i>Ia-3d</i> | <i>Ia-3d</i> | <i>Ia-3d</i> | |
| Z | 8 | 8 | 8 | 8 | |
| F(000) | 1620 | 1808 | 1808 | 1512 | |
| Absorption coefficient | 1.51 mm ⁻¹ | 3.25 mm ⁻¹ | 3.34 mm ⁻¹ | 3.05 mm ⁻¹ | |
| Unit-cell parameters | | | | | |
| <i>a</i> (Å) | 11.4643(4) | 11.2305(1) | 11.1345(1) | 11.0874(1) | |
| <i>V</i> (Å ³) | 1506.76(9) | 1416.44(2) | 1380.42(2) | 1362.98(2) | |

Details of atomic positions and displacement parameters at ambient conditions and at high pressures for both samples are reported in Table 3.2-4 and 3.2-5 respectively.

Table 3.2-4. Atomic coordinates and displacement parameters of majoritic garnet at ambient conditions

| Atom site | Wyckoff position | x | y | z | U ₁₁ | U ₂₂ | U ₃₃ | U ₂₃ | U ₁₃ | U ₁₂ | U _{eq} |
|------------------------------------|------------------|------------|------------|------------|-----------------|-----------------|-----------------|-----------------|-----------------|-----------------|-----------------|
| O | 96h | 0.03294(8) | 0.05010(9) | 0.65350(8) | 0.0092(4) | 0.0139(4) | 0.0102(4) | 0.0014(3) | -0.0012(3) | 0.0013(3) | 0.0111(2) |
| Si | 24d | 0.375 | 0 | 0.25 | 0.0056(3) | 0.0075(2) | 0.0075(2) | 0 | 0 | 0 | 0.0069(2) |
| Si | 16a | 0 | 0 | 0 | 0.0071(2) | 0.0071(2) | 0.0071(2) | -0.0002(2) | -0.0002(2) | -0.0002(2) | 0.0071(2) |
| Al | 16a | 0 | 0 | 0 | 0.0071(2) | 0.0071(2) | 0.0071(2) | -0.0002(2) | -0.0002(2) | -0.0002(2) | 0.0071(2) |
| Mg | 16a | 0 | 0 | 0 | 0.0071(2) | 0.0071(2) | 0.0071(2) | -0.0002(2) | -0.0002(2) | -0.0002(2) | 0.0071(2) |
| Mg | 24c | 0 | 0.25 | 0.125 | 0.0169(3) | 0.0169(3) | 0.0082(4) | 0 | 0 | 0.0052(4) | 0.0140(2) |
| <i>Fe-bearing majoritic garnet</i> | | | | | | | | | | | |
| O | 96h | 0.03302(9) | 0.05007(9) | 0.65340(9) | 0.0101(5) | 0.0120(5) | 0.0095(5) | 0.0004(4) | -0.0012(4) | 0.0013(4) | 0.0105(2) |
| Si | 24d | 0.375 | 0 | 0.25 | 0.0063(3) | 0.0074(2) | 0.0074(2) | 0 | 0 | 0 | 0.0071(2) |
| Si | 16a | 0 | 0 | 0 | 0.0066(2) | 0.0066(2) | 0.0066(2) | -0.0002(2) | -0.0002(2) | -0.0002(2) | 0.0066(2) |
| Al | 16a | 0 | 0 | 0 | 0.0066(2) | 0.0066(2) | 0.0066(2) | -0.0002(2) | -0.0002(2) | -0.0002(2) | 0.0066(2) |
| Mg | 16a | 0 | 0 | 0 | 0.0066(2) | 0.0066(2) | 0.0066(2) | -0.0002(2) | -0.0002(2) | -0.0002(2) | 0.0066(2) |
| Mg | 24c | 0 | 0.25 | 0.125 | 0.0152(4) | 0.0152(4) | 0.0080(4) | 0 | 0 | 0.0036(4) | 0.0128(3) |
| Fe | 24c | 0 | 0.25 | 0.125 | 0.0152(4) | 0.0152(4) | 0.0080(4) | 0 | 0 | 0.0036(4) | 0.0128(3) |

3. HP-HT single-crystal elasticity of majoritic garnet

Table 3.2-5. Atomic coordinates and displacement parameter of majoritic garnet at high pressure

| Atom | site | Wyckoff position | x | y | z | U_{eq} |
|------------------------------------|------|------------------|-----------|-----------|-----------|------------|
| <i>majoritic garnet</i> | | | | | | |
| <i>P = 12.15 GPa</i> | | | | | | |
| O | O | 96h | 0.0330(3) | 0.0536(4) | 0.6531(3) | 0.0095(8) |
| Si | Z | 24d | 0.375 | 0 | 0.25 | 0.0072(6) |
| Si | Y | 16a | 0 | 0 | 0 | 0.0052(5) |
| Al | Y | 16a | 0 | 0 | 0 | 0.0052(5) |
| Mg | Y | 16a | 0 | 0 | 0 | 0.0052(5) |
| Mg | X | 24c | 0 | 0.25 | 0.125 | 0.0090(9) |
| <i>P = 15.50 GPa</i> | | | | | | |
| O | O | 96h | 0.0329(3) | 0.0534(4) | 0.6531(3) | 0.0097(9) |
| Si | Z | 24d | 0.375 | 0 | 0.25 | 0.0071(7) |
| Si | Y | 16a | 0 | 0 | 0 | 0.0054(6) |
| Al | Y | 16a | 0 | 0 | 0 | 0.0054(6) |
| Mg | Y | 16a | 0 | 0 | 0 | 0.0054(6) |
| Mg | X | 24c | 0 | 0.25 | 0.125 | 0.0084(10) |
| <i>P = 19.62 GPa</i> | | | | | | |
| O | O | 96h | 0.0327(7) | 0.0558(6) | 0.6538(2) | 0.0098(18) |
| Si | Z | 24d | 0.375 | 0 | 0.25 | 0.0102(12) |
| Si | Y | 16a | 0 | 0 | 0 | 0.0057(10) |
| Al | Y | 16a | 0 | 0 | 0 | 0.0057(10) |
| Mg | Y | 16a | 0 | 0 | 0 | 0.0057(10) |
| Mg | X | 24c | 0 | 0.25 | 0.125 | 0.0065(14) |
| <i>P = 15.72 GPa, T = 558 K</i> | | | | | | |
| O | O | 96h | 0.0330(5) | 0.0548(5) | 0.6532(2) | 0.0104(13) |
| Si | Z | 24d | 0.375 | 0 | 0.25 | 0.0080(11) |
| Si | Y | 16a | 0 | 0 | 0 | 0.0058(8) |
| Al | Y | 16a | 0 | 0 | 0 | 0.0058(8) |
| Mg | Y | 16a | 0 | 0 | 0 | 0.0058(8) |
| Mg | X | 24c | 0 | 0.25 | 0.125 | 0.0120(17) |
| <i>Fe-bearing majoritic garnet</i> | | | | | | |
| <i>P = 12.07 GPa</i> | | | | | | |
| O | O | 96h | 0.0328(3) | 0.0535(4) | 0.6537(4) | 0.0062(9) |
| Si | Z | 24d | 0.375 | 0 | 0.25 | 0.0054(8) |
| Si | Y | 16a | 0 | 0 | 0 | 0.0046(6) |
| Al | Y | 16a | 0 | 0 | 0 | 0.0046(6) |
| Mg | Y | 16a | 0 | 0 | 0 | 0.0046(6) |
| Mg | X | 24c | 0 | 0.25 | 0.125 | 0.0078(12) |
| Fe | X | 24c | 0 | 0.25 | 0.125 | 0.0078(12) |
| <i>P = 17.96 GPa</i> | | | | | | |
| O | O | 96h | 0.0329(3) | 0.0545(4) | 0.6536(4) | 0.0064(7) |
| Si | Z | 24d | 0.375 | 0 | 0.25 | 0.0050(8) |
| Si | Y | 16a | 0 | 0 | 0 | 0.0049(6) |
| Al | Y | 16a | 0 | 0 | 0 | 0.0049(6) |
| Mg | Y | 16a | 0 | 0 | 0 | 0.0049(6) |
| Mg | X | 24c | 0 | 0.25 | 0.125 | 0.0073(12) |
| Fe | X | 24c | 0 | 0.25 | 0.125 | 0.0073(12) |
| <i>P = 21.10 GPa</i> | | | | | | |
| O | O | 96h | 0.0327(3) | 0.0551(4) | 0.6536(4) | 0.0061(10) |
| Si | Z | 24d | 0.375 | 0 | 0.25 | 0.0060(8) |
| Si | Y | 16a | 0 | 0 | 0 | 0.0053(6) |
| Al | Y | 16a | 0 | 0 | 0 | 0.0053(6) |
| Mg | Y | 16a | 0 | 0 | 0 | 0.0053(6) |
| Mg | X | 24c | 0 | 0.25 | 0.125 | 0.0066(11) |
| Fe | X | 24c | 0 | 0.25 | 0.125 | 0.0066(11) |

3.3 Results and discussion

3.3.1 Elasticity

The acoustic velocities of Mj and Fe-Mj samples measured in different crystallographic directions as a function of χ angle at room conditions are shown in Figure 3.3-1. Typical Brillouin spectra are also reported as insets in the same Figure.

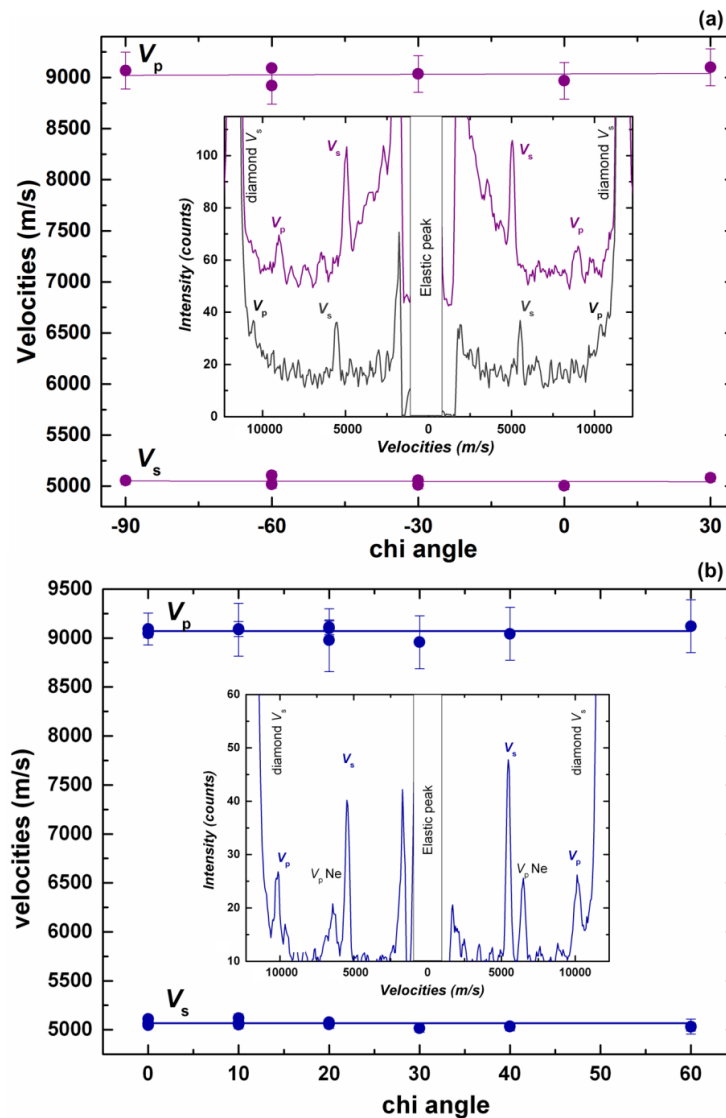


Figure 3.3-1. (a) Compressional and shear wave velocities of majoritic garnet (Mj) as a function of crystallographic direction at room pressure and temperature. Brillouin spectra collected for a given crystallographic orientation at room pressure and temperature (purple) and at 28.04 GPa and 558 K (dark grey) also are shown as inset. (b) Compressional and shear wave velocities of Fe-bearing majoritic garnet (Fe-Mj) as a function of crystallographic direction at room pressure and temperature. The Brillouin spectrum reported in the inset was collected at 21.10 GPa.

As shown in Figure 3.3-1, the elastic anisotropy of majoritic-garnet is practically negligible at ambient conditions and it appears to have an identical behaviour at high pressures, as also observed for other garnet samples (e.g. Sinogeikin and Bass, 2000; Murakami et al., 2008) even at high temperatures (Lu et al., 2013). The experimental sound velocities are a function of the crystallographic orientation q , the elastic moduli C_{ij} and the density of a given material, according to the Christoffel equation:

$$|C_{rlsm}q_l q_m - \rho V^2 \delta_{rs}| = 0, \quad (3.1)$$

where δ_{rs} is the Kronecker delta. Elastic constants can thus be obtained by fitting the solutions of the equation of motion (3.1) to the measured sound velocities. However, as reported in previous studies (Sinogeikin and Bass, 2000; Murakami et al., 2008) the elastic constants of majoritic garnet also can be calculated by averaging the measured acoustic velocities over several non-symmetric directions given the negligible anisotropy. The aggregate values so obtained are indistinguishable, within experimental uncertainties, from those derived from the least-squares fitting to the Christoffel's equation. In this study, aggregate V_p and V_s were obtained as the average of all longitudinal and transverse velocity measurements (for up to three orientations) at each pressure and temperature. The aggregate elastic moduli were then calculated from these aggregate velocities. The majoritic single-crystal elastic moduli can then be related to the aggregate moduli through the following equations:

$$C_{11} = K + 4/3G = \rho V_p^2 \quad (3.2)$$

$$C_{44} = G = \rho V_s^2 \quad (3.3)$$

$$C_{12} = K - 2/3G = \rho(V_p^2 - 2V_s^2) \quad (3.4)$$

assuming the following equality:

$$2C_{44} = C_{11} - C_{12} \quad (3.5)$$

The elastic properties and sound velocities of both samples as a function of density, pressure and temperature are summarized in Table 3.3-1.

3. HP-HT single-crystal elasticity of majoritic garnet

Table 3.3-1. Single-crystal and aggregate elastic properties, aggregate sound velocities as a function of absolute pressure, temperature and density of majoritic garnets.

| ρ (g/cm ³) | P_{abs} (GPa) | P_{VAG} (GPa) | P_{ruby} (GPa) | T (K) | C_{11} (GPa) | C_{12} (GPa) | C_{44} (GPa) | V_s (km/s) | V_p (km/s) | K_s (GPa) | G (GPa) |
|------------------------------------|------------------------|------------------------|-------------------------|-------|----------------|----------------|----------------|--------------|--------------|-------------|-----------|
| <i>Majoritic garnet (Mj)</i> | | | | | | | | | | | |
| 3.552 | 0.0001 | 0.0001 | 0.0001 | 298 | 290(3) | 109(2) | 91(1) | 5.05(1) | 9.03(3) | 169(3) | 91(1) |
| 3.692 | 7.04 | 8.02 | 7.53 | 298 | 333(6) | 128(6) | 102(1) | 5.26(2) | 9.50(8) | 197(6) | 102(1) |
| 3.729 | 9.06 | 9.32 | 9.11 | 298 | 349(4) | 139(3) | 105(1) | 5.30(2) | 9.67(2) | 209(3) | 105(1) |
| 3.75 | 10.24 | 10.36 | 10.27 | 298 | 351(8) | 140(8) | 106(1) | 5.31(2) | 9.68(10) | 210(8) | 106(1) |
| 3.783 | 12.15 | 13.19 | 12.58 | 298 | 363(30) | 145(30) | 109(1) | 5.37(2) | 9.80(40) | 218(30) | 109(1) |
| 3.844 | 15.81 | 16.97 | 16.62 | 298 | 390(4) | 166(2) | 112(1) | 5.40(2) | 10.080(8) | 241(3) | 112(1) |
| 3.839 | 15.50 | 16.86 | 16.07 | 298 | 385(9) | 161(9) | 112(1) | 5.41(5) | 10.01(10) | 235(9) | 112(1) |
| 3.892 | 18.84 | 19.74 | 19.30 | 298 | 406(4) | 176(2) | 115(1) | 5.436(7) | 10.22(2) | 253(3) | 115(1) |
| 3.904 | 19.62 | 21.15 | 20.59 | 298 | 414(10) | 180(9) | 117(2) | 5.47(2) | 10.29(11) | 258(9) | 117(2) |
| 3.834 | 15.72 | 17.17 | 16.44 | 558 | 382(6) | 160(6) | 111(2) | 5.38(3) | 9.98(7) | 234(6) | 111(2) |
| 3.926 | 21.44 | 22.33 | 21.18 | 558 | 409(9) | 181(9) | 114(2) | 5.39(5) | 10.21(10) | 257(9) | 114(2) |
| 3.98 | 25.01 | 25.19 | 24.15 | 558 | 422(17) | 185(17) | 119(3) | 5.46(4) | 10.30(20) | 264(14) | 119(3) |
| 4.024 | 28.04 | 27.99 | 27.15 | 558 | 463(14) | 216(14) | 123(3) | 5.53(5) | 10.72(15) | 298(14) | 123(3) |
| <i>Fe-majoritic garnet (Fe-Mj)</i> | | | | | | | | | | | |
| 3.601 | 0.0001 | 0.0001 | 0.0001 | 298 | 296(4) | 111(2) | 92(1) | 5.068(8) | 9.07(3) | 173(3) | 92(1) |
| 3.622 | 1.00 | 0.93 | 0.93 | 298 | 301(5) | 111(5) | 95(1) | 5.11(1) | 9.11(7) | 174(5) | 95(1) |
| 3.664 | 3.07 | 2.88 | 2.84 | 298 | 314(7) | 120(7) | 97(1) | 5.14(2) | 9.26(9) | 185(7) | 97(1) |
| 3.757 | 7.90 | 8.08 | 7.81 | 298 | 345(14) | 138(14) | 104(2) | 5.25 (3) | 9.58(19) | 207(14) | 104(2) |
| 3.832 | 12.07 | 12.36 | 11.90 | 298 | 364(11) | 150(11) | 107(1) | 5.28(1) | 9.75(14) | 222(11) | 107(1) |
| 3.865 | 13.99 | 14.88 | 14.25 | 298 | 374(7) | 150(8) | 112(2) | 5.38(5) | 9.84(8) | 225(7) | 112(2) |
| 3.931 | 17.96 | 18.89 | 18.01 | 298 | 398(6) | 168(5) | 115(1) | 5.40(1) | 10.06(6) | 245(5) | 115(1) |
| 3.981 | 21.10 | 22.54 | 21.44 | 298 | 412(7) | 176(7) | 118(1) | 5.45(1) | 10.18(7) | 255(6) | 118(1) |
| 3.826 | 12.10 | 12.53 | 12.30 | 470 | 362(20) | 151(20) | 106(1) | 5.25(3) | 9.73(27) | 221(20) | 106(1) |
| 3.897 | 16.18 | 16.76 | 16.27 | 470 | 389(9) | 164(9) | 113(1) | 5.37(2) | 9.99(11) | 239(9) | 113(1) |
| 3.961 | 20.04 | 20.65 | 20.21 | 470 | 396(20) | 170(20) | 113(2) | 5.34(4) | 10.00(24) | 245(20) | 113(2) |
| 4.022 | 23.90 | 24.29 | 24.00 | 470 | 435(9) | 195(9) | 120(2) | 5.46(3) | 10.40(17) | 275(15) | 120(2) |
| 4.047 | 25.53 | 26.75 | 26.17 | 470 | 438(13) | 195(12) | 121(1) | 5.47(1) | 10.40(15) | 276(13) | 121(1) |

Brillouin spectra collected with diamond anvil cells at different pressures, temperatures and orientations have typically different signal to noise ratios, depending on the crystal optical quality, its orientation, as well as on laser focusing, sample alignment and collection time. The resolution of such spectra will influence the uncertainties on the V_s and V_p values used to obtain the elastic constants. The uncertainties on the velocities of majoritic garnets were assessed considering a "calibration curve" constructed by collecting a set of measurements of the same Brillouin spectrum with different signal to noise ratios and relating their standard deviations to their resolution (see Appendix A1).

The bulk and shear moduli and the single crystal elastic constants of majoritic garnets are reported as a function of density in Figure 3.3-2 and 3.3-3.

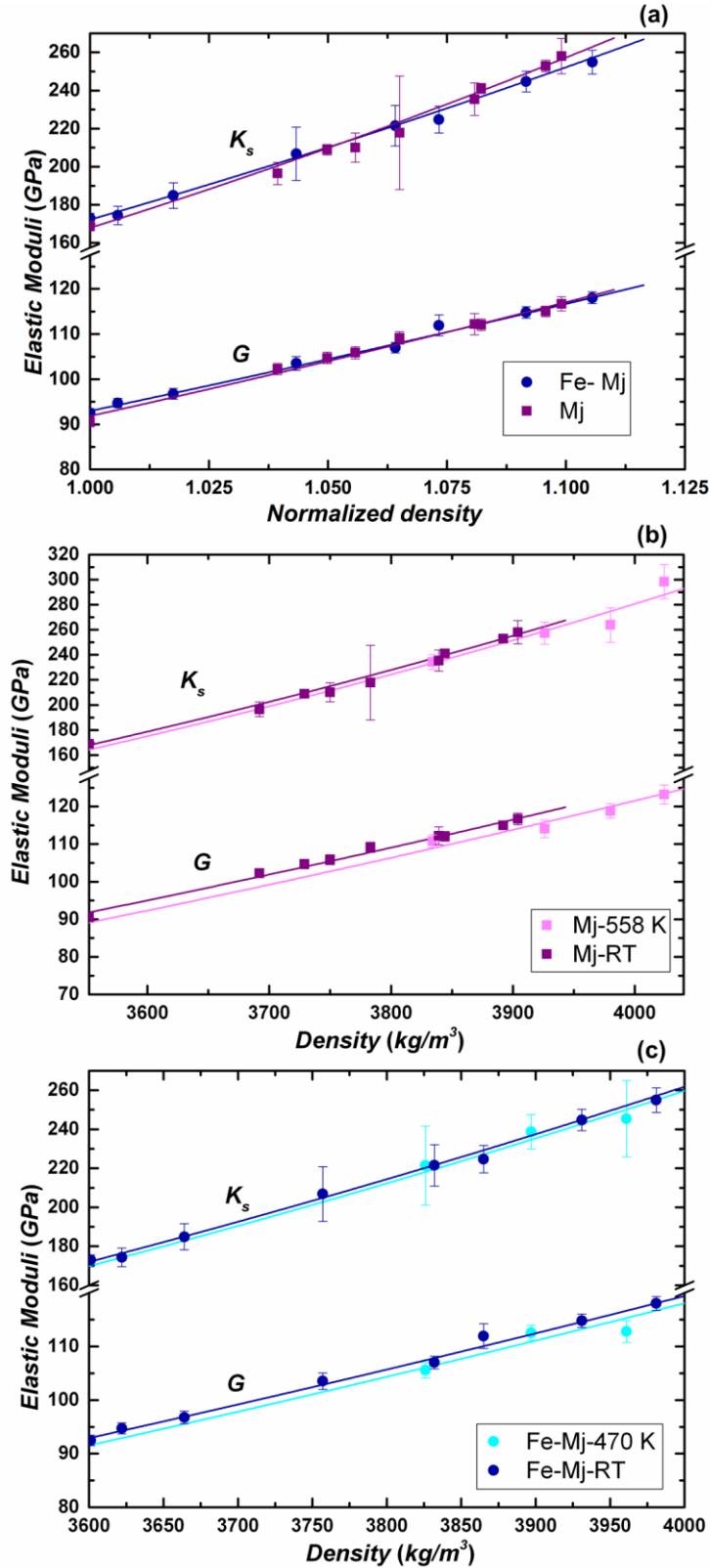


Figure 3.3-2. Variation of the Bulk (K_s) and shear (G) moduli as a function of normalized density (ρ/ρ_0) and density of (a) $\text{Mg}_{3.24}\text{Al}_{1.53}\text{Si}_{3.23}\text{O}_{12}$ (Mj) and $\text{Mg}_{3.01}\text{Fe}_{0.17}\text{Al}_{1.68}\text{Si}_{3.15}\text{O}_{12}$ (Fe-Mj) at room temperature and high pressures, (b) $\text{Mg}_{3.24}\text{Al}_{1.53}\text{Si}_{3.23}\text{O}_{12}$ (Mj) at 298 and at 558 K and at high pressures and (c) $\text{Mg}_{3.01}\text{Fe}_{0.17}\text{Al}_{1.68}\text{Si}_{3.15}\text{O}_{12}$ (Fe-Mj) at 298 and at 470 K and at high pressures. The solid lines correspond to the Birch-Murnaghan equation of state fits.

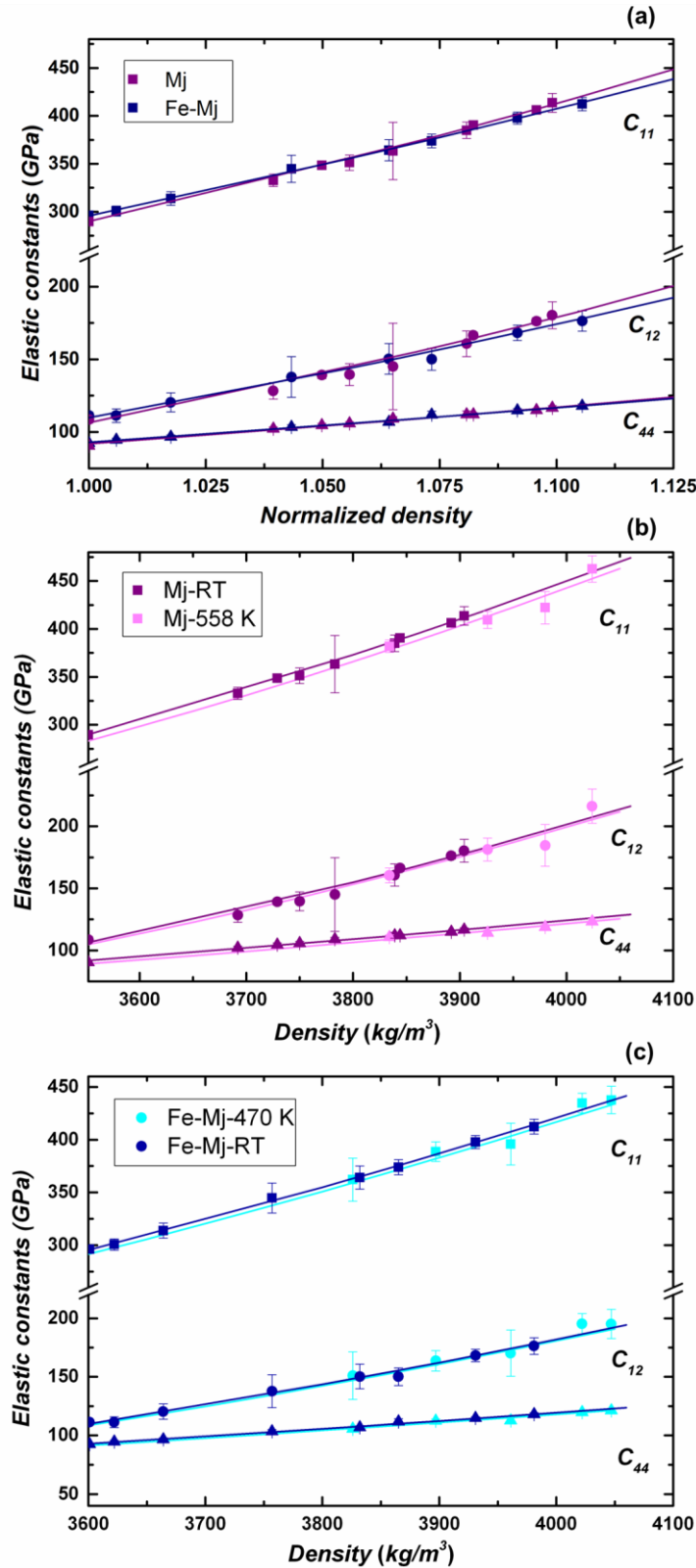


Figure 3.3-3. Variation of the elastic constants (C_{11} , C_{12} , C_{44}) as a function of normalized density (ρ/ρ_0) and density of (a) $Mg_{3.24}Al_{1.53}Si_{3.23}O_{12}$ (Mj) and $Mg_{3.01}Fe_{0.17}Al_{1.68}Si_{3.15}O_{12}$ (Fe-Mj) at room temperature and high pressures, (b) $Mg_{3.24}Al_{1.53}Si_{3.23}O_{12}$ (Mj) at 298 and at 558 K and at high pressures and (c) $Mg_{3.01}Fe_{0.17}Al_{1.68}Si_{3.15}O_{12}$ (Fe-Mj) at 298 and at 470 K and at high pressures. The solid lines correspond to the Birch-Murnaghan equation of state fits.

The variation of the bulk (K_s) and shear (G) moduli as a function of density for both samples at room temperature and high pressure are reported in Figure 3.3-2a. The pressure derivatives of the elastic moduli were obtained by fitting the moduli at high pressure using a third-order Birch-Murnaghan equation of state:

$$K_s = (1 + 2f)^{5/2} \left\{ K_{s_0} + \left[3K_{s_0} \left(\frac{\partial K_s}{\partial P} \right)_T - 5K_{s_0} \right] f + \frac{27}{2} \left[K_{s_0} \left(\frac{\partial K_s}{\partial P} \right)_T - 4K_{s_0} \right] f^2 \right\} \quad (3.6)$$

$$G = (1 + 2f)^{5/2} \left\{ G_0 + \left[3K_{s_0} \left(\frac{\partial G}{\partial P} \right)_T - 5G_0 \right] f \right\} \quad (3.7)$$

$$\text{with } f = (1/2) \left[\left(\frac{\rho}{\rho_0} \right)^{2/3} - 1 \right] \quad (3.8)$$

where $(\partial K_s / \partial P)_T$ and $(\partial G / \partial P)_T$ are the pressure derivatives of the bulk and shear moduli at constant temperature, respectively, f is the normalized strain, ρ is density at a given pressure, and ρ_0 is the density at ambient conditions. The temperature effect under high pressure of the elastic properties of both samples is shown in Figures 3.3-2b-c and 3.3-3b-c.

Temperatures inside the diamond anvil cell are in general determined using a thermocouple, and can be maintained at a constant value for several hours when using an electrical heater. However, the thermocouple has to be carefully placed close to the sample in order to measure the correct temperature inside the DAC. Accurate temperature measurements require, therefore, a calibration of the thermocouple reading (see section 2.3.1). To constrain the temperature inside the pressure chamber without relying uniquely on the thermocouple, an alternative approach has been used in this study. The fluorescence shifts of Sm:YAG which is independent of temperature were used to determine pressure, whereas temperature was determined using the fluorescence of ruby by fixing the pressure value obtained from the YAG measurement (see section 2.3.2.1). Temperatures were estimated in this way to be 558 K and 470 K for Mj and Fe-Mj respectively. It is worth noticing that the temperature readings from the thermocouples used in the two experiments were 600 K for Mj and 650 K for Fe-Mj, i.e. much larger than the actual temperatures experienced by the majoritic samples.

In this chapter a high-temperature form of the 3rd-order Birch-Murnaghan EoS (Duffy and Wang, 1998) has been applied to obtain the temperature derivatives of the elastic moduli at high pressures (see section 2.3.3.1.2) in accordance with the procedure followed in the majority of the experimental works present in the literature:

$$K_s(T) = K_{s_0}(T_0) + \left(\frac{\partial K_s}{\partial T} \right)_P (T - T_0) \quad (3.9)$$

$$G(T) = G_0(T_0) + \left(\frac{\partial G}{\partial T} \right)_P (T - T_0) \quad (3.10)$$

where T_0 is the reference temperature (usually 298 K). The high-temperature values for the volume were obtained according to equation (2.15) reported in section 2.3.3.1.2, which takes into account the thermal expansion. A more self-consistent high-pressure high-temperature model which makes use of a Mie-Grüneisen equation of state for evaluating the thermal pressure will be presented in Chapter 6.

The elastic moduli were extracted by simultaneously fitting equations (3.6), (3.7), and (3.9) and (3.10) above using the quasi-Newton minimization of the sum of all residuals. The resulting EoS parameter uncertainties were calculated from the variance-covariance matrix. The adiabatic bulk and shear moduli were determined to be $K_{S0} = 168(2)$ GPa, $G_0 = 91.8(7)$ GPa for Mj and, $K_{S0} = 172(1)$ GPa, $G_0 = 93.0(6)$ GPa for Fe-Mj. The pressure derivatives of the bulk and shear moduli at constant temperature are $(\partial K / \partial P)_T = 4.7(2)$, $(\partial G / \partial P)_T = 1.40(5)$ for Mj and $(\partial K / \partial P)_T = 4.2(1)$, $(\partial G / \partial P)_T = 1.30(5)$ for Fe-Mj. The temperature derivatives of these moduli at constant pressure are $(\partial K / \partial T)_P = -0.014(15)$ GPa/K and $(\partial G / \partial T)_P = -0.0104(3)$ GPa/K for Mj. and $(\partial K / \partial T)_P = -0.014$ GPa/K and $(\partial G / \partial T)_P = -0.008(4)$ GPa/K for Fe-Mj. Note, that due to the small thermal effect on the elastic properties of Fe-Mj, the temperature derivative of the shear modulus of Fe-Mj was evaluated by fixing the $(\partial K / \partial T)_P$ value to that obtained for Mj. The resulting value of $(\partial G / \partial T)_P$ for Fe-Mj is $-0.008(4)$ GPa/K.

From the data obtained in this study it is clear that Fe substitution affect the elastic properties of majoritic garnets. The adiabatic bulk and shear moduli of the two samples are compared in Figure 3.3-2a. The K_s and G values are very similar at room pressure, with Fe-Mj garnet only slightly less compressible than Mj. However at higher pressures, Fe-Mj becomes more compressible than Mj due to its smaller $(\partial K / \partial P)_T$ value. This difference is also visible in Figure 3.3-3a where the C_{11} and C_{12} clearly display a different behaviour. The two samples display a similar pressure dependency of the shear moduli and consequently C_{44} . The temperature effect under high pressure of the elastic properties of Mj and Fe-Mj samples is shown in Figures 3.3-2b and 3.3-2c, respectively. The thermal effect on the elastic properties of Fe-Mj, particularly in the bulk moduli, is smaller compared to Mj, probably due to the lower temperature at which the measurements were performed.

3.3.1.1 Absolute pressure determination

An important advantage in making simultaneous measurements of density and sound velocities for the same sample at the same conditions is that it allows pressure to be determined absolutely without having to rely on a secondary pressure scale, such as that of the ruby fluorescence scale. For each experimental point, the absolute pressure was determined according to the equation (2.3) reported in Section 2.3.2.2

The isothermal bulk modulus K_T was derived from the adiabatic bulk modulus K_S (equation 2.4), calculated using the sound velocities obtained from Brillouin spectroscopy whereas the unit-cell volume (V) was determined by means of X-ray diffraction. The ambient-pressure thermal expansion α and the Grüneisen parameter γ are defined as $\alpha(T) = a_0 + a_1T + a_2T^{-2}$, $\gamma = \alpha K_s / \rho C_p$. The values of α and γ for the majorite-pyrope solid solutions were assumed to be equal to those of pyrope and were taken from Fei (1995) and Anderson and Isaak (1995) respectively. A comparison between the pressures obtained from the ruby and Sm:YAG fluorescence pressure scales and the absolute pressure determined from the experiments is reported in Table 3.3-1. The differences in pressure scales and their effect on the determination of the EoS parameters of majoritic garnet will be discussed in the following section.

The variation of the shear (V_s) and compressional (V_p) wave velocities as a function of absolute pressure obtained in this study at high pressures and temperatures are reported in Figure 3.3-4. The effect of the substitution of Fe in majoritic garnet is also visible in the different behaviour of the sound velocities. Both values of the shear (V_s) and compressional (V_p) wave velocities are very similar at room pressure. The sound velocities deviate at high pressures, with Mj displaying faster velocities due to the higher pressure derivatives of the elastic moduli as described above. As for the elastic moduli, the effect of temperature on the sound velocities of Fe-Mj, is smaller compared to Mj, particularly for V_p .

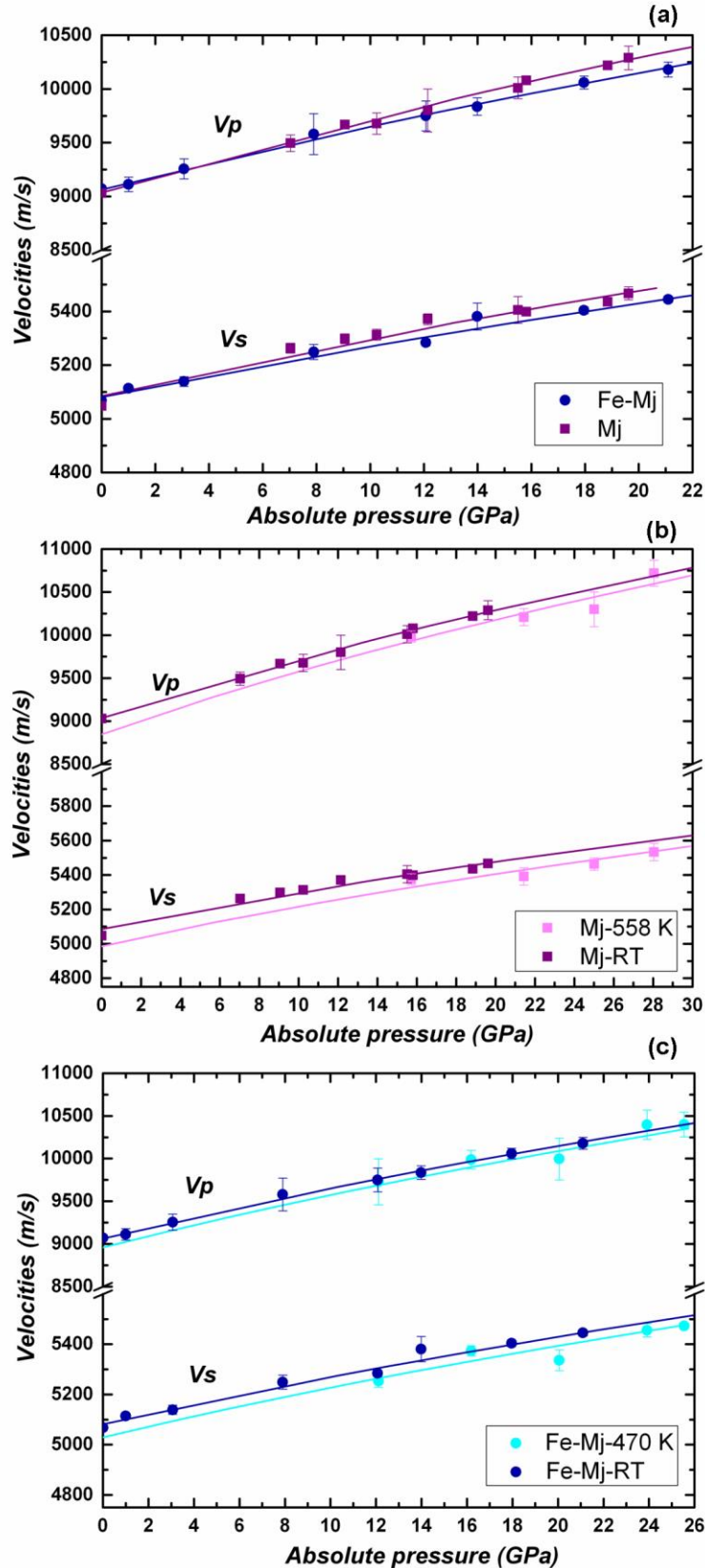


Figure 3.3-4. Variation of the shear (V_s) and compressional (V_p) wave velocities as a function of absolute pressure of (a) $Mg_{3.24}Al_{1.53}Si_{3.23}O_{12}$ (Mj) and $Mg_{3.01}Fe_{0.17}Al_{1.68}Si_{3.15}O_{12}$ (Fe-Mj) at room temperature, (b) of $Mg_{3.24}Al_{1.53}Si_{3.23}O_{12}$ (Mj) at room temperature and at 558 K and (c) $Mg_{3.01}Fe_{0.17}Al_{1.68}Si_{3.15}O_{12}$ (Fe-Mj) at room temperature and at 470 K.

3.3.1.2 *P-V Equation of state*

The P – V data obtained from X-ray diffraction measurements were fit using a third-order Birch–Murnaghan equation of state (Birch, 1947) with the software EOSFIT-5.2 (Angel, 2002). Simultaneous refinement of the unit-cell volume V_0 , the bulk modulus K_{T0} and the first pressure derivative K_T' for each crystal resulted in the following coefficients: $V_0 = 1506.8(7) \text{ \AA}^3$, $K_{T0} = 165(3) \text{ GPa}$ and $K_T' = 4.8(2)$ for Mj and $V_0 = 1506.8(2) \text{ \AA}^3$, $K_{T0} = 172(1) \text{ GPa}$ and $K_T' = 4.0(1)$ for Fe-Mj. Note that the reported values of EoS parameters were obtained considering the values of absolute pressures obtained in this study. For purpose of comparison the EoS parameters obtained using the Sm:YAG and the ruby pressure scales reported by Trots et al. (2013) and Mao et al. (1986) respectively, are also presented, in Table 3.2-2.

Table 3.3-2. EoS parameters of majoritic garnet

| IIIBM | V_0 (\AA^3) | K_{T0} (GPa) | K_T' | K_T'' (GPa^{-1}) |
|--------------------|--------------------------|----------------|----------|-------------------------------|
| Mj ^a | 1506.8(7) | 165(3) | 4.8(2) | [-0.033] |
| Mj ^b | 1507(5) | 171(20) | 5.7(1.9) | [-0.049] |
| Mj ^c | 1507(3) | 162(12) | 6.1(1.2) | [-0.063] |
| Fe-Mj ^a | 1506.8(2) | 172(1) | 4.0(1) | [-0.023] |
| Fe-Mj ^b | 1506(1) | 174(6) | 5.3(7) | [-0.039] |
| Fe-Mj ^c | 1505.9(9) | 169(6) | 4.8(6) | [-0.031] |

Numbers in parentheses are the standard deviations

Numbers in square brackets are implied values

^a Absolute pressure scale

^b Sm:YAG pressures scale

^c Ruby pressures scale

The different pressure standards usually do not yield identical pressures (see Table 3.3-1) at the same experimental conditions, leading to considerable uncertainty in the determination of the physical properties and their pressure dependences. When fitting EoS to compressional data, it is normal to find a negative correlation coefficient between K_{T0} and K_T' , indicating that the data can be fitted equally well by decreasing the value of K_{T0} and increasing the value of K_T' , or vice-versa (Angel, 2000). To better visualize this correlation, confidence ellipses can be calculated from the variances-covariances of K_{T0} and K_T' obtained from the least-square refinements (Angel, 2000). A detailed comparison of the EoS parameters (K_{T0} and

K_T') of majoritic garnets (Mj and Fe-Mj) obtained considering different pressure scales is illustrated in Figure 3.3-5.

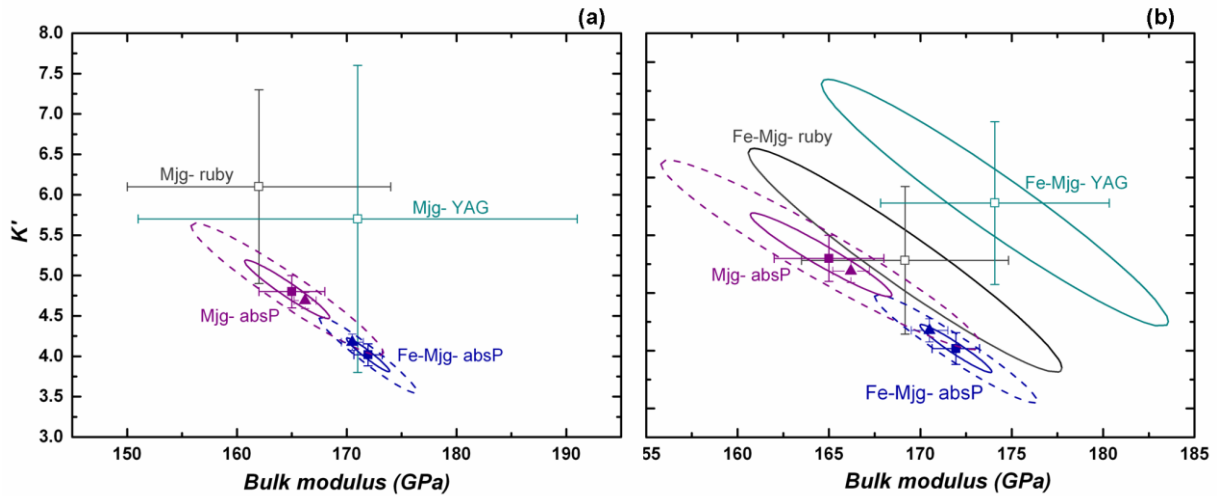


Figure 3.3-5. Confidence ellipses in K_0 and K' for the fit of the third order BM EoS using the values of absolute pressure for Mj and Fe-Mj calculated at the 68.3% confidence level (internal ellipses indicated by solid lines) and at the 99.7% confidence level (external ellipses represented by dashed lines). The isothermal bulk moduli derived from the corresponding adiabatic moduli obtained from Brillouin measurements also are reported (triangles). The 1σ error bars of K_{T0} and K_T' are those obtained from the least square refinements. For comparison the values of K_{T0} and K_T' as well as their 1σ uncertainties obtained using the pressure values from Sm:YAG and ruby pressure scales are reported in (a) for Mj and in (b) for Fe-Mj. Confidence ellipses at the 68.3% level are also drawn in (b) and are even larger for Mj.

The internal ellipses represent a K_{T0} - K_T' parameter space with the 68.3 % probability level that the true values of K_{T0} and K_T' lie within the areas restricted by the ellipses, whereas the external ellipses represent the 99.7 % confident level. The ellipses are elongated with a negative slope, indicating the negative correlation of the parameters K_{T0} and K_T' . Also shown are the 1σ error bars for K_{T0} and K_T' obtained from the least square refinements. Note that these values are smaller than the total range of K_{T0} and K_T' covered by the 68.3 % confidence ellipses for the two parameters together. This indicates that the standard deviations alone do not represent the true values of K_{T0} and K_T' .

For the purpose of comparison, the K_{T0} and K_T' for both samples derived from the adiabatic bulk moduli obtained from Brillouin measurements are also reported in Figure 3.3.-5 as triangles. These data points lie within the confidence ellipses representing the P - V data obtained using the values of the absolute pressure scale.

The EoS results obtained using the pressure scales of Sm:YAG and ruby are also shown for comparison together with their 1σ errors. Due to the large uncertainties in K and K' for Mj (Figure 3.3-5), the confidence ellipses for these parameters were not drawn. The values obtained from the pressure scales of both secondary standards are clearly very different from the adiabatic values obtained from Brillouin spectroscopy. An important aspect in terms of accurate determination of pressure from the fluorescence shift of standard materials is that the measurements are made of the fluorescence spectrum from a reference sample at ambient pressure (1 bar) as well as the spectrum of the equivalent material within the sample chamber at high pressure (section 2.3.2.1). In this study, the pressure inside the cell was monitored before and after each Brillouin and X-ray measurement, however, it was not possible to measure the reference standard. The lack of an appropriate reference value very likely is affecting the pressure determination, since small variations in the wavelength of the reference standard cause large variations in the pressure values and as a consequence gives rise to the large uncertainties shown in Figure 3.3-5.

3.3.2 Effect of Fe substitution on the structure and elasticity of majoritic garnet

As reported in Section 3.3.1, the substitution of Fe affects the elastic properties of majoritic garnets, with Fe-Mj becoming more compressible than Mj at higher pressures. In order to understand this difference in behaviour in elastic properties between the two samples investigated in this study, it is important to understand the factors controlling the garnet compression and therefore it is necessary to compare their crystal structures as a function of pressure.

The garnet crystal structure consists of a relatively rigid, three-dimensional network of alternating corner-shared ZO_4 tetrahedra and YO_6 octahedra, with Mg^{2+} , Al^{3+} , and Si^{4+} occupying the octahedral sites. The resulting cavities define an 8-fold coordinated dodecahedral site, containing the X cations, Mg^{2+} and Fe^{2+} in the samples from this study. The different polyhedra are linked in a complex way. Each ZO_4 tetrahedron shares edges with two XO_8 dodecahedra while each YO_6 octahedron shares edges with six XO_8 dodecahedra. Each XO_8 dodecahedron shares edges with two ZO_4 tetrahedra, four YO_6 octahedra, and four XO_8 dodecahedra.

A section of the crystal structure of the Fe-bearing majoritic garnet investigated in this study is reported in Figure 3.3-6. The interatomic distances in the different polyhedra are also displayed in the Figure.

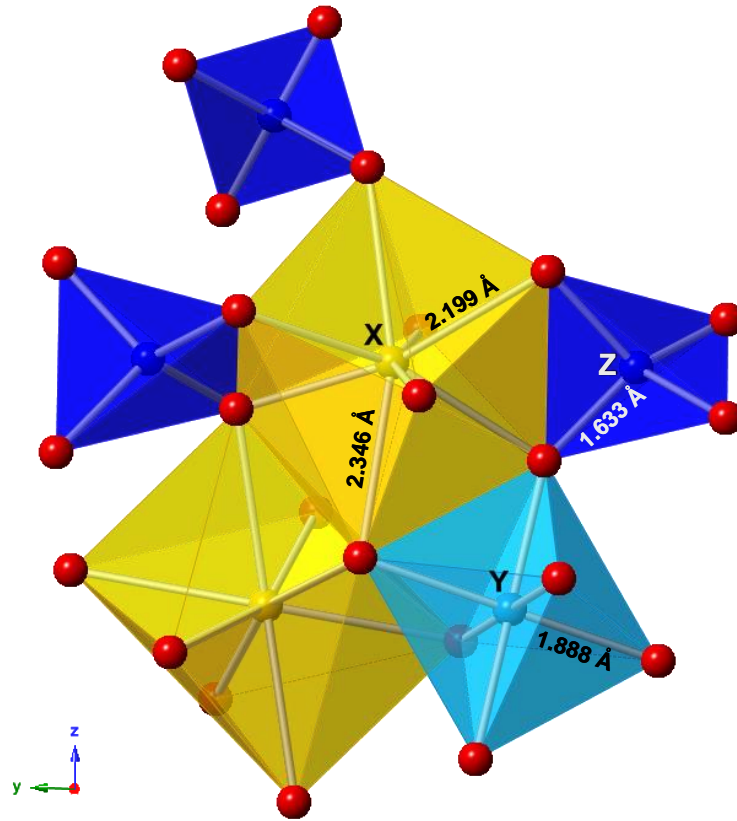


Figure 3.3-6. Section of the crystal structure of majoritic garnets. The dark-blue tetrahedra correspond to the Z site occupied by Si. Al, Si and Mg occupy the Y octahedral site (light-blue). The dodecahedral sites (yellow) are occupied by Mg and Fe.

Selected interatomic distances and angles of the two majoritic garnet samples are reported in Table 3.3-3 and are compared with the data from pyrope (Zhang et al., 1998) and from majorite (Angel et al., 1989).

Table 3.3-3. Comparison of the interatomic distances and angles between majoritic garnets of this study and pyrope and majorite end-member

| | <i>majoritic garnet (this study)</i> | <i>Fe- majoritic garnet (this study)</i> | <i>pyrope^(a)</i> | | <i>majorite^(b)</i> |
|--------------|--|--|-----------------------------|--------------------|-------------------------------|
| Sites | | Distance (Å) | | Sites | Distance (Å) |
| X-O x4 | 2.1985(10) | 2.1995(10) | 2.197(2) | X1-O x4 | 2.168 * |
| X-O x4 | 2.3458(10) | 2.3458(11) | 2.348(2) | X1-O x4 | 2.400 * |
| | | | | X2-O x4 | 2.346 * |
| | | | | X2-O x4 | 2.212 * |
| Y-O x6 | 1.8895(9) | 1.8882(10) | 1.889(2) | Y1-O x6 | 1.998 * |
| | | | | Y2-O x6 | 1.807 * |
| Z-O x4 | 1.6335(9) | 1.6334(11) | 1.627(2) | Z1-O x4 | 1.622(7) |
| | | | | Z2-O x4 | 1.652(7) |
| | | | | Z3-O x4 | 1.641 * |
| | | Angle (deg) | | Angle (deg) | |
| Z-O-Y | 130.78(6) | 130.85(6) | 131.0(2) | Z-O-Y1 | 125.57 * |
| | | | | Z-O-Y2 | 135.46 * |

^(a) Zhang et al. (1998); ^(b) Angel et al. (1989); *calculated mean values

In the case of the majorite end-member (MgSiO_3), ordering of Si and Mg into the octahedral site gives rise to a tetragonal distortion of the garnet structure (Angel et al., 1989). The values of the bond distances and angles determined at high-pressures and temperatures for the samples investigated in this study are reported in Table 3.3-4.

Table 3.3-4. Comparison of the interatomic distances and angles between majoritic garnets at high pressure and temperature.

| | <i>majoritic garnet</i> | | | |
|----------------|-------------------------|------------------------------------|----------------------|--------------|
| <i>P (GPa)</i> | <i>12.15</i> | <i>15.50</i> | <i>15.72 (558 K)</i> | <i>19.62</i> |
| Sites | | | Distance (Å) | |
| X-O x4 | 2.166(3) | 2.153(3) | 2.159(5) | 2.143(6) |
| X-O x4 | 2.258(5) | 2.249(5) | 2.234(6) | 2.210(8) |
| Y-O x6 | 1.858(3) | 1.848(3) | 1.855(3) | 1.854(2) |
| Z-O x4 | 1.616(4) | 1.608(4) | 1.614(5) | 1.605(7) |
| | | | Angle (deg) | |
| Z-O-Y | 129.0(3) | 129.1(2) | 128.3(3) | 127.5(5) |
| | | <i>Fe-bearing majoritic garnet</i> | | |
| <i>P (GPa)</i> | <i>12.07</i> | <i>17.96</i> | <i>21.1</i> | |
| Sites | | | Distance (Å) | |
| X-O x4 | 2.161(4) | 2.147(4) | 2.139(4) | |
| X-O x4 | 2.261(4) | 2.230(4) | 2.214(4) | |
| Y-O x6 | 1.864(5) | 1.852(5) | 1.845(4) | |
| Z-O x4 | 1.613(4) | 1.604(4) | 1.601(4) | |
| | | | Angle (deg) | |
| Z-O-Y | 128.9(2) | 128.3(2) | 128.0(2) | |

At room P and T conditions, the polyhedral bond distances are indistinguishable between the two majoritic samples of this study and are comparable to those of pyrope reported by Zhang et al. (1998). Only the Z-O distances determined for the majoritic garnets (1.6335(9) Å and 1.6334(11) Å, Table 3.3-3) are slightly larger than those reported for pyrope (1.627(2) Å) by Zhang et al. (1998). Note, however, that the values obtained in this study are even closer to the values for end member pyrope proposed by Merli et al. (1995). It appears therefore that both the small amount of Fe substitution as well as the coupled substitution of Mg + Si onto the octahedral site along the pyrope – majorite system has little influence on the average garnet structure determined by means of X-ray diffraction for the compositions examined.

The most significant feature of the structural refinements reported in this study is the large Mg atomic displacement parameter (ADP) at the dodecahedral site (Tables 3.2-4 and 3.2-5) suggesting either static or dynamic disorder of this cation. The dodecahedral cavity in fact is too large for the ionic radius of Mg which therefore appears to “rattle” in such an atomic site (Armbruster et al., 1992). On the basis of a recent single-crystal X-ray diffraction structure analyses at low and high temperatures, Nakatsuka et al. (2011) reported the presence of static disorder for Mg in pyrope. These authors concluded that the static disorder of Mg is responsible for the anomalously large ADP of Mg and anomalously high heat capacity at low temperature observed in pyrope. The same static disorder of Mg in the dodecahedral site has to be expected also in majoritic garnets, given the similarity in their ADPs with pyrope. It appears, however, that the small amount of Fe present in the Fe-Mj sample investigated in this study may already hinder the static disorder as suggested by its smaller ADP at the dodecahedral site (Table 3.3-3 and Figure 3.3-7). With increasing pressure, a remarkable decrease in the isotropic displacement parameters can be observed for both majoritic garnets due likely to the compression of the dodecahedral site resulting in a closer coordination of the Mg atoms (Figure 3.3-7). As expected the ADP of the dodecahedral atom in Mj increases with temperature at a given pressure due to the unit cell thermal expansion.

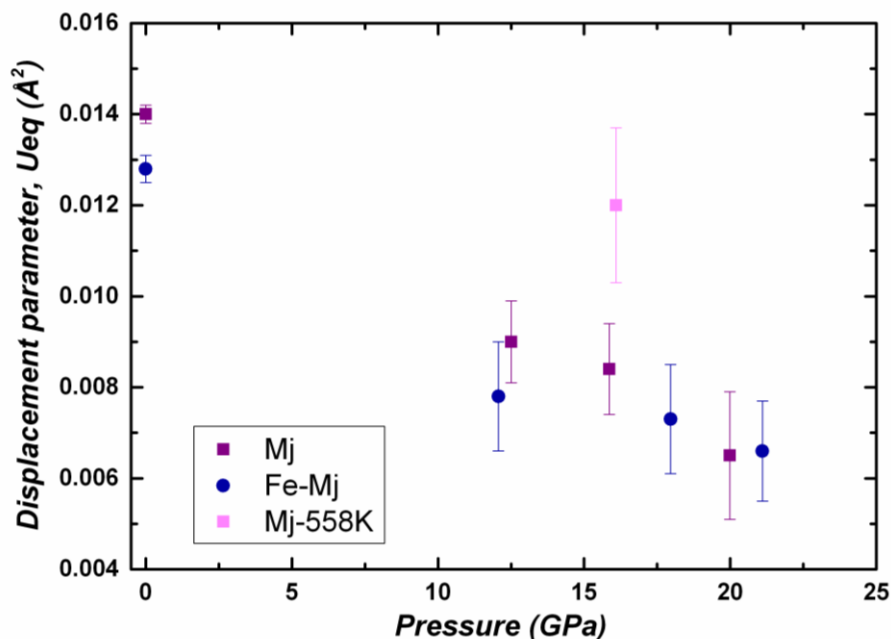


Figure 3.3-7. Isotropic displacement parameters of Mg and Fe in the dodecahedral site as a function of pressure. Note that for the room pressure values the U_{eq} is used instead since the refinements have been performed with anisotropic displacement parameters. Blue circles: displacement parameters of Fe and Mg in the Fe-Mj sample; purple circles: displacement parameters of Mg in the Mj sample. The effect of temperature on the displacement parameter of Mg in the dodecahedral site of Mj is shown in magenta.

As reported by Hazen et al. (1994), the extent to which the tetrahedral-octahedral framework varies with pressure controls largely the mechanism of compression of garnets. In particular, as shown by Zhang et al. (1998), the compressibility of garnets may be controlled by the kinking of the Z-O-Y angle. The tetrahedral-octahedral framework in the majoritic garnets investigated in this study is practically identical and the two samples have very similar Z-O-Y angles at room pressure. Also the K_{T0} values at room pressure are very similar, with Fe-Mj garnet only slightly less compressible than Mj (Table 3.3-2). At pressures of the transition zone, however Fe-Mj becomes more compressible than Mj due to its smaller $(\partial K / \partial P)_T$ value. This is clearly visible in Figure 3.3-2a where the adiabatic bulk moduli of the two samples are compared. One may expect therefore the Z-O-Y angle of Fe-Mj to decrease more rapidly than that of Mj in order to accommodate the larger compression of the garnet framework. This, however, is not the case since the variation with pressure of the kinking angle of Fe-Mj is smaller (0.135 deg/GPa) than that of Mj (0.164 deg/GPa). The slightly larger compression of Fe-Mj appears instead to be related to the compression of the tetrahedral site (Figure 3.3-8).

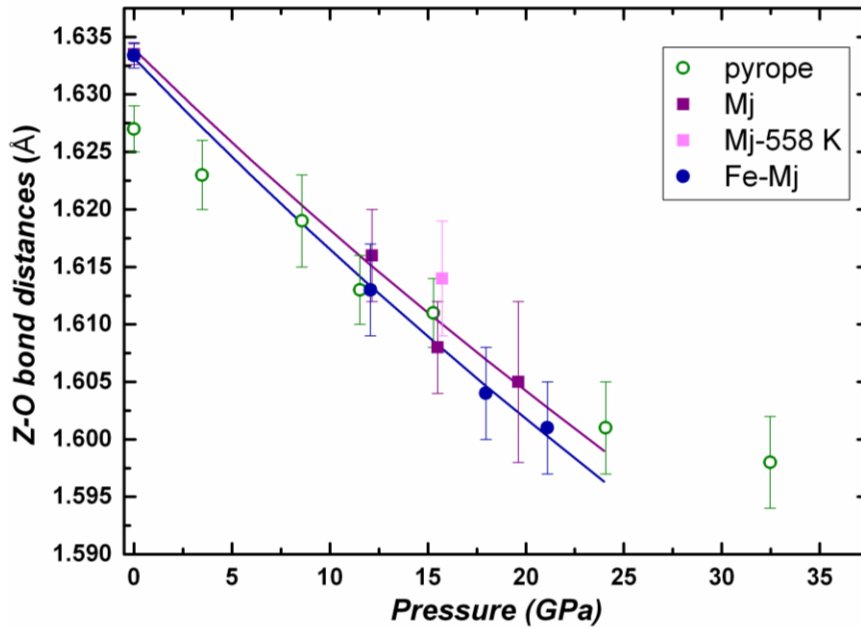


Figure 3.3-8. Variation of the tetrahedral bond length as a function of pressure for Mj (purple) and Fe-Mj (blue) garnets. For comparison are reported data on pyrope from Zhang *et al.* (1998).

As the tetrahedra in Fe-Mj are more compressible than those in Mj, the kinking of the Z-O-Y angle plays only a secondary role in the compression mechanism, as opposed to Mj where due to the more rigid tetrahedra, the compression is accommodated by the tilting of the tetrahedral-octahedra framework.

3.3.3 Comparison with literature data

The measured elastic moduli and their pressure derivatives for Mj and Fe-Mj investigated in this study are summarized in Table 3.3-5 along with literature data for pyrope, majorite (Mj₁₀₀) and garnets along the majorite-pyrope solid solution.

The adiabatic bulk and shear moduli determined in this study are generally in good agreement, within the experimental uncertainties, with those reported in the literature by means of Brillouin scattering (Sinogeikin and Bass, 2000) and ultrasonic interferometry on polycrystalline samples (Chen *et al.*, 1999).

Table 3.3-5. Elastic parameters of majorite, pyrope and pyrope-majorite solid solution

| Composition | K_0 (GPa) | dK/dP | dK/dT (GPaK ⁻¹) | G (GPa) | dG/dP | dG/dT (GPaK ⁻¹) | Reference | Specimen |
|---|-------------|---------|-------------------------------|-----------|---------|-------------------------------|-----------------------------|-----------------|
| <i>Brillouin</i> | | | | | | | | |
| Mg _{3.24} Al _{1.53} Si _{3.23} O ₁₂ | 168(2) | 4.7(2) | -0.014(15) | 91.8(7) | 1.40(5) | -0.0104(3) | This study | Single crystal |
| Mg _{3.01} Fe _{0.17} Al _{1.68} Si _{3.15} O ₁₂ | 172(1) | 4.2(1) | -0.014 | 93.0(6) | 1.30(5) | -0.008(4) | This study | Single crystal |
| Py ₁₀₀ | 171 | 3.22 | - | 92 | 1.4 | - | Conrad et al. (1999) | Single crystal |
| Py ₁₀₀ | 171(3) | 4.1(3) | - | 94(2) | 1.3(2) | - | Sinogeikin and Bass (2000) | Single crystal |
| Mj ₅₀ Py ₅₀ | 167(3) | 4.2(3) | - | 90(2) | 1.4(2) | - | Sinogeikin and Bass (2002a) | Polycrystalline |
| Mj ₅₀ Py ₅₀ | 167(3) | - | -0.0145(20) | - | - | -0.0082(10) | Sinogeikin and Bass (2002b) | Polycrystalline |
| Mj ₁₀₀ | 166(3) | 4.2(3) | - | 85(2) | 1.4(2) | - | Sinogeikin and Bass (2002a) | Polycrystalline |
| Mg _{3.16} Fe _{0.32} Al _{1.2} Si _{3.36} O ₁₂ | 166(2) | 4.2(2) | - | 88.8(5) | 1.28(8) | - | Murakami et al. (2008) | Single crystal |
| Py ₆₈ Alm ₂₄ Gr ₅ Sp ₁ | 168.2(1.8) | 4.4(1) | -0.0168(13) | 92.1(1.1) | 1.28(1) | -0.0051(11) | Lu et al. (2013) | Single crystal |
| <i>Ultrasonic</i> | | | | | | | | |
| Mj ₃₈ Py ₆₂ | 169(6) | 5.3(2) | - | 89(5) | 2.0(1) | - | Rigden et al. (1994) | Polycrystalline |
| Py ₁₀₀ | 171(2) | 5.3(4) | - | 92(1) | 2.0(1) | - | Chen et al. (1999) | Polycrystalline |
| Mj ₃₈ Py ₆₂ | 171(5) | 6.2(5) | - | 90(1) | 1.9(2) | - | Liu et al. (2000) | Polycrystalline |
| Mj ₅₀ Py ₅₀ | 170(5) | 6.4(5) | - | 89(1) | 2.1(2) | - | Liu et al. (2000) | Polycrystalline |
| Mj ₁₀₀ | 167(3) | 6.7(4) | - | 88(2) | 1.9(1) | - | Gwanmesia et al. (1998) | Polycrystalline |
| Py ₁₀₀ | 175(2) | 3.9(3) | -0.0180(20) | 91(1) | 1.7(2) | -0.0100(10) | Gwanmesia et al. (2006) | Polycrystalline |
| pyrope minus olivine | 164.4(5) | 4.24(6) | -0.0129(8) | 94.9(2) | 1.11(3) | -0.0103(4) | Irifune et al. (2008) | Polycrystalline |
| <i>Isothermal</i> | | | | | | | | |
| Mg _{3.24} Al _{1.53} Si _{3.23} O ₁₂ | 165(3) | 4.8(2) | - | - | - | - | This study | Single crystal |
| Mg _{3.01} Fe _{0.17} Al _{1.68} Si _{3.15} O ₁₂ | 172(1) | 4.0(1) | - | - | - | - | This study | Single crystal |
| Py ₁₀₀ | 171(2) | 4.4(2) | - | - | - | - | Zhang et al. (1998) | Single crystal |

Also the pressure derivatives the bulk and shear moduli at constant temperature $(\partial K / \partial P)_T$ and $(\partial G / \partial P)_T$ agree with those obtained from Brillouin scattering measurements on other majoritic garnets which exhibit values ranging from 4.1–4.2 for $(\partial K / \partial P)_T$, and from 1.3–1.4 for $(\partial G / \partial P)_T$. The only noticeable difference is the $(\partial K / \partial P)_T$ value of Mj obtained in this study, which is larger than all values reported in the literature.

The bulk and shear moduli and elastic constants of Mj and Fe-Mj are reported as a function of density in Figure 3.3-9 and they also are compared with literature data on other majoritic garnets obtained by means of polycrystalline Brillouin scattering and ultrasonic measurements. Single-crystal Brillouin scattering results on Fe-bearing majoritic garnet from Murakami et al. (2008) are also reported.

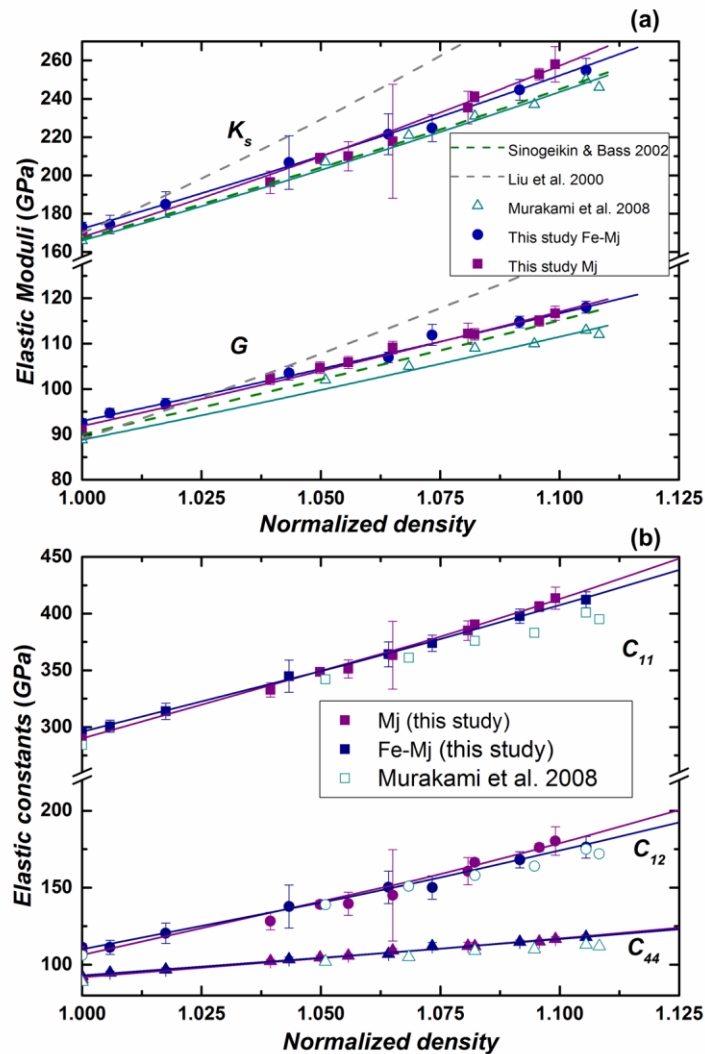


Figure 3.3-9. Variation as a function of normalized density (ρ/ρ_0) of (a) bulk (K_s) and shear (G) moduli and (b) elastic constants (C_{11} , C_{12} , C_{44}) of majoritic garnet determined in this study compared with literature data. The solid lines correspond to the Birch-Murnaghan equation of state fits.

Murakami et al. (2008) suggested that the incorporation of ~5 wt.% iron in majoritic garnet does not affect significantly the elastic moduli. However, as shown in Figure 3.3-9, the data reported by these authors are clearly more compressible at all pressures than those obtained for Mj and Fe-Mj in this study.

From the data obtained in this study it is clear that Fe substitution affects the elastic properties of majoritic garnets as it affects the compression mechanism as discussed in the previous session. The major difference between Fe-Mj and the sample studied by Murakami et al. (2008) may therefore be the larger amount of Fe present in the latter (Table 3.3-5). However, it cannot be excluded that such a large difference may also be due to the fact that the crystal studied by Murakami et al. (2008) was loaded in a mixture of methanol:ethanol:water which is known to solidify at pressures above 10-11 GPa (Angel et al., 2007) and therefore provide quite inhomogeneous stresses in the DAC above this pressure. The data for $Mj_{50}Py_{50}$ measured on polycrystalline samples studied by Sinogeikin and Bass (2002a) are slightly more compressible at high pressure due to the lower pressure derivative reported by these authors. Note that their sample also was loaded methanol:ethanol:water which may of course affect its high-pressure behaviour. The much larger values obtained by Liu et al. (2000) by means of ultrasonic measurements on the other hand are due to the very large pressure derivatives of the elastic moduli. The temperature derivatives of the bulk and shear moduli obtained for Mj and Fe-Mj are in good agreement with those obtained for a pyrolite-minus olivine composition reported by Irifune et al. (2008) and are comparable with those reported by Sinogeikin and Bass (2002b) on a majoritic garnet with a composition $Mj_{50}Py_{50}$, using Brillouin scattering at room pressure. The differences in pressure derivatives of elastic moduli observed among different studies can lead to considerably different conclusions concerning the properties of minerals under deep mantle conditions. In particular, differences in the pressure derivatives of elastic moduli can affect not only absolute velocities, but also the density at high pressure which is essential for understanding buoyancy forces in the mantle. The data gathered in this study are used to derive a thermo-elastic model for the transition zone which is then compare with seismic data in chapter 6.

4. Hexagonal $\text{Na}_{0.41}[\text{Na}_{0.125}\text{Mg}_{0.79}\text{Al}_{0.085}]_2[\text{Al}_{0.79}\text{Si}_{0.21}]_6\text{O}_{12}$ (NAL phase): Crystal structure refinement and elasticity

4.1 Introduction

As a consequence of plate tectonics, basaltic oceanic crust is subducted into the mantle. The subduction of oceanic lithosphere plays an important role in the dynamics of mantle convection and is believed to be responsible for the creation of lateral chemical heterogeneity in the mantle (Helfrich and Wood, 2001). In this context, the high pressure and temperature metamorphic phases which recrystallize from basic rocks that form the oceanic crust are likely to be important components of the lower mantle and as such to influence its physical and chemical properties. Several high pressure studies employing MORB bulk compositions have shown that various Al rich phases can form under lower mantle conditions (Irifune and Ringwood, 1993; Kesson et al., 1994; Irifune et al., 1996; Akaogi et al., 1999; Miyajima et al., 1999, 2001). In particular, Irifune and Ringwood (1993) first reported the breakdown of majorite garnet to an assemblage of Mg-Perovskite, Ca-Perovskite and a separate aluminous phase at pressure and temperature conditions of the lower mantle. This so called new Al phase or NAL has a hexagonal crystal structure and can contain several different cations, such as Na, K, Ca, Mg and Fe (Akaogi et al., 1999; Miura et al., 2000; Gasparik et al., 2000; Miyajima et al., 1999, 2001). NAL is therefore likely to be the main host for alkali elements in oceanic crust that has been subducted to ~ 600-1300 km (Miyajima et al., 2001). Due to the extremely long time scale required for the chemical equilibration of subducted crustal heterogeneities in the lower mantle (Holzapfel et al., 2005), it has also been proposed that the bulk of the mantle might be a mechanical mixture between a depleted mantle residue and subducted crustal components (Xu et al., 2008). In this case NAL is likely to form a major part of the crustal component.

Recently, Walter et al. (2011) described sub-lithospheric diamonds hosting composite multiphase inclusions with compositions encompassing phase assemblages expected to crystallize from basic crustal material under lower-mantle conditions. In particular, Walter et al. (2011) suggested that some of these inclusions were present as the NAL phase at lower mantle conditions, giving further support for the existence of this phase in the Earth's lower mantle. The elastic properties of NAL, hence, may influence the bulk elastic properties of the lower mantle.

NAL phases crystallising in MORB compositions display complex solid solutions and have the general formula $XY_2Z_6O_{12}$ where X represents a large monovalent or divalent cation (Ca^{2+} , K^+ , Na^+), Y a middle-sized cation (Mg^{2+} , Fe^{2+} or Fe^{3+}), and Z a small cation (Al^{3+} and Si^{4+}).

To date several studies have been conducted on the structure, stability and compression of NAL phases both in complex and simplified systems (Gasparik et al., 2000; Miura et al., 2000; Kojitani et al., 2011; Imada et al., 2011, 2012; Kawai and Tsuchiya, 2012). However, only in one study (Gasparik et al., 2000), has a single-crystal structural analysis been reported on NAL with the formula $[K_{0.56}Na_{0.32}][Ca_{0.04}Mg_{1.66}Fe^{2+}_{0.3}][Mg_{0.98}Fe^{3+}_{0.3}Al_{2.62}Si_{2.1}]O_{12}$. All other studies (Miura et al., 2000; Kojitani et al., 2011) dealt with powdered samples. The crystal structure of NAL consists of a double chain of $M1O_6$ octahedra connected by shared edges, occupied by the Z cations. The M2 site is a six fold coordinated triangular prism occupied by the Y cations and surrounded by three double chains of $M1O_6$ octahedra. The larger channels (M3 site) are formed by six double chains of $M1O_6$ octahedra and are occupied by the large X cations.

In spite of all these studies, there are still no data on the single crystal elasticity of the NAL phase determined experimentally. Apart from theoretical calculations (Kawai and Tsuchiya, 2012; Mookherjee et al., 2012) only in one study have elasticity measurements been performed on a polycrystalline sample (Dai et al., 2013). These experiments only provide aggregate properties and, therefore, do not give any information on the anisotropy of the sound velocities nor can they constrain the complete elastic tensor of this low symmetry material.

The main aim of the work reported in this chapter is to experimentally determine the full elastic tensor of NAL by Brillouin scattering. To this end, single-crystals of $Na_{0.41}[Na_{0.125}Mg_{0.79}Al_{0.085}]_2[Al_{0.79}Si_{0.21}]_6O_{12}$ NAL have been synthesized at lower mantle conditions with a composition close to that expected to crystallise in a subducting slab. The experimental observations were complimented with first-principles calculations, performed using density-functional theory and density-functional perturbation theory.

4.2 Experimental methods

4.2.1 Sample synthesis and characterization

For the synthesis of NAL phase, a simple composition containing only Na, Mg, Al and Si was chosen in order to better constrain the effect of cation substitution on its elastic properties. Two starting compositions referred to as anhydrous and hydrous were prepared by mixing SiO₂, MgO (for the anhydrous composition) or Mg(OH)₂ (for the hydrous composition), Al₂O₃, and Na₂CO₃ in different proportions (Table 4.2-1). As for the synthesis of garnet crystals (chapter 3), water bearing mixtures were prepared in order to enhance the growth of large single crystals suitable for X-ray diffraction and Brillouin measurements. The reagents were first dried, then weighted in the required proportions and mixed. The mixture was placed in a platinum (Pt) crucible and heated up to 1000 °C in 10 hours and kept at this temperature for 6-7 hours in order to decarboxylate Na₂CO₃.

Table 4.2-1. Chemical composition in wt. % of oxides of the starting materials for NAL syntheses

| | Starting material (anhydrous) | Starting material (hydrous) |
|--------------------------------|----------------------------------|--------------------------------|
| Na ₂ O | 10.9 | 10.25 |
| MgO | 14.2 | 13.33 |
| SiO ₂ | 21.1 | 19.87 |
| Al ₂ O ₃ | 53.8 | 50.59 |
| H ₂ O* | - | 5.95 |
| Total | 100 | 100 |

The numbers in parenthesis correspond to the standard deviation; * water added in form of brucite

High pressure experiments were carried out using a 1200 t Kawai type multianvil apparatus at the Bayerisches Geoinstitut (BGI). For pressures up to 24 GPa a 10/4 assembly was used (section 2.1.2). A cylindrical LaCrO₃ furnace was employed, which was surrounded by an insulating ZrO₂ sleeve. The samples were loaded into platinum capsules made of 1.2 mm outer diameter platinum tubing that had initial lengths of 2.8 mm. The temperature was measured using W3%Re / W25%Re (type D) thermocouple wires (0.13 mm thick) that were inserted axially into the octahedral assembly, with the hot junction in contact with the capsule.

For pressures of 26 GPa a 7/3 type assembly was used. In this type of assembly, the LaCrO_3 tube was placed directly into the octahedron and no insulating ZrO_2 sleeves were used. Type D thermocouple wires (0.07 mm thick) were inserted longitudinally, through the wall of the heater, with the hot junction at the midpoint of the furnace. Two platinum capsules (made of 1mm outer diameter platinum tubing) and containing each a different starting material were used. In total, six synthesis experiments were performed. The experimental conditions, analytical methods and run products of the experiments performed in this study, are summarized in Table 4.2-2.

Table 4.2-2. Experimental conditions for NAL syntheses

| Run n° | starting composition | assembly | P (GPa) | T (°C) | t(min) | Run products |
|--------------------|-----------------------|----------|---------|--------|--------|---------------------------------|
| S5180_1 S5180_2 | hydrous, anhydrous | 7/3 | 26 | 1600 | 40 | NAL + δAlOOH ? |
| S5202 | hydrous | 7/3 | 26 | ~1700 | 15 | NAL + δAlOOH ? |
| S5214 | hydrous | 7/3 | 26 | 1300 | 60 | NAL + δAlOOH ? |
| S5224* | hydrous | 10/4 | 24 | - | - | - |
| S5229* | hydrous | 10/4 | 24 | ~1800 | 5 | NAL |
| S5253 | anhydrous | 10/4 | 20 | ~2260 | 5 | NAL+melt |

*heater was not stable

The first experiments were not successful in terms of growing large single crystals of NAL. At 26 GPa (S5180, S5202 and S5214) a two-phase assemblage consisting of small crystals of NAL (Figure 4.2-1) and a hydrous aluminum rich phase (possibly δAlOOH) was found.

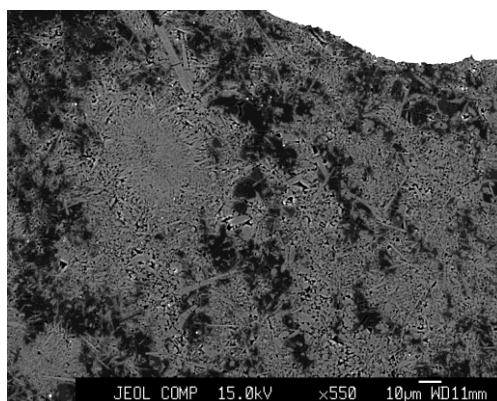


Figure 4.2-1. Electron backscattered image of sample S5214 showing its phase assemblage. The dark phase corresponds to the hydrous aluminum rich phase and the bright one corresponds to NAL.

At 24 GPa (S5224 and S5229) the heater failed during heating and the experiments were quenched immediately. For the synthesis of high quality single-crystals of NAL it was necessary to perform experiments slightly above the dry melting solidus at temperatures in excess of 2200 °C and pressures of 20 GPa. This high melting temperature demonstrates a remarkable change in the melting behaviour of Na-rich phases compared to lower pressures.

Contrary to majoritic garnet, only anhydrous compositions gave large single crystals.

The successful experiment (S5253) was performed at 20 GPa employing a 10/4 assembly. The powdered anhydrous sample was loaded into a capsule fabricated from a 1 mm diameter rhenium rod spark eroded with holes of approximately 0.5 mm deep and 0.5 mm in diameter. The capsule was closed by placing two rhenium foils on top of the chamber. The sample was first pressurized up to the desired pressure followed by slow heating to 1500 °C. The temperature was kept at 1500 °C for 15 minutes and finally rapidly heated to 2260 °C for 5 minutes. The experiment was then quenched and the sample was recovered after slow decompression over 18 hours.

Recovered samples were mounted in epoxy resin and polished. Single-crystals of the NAL phase (up to 120 µm in length) were found coexisting with quenched melt in the mounted sample (Figure 4.2-2).

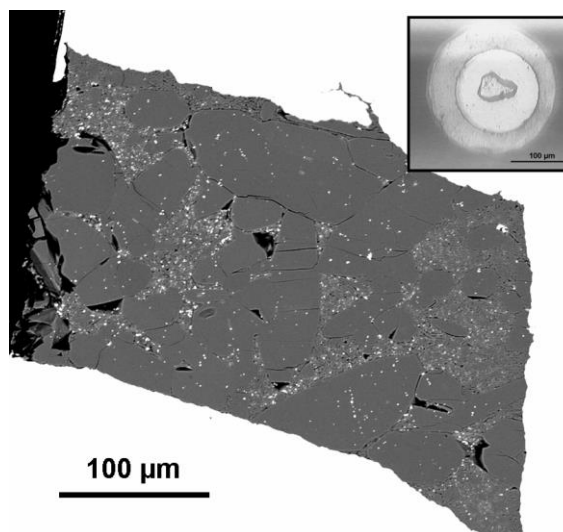


Figure 4.2-2. Electron backscattered image showing crystals of NAL coexisting with melt. Single crystal of NAL (s5253x5) inside the diamond anvil cell at room pressure (inset).

The chemical analysis obtained following the procedure described in Section 2.2.1 indicated the following composition of the NAL phase (run number S5253) in weight %: 7.8 (2)%

Na₂O, 14.9 (3)% MgO, 17.7 (4)% SiO₂, 58.8 (4)% Al₂O₃, which recalculates to the chemical formula Na_{1.07}Mg_{1.58}Al_{4.91}Si_{1.26}O₁₂. Raman spectroscopy was performed on the same NAL single-crystal (s5253x5) used for the elasticity study employing a Dilor XY system operating with a 514 nm Ar⁺ ion laser equipped with a liquid nitrogen-cooled CCD detector.

4.2.2 Single-crystal data collection and structure refinements

A NAL single-crystal (s5253x5) of a suitable size (70x50x15μm) and optically free of defects was selected from the capsule and mounted on a glass fibre for single crystal diffraction. Data collection was performed on an Xcalibur diffractometer (operated at 50 kV and 40 mA and equipped with a CCD detector) using MoK α radiation (graphite monochromator). Several ω scans were chosen to obtain coverage of the full reciprocal sphere up to $2\theta_{\max} = 70^\circ$, with an exposure time of 80 s/frame and a crystal detector distance of 45 mm. Lorentz and polarization factors together with an analytical absorption correction based on the crystal shape were employed for the correction of the reflection intensities using the CrysAlis package (Oxford Diffraction 2006).

The measured reflections were consistent with the hexagonal space group $P6_3/m$ and resulted in a total of 328 unique reflections with a discrepancy factor $R_{\text{int}} = 0.031$. Structure refinements were performed based on F^2 using the SHELX97 program package (Sheldrick, 2008) in the WingX System (Farrugia, 1999) starting from the atomic structural parameters reported by Gasparik et al. (2000). Atomic scattering factors for Si, Al, Mg, Na and O were used and all atoms were refined anisotropically. The resulting discrepancy factor after convergence of the refinement cycles, however, resulted in a quite large value, i.e. $R1 = 0.135$ for the 308 observable reflections [$F_o > 4\sigma(F_o)$]. A test for possible merohedral

twinning of the crystal gave a positive result, with the following twin law: $R = \begin{pmatrix} 0 & 1 & 0 \\ 1 & 0 & 0 \\ 0 & 0 & -1 \end{pmatrix}$.

Where R is the matrix that transforms the hkl indices of one component into the other. By introducing such a transformation into the refinement process the discrepancy factor decreases to $R1 = 0.028$ and the resulting proportions of the two twin components were refined as 75 % and 25 %, respectively. In the final refinement cycles the chemistry of the crystal obtained from the microprobe analysis was taken into account, therefore the site occupancies of the different sites were fixed as follows: 0.79 Al + 0.21 Si for M1; 0.085 Al +

0.79 Mg + 0.125 Na for M2 and the remaining Na was inserted into M3, which has therefore an occupancy of only 0.41. The anisotropic displacement parameter indicates that the thermal ellipsoid of Na at the M3 site is elongated along the c axis. A refinement that included a split-site model with isotropic displacement parameters was also tested, but this resulted in no improvement of the discrepancy factor and gave a negative displacement parameter for one of the split sites. Therefore, the split-site model was abandoned. Details of the data collection and structural refinements are reported in Table 4.2-3.

Table 4.2-3. Structural refinement details and unit cell parameters of the NAL phase

| | |
|-----------------------------|--------------------------|
| Measured reflections | 1623 |
| Unique reflections | 328 |
| Fo > 4sig(Fo) | 308 |
| Rint | 3.05% |
| Rw for Fo > 4sig(Fo) | 2.85% |
| Rall | 3.19% |
| wR2 | 7.12% |
| GooF | 1.109 |
| No. parameters | 24 |
| Space group | $P6_3/m$ |
| Z | 1 |
| Crystal size | 70x70x15 μm^3 |
| F(000) | 235 |
| Absorption coefficient | 1.49 mm^{-1} |
| Unit-cell parameters | |
| $a(\text{\AA})$ | 8.7225(4) |
| $c(\text{\AA})$ | 2.7664(2) |
| $V(\text{\AA}^3)$ | 182.3(2) |

4.2.3 Simultaneous X-ray diffraction and Brillouin scattering

Both the single-crystal used for the X-ray data collection and structure refinements (s5253x5) and another high quality single-crystal (70x70 μm) made in the same experiment (s5352x3) were selected for Brillouin scattering measurements and were polished into parallel plates with a thickness of approximately 15 μm . The crystals were then loaded into two piston cylinder diamond anvil cells (Kantor et al., 2012) for X-ray and Brillouin measurements (see inset of Figure 4.2-2). No pressure medium was employed in the cells as the measurements were performed at room pressure.

Simultaneous acquisition of density and sound velocities of the NAL crystals was performed at the Bayerisches Geoinstitut. The lattice parameters were determined using the eight-

position centring of 10-16 Bragg reflections ($20 < 2\theta < 29$ degrees) according to the procedure of King and Finger (1979) (see Section 2.3.3.2). The resulting unit cell volumes are 182.00 (5) Å³ and 181.92 (7) Å³ for s5253x3 and s5253x5, respectively, in agreement with the value obtained for sample s5253x5, 182.3 (2) which has a lower accuracy due to the use of an area detector. Typical half-widths of the reflections were between 0.080 and 0.090° in ω profiles. Brillouin scattering measurements were performed with a six-pass Sandercock-type tandem Fabry-Pérot interferometer (see Section 2.3.4.1). The measured sample plates have normal vectors of (0.04397, -0.07541, 0.0997) and (0.05505, 0.11433, -0.03807) and starting phonon directions of (0.33506, 0.12554, -0.05278) and (0.32600, -0.15670, 0.00125). All spectra were collected in 80° forward symmetric/platelet scattering geometry. Brillouin spectra of the NAL crystals were collected with a laser power of 150 mW. Typical collection times for each crystal orientation were 4 hours. In total, 14 crystallographic directions were sampled, 4 for crystal s5253x3 and 10 for crystal s5253x5. Sound velocities were determined from the frequency shifts using the relationship (2.17) described in Section 2.3.4. Dispersion curves of sound velocities versus crystallographic orientation were collected by changing the crystal orientation through movement of the χ -circle of the Eulerian cradle. The phonon direction (obtained from the UB orientation matrix determined from the diffraction experiments) was related to the orientation at any χ via a general Cartesian rotation matrix. The experimental sound velocities, obtained from the previous equation, are a function of the crystallographic orientation q , the single crystal elastic moduli C_{ij} and the density, and are related through the Christoffel equation (3.1) reported in chapter 3. This equation is cubic in V^2 , i.e., its solutions result in three acoustic velocities $V_{P,S1,S2} = f(\rho, C_{ij}, q)$ with quasi-compressional wave (for arbitrary crystallographic orientation) velocity V_P and slow and fast quasi-shear wave velocities V_{S1} and V_{S2} . It is therefore possible to determine both crystal orientation and elastic constants by fitting solutions of the equation of motion to measured sound velocities. In our case, however, crystallographic orientation and density were obtained very precisely through single crystal X-ray diffraction measurements and were therefore fixed. The form of the solutions $V_{P,S1,S2} = f(\rho, C_{ij}, q)$ depend strictly on crystal symmetry and were derived for elastically anisotropic solids as a function of point group symmetry by Every (1980). NAL crystallizes in the hexagonal space group $P6_3/m$ with point group $6/m$ and the corresponding solution of Every (1980) was employed.

The elastic constants C_{ij} were extracted by simultaneously fitting 6 dispersion curves (3 solutions for each crystal) to the experimentally measured acoustic velocities $V_{P,S1,S2} = f(C_{ij})$,

using the quasi-Newton minimization of the sum of all residuals squared. The C_{ij} values obtained from ab initio calculations in this study were used as starting values for the minimization process.

4.2.4 First-principles calculations⁴

First-principles calculations based on density-functional theory (Kohn and Sham, 1965; Payne et al., 1992; Martin, 2003) were performed in parallel with the experiments. The ABINIT implementation, with planewaves and pseudopotentials (Gonze et al., 2002, 2009) was used. To this end, the crystal structure for the $\text{Na}_{1.3}\text{Mg}_{1.6}\text{Al}_{4.9}\text{Si}_{1.2}\text{O}_{12}$ composition was first obtained. While in the experimental structure the Na atoms occupy the $2d$ position of the $P6_3/m$ space group, with 0.41 occupancy, in the ab initio structure, in order to avoid dealing with supercells and disordered structures the Na atoms were ordered on one of the two sites inside the channels, breaking the inversion centre and thus lowering the symmetry to $P-6$. Moreover, ideal solid solutions of Na – Al and Al – Si on the $2d$ and $6h$ crystallographic sites, respectively, were considered and were treated using alchemical pseudopotentials (Cohen, 2007; Caracas and Banigan, 2009). A $4 \times 4 \times 8$ grid of regular k points (Monkhorst and Pack, 1976) 40 Ha (1Ha = 27.2116 eV) kinetic energy cut-off and the standard local-density approximation for the exchange-correlation energy was used. The elastic constant tensors, the vibrational modes and Raman spectrum, with both peak positions and intensity, were then computed in the framework of the density-functional perturbation theory (Baroni et al., 2001; Gonze et al., 2005; Hamann et al., 2005; Veithen et al., 2005; Caracas and Gonze, 2010).

4.3 Results and Discussion

4.3.1 Structural model from single-crystal X-ray diffraction

Details of the atomic positions and displacement parameters are reported in Table 4.3-1.

⁴ Theoretical calculations were performed by Dr. Razvan Caracas who also contributed to write this paragraph that is part of the manuscript (Pamato et al., 2014)

Table 4.3-1. Experimental atomic coordinates and displacement parameters of the NAL phase

| Site | Wyckoff position | x | y | z | U ₁₁ | U ₂₂ | U ₃₃ | U ₁₂ | U _{eq} |
|------|------------------|------------|------------|-----|-----------------|-----------------|-----------------|-----------------|-----------------|
| M1 | 6h | 0.98946(8) | 0.34353(9) | 1/4 | 0.0058(3) | 0.0057(3) | 0.0053(3) | 0.0029(2) | 0.0056(2) |
| M2 | 2d | 2/3 | 1/3 | 1/4 | 0.0093(4) | 0.0093(4) | 0.0094(6) | 0.0047(2) | 0.0093(3) |
| M3 | 2a | 0 | 0 | 1/4 | 0.007(1) | 0.007(1) | 0.25(2) | 0.0035(5) | 0.089(7) |
| O1 | 6h | 0.1283(2) | 0.5989(2) | 1/4 | 0.0069(6) | 0.0070(6) | 0.0125(7) | 0.0029(5) | 0.0090(3) |
| O2 | 6h | 0.3124(2) | 0.2024(2) | 1/4 | 0.0090(7) | 0.0088(6) | 0.0100(7) | 0.0053(5) | 0.0089(3) |

Selected interatomic distances and angles of the NAL phase are reported in Table 4.3-2 and are compared to powder diffraction data from Kojitani et al. (2011).

Table 4.3-2. Comparison of the interatomic distances and angles between two NAL phases.

| Sites | NAL this study | NAL Kojitani et al. (2011) |
|-----------------------|----------------|----------------------------|
| Distance (Å) | | |
| M1-O2 x2 | 1.838(1) | 1.817(3) |
| M1-O2' | 1.881(2) | 1.890(4) |
| M1-O1' | 1.932(2) | 1.903(5) |
| M1-O1 x2 | 1.933(1) | 1.940(3) |
| M2-O1 x6 | 2.098(1) | 2.128(3) |
| M3-O2' x3 | 2.394(2) | 2.393(3) |
| M3-O2 x6 | 2.765(1) | 2.764(3) |
| O2-O2' | 2.765(3) | 2.764(3) |
| O1-O1' | 2.457(2) | 2.373(6) |
| Bond angle (°) | | |
| O2-M1-O2 | 97.61(8) | 99.2(2) |
| O2'-M1-O2 x2 | 96.02(8) | 96.45* |
| O2 x2-M1-O1' | 95.46(6) | 95.74* |
| O2'-M1-O1' | 162.53(8) | 161.2(2) |
| O2-M1-O1 x2 | 173.99(7) | 171.55* |
| O2-M1-O1 x2 | 85.27(5) | 84.48* |
| O2'-M1-O1 x2 | 88.89(6) | 90.7(2) |
| O1'-M1-O1 x2 | 78.98(7) | 76.3(2) |
| O1-M1-O1 | 91.38(7) | 90.9(2) |
| O1-M2-O1 x3 | 82.48(6) | 81.07* |
| O1-M2-O1'' x6 | 135.83(2) | 135.33* |
| O1'-M2-O1'' x6 | 81.27(4) | 82.32* |

*Calculated value using the data from Kojitani et al. (2011)

The size of the (Al,Si)O₆ site of NAL in this study is comparable to that of the Na-Hex phase reported by Kojitani et al. (2011), as well as the average M1-O distances and M3-O distances. The M2-O distance of 2.098 (1) Å determined in this study is smaller than that of 2.128 (3) in Na-Hex phase, but it is similar to that of K-Hex and Ca-Hex phases reported in the same

study and in Miura et al. (2000), respectively. This suggests that the size of the trigonal prism sites does not depend on the presence of Na as previously reported by Kojitani et al. (2011), since in the sample investigated in this study the amount of Na in M2 is larger than that reported for their sample.

The most striking feature of the structural refinement reported in this study is the very large Na displacement parameter at the M3 site, which is elongated along the c axis, suggesting dynamic disorder of the Na atoms in the channels along this direction (Figure 4.3-1).

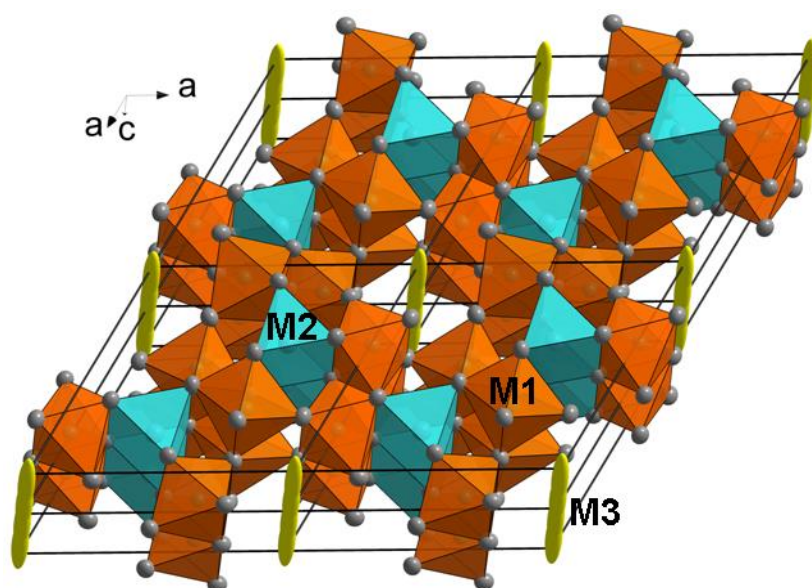


Figure 4.3-1. Crystal structure of the NAL phase projected along the c axis. The orange octahedra correspond to the M1 sites, occupied by Al and Si. Mg, Al and Na occupy the M2 sites, represented by triangular prisms in turquoise. The ellipsoids in green elongated along the c axis represent Na occupying partially the M3 site.

Gasparik et al. (2000) also observed a pronounced distribution of electron density in the M3 site along the channels. Thus, they reported a model with the M3 site refined at a general position $(0, 0, z)$ instead of the ideal site at $(0, 0, \frac{1}{4})$. However, since they used an isotropic displacement parameter, they did not observe the large elongation along the c axis as in our case.

It is difficult to speculate on the type of dynamic disorder that the Na atoms may have at the conditions of the lower mantle. The effects of increasing P and T are likely to act in opposite directions. With increasing pressure we might expect freezing of the Na atom motion in one of the two $2d$ positions of the channels and a consequent phase transition to a lower symmetry, whereas higher temperatures will favour greater motion and possibly free

movement of Na within the NAL M3 channels. Room temperature high-pressure studies (Vanpeteghem et al., 2003; Guignot and Andrault, 2004; Shinmei et al., 2005; Sanehira et al., 2006; Imada et al., 2012) have not revealed any phase transformation, suggesting that such dynamic disorder may be present also at pressures of the lower mantle. Note, however, that these previous studies have all used powder diffraction information and, therefore, may not have the accuracy required to observe subtle changes driven by ordering of Na in the channels.

4.3-2 Atomic vibrations

The observed and theoretical Raman spectra of NAL are reported in Figure 4.3-2.

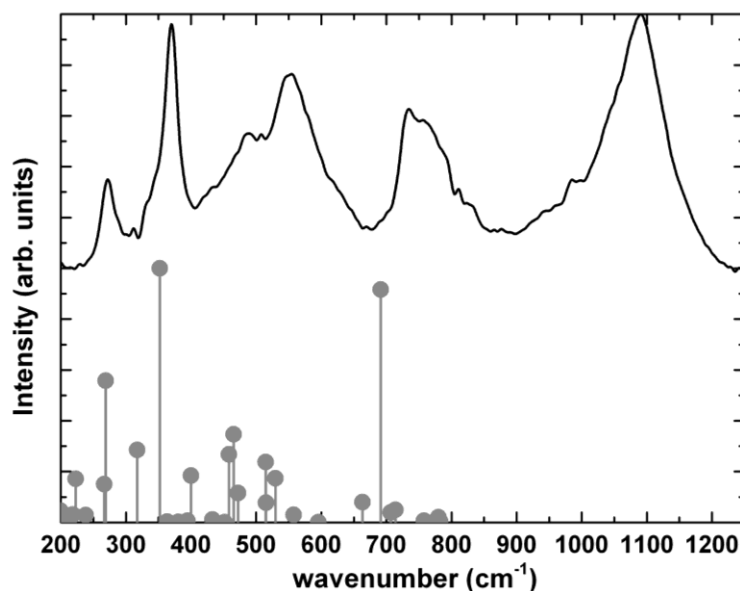


Figure 4.3-2. A comparison between the experimental (solid line) and calculated (vertical grey lines) Raman spectra of the NAL phase.

The observed spectrum of the experimentally synthesised NAL consists of broad bands centred at approximately 273, 370, 507, 553, 735, 757 and 1091 cm^{-1} . These broad features are likely due to the Al/Si and Mg/Al/Na disorder in the M1 and M2 sites, respectively. These broad bands clearly consist of several Raman active modes having very close frequencies as shown by the theoretical calculations. The only major discrepancy between the observed spectrum and the theoretical calculations is the broad experimental peak around 1000-1200 cm^{-1} that very likely is an overtone of the 553 cm^{-1} band and/or a combination mode of several bands from lower frequency. The differences in peak position between observed and

calculated spectrum can be due to both the slightly different chemistry and disorder of the cations among the sites and the different temperature (experiments are at room temperature, whereas calculations are static, i.e. at 0 K). In particular, as stated above, the ordering of Na on one position in the theoretical structure lowers the symmetry and breaks the inversion centre. This results into a different number of Raman-active modes between the experiment and calculations, as some of the E_u modes of $P6_3/m$ become Raman-active in $P-6$. But the peak width and the structural disorder make it hard to distinguish individual peaks in the observed spectrum. With these considerations in mind, all major Raman peaks in NAL can be interpreted in terms of the atomic displacement pattern derived from calculations, given the similarity between the calculated and observed spectra. The modes corresponding to the vibration of the Na cations inside the channels lay at the lowermost frequencies, below the experimentally observable range. The Na displacement parallel to the channel axis is an unstable theoretical mode at static conditions ($T = 0$ K), where the Na atoms are frozen. At high temperatures this instability can be correlated to the observed dynamic disorder of Na along the channels. The in-plane Na displacements within the hexagonal basal plane are found at 148 cm^{-1} in the calculations. The sublattice of octahedra forming the channel walls also participate in this vibration. The other vibrations up to 307 cm^{-1} are various lattice modes, dominated by rigid displacements of the (Si,Al) O_6 octahedra or (Mg,Al) O_6 polyhedra. The broad features at higher frequency represent different types of asymmetric stretching and bending modes of (Si,Al)-O and (Mg,Al)-O bonds.

The complete description of all theoretical Raman modes, containing the relative intensity, the symmetry labels, the description of the atomic vibrations and the proposed correspondence to the experimental modes are given in Table 4.3-3. The full description of the theoretical vibrational modes in the zone-centre for the NAL phase at experimental density is reported on the WURM website (<http://wurm.info>; Caracas and Bobocioiu, 2011). Both the experimental Raman spectrum and the full description of the theoretical Raman modes could be used to identify possible NAL phases present in inclusions in diamonds or in meteoritic veins.

Table 4.3-3. Experimental and calculated Raman modes of the NAL phase at room pressure.

| v obs (cm ⁻¹) | v calc (cm ⁻¹) | I calc [*] (symmetry label) | Description |
|------------------------------|-------------------------------|--|---|
| | 148.35 | 0.31 (E'') | Na atoms vibrating in plane |
| | 199.54 | 0.05 (E'') | Lattice mode; stretching of the octahedral framework of channels |
| | 218.62 | 0.03 (A') | Lattice mode; Tilt of the channel walls |
| | 223.13 | 0.17 (E') | Lattice mode; Mainly Si movements (octahedral sites) along the z axis |
| | 238.22 | 0.03 (E'') | Lattice mode; Tilts of the channels; rigid motion of the polyhedral sub-lattice |
| | 266.54 | 0.15 (A') | Lattice mode; Tilts of the channels; rigid motion of the polyhedral sub-lattice |
| 272.5 | 268.83 | 0.56 (E'') | Stretching of the Si-O-Al angle |
| | 317.35 | 0.29 (A') | Tilts of the octahedra from the channels' walls |
| 370.6 | 351.99 | 1.00 (A') | Has a strong breathing component of the SiO ₆ octahedra |
| | 400.04 | 0.18 (E'') | Breathing of the Si-Al-Si cavities |
| | 433.14 | 0.01 (A') | Tilt of the Al polyhedra; |
| | 458.34 | 0.27 (E') | Tilt of the Al polyhedra |
| 487.63 | 465.58 | 0.35 (E') | O-Si-O rigid tilt of the octahedra |
| 507.97 | 472.55 | 0.12 (E'') | Asymmetric stretching of the Al-O polyhedra |
| 553.16 | 514.59 | 0.24 (A') | Asymmetric stretching of the Si-O bonds of the octahedral |
| | 515.15 | 0.08 (E') | Rolling mode of the apical Si-O bonds in the octahedra |
| | 529.74 | 0.17 (E') | Rolling mode of the apical Si-O bonds in the octahedra |
| | 557.51 | 0.03 (E'') | Si-O stretching mode in the octahedra |
| | 663.07 | 0.08 (E'') | O-Si-O stretching mode |
| 735.73 | 691.32 | 0.92 (A') | Breathing mode of the Al-O polyhedra |
| 757.65 | 706.43 | 0.04 (A') | Breathing mode of the Si-O octahedra |
| | 713.84 | 0.05 (A') | Asymmetric stretching of the Si-O bonds of the octahedral |
| | 757.43 | 0.01 (E'') | Asymmetric stretching of the Al-O polyhedra |
| | 780 | 0.02 (E'') | Breathing mode of the Si-O octahedra |
| 1091.38 | - | - | Overtone of the 553 cm ⁻¹ band or combination mode |

* Relative intensities

4.3-3 Elasticity

A typical Brillouin spectrum of the NAL phase is shown in Figure 4.3-3.

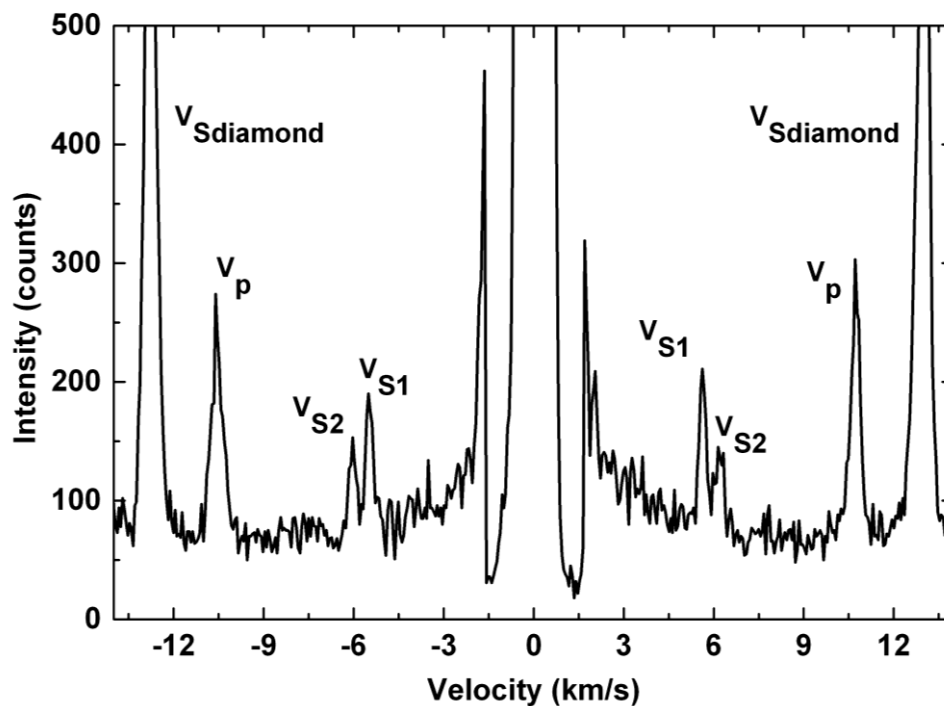


Figure 4.3-3. Representative Brillouin spectrum of the NAL phase at a selected orientation at room pressure in the diamond anvil cell.

The collected Brillouin spectra were of excellent quality with a high signal-to-noise ratio and with V_p and the two V_s displaying sharp peaks. The measured acoustic velocities in different crystallographic orientations as a function of χ angle for both crystals at room pressure are shown in Figure 4.3-4.

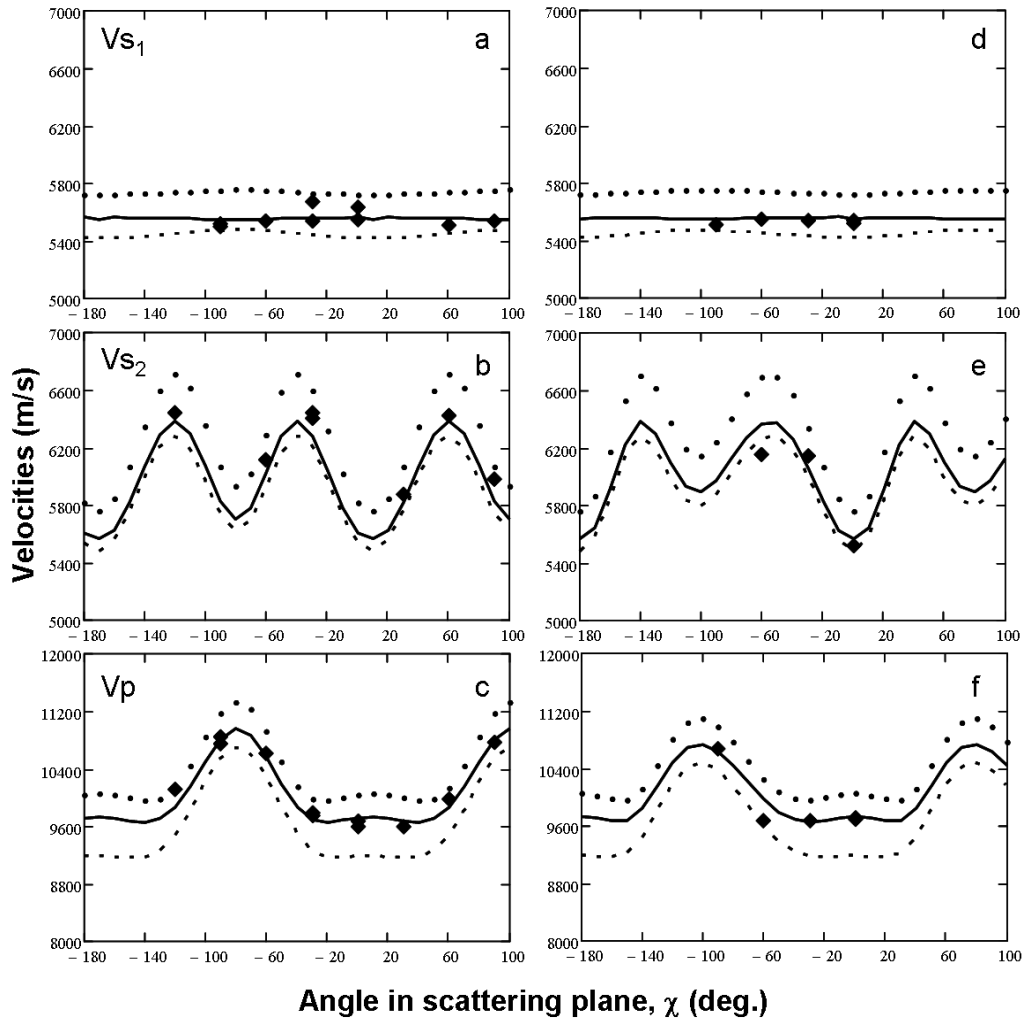


Figure 4.3-4. Measured acoustic velocities for NAL sample S5253x5 (a,b,c) and S5253x3 (d,e,f) as functions of χ angle. Solid lines are the fit of Christoffel's equation to both sets of data simultaneously. Calculated velocities from density functional theory are shown as a dashed line (this study) and dotted line (Kawai and Tsuchiya, 2012).

The structural refinement model revealed the presence of merohedral twinning. By multiplying the twin law transformation matrix to the orientation matrix of the crystal it was possible to obtain the crystallographic orientation of the twin component. The calculated acoustic velocities as a function of crystallographic angle for the twin component according to the twin matrix are exactly the same as those collected, indicating that this type of twinning does not modify the measured elastic properties of the sample (Figure 4.3-5).

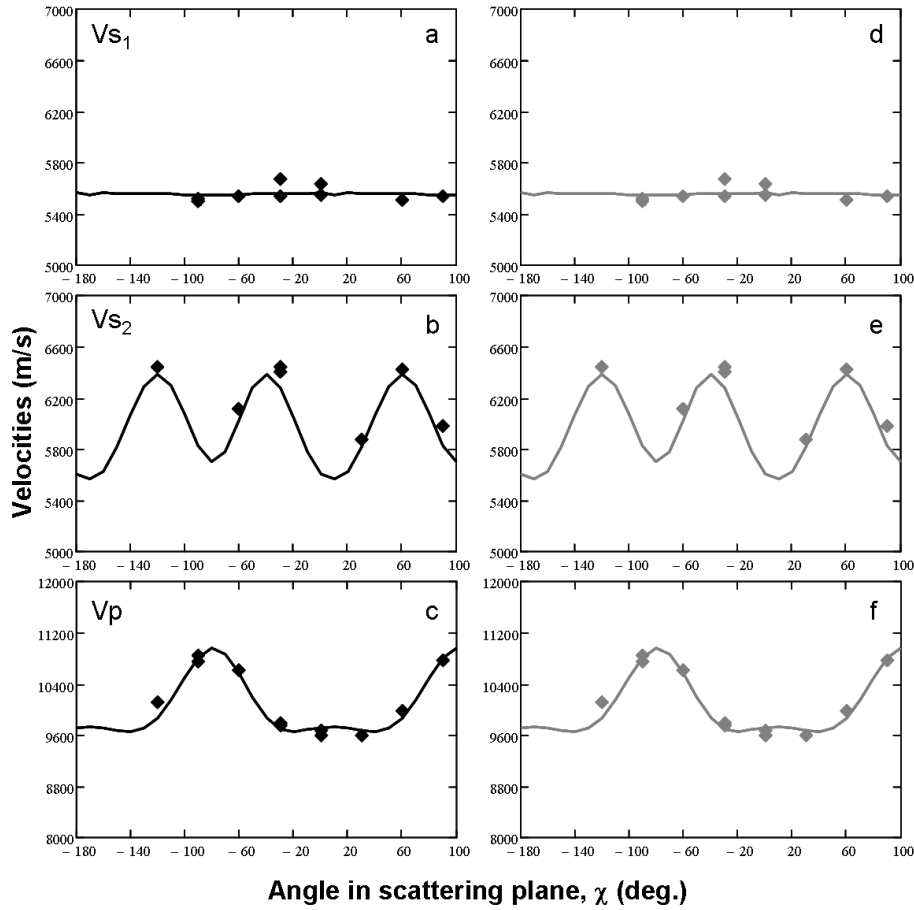


Figure 4.3-5. Measured acoustic velocities for S5253x5 (a,b,c) and velocities calculated according to the twin matrix for the twin component (d,e,f) as functions of χ angle. Solid lines are the fit of Christoffel's equation as in Figure 4.3-4.

The five elastic constants C_{ij} , extracted by fitting the dispersion curves (3 solutions for each crystal) to the experimentally measured acoustic velocities are reported in Table 4.3-4.

Table 4.3-4. Elastic constants and aggregate properties of the NAL phase at room pressure.

| | Na _{1.07} Mg _{1.58} Al _{4.91} Si _{1.26} O ₁₂ experimental (this study) [*] | Na _{1.3} Mg _{1.6} Al _{4.9} Si _{1.2} O ₁₂ theoretical (this study) | NaMg ₂ Al ₅ SiO ₁₂ theoretical ^a | Na _{0.4} Mg _{0.6} Al _{1.6} Si _{0.4} O ₄ experimental ^b |
|----------|---|---|---|---|
| C_{11} | 365 | 326 | 390 | - |
| C_{12} | 126 | 99 | 137 | - |
| C_{13} | 100 | 77 | 98 | - |
| C_{33} | 477 | 457 | 510 | - |
| C_{44} | 119 | 116 | 128 | - |
| K_s | 206 | 178 | 217 | - |
| G | 129 | 125 | 138 | 121.96 (9) |
| V_p | 9.9 | 9.99 | 10.1 | 9.643 (9) |
| V_s | 5.8 | 6.01 | 5.90 | 5.601 (5) |
| ρ | 3.86 | 3.45 | 3.97 | 3.89 ^c |

^a Kawai and Tsuchiya (2012), ^b Dai et al. (2013), ^c density from data reported by Imada et al. (2012).^{*}

In this study uncertainties in elastic moduli and in sound velocities are less than 2 % and 1 %, respectively.

An analysis of the correlations between the elastic constants, which takes into account the covariance matrix, was performed. The correlation between the constants is small, with a maximum value of 0.814 between C_{11} and C_{12} constants. Aggregate velocities as well as elastic moduli were calculated from the C_{ij} 's using the Voigt-Reuss-Hill averaging scheme (Hill 1952) and are also listed in Table 4.3-4. Uncertainties in the elastic constants were calculated from the covariance matrix but these were supplemented by considering other sources of error inherent to diamond anvil cell measurements (see Sinogeikin and Bass, 2000). In this study typical errors are less than 2% in elastic moduli and less than 1% in sound velocities. We obtained $K_S = 206$ (2) GPa and $G = 129$ (1) GPa for the aggregate elastic moduli and $V_P = 9.9$ and $V_S = 5.8$ km/s for the isotropic compressional and shear sound velocities. These values, as well as the experimental C_{ij} appear to lie in between the values obtained from theoretical calculations in this study and those previously reported by Kawai and Tsuchiya (2012) (Table 4.3-4 and Figure 4.3-4).

The discrepancy between experimental and theoretical values is very likely due to the fact that in the synthetic samples the cations are randomly distributed among the crystallographic sites, whereas theoretical calculations have to deal either with ordered structures (as in the case of this study where Na has been allocated only in one of the $2d$ positions breaking the symmetry) or with super-cells which preserve the symmetry but have prescribed local ordered configurations (Kawai and Tsuchiya, 2012).

Note the shear velocity and shear modulus obtained in this study are higher than those reported by Dai et al. (2013) for a $\text{Na}_{0.4}\text{Mg}_{0.6}\text{Al}_{1.6}\text{Si}_{0.4}\text{O}_4$ NAL phase determined by means of Brillouin scattering on a powdered sample (Table 4.3-4) likely due to the highly anisotropic behaviour of the NAL phase. Single-crystal data are in general more reliable than the measurements on polycrystalline samples, which can be affected by uncertainties in texture, grain size, stress state, and most importantly overlook the intrinsic anisotropy of most mantle minerals, such as the NAL phase.

Using the single-crystal elastic constants and density obtained in this study it is possible to define the room pressure seismic anisotropy (see equation 1.5) by analysing a hemisphere of all possible propagation directions (Figure 4.3-6).

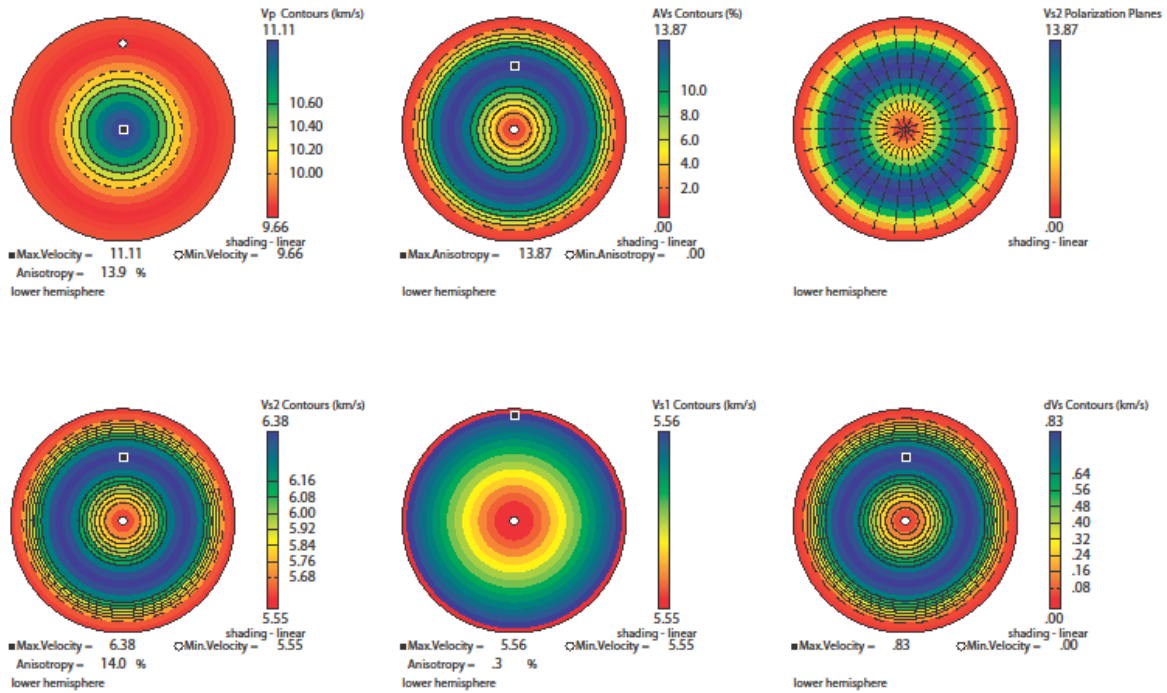


Figure 4.3-6. Single crystal compressional wave velocity (V_p), shear wave anisotropy (AV_s), fastest wave polarization (V_{S2}), V_{S2} , V_{S1} anisotropy and dV_s , plotted as Lambert azimuthal equal-area lower hemisphere pole figures (Mainprice, 1990), with the elastic tensor orthogonal axes $X1 = a$ axis (east) and $X3 = c$ axis (centre).

The NAL phase displays 13.9 % shear wave anisotropy (AV_s), which is mainly due to the high anisotropic feature of V_{S2} (14 % anisotropy) given that V_{S1} is essentially isotropic (0.3 % anisotropy) (Figure 4.3-6). In particular, the V_{S1} velocity ranges from 5.55 to 5.56 km/s, while the V_{S2} ranges from 5.55 to a maximum of 6.38 km/s. Dai et al. (2013) reported an aggregate shear wave velocity of 5.601 (5) km/s, which is very similar to that of V_{S1} obtained in this study. This suggests that in their measurements on a polycrystalline sample only V_{S1} was observed as a sharp peak, whereas V_{S2} was probably hidden in the background due to its broader appearance as a result of its large anisotropy. This is a reasonable explanation given that in the same study V_p , which has a similar anisotropy as V_{S2} , also was not observed.

High pressure-high temperature experiments (Ono et al., 2009; Imada et al., 2011) have revealed that a NAL phase with $\text{Na}_{0.4}\text{Mg}_{0.6}\text{Al}_{1.6}\text{Si}_{0.4}\text{O}_4$ composition transforms to the calcium ferrite type aluminum phase (CF) at approximately 40 GPa and 1850 K. According to Dai et al. (2013) such a phase transition would result in 2.5 % shear wave velocity increase. However, the present result on the room pressure elasticity of the NAL phase brings into question the previous conclusion of Dai et al. (2013). Experiments on NAL single crystals at

high pressure are therefore necessary to constrain the full elastic tensor and hence the anisotropy of this phase.

5. High-pressure single-crystal elasticity of the hexagonal $\text{Na}_{0.41}[\text{Na}_{0.125}\text{Mg}_{0.79}\text{Al}_{0.085}]_2[\text{Al}_{0.79}\text{Si}_{0.21}]_6\text{O}_{12}$ (NAL phase) and seismic anisotropy in the deep mantle

5.1 Introduction

Subduction introduces chemically differentiated and hydrothermally altered mid-oceanic ridge basaltic (MORB) rocks into the Earth. At lower mantle conditions experiments indicate that a MORB bulk composition can contain more than 20% of an aluminium rich phase, the nature of which changes with pressure. One of these Al-rich phases with general formula $(\text{Na,Ca})(\text{Mg,Fe})_2(\text{Al,Si})_6\text{O}_{12}$ has been proposed to have a hexagonal structure (Akaogi et al., 1999; Miura et al., 2000; Gasparik et al., 2000) and is referred to as NAL (short for new aluminium phase). Other authors have reported the occurrence of an Al-rich phase with formula $(\text{Na,Mg})(\text{Al,Si})_2\text{O}_4$ and a calcium-ferrite type structure (CF) (Irifune and Ringwood, 1993; Kesson et al., 1994; Hirose et al., 1999, 2005; Ono et al., 2001, 2005). Both NAL and CF are found to coexist in the upper part of the lower mantle.

At pressures corresponding to ~1000 km (~40 GPa), NAL is expected to transform to the calcium ferrite type aluminum phase (CF) (Kawai and Tsuchiya, 2012). According to Dai et al. (2013) such a phase transition would result in an increase of 2.5 % in shear wave velocity. However, as shown in Chapter 4, there is a large discrepancy between the zero pressure shear modulus derived from single-crystal Brillouin measurements (see Chapter 4) and the one derived from the polycrystalline sample measured also by means of Brillouin spectroscopy by Dai et al. (2013). Single-crystal data are in general more reliable than measurements on polycrystalline samples, which can be affected by uncertainties in texture, grain size, stress state, and most importantly overlook the intrinsic anisotropy of most mantle minerals, such as the NAL phase. The present results on the room pressure elasticity of the NAL phase, therefore, bring into question the previous conclusion of Dai et al. (2013). Kawai and Tsuchiya (2012) argued that NAL and CF phase would have comparable shear wave velocities producing less than 1% velocity difference across the phase transition. They also reported a significant change in the seismic wave anisotropy associated with the phase transition, which might lead to a seismically detectable discontinuity as a result of favorable crystallographic preferred orientation. In particular, they found that CF is significantly more anisotropic than the NAL phase.

Experimentally, it has been found that the NAL phase displays 13.9 % compressional wave anisotropy (AV_P) and shear wave anisotropy (AV_S) (Chapter 4), in good agreement with the values and degree of anisotropy calculated by Kawai and Tsuchiya (2012). It remains to be determined whether single-crystal experimental data agree with the first principle calculation results also at high pressures.

The aim of this study is therefore to determine the full elastic tensor of the NAL phase as a function of density and absolute pressure under hydrostatic conditions by combining single-crystal Brillouin scattering with X-ray diffraction. This will provide information on the variation with pressure of the anisotropy of the sound velocities of the NAL phase. Moreover, the P - V EoS of NAL phase will be determined based on the absolute pressure determination performed by combining X-ray diffraction and Brillouin spectroscopy. To date several studies have been conducted on the compression of NAL phases both in complex and simplified systems. However, large discrepancies among the equations of state parameters present in the literature are observed, most likely due to uncertainties in the pressure determination.

5.2 Experimental methods

Two separate sets of high-pressure X-ray diffraction and Brillouin scattering measurements were performed. The single-crystals of the NAL phase studied in Chapter 4 were loaded into two piston cylinder diamond anvil cells (Figure 5.2-1).

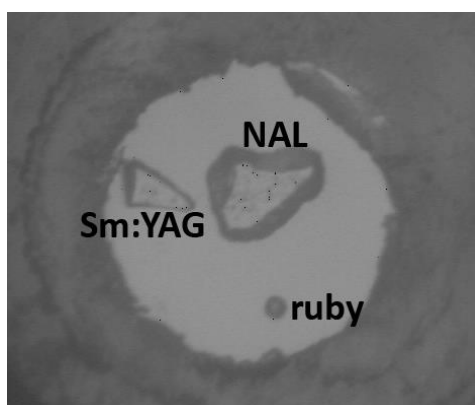


Figure 5.2-1. Detail of the pressure chamber at 8.03 GPa showing a crystal of NAL ($s5253x5$, $70 \times 50 \times 15 \mu\text{m}^3$ in size) together with Sm:YAG and ruby loaded in He pressure medium.

Boehler-Almax diamonds were employed with 500-400 μm culets in combination with tungsten carbide seats. Rhenium gaskets of 200 μm in thickness were pre-indented to 66-55 μm and cylindrical holes of 300-250 μm were drilled using a spark erosion machine. A single-crystals of Sm:YAG was used as pressure calibrant in both experiments, in the second set of experiments also ruby chips were used together with YAG (see Figure 5.2-1). The first crystal (s5253x3) 50 \times 50 \times 15 μm in size was measured up to 19.93 GPa. The maximum pressure was constrained by the point at which broadening of the diffraction lines was observed. The second single-crystal of NAL (s5253x5) was measured up to 24.6 GPa before broadening of the diffraction lines occurred.

The pressure inside the cell was monitored before and after each Brillouin and X-ray measurement using a Dilor XY system operating with a 514 nm Ar⁺ ion laser equipped with a liquid nitrogen-cooled CCD detector. A neon gas was used as hydrostatic pressure medium in the first set of experiments, whereas helium was loaded into the sample chamber in the second experiments.

Unit-cell lattice parameters were determined using the eight-position centring of 10-16 Bragg reflections ($20 < 2\theta < 29$ degrees) according to the procedure of King and Finger (1979). The first crystal was measured up to 6.22 GPa using a four-circle Huber diffractometer (MoK α radiation) equipped with a conventional tube, at operating conditions of 50 kV and 40 mA. At higher pressures as well as at all pressures of the experiment with the second crystal, the unit-cell parameters were determined using a four-circle Huber diffractometer (with MoK α radiation) equipped with an ultrahigh-intensity rotating anode (see Section 2.3.3.2).

Brillouin spectra were collected in 80° forward symmetric/platelet scattering geometry with a laser power of 150-200 mW. Collection times for each crystal orientation at high pressures ranged between 4 and 12 hours. The elastic constants C_{ij} were extracted by fitting the dispersion curves to the experimentally measured acoustic velocities following the procedure described in Chapter 4.

5.3 Results and discussion

5.3.1 Elasticity

A typical Brillouin spectrum of one of the NAL crystals collected at high pressure is shown in Figure 5.3-1.

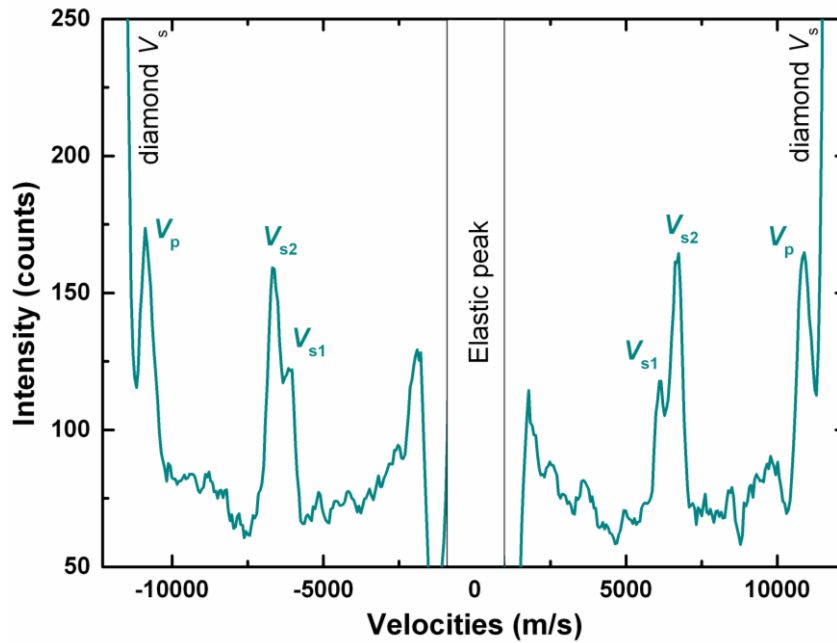


Figure 5.3-1. Representative Brillouin spectrum of the NAL phase (s5352x3) measured at a selected angle at 19.93 GPa in the diamond anvil cell.

The measured acoustic velocities in different crystallographic orientations as a function of χ angle for both crystals at high pressure are shown in Figure 5.3-2 and are compared to calculated velocities obtained from density functional theory using the elastic constants reported by Kawai and Tsuchiya (2012).

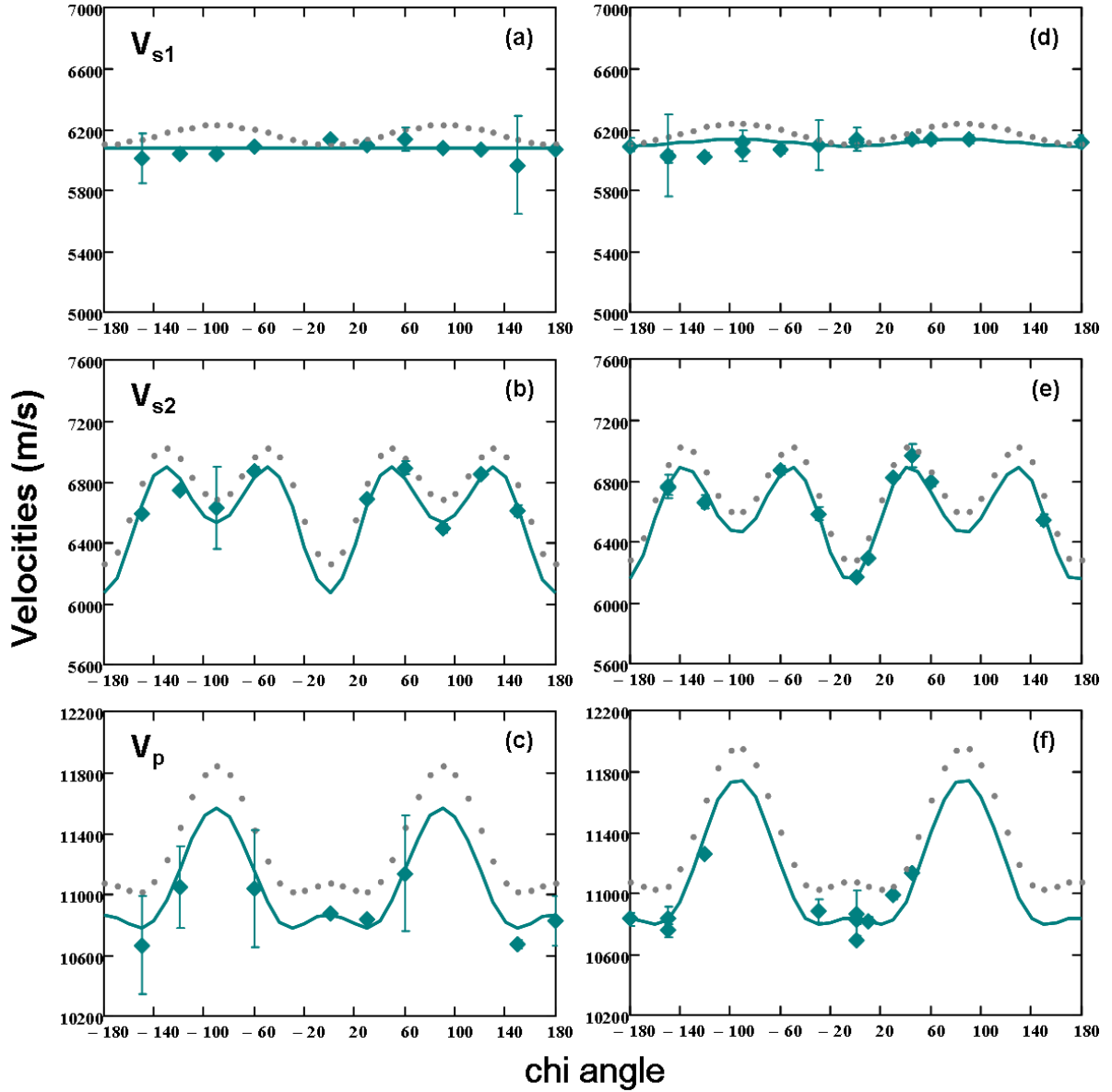


Figure 5.3-2. Measured acoustic velocities for NAL sample S5253x3 (a,b,c) and S5253x5 (d,e,f) as a functions of χ angle at 19.93 and 19.66 GPa respectively. Solid lines are the fit of Christoffel's equation to the sets of data. Calculated velocities from density functional theory are shown as dotted line (Kawai and Tsuchiya, 2012).

The elastic constants C_{ij} , extracted by fitting the dispersion curves (3 solutions for each crystal) to the experimentally measured acoustic velocities (see Section 4.2.3 for details) are shown in Figure 5.3-3 as a function of absolute pressure which has been determined as described in the following session.

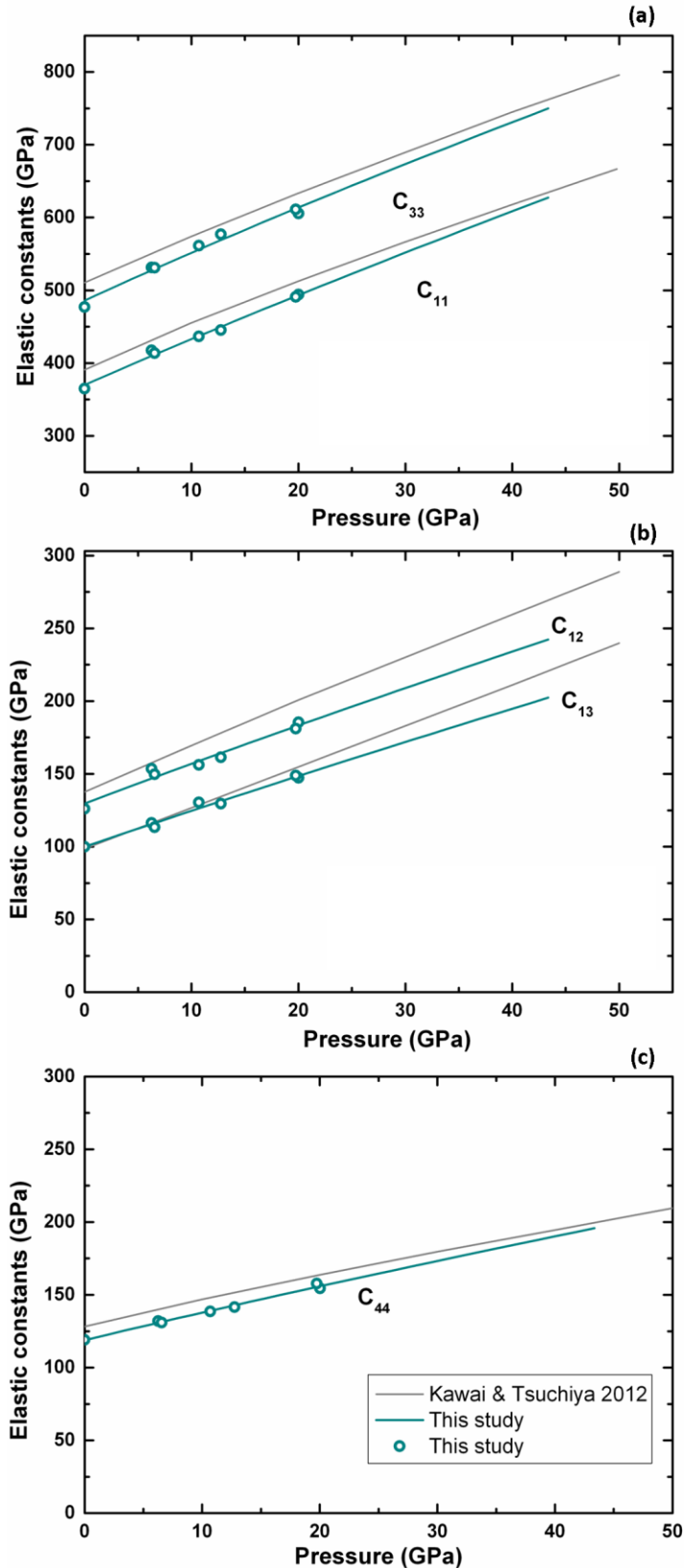


Figure 5.3-3. Pressure-dependencies of the elastic constants for the NAL phase determined in this study are shown as open circles. The solid lines are Birch-Murnaghan equation of state fits through the experimental data. The grey solid curves represent the variation of the elastic constants calculated by Kawai and Tsuchiya (2012).

All five elastic constants increase monotonically with increasing pressure indicating that there is no elastic instability up to the highest pressures investigated. Moreover, C_{ij} values are smaller than those determined from theoretical calculations (Kawai and Tsuchiya, 2012) (Figure 5.3-3) and they clearly display a lower pressure dependency, for C_{12} and C_{13} in particular. These differences will have an effect on the evolution of the elastic moduli and hence sound velocities (Section 5.3.3). Smaller values in elastic constants (e.g C_{11} and C_{33}) will result in a more compressible material than predicted by DFT calculations. Furthermore, the different behaviour of C_{12} , C_{13} and C_{44} will affect the pressure dependency of both bulk and shear moduli.

The single-crystal elastic constants as a function of density and absolute pressure are summarized along with aggregate properties in Table 5.3-1.

Table 5.3-1. Single-crystal and aggregate elastic properties, aggregate sound velocities as a function of absolute pressure and density of the NAL phase.

| P_{abs} (GPa) | ρ (g/cm ³) | C_{11} (GPa) | C_{12} (GPa) | C_{13} (GPa) | C_{33} (GPa) | C_{44} (GPa) | K_s (GPa) | G (GPa) | V_s (km/s) | V_p (km/s) |
|---------------------------|--------------------------------|-------------------|-------------------|-------------------|-------------------|-------------------|----------------|--------------|-----------------|-----------------|
| 0 ^{a,b} | 3.855 | 365 | 126 | 100 | 477 | 119 | 206 | 129 | 5.8 | 9.9 |
| 6.22 ^a | 3.967 | 418 | 154 | 116 | 531 | 132 | 237 | 143 | 5.99 | 10.37 |
| 12.69 ^a | 4.074 | 446 | 161 | 130 | 577 | 142 | 256 | 153 | 6.131 | 10.62 |
| 19.93 ^a | 4.185 | 494 | 185 | 147 | 605 | 154 | 283 | 165 | 6.286 | 10.97 |
| 6.49 ^b | 3.972 | 414 | 150 | 113 | 531 | 131 | 234 | 142 | 5.988 | 10.32 |
| 10.64 ^b | 4.041 | 437 | 156 | 130 | 561 | 139 | 251 | 150 | 6.089 | 10.56 |
| 19.66 ^b | 4.181 | 491 | 181 | 149 | 611 | 158 | 283 | 167 | 6.319 | 10.99 |

^a s5253x3; ^b s5253x5

Uncertainties in the elastic constants were calculated from the variance-covariance matrix and by considering other sources of errors inherent to diamond anvil cell measurements (see Sinogeikin and Bass, 2000). In this study typical errors are less than 2 % in elastic moduli and less than 1 % in sound velocities.

5.3.2 EoS formalism and absolute pressure determination

A third-order Eulerian finite strain EoS, based on a thermodynamically consistent formulation and described in detail in Chapter 6 was used for the analysis of the volume data and variation of the elastic moduli upon compression at room temperature according to the following equations:

$$K_s = (1 + 2f)^{\frac{5}{2}} \left[K_{T_0} + (3K_{T_0}K'_{T_0} - 5K_{T_0})f + \frac{27}{2}(K_{T_0}K'_{T_0} - 4K_{T_0})f^2 \right] + \gamma^2 \rho C_V T \quad (5.1)$$

$$G = (1 + 2f)^{\frac{5}{2}} \left[G_0 + (3K_{T_0}G'_0 - 5G_0)f + (6K_{T_0}G'_0 - 24K_{T_0} - 14G_0 + \frac{9}{2}K_{T_0}K'_{T_0})f^2 \right] \quad (5.2)$$

where K_{T_0} and K'_{T_0} are the isothermal bulk modulus and its derivative at ambient conditions, and the conversion to adiabatic bulk modulus has been taken into account according to equation (2.4), γ is the Grüneisen parameter, T is the temperature, C_V the heat capacity and $f = \frac{1}{2} \left[(V_0/V)^{2/3} - 1 \right]$.

The Grüneisen parameter is obtained as derived in detail in Chapter 6 using the following equation:

$$\gamma = \frac{1}{6} \frac{1}{\left[1 + 6\gamma_0 f + \frac{1}{2}(-12\gamma_0 + 36\gamma_0^2 - 18\gamma_0 q_0)f^2 \right]} (2f + 1) \left[6\gamma_0 + (-12\gamma_0 + 36\gamma_0^2 - 18\gamma_0 q_0)f \right] \quad (5.3)$$

where q_0 is the logarithmic volume derivative of the effective Debye temperature and $\gamma_0 = 2.12$ is the room pressure Grüneisen parameter calculated according to:

$$\gamma_0 = \alpha_0 K_{s0} / \rho_0 C_{p0} \quad (5.4)$$

where $C_{p0} = 848.74 \text{ J*kg}^{-1}\text{*K}^{-1}$ is the experimental isobaric heat capacity of NAL at room temperature determined by Ono et al. (2009). The value of $\alpha_0 = 33.7 \cdot 10^{-6} \text{ K}^{-1}$ for the NAL phase was also taken from Ono et al. (2009).

The isochoric heat capacity was evaluated within the framework of the Debye theory:

$$C_V = 9nN_A k_B \left(\frac{\theta}{T} \right)^{-3} \int_0^{\theta/T} \frac{x^4 e^x}{(e^x - 1)^2} dx \quad (5.5)$$

$$\theta = \theta_0 \left[1 + 6\gamma_0 f + \frac{1}{2}(-12\gamma_0 + 36\gamma_0^2 - 18\gamma_0 q_0)f^2 \right]^{\frac{1}{2}} \quad (5.6)$$

where N_A is the Avogadro number and θ_0 is the room pressure value for the Debye temperature ($\theta_0 = 931 \text{ K}$) calculated from the experimental sound velocities according to the equations from Robie and Edwards (1966):

$$\theta_0 = \frac{h}{k} \left(3 \frac{n}{4\pi V_0} \right)^{\frac{1}{3}} \left[3^{\frac{1}{3}} \left(\frac{1}{V_{P0}^3} + \frac{2}{V_{S0}^3} \right)^{\frac{1}{3}} \right] \quad (5.7)$$

where h is the Plank constant, k is the Boltzmann constant, $n = 21$ (the number of atoms in the unit cell), and V_{P0} and V_{S0} are the experimental longitudinal and transverse velocities at ambient conditions reported in Chapter 4, respectively.

The experimental K_S and G values were performed with fixed values of K_{T0} , γ_0 and θ_0 calculated through equations (2.4), (5.4) and (5.7), respectively. The parameters K_{T0}' , G_0 , G_0' were refined, and q_0 was kept fixed to a value of 1. As reported by Trots et al. (2013), different q_0 values give rise to only negligible changes in the values of the K_{T0}' , G_0 , G_0' parameters. The resulting EoS parameters are compared to those obtained by using equations (3.6) and (3.7) which were fitted directly to the adiabatic moduli values in Table 5.3-2. No difference among the values obtained using the two different approaches are visible.

Table 5.3-2. EoS paramaters of the NAL phase.

| K_{T0} (GPa) | K_{T0}' | K_{s0} (GPa) | K_{s0}' | G_0 (GPa) | G_0' | γ_0 | q_0^b |
|--------------------|-----------|------------------|-----------|-------------|---------|------------|---------|
| 204.3 ^a | 4.15(7) | | | 130.6(7) | 1.92(5) | 2.12 | 1 |
| | | 206 ^a | 4.09(7) | 129.8(7) | 1.94(5) | | |

^a Fixed at a value derived from ambient pressure Brillouin scattering experiments

^b Fixed to 1

As for the majoritic garnets reported in Chapter 3 (Section 3.3.1.1), measuring simultaneously density and sound velocities for the same sample at the same conditions gives the advantage of being able to determine accurately absolute pressure. For each experimental point, the absolute pressure (Section 2.3.2.2, equation 2.3) was determined from the variation of the isothermal bulk modulus with pressure. Pressures also were determined from the fluorescence shift of Sm:YAG (Trots et al., 2013) and of ruby (Mao et al., 1986; Jacobsen et al., 2008). The ruby pressure scale reported by Jacobsen et al. (2008) has been introduced for high pressure studies of minerals compressed with helium in the 25-140 GPa range since, according to these authors, the pressure scale reported by Mao et al. (1986) underestimates the pressure by 8% at 100 GPa when compared with the primary MgO scale of Zha et al. (2000).

A comparison between the pressure values obtained from ruby and Sm:YAG with the absolute pressures determined from the variation of the bulk modulus of NAL with density is reported in Figure 5.3-4.

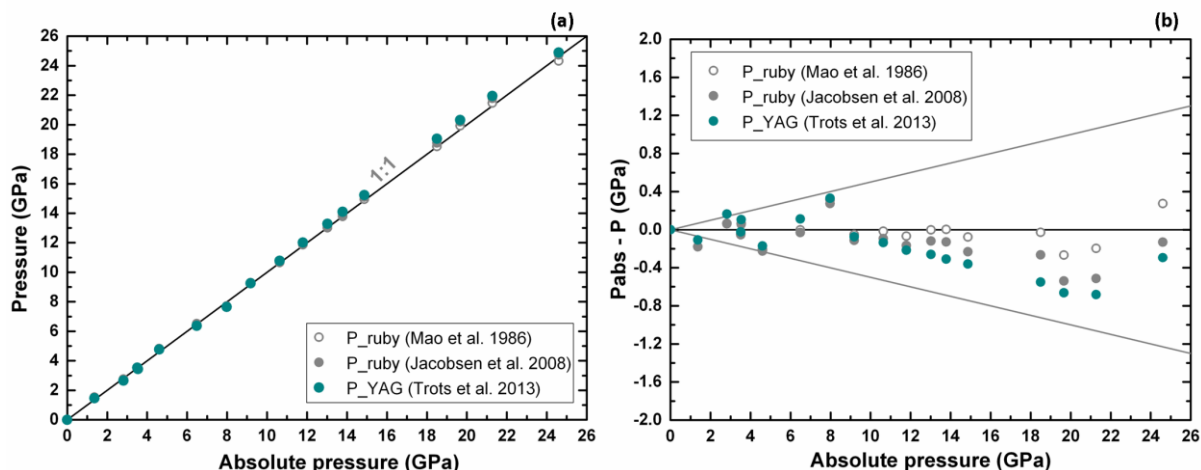


Figure 5.3-4. Comparison between the absolute pressure derived in this study and the ruby and Sm:YAG pressure scales. Grey open symbols: ruby pressure scale according to Mao et al. (1986); grey filled symbols: ruby pressure scale according to Jacobsen et al. (2008); dark cyan symbols: Sm:YAG pressure scale according to Trots et al. (2013). Grey lines represent the uncertainty ($\pm 5\%$) of the ruby pressure scale (Mao et al., 1986).

From the results reported in Figure 5.3-4 it appears that at pressures above 18 GPa both Sm:YAG and ruby fluorescence (according to Jacobsen et al., 2008) slightly overestimate the real pressure at which the sample is subjected, with a maximum difference in pressure (ΔP) of 0.6 at 22 GPa. However, the data points all lie within the uncertainties ($\pm 5\%$) of the ruby pressure scale (Mao et al., 1986). The differences in pressure scales and their effect on the determination of the EoS parameters of the NAL phase will be presented in the following section.

5.3.3 Compressibility and Equation of state (Eos)

The unit cell volumes variation with pressure is reported for both crystals in Table 5.3-3.

Table 5.3-3. Unit-cell lattice parameters of NAL measured at different pressures

| P_{abs} (GPa) | P_{YAG} (GPa) ^a | P_{ruby} (GPa) ^a | P_{ruby} (GPa) ^b | $a(\text{\AA})$ | $c(\text{\AA})$ | $V(\text{\AA}^3)$ | V/V_0 | c/a |
|----------------------------|--|---|---|-----------------|-----------------|-------------------|---------|--------|
| <i>crystal 1 (s5253x3)</i> | | | | | | | | |
| 0.0001* | 0.0001 | - | - | 8.7247(3) | 2.7673(3) | 182.43(2) | 1.0000 | 0.3172 |
| 2.03* | 2.24 | - | - | 8.6896(3) | 2.7586(4) | 180.40(3) | 0.9889 | 0.3175 |
| 2.84* | 3.06 | - | - | 8.6776(5) | 2.7558(5) | 179.71(4) | 0.9851 | 0.3176 |
| 4.03* | 4.38 | - | - | 8.6610(5) | 2.7514(6) | 178.73(4) | 0.9798 | 0.3177 |
| 5.21* | 5.47 | - | - | 8.6443(5) | 2.7475(6) | 177.80(4) | 0.9746 | 0.3178 |
| 6.22* | 6.55 | - | - | 8.6306(6) | 2.7439(7) | 177.01(5) | 0.9703 | 0.3179 |
| 0.0001 | 0.0001 | - | - | 8.7183(7) | 2.7649(7) | 182.00(5) | 1.0000 | 0.3171 |
| 8.48 | 8.11 | - | - | 8.6005(4) | 2.7367(5) | 175.31(3) | 0.9632 | 0.3182 |
| 10.05 | 10.23 | - | - | 8.5811(8) | 2.7313(7) | 174.18(5) | 0.9570 | 0.3183 |
| 12.69 | 13.32 | - | - | 8.5489(17) | 2.7231(16) | 172.35(11) | 0.9470 | 0.3185 |
| 16.13 | 16.81 | - | - | 8.5094(17) | 2.7126(15) | 170.10(10) | 0.9346 | 0.3188 |
| 19.93 | 21.01 | - | - | 8.467(4) | 2.702(3) | 167.78(9) | 0.9218 | 0.3192 |
| <i>crystal 2 (s5253x5)</i> | | | | | | | | |
| 0.0001 | 0.0001 | 0.0001 | 0.0001 | 8.7205(3) | 2.7659(3) | 182.16(2) | 1.0000 | 0.3172 |
| 1.36 | 1.47 | 1.54 | 1.54 | 8.6994(2) | 2.7611(3) | 180.97(2) | 0.9935 | 0.3174 |
| 2.82 | 2.66 | 2.75 | 2.76 | 8.6783(4) | 2.7556(6) | 179.73(4) | 0.9867 | 0.3175 |
| 3.54 | 3.43 | 3.47 | 3.48 | 8.6680(5) | 2.7531(6) | 179.14(4) | 0.9834 | 0.3176 |
| 3.51 | 3.53 | 3.56 | 3.57 | 8.6676(2) | 2.7537(2) | 179.16(2) | 0.9835 | 0.3177 |
| 4.60 | 4.77 | 4.81 | 4.83 | 8.6524(2) | 2.7498(3) | 178.28(2) | 0.9787 | 0.3178 |
| 6.49 | 6.37 | 6.49 | 6.52 | 8.6266(2) | 2.7434(2) | 176.80(2) | 0.9706 | 0.3180 |
| 7.98 | 7.65 | 7.67 | 7.71 | 8.6071(3) | 2.7382(4) | 175.68(3) | 0.9644 | 0.3181 |
| 9.18 | 9.25 | 9.23 | 9.29 | 8.5913(4) | 2.7346(4) | 174.80(3) | 0.9596 | 0.3183 |
| 10.64 | 10.77 | 10.65 | 10.73 | 8.5731(1) | 2.7299(2) | 173.76(1) | 0.9539 | 0.3184 |
| 11.79 | 12.01 | 11.86 | 11.96 | 8.5587(4) | 2.7264(4) | 172.96(3) | 0.9495 | 0.3186 |
| 13.02 | 13.28 | 13.02 | 13.14 | 8.5442(2) | 2.7225(2) | 172.13(2) | 0.9449 | 0.3186 |
| 13.78 | 14.09 | 13.78 | 13.91 | 8.5351(4) | 2.7203(6) | 171.62(4) | 0.9421 | 0.3187 |
| 14.87 | 15.23 | 14.95 | 15.10 | 8.5223(3) | 2.7172(4) | 170.91(2) | 0.9382 | 0.3188 |
| 18.50 | 19.05 | 18.53 | 18.76 | 8.4816(8) | 2.7069(9) | 168.64(6) | 0.9258 | 0.3191 |
| 19.66 | 20.32 | 19.93 | 20.20 | 8.4686(7) | 2.7040(12) | 167.94(8) | 0.9219 | 0.3193 |
| 21.28 | 21.96 | 21.47 | 21.79 | 8.4520(8) | 2.6993(13) | 166.99(8) | 0.9168 | 0.3194 |
| 24.60 | 24.89 | 24.33 | 24.73 | 8.4180(13) | 2.6907(18) | 165.13(12) | 0.9065 | 0.3196 |

Standard deviations are in parentheses

^a pressure calculated according to Mao et al., 1986; ^b pressure calculated according to Jacobsen et al., 2008; * data collected using a conventional X-ray tube

Note that for the first crystal, the data points indicated with the different symbol (*) were measured using a conventional X-ray tube (see section 5.2). In the table are also reported the different pressures calculated according to Trots et al. (2013) for Sm:YAG as well as according to Mao et al (1986) and Jacobsen et al. (2008) for ruby, and are compared with the absolute pressure values obtained from the bulk modulus variation (equation 2.3). The evolution of the unit-cell volumes as a function of absolute pressure is shown in Figure 5.3-5.

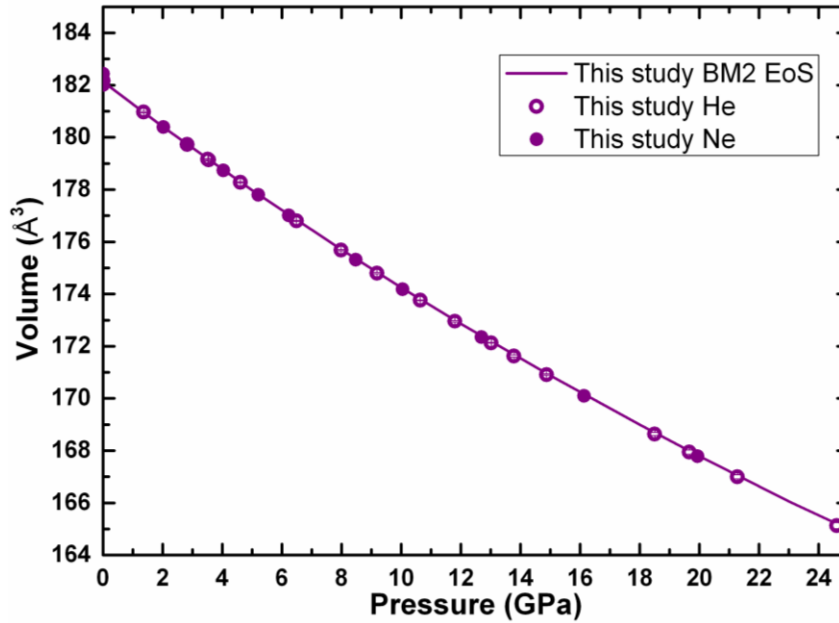


Figure 5.3-5. Evolution of the unit-cell volumes as a function of absolute pressure. Filled symbols: crystal s5253x3 loaded in Ne; open symbols: crystal s5253x5 loaded in He. Solid line: 2nd order Birch-Murnaghan equation of state. Standard deviations are within the size of the symbols.

The data show a smooth, continuous trend, indicating that there is no phase transition within the pressure range investigated.

A useful visual evaluation of the quality of an EoS fit is provided by the so-called F_E - f_E plot (Angel et al., 2000) (see Section 2.3.3.1.1). The P - V data of NAL have been therefore transformed into an F_E - f_E plot according to equations (2.9) and (2.10) (Figure 5.3-6).

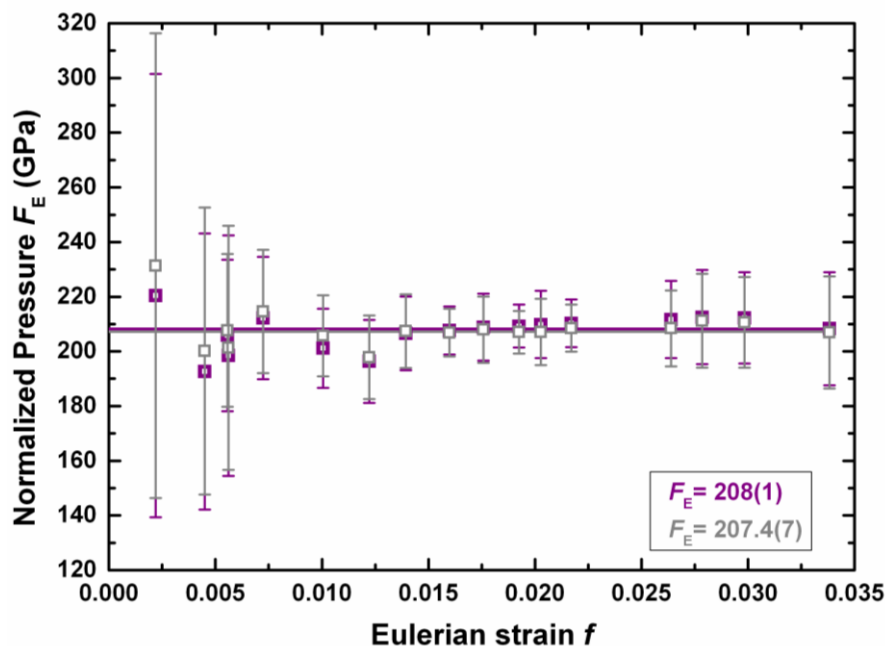


Figure 5.3-6. Normalized stress, F_E , versus Eulerian strain, f_E plots for S5253x5 crystal. The solid lines are weighted linear fits through the data. Grey symbols: P - V data using the ruby scale from Jacobsen et al. (2008); purple symbols: P - V data using Sm:YAG pressure scale (Trots et al., 2013).

Both sets of data fall on a horizontal line of constant F in the F_E - f_E plot (Figure 5.3-6) indicating that the P - V data are adequately described by a second order truncation of the Birch Murnaghan EoS with a value of K' equal to 4. Therefore, the P - V data reported in Table 5.3-3 were fitted using a second-order Birch–Murnaghan equation of state (Birch, 1947) with the software EOSFIT-5.2 (Angel, 2002). Note that for the first crystal (S5253x3) only the data measured with the rotating anode source were included in the fitting given a slight mismatch between the two different diffractometers. Simultaneous refinement of the unit-cell volume, V_0 , and the bulk modulus K_0 , resulted in the following values: $V_0 = 182.13(2) \text{ \AA}^3$ and $K_0 = 207(6) \text{ GPa}$ with K' fixed to the value of 4 when values of absolute pressure were used. For comparison, the EoS parameters obtained by fitting the same data but using either the pressures calculated according to Trots et al. (2013) for Sm:YAG or those for Mao et al. (1986) and Jacobsen et al. (2008) for ruby are reported in Table 5.3-4.

Table 5.3-4. EoS parameters of the NAL phase for a BM2 EoS

| crystal | V_0 (\AA^3) | K_0 (GPa) |
|------------------------|--------------------------|-------------|
| s5253x3-5 ^a | 182.13(2) | 206(1) |
| s5253x3-5 ^b | 182.02(6) | 212(2) |
| s5253x5 ^a | 182.15(2) | 205.5(7) |
| s5253x5 ^b | 182.05(6) | 211(2) |
| s5253x5 ^c | 182.18(5) | 205(1) |
| s5253x5 ^d | 182.14(5) | 208(1) |

Numbers in parentheses are the standard deviations in the last digit

^a EoS obtained using absolute pressure scale

^b EoS obtained using the Sm:YAG (Trots et al., 2013)

^c EoS obtained using ruby (Mao et al., 1986)

^d EoS obtained using ruby (Jacobsen et al., 2008)

There are not substantial discrepancies among the EoS parameters obtained using the different pressures scales, although Sm:YAG appears to give larger bulk moduli. Hereafter, therefore, we will refer to the EoS parameters obtained considering the absolute pressure.

Several studies have been conducted on the compression of NAL phases using polycrystalline materials both in complex and simplified systems resulting in a wide range of equations of state parameters (Table 5.3-5).

Table 5.3-5. EoS parameters of the Nal phase with different stoichiometry

| Composition | $V_0(\text{\AA}^3)$ | $K_0(\text{GPa})$ | K' | P scale | P_{Max} | References |
|--|---------------------|-------------------|--------|----------------------------|------------------|---------------------------|
| | | | | | | <i>experimental</i> |
| ^a | 182.13(2) | 206(1) | 4 | absolute pressure | 24.6 | this study |
| $\text{Na}_{0.4}\text{Mg}_{0.6}\text{Al}_{1.6}\text{Si}_{0.4}\text{O}_4$ | 182.27(24) | 199(6) | 5.0(6) | Au (Fei et al. 2007) | 31.2 | Imada et al. (2012) |
| | | 208(1) | 4 | Au (Fei et al. 2007) | | Imada et al. (2012) |
| | | 198(6) | 4.7(6) | Au (Anderson et al. 1989) | 30.6 | Imada et al. (2012) |
| | | 205(1) | 4 | Au (Anderson et al. 1989) | | Imada et al. (2012) |
| | | 198(5) | 4.3(6) | Au (Shim et al. 2002) | 29.7 | Imada et al. (2012) |
| | | 200(1) | 4 | Au (Shim et al. 2002) | | Imada et al. (2012) |
| ^b | 182.77(6) | 176(2) | 4.9(3) | Au (Anderson et al. 1989) | 17.9 | Shinmei et al. (2005) |
| | | 181.7(4) | 4 | Au (Anderson et al. 1989) | | Shinmei et al. (2005) |
| | | 185.5(4) | 4 | Au (Tsuchiya 2003) | | Shinmei et al. (2005) |
| | | 178.8(4) | 4 | Au (Fei et al. 2004) | | Shinmei et al. (2005) |
| $\text{NaAlSiO}_4\text{-MgAl}_2\text{O}_4$ | 188(2) | 184(16) | 4 | Ar (Guignot&Andrault 2004) | 59.4 | Guignot&Andrault (2004) |
| ^c | 184.55(6) | 214(2) | 3.0(1) | ruby (Mao et al. 1986) | 36 | Vanpeteghem et al. (2003) |
| | | 202.3(9) | 4 | ruby (Mao et al. 1986) | | Vanpeteghem et al. (2003) |
| ^d | 185.9(2) | 198(3) | 4 | Pt (Holmes et al. 1989) | 63 | Ono et al. (2002) |
| | | | | | | <i>calculations</i> |
| $(\text{Ca})(\text{Mg})_2\text{Al}_6\text{O}_{12}$ | 181.8(60.6) | 212 | 4.2 | | 119 | Mookherjee et al. (2012) |
| $\text{NaMg}_2\text{Al}_5\text{SiO}_{12}$ | 178.35 | 217.7 | 4.08 | | 50 | Kawai&Tsuchiya (2012) |

^a $\text{Na}_{0.41}[\text{Na}_{0.125}\text{Mg}_{0.79}\text{Al}_{0.085}]_2[\text{Al}_{0.79}\text{Si}_{0.21}]_6\text{O}_{12}$
^b $\text{Na}_{1.13}\text{Mg}_{1.15}\text{Al}_{4.47}\text{Si}_{1.62}\text{O}_{12}$
^c $[\text{K}_{0.07}\text{Na}_{0.81}\text{Ca}_{0.12}]_{1.01}[\text{Mg}_{1.62}\text{Fe}_{0.38}]_2[\text{Al}_{4.98}\text{Fe}_{0.10}\text{Ti}_{0.05}\text{Si}_{0.88}]_{6.01}\text{O}_{12}$
^d $[\text{K}_{0.15}\text{Na}_{1.66}\text{Ca}_{0.11}]_{1.92}[\text{Mg}_{1.29}\text{Fe}_{0.71}]_2[\text{Al}_{3.13}\text{Fe}_{0.15}\text{Ti}_{0.09}\text{Si}_{1.98}]_{5.35}\text{O}_{12}$

The variation with pressure of the volumes normalized with respect to their room pressure values of previous experimental and theoretical studies present in the literature are reported in Figure 5.3-7 together with the data collected for this project.

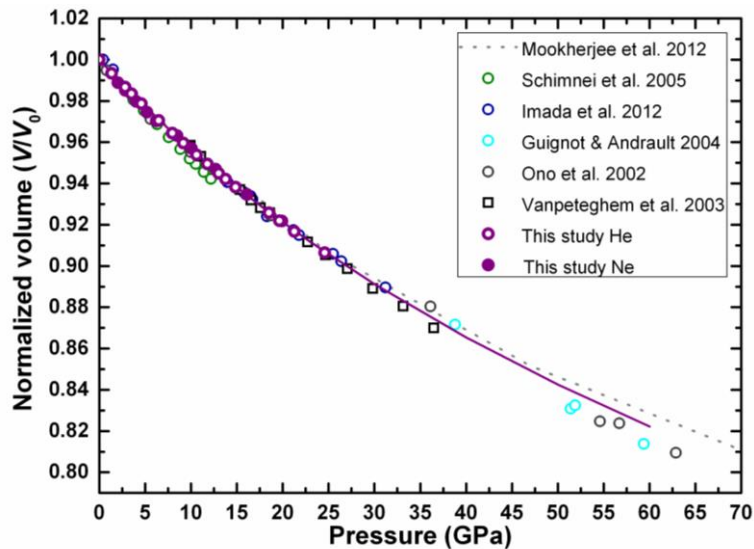


Figure 5.3-7. Normalized volume (V/V_0) as a function of pressure for the NAL phase. Solid line: 2nd order Birch-Murnaghan equation of state fit through the data collected for this project.

The bulk moduli reported in the literature range from 176 to 217.7 GPa (a much larger range than those obtained using difference pressure scales in this study), while the bulk moduli pressure derivatives range from 3 to 5. The adiabatic bulk modulus $K_{S0} = 207(6)$ GPa and the ambient pressure unit cell volume $V_0 = 182.13(2) \text{ \AA}^3$ determined in this study are in excellent agreement with the values reported by Imada et al. (2012) for a $K' = 4$ for a sample with similar amount of Al and Si. As reported by these authors, the relatively small K_{T0} for the NAL phase reported by Shinmei et al. (2005) may be due to the fact that the volumes were measured under non-hydrostatic conditions as the measurements were performed during decompression without thermal annealing. Small values of K_{T0} were also reported by Guignot and Andraut (2004). Note that the ambient volume of the NAL phase ($V_0 = 188 \text{ \AA}^3$) reported by these authors is much larger than that determined in this study. Larger volumes are also reported by Vanpeteghem et al. (2003) and Ono et al. (2002) for NAL phases with complex chemical compositions (see Table 5.3-5).

In addition to the differences in chemical composition of the NAL phases, the discrepancies in the EoS parameters among the studies also may due to uncertainties in the pressure determination in the different experiments. As discussed in Chapter 1, results obtained using extrapolation of slightly different EoS reported for gold in the literature can give different pressure estimates from the same unit cell values. Consequently, large uncertainties on the pressure values can cause inaccuracy in the equations of state (EoS) and in density calculations.

5.3.3.1 Axial compressibility

The unit cell parameters of NAL phase show anisotropic behaviour when plotted as relative compression as a function of pressure. A linearised second order Birch-Murnaghan EoS in which the cube of the unit-cell axis is used instead of the volume (Angel, 2000) was used to fit the unit cell a and c parameters of NAL. The refined coefficients are reported in Figure 5.3-8.

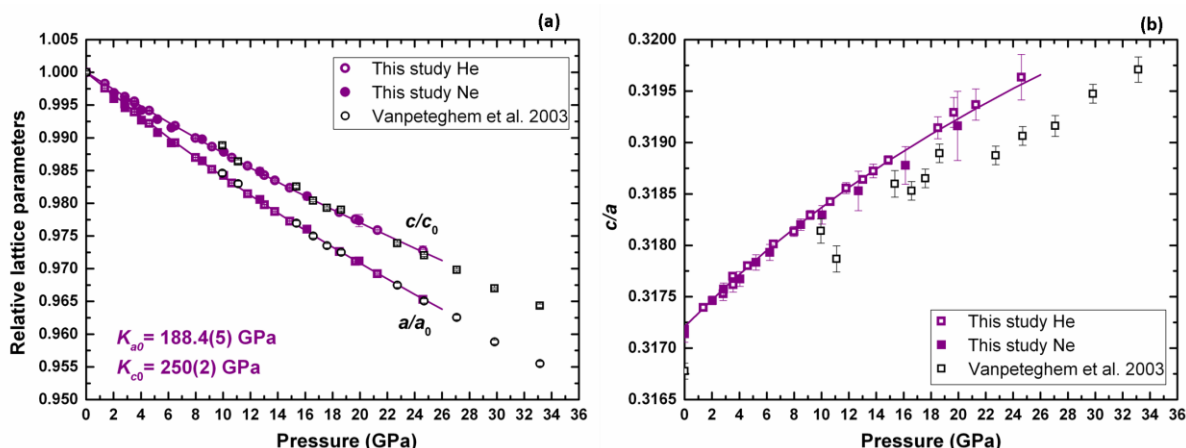


Figure 5.3-8. (a) Variation of the unit-cell lattice parameters normalized with respect to their room pressure values as a function of pressure. Standard deviations are within the size of the symbols. (b) Variation of the c/a ratio as a function of pressure. Solid curves: 2^{nd} order Birch-Murnaghan equation of state fits.

The a axis of NAL is more compressible than the c axis (Figure 5.3-8) with a consequent increase with pressure of the c/a axes ratio. The stiffness of the c -axis may be due to the large Na displacement parameter at the M3 site, which suggests a dynamic disorder of this cation along the c axis, as determined from the single crystal structure refinement (Chapter 4). A similar behaviour has been observed in a NAL sample with complex composition, $[K_{0.07}Na_{0.81}Ca_{0.12}]_{1.01}[Mg_{1.62}Fe_{0.38}]_2[Al_{4.98}Fe_{0.10}Ti_{0.05}Si_{0.88}]_{6.01}O_{12}$, (Vanpeteghem et al., 2003), although in this latter case the anisotropy appears to be smaller. The c axis of the NAL phase reported by Vanpeteghem et al. (2003) is slightly more compressible than the one reported here, likely due to the more complex substitution at the M3 site that could hinder the dynamic disorder and therefore influence the compressibility along the c direction.

5.3.4 Sound velocities

Aggregate velocities as well as elastic moduli were calculated from the C_{ij} 's using the Voigt-Reuss-Hill averaging scheme (Hill, 1952) and are listed in Table 5.3-1. The aggregate velocities of NAL as a function of absolute pressure are reported in Figure 5.3-9, whereas the variation of the bulk (K_s) and shear (G) moduli as a function of absolute pressure are reported in Figure 5.3-10.

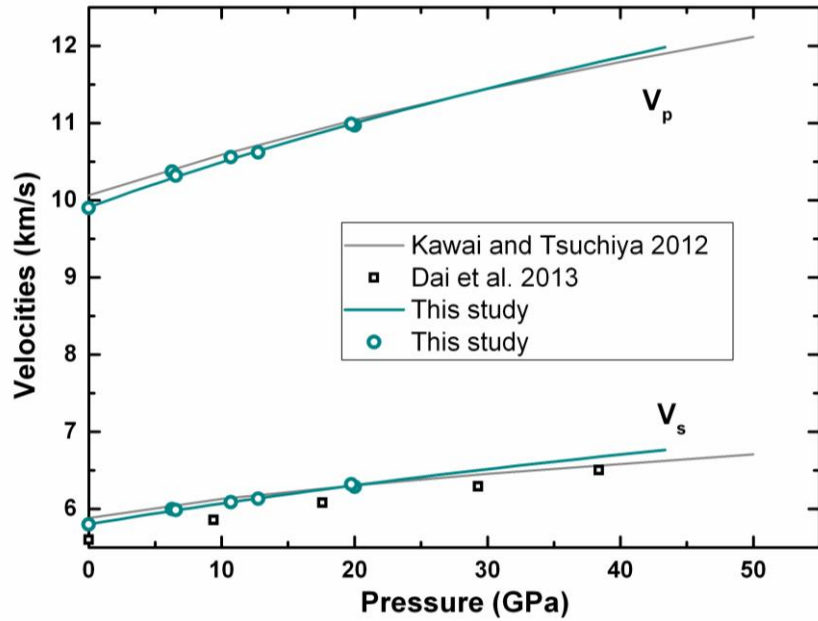


Figure 5.3-9. Variation of shear (V_s) and compressional (V_p) wave velocities of $\text{Na}_{1.07}\text{Mg}_{1.58}\text{Al}_{4.91}\text{Si}_{1.26}\text{O}_{12}$ NAL as a function of pressure. Open circles this study; open squares experimental results from Dai et al. (2013) obtained for a polycrystalline sample. Theoretical calculation results are reported as solid grey curve (Kawai and Tsuchiya, 2012).

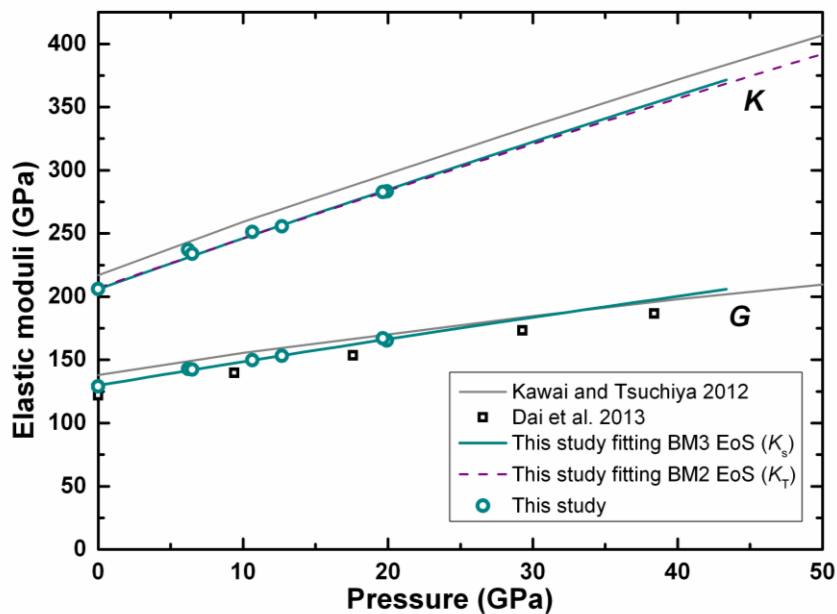


Figure 5.3-10. Pressure-dependences of bulk and shear moduli for the NAL phase (open circles). Cyan curves: Birch-Murnaghan equation of state fits through the experimental data of this study. Grey curves: bulk moduli calculated by Kawai and Tsuchiya (2012). Open squares are measurements from Dai et al. (2013).

The pressure derivatives of the elastic moduli were obtained by fitting the moduli at high pressure as reported in Section 5.3.2. The adiabatic bulk modulus and its pressure derivatives

are in excellent agreement with the isothermal bulk modulus and the pressure derivative obtained from the fitting of P - V data considering absolute pressure (Table 5.3-4, Figure 5.3-10). The experimental values obtained in this study are smaller than those obtained from theoretical calculations reported by Kawai and Tsuchiya (2012) and by Mookherjee et al. (2012) summarized in Table 5.3-5, but are clearly larger than those reported for a polycrystalline sample (Dai et al., 2013) likely due to the anisotropic behavior of the NAL phase also at high pressures.

Table 5.3-6. Elastic parameters of the NAL phase

| Composition | K_0 (GPa) | $\partial K/\partial P$ | G (GPa) | $\partial G/\partial P$ | Reference |
|---|------------------|-------------------------|--------------------|-------------------------|------------------------|
| | | | | | <i>experimental</i> |
| $\text{Na}_{1.07}\text{Mg}_{1.58}\text{Al}_{4.91}\text{Si}_{1.26}\text{O}_{12}$ | 206 ⁺ | 4.15(7) | 130.6(7) | 1.92(5) | This study |
| $\text{Na}_{0.4}\text{Mg}_{0.6}\text{Al}_{1.6}\text{Si}_{0.4}\text{O}_4$ | - | - | 126.96 (9) | 1.961(9) | Dai et al. 2013 |
| | | | | | <i>calculations</i> |
| $\text{NaMg}_2\text{Al}_5\text{SiO}_{12}$ | 220 [*] | 4.04 [*] | 139.8 [*] | 1.6 [*] | Kawai & Tsuchiya 2012 |
| $\text{CaMg}_2\text{Al}_6\text{O}_{12}$ | 216 | 3.8 | 143 | 1.6 | Mookherjee et al. 2012 |

⁺ value derived from ambient pressure Brillouin scattering experiments; ^{*} values obtained by fitting the digitalized data from Kawai and Tsuchiya (2012)

Note however, that the pressure derivative of the shear modulus obtained in this study ($\partial G / \partial P$)_T = 1.92(5) is higher than those obtained from theoretical calculations ($\partial G / \partial P$)_T = 1.6 (Figure 5.3-10, Table 5.3-6). As discussed in Chapter 4, the discrepancy between experimental and theoretical values is very likely due to the differences in cation distributions among the crystallographic sites as well as in different chemical compositions (see Table 5.3-6).

5.3.5 Seismic anisotropy

At ~ 1000 km, NAL is expected to transform to a calcium ferrite type aluminum phase (CF) (Kawai and Tsuchiya, 2012). According to these theoretical calculations, NAL and CF phase would have comparable shear wave velocities across the phase transition, implying that the transformation to CF would not be seismically detectable. However, these authors reported a significant change in the seismic wave anisotropy associated with the phase transition, which might lead to a seismically detectable discontinuity as a result of favorable crystallographic preferred orientation.

Using the single crystal elastic constants and density obtained in this study, the seismic anisotropy (see equation 1.5, Chapter 1) was calculated at different pressures by analyzing a hemisphere of all possible propagation directions. An example of the single crystal compressional (AV_p) and shear wave anisotropy (AV_s) at 19.93 GPa is shown in Figure 5.3-11.

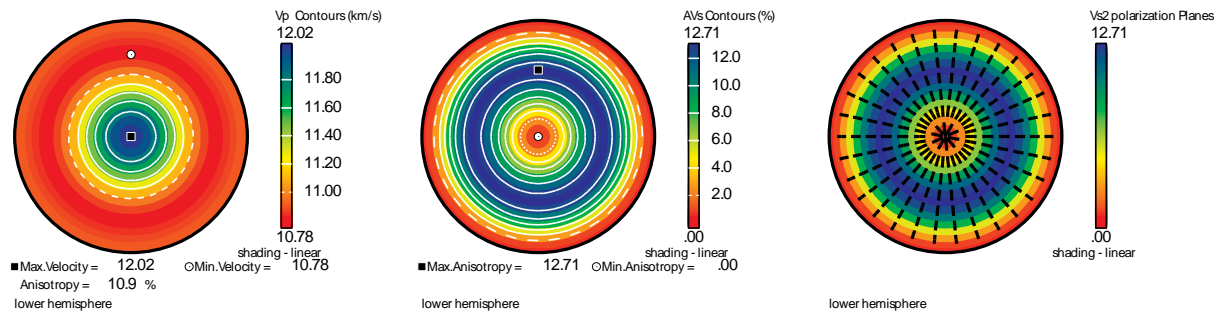


Figure 5.3-11. Single crystal compressional wave velocity (V_p), shear wave anisotropy (AV_s), fastest wave polarization (V_{S2}) plotted as Lambert azimuthal equal-area lower hemisphere pole figures (Mainprice, 1990), with the elastic tensor orthogonal axes $X1 = a$ axis (east) and $X3 = c$ axis (centre).

At this pressure, the NAL phase displays 10.9 % compressional (AV_p) and 12.71 % shear wave anisotropy (AV_s). The latter is mainly due to the high anisotropic feature of V_{S2} given that V_{S1} is essentially isotropic.

The evolution of the elastic anisotropy as a function of pressure of the NAL phase determined in this study up to 20 GPa and extrapolated to 40 GPa is reported in Figure 5.3-12 and it is compared to that of NAL and CF phases reported by Kawai and Tsuchiya (2012).

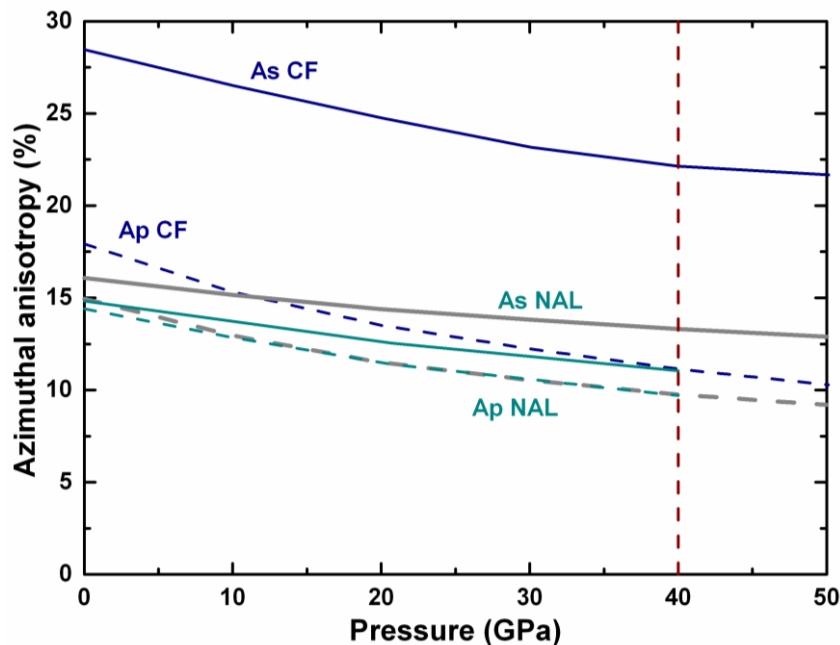


Figure 5.3-12. Elastic anisotropy as a function of pressure of the NAL phase determined in this study (dark cyan), compared to those of NAL (grey) and CF (blue) reported by Kawai and Tsuchiya (2012). Dashed curves indicate the compressional wave anisotropy (AV_p), whereas solid curves indicate the shear wave anisotropy (AV_s). The red dashed line represents the transition from NAL to CF at approximately 40 GPa.

Both the shear (AV_s) and compressional wave anisotropy (AV_p) have comparable values at room pressure and they decrease with increasing pressure (Figure 5.3-12). The difference between shear and compressional anisotropy obtained in this study is slightly smaller at all pressures than that reported in the theoretical calculations study (Kawai and Tsuchiya, 2012). These authors also found that CF is significantly more anisotropic ($AV_p = 11.1\%$; $AV_s = 22.1\%$) than the NAL phase ($AV_p = 9.8\%$; $AV_s = 13.3\%$) (Figure 5.3-12). Based on the experimental data obtained in this study, the phase transition from NAL to CF may result in a remarkable change in the elastic anisotropy.

The accurate data obtained in this study will be fitted into a larger scale model of the lower mantle and will be compared with seismic data. Also, the variation of density with pressure will be used to evaluate the buoyancy of subducting slabs. As for majoritic garnets, this part will be discussed in Chapter 6.

6. Velocity and density models of the Earth's transition zone and uppermost lower mantle.

The principal method for constraining the thermal and chemical structure of the Earth's mantle is through the interpretation of seismic observations based on phase equilibria and mineral physics models. As reported in Chapter 1, the approach is to assume a mantle bulk composition, perhaps based on a particular mantle lithology, determine the mineralogy of this composition as a function of depth and then calculate the acoustic velocities for this assemblage using mineral-physics data. The difference between the observed seismic properties and those calculated for the assumed mineral assemblage (Cammarano et al., 2005) gives a measure of the model goodness of fit. In this regard, the transition zone, between 410 and 660 km, is an excellent region to perform such a comparison because it is free of the complex thermal and chemical structure imparted on the shallow mantle by the lithosphere and melting processes (Frost, 2008). In addition the transition zone has a number of characteristic seismic properties that provide vital additional constraints on the chemistry and thermal state of the mantle. This region is characterized by a high gradient in seismic-wave velocity and density that occurs as a result of a series of mineral phase transformations (Agee, 1998).

A number of studies (Duffy and Anderson, 1989 and references therein) have compared seismic reference models with acoustic wave velocities calculated for mineral assemblages. Some studies have proposed that the mantle transition region is characterized by an olivine-rich pyrolitic composition (Ringwood, 1975; Duffy and Anderson, 1989) whereas others (Bass and Anderson, 1984; Anderson and Bass, 1986) have suggested that it has a pyroxene- and garnet-rich composition (piclogite) because the seismic velocities that have been calculated for a pyrolite composition are significantly higher than those observed in the reference models. At a depth of 410 km, $(\text{Mg,Fe})_2\text{SiO}_4$ olivine, or α phase, transforms to the high-pressure polymorph wadsleyite, also referred to as the β phase. This transition is now widely accepted to cause a discontinuity in seismic wave velocity observed globally at this depth. One approach to discriminate between compositional models is to constrain the olivine content of the mantle by comparing the calculated magnitude of the velocity jump at the olivine-wadsleyite transformation with the reference model jump at the discontinuity (Duffy and Anderson, 1989). This method may not be that accurate, however, as no seismic

reference model is a unique fit to the global seismic data from which it is refined. This is due, for instance, to trade-offs between the magnitude of a discontinuity and the local velocity gradient (Cammarano et al., 2005).

Another distinctive feature of the transition zone are the high velocity and density gradients between discontinuities. It has been suggested that these transition zone velocity gradients may be caused by unusually high pressure derivatives of the elastic moduli of majoritic garnet, as reported in some ultrasonic measurements on polycrystalline samples (Gwanmesia et al., 1998; Liu et al., 2000). However, some compression (Zhang et al., 1998; 1999) and Brillouin studies (including the work in Chapter 3) on majorite-garnet solid solutions report much lower pressure derivatives of the elastic moduli. Furthermore, Sinogeikin and Bass (2002a) proposed that even the high pressure derivatives reported by some ultrasonic measurements fail to match the large gradients in the transition zone. Alternatively, high velocity gradients have been attributed to gradual transformations between minerals with very different elastic properties (Bass and Anderson, 1984) such as the transformation of approximately 25% or more of clinopyroxene into majorite above 520 km, and the formation of Ca silicate perovskite below 520 km (Sinogeikin and Bass, 2002a). Accurate measurements of phase relations combined with elasticity data for the mineral compositions of interest are required to assess these scenarios, however.

The transition zone has also been proposed as a region where, at least, temporary stagnation of subducting slabs may occur due to either buoyancy or viscosity driven resistance to entering the lower mantle (Ringwood, 1982). Subducting slabs are products of mid ocean ridge melting and are composed of a lithologically stratified unit of approximately 80 km thickness (see Chapter 1). When such differentiated oceanic lithospheric plates sink into the mantle, phase transformations in the respective mafic, harzburgite and lherzolite layers will occur at different depths as a result of the different chemical compositions. This will result in differences in buoyancy between the lithologies that may result in the accumulation of certain lithologies at particular depths.

In this chapter, the new elasticity data on majoritic garnets and the NAL phase are fitted to a thermo-elastic self-consistent model to enable them to be extrapolated, principally in chemical composition and temperature. Using the data on the different garnet compositions,

properties of garnet end-members are evaluated. The end member properties are then combined to determine the elasticity of complex garnet solid solutions. By fitting a fictive majorite end member, for example, using solid solution data rather than using data on the end member itself, the chemical range over which the model is refined remains closer to that over which it will be employed. This model combined with data from the literature, mainly for $(\text{MgFe})_2\text{SiO}_4$ phases, and with a thermodynamic model for phase relations along a typical mantle adiabat, is then used to calculate acoustic velocities and densities of mafic, harzburgitic and lherzolithic bulk compositions in the Earth's transition zone and uppermost lower mantle. These models are then compared with seismic reference models over the same depth interval to constrain the likely conditions and chemistry. Furthermore by comparing the calculated densities over the same interval, levels can be identified where slab units are likely to accumulate and potentially create enduring chemical and thermal anomalies.

6.1 Determination of P-V-T EoS of majoritic garnets

The high-pressure high-temperature elasticity of majoritic garnets has been described in Chapter 3 using a high-temperature form of the Birch-Murnaghan equation of state. In this form the elastic moduli at high temperature were described by linear equations such as (3.9) and (3.10). In the current Chapter, however, a self-consistent thermodynamic potential formalism is used to determine the elastic properties for the same compounds. The model has a more theoretically justified thermal component compared to the linear moduli dependences described in Chapter 3. In this formalism the Helmholtz free energy, $F(V,T)$ of a solid is divided into a reference part, F_0 , a term $F_C(V,T_0)$ describing compression at room temperature and a thermal term ΔF_{TH} :

$$F(V, T) = F_0 + F_C(V, T_0) + [F_{TH}(V, T) - F_{TH}(V, T_0)] \quad (6.1)$$

where V is the molar volume, T is temperature and the subscript zero indicates a reference state, normally 300 K.

The term $F_C(V,T_0)$ is expressed as a polynomial function of the Eulerian strain, ε (Birch, 1952) normally truncated to the third order:

$$F_C(V, T_0) = 9K_0V_0(f^2/2 + a_1 f^3/3) \quad (6.2)$$

with

$$f = \frac{1}{2} \left[\left(\frac{V_0}{V} \right)^{2/3} - 1 \right] = -\varepsilon \quad (6.3)$$

and

$$a_1 = \frac{3}{2} (K'_0 - 4) \quad (6.4)$$

where K_0 and K'_0 are the isothermal bulk modulus and its pressure derivative.

The thermal term ΔF_{TH} is evaluated using the Mie-Grüneisen equation of state and makes use of the Debye model to take into account a quasi-harmonic approximation for the vibrational energy (Davies, 1974). The exact form of this term (Stixrude and Lithgow-Bertelloni, 2005a) includes a sum over all vibrational modes λ whose eigenfrequencies ν_λ are strain dependent:

$$\Delta F_{TH} = kT \sum_\lambda \ln \left[1 - \exp \left(-\frac{h\nu_\lambda}{kT} \right) \right] - kT_0 \sum_\lambda \ln \left[1 - \exp \left(-\frac{h\nu_\lambda}{kT_0} \right) \right] \quad (6.5)$$

where k is the Boltzmann constant and h is a constant.

The adiabatic elastic tensor can then be expressed as a derivative with respect to the Eulerian strain, according to the formulation of Thomsen (1972), which is strictly valid only for isotropic bodies (Stixrude and Lithgow-Bertelloni, 2005b):

$$c_{ijkl} = (1 + 2f)^{5/2} \left\{ c_{ijkl0} + (3K_0 c'_{ijkl0} - 5c_{ijkl0})f + \left[6K_0 c_{ijkl0} - 14c_{ijkl0} - \frac{3}{2} K_0 \delta_{kl}^{ij} (3K'_0 - 16) \right] f^2 \right\} + \left(\frac{\gamma_{ij} \delta_{kl} + \gamma_{kl} \delta_{ij}}{2} + \gamma_{ij} \gamma_{kl} - \eta_{ijkl} \right) \frac{\Delta E_{TH}(V,T)}{V} \quad (6.6)$$

where δ_{ij} is the Kroenecker delta, ΔE_{TH} is the difference in the quasi-harmonic thermal energy between T and T_0 , γ_{ij} is the tensorial generalization of the Grüneisen, parameter and η_{ijkl} is its strain derivative. Both of the last quantities have been calculated assuming that their values are the same for all vibrational modes λ (according to the Grüneisen approximation):

$$\gamma_{ij} = \gamma \delta_{ij} \quad \text{with} \quad \gamma = V \left(\frac{\partial P}{\partial E} \right)_V \quad (6.7)$$

and

$$\eta_{ijkl} = \gamma q \delta_{ij} \delta_{kl} + \eta_S \left(\delta_{ik} \delta_{jl} + \delta_{il} \delta_{jk} - \frac{2}{3} \delta_{ij} \delta_{kl} \right) \quad \text{with} \quad q = \left(\frac{\partial \ln \gamma}{\partial \ln V} \right) \quad (6.8)$$

For an isotropic material the vibrational frequencies can be expressed as a Taylor expansion in the Eulerian finite strain, whose strain derivatives give rise to equation (5.3) for the Grüneisen parameter γ (Chapter 5) and to the following equation for γq and η_S :

$$\gamma q = \frac{1}{9} \left\{ 18\gamma^2 - 6\gamma - \frac{1}{2[1+6\gamma_0 f + \frac{1}{2}(-12\gamma_0 + 36\gamma_0^2 - 18\gamma_0 q_0)]} (2f+1)^2 (-12\gamma_0 + 36\gamma_0^2 - 18\gamma_0 q_0) \right\} \quad (6.9)$$

$$\eta_S = -\gamma + \frac{1}{[1+6\gamma_0 f + \frac{1}{2}(-12\gamma_0 + 36\gamma_0^2 - 18\gamma_0 q_0)]} (2f+1)^2 (\gamma_0 + \eta_0) \quad (6.10)$$

The isothermal bulk modulus, K_T , is obtained as the second derivative of the Helmholtz free energy:

$$K_T = (1+2f)^{5/2} \left[K_0 + (3K_0 K'_0 - 5K_0) f + \frac{27}{2} (K_0 K'_0 - 4K_0) f^2 \right] + (\gamma + 1 - q) \gamma \frac{\Delta E_{TH}(V,T)}{V} - \frac{\gamma^2}{V} [T C_V(V,T) - T_0 C_V(V,T_0)] \quad (6.11)$$

where C_V is the heat capacity at constant volume and is evaluated in the framework of the Debye theory according to equation (5.5) reported in Chapter 5.

The isothermal bulk modulus can be converted to the adiabatic bulk modulus K_S according to equation (2.4) in Chapter 2. The shear modulus of an isotropic material can be calculated directly from equation (6.6) and results in:

$$G = (1+2f)^{5/2} \left[G_0 + (3K_0 G'_0 - 5G_0) f + \left(6K_0 G'_0 - 24K_0 - 14G_0 + \frac{9}{2} K_0 K'_0 \right) f^2 \right] - \eta_S \frac{\Delta E_{TH}(V,T)}{V} \quad (6.12)$$

The formalism described above has been used to compute the aggregate wave velocities V_P and V_S of $\text{Mg}_{3.24}\text{Al}_{1.53}\text{Si}_{3.23}\text{O}_{12}$ (Mj) and of $\text{Mg}_{3.01}\text{Fe}_{0.17}\text{Al}_{1.68}\text{Si}_{3.15}\text{O}_{12}$ (Fe-Mj) garnet according to equations (1.1) and (1.2) (Chapter 1). The values of the EoS parameters K_{T0} , K'_{T0} , G_0 , G'_0 and η_{S0} were obtained from a least square minimization of the differences between observed and calculate aggregate wave velocities, whereas the volumes V_0 was fixed to the room pressure values obtained from X-ray diffraction (see Section 3.2.2). The Grüneisen parameter γ_0 and the logarithmic volume derivative of the effective Debye temperature, q_0 are relatively insensitive and were kept at typical values reported for garnets (Stixrude and Lithgow-Bertelloni, 2011). The Debye temperature was calculated according to equation (5.7) reported in Chapter 5.

The nine EoS parameters, V_0 , K_{T0} , K'_{T0} , θ_0 , γ_0 , q_0 , G_0 , G'_0 , η_{S0} , that are used to describe the variation of shear V_S and compressional V_P wave velocities for the two majoritic garnets examined as a function of pressure and temperature are summarized in Table 6.1-1.

Table 6.1-1. EoS parameters of majoritic garnets

| Sample | V_0 ($\text{cm}^3\text{mol}^{-1}$) | K_{T0} (GPa) | K'_{T0} | θ_0 (K) ^a | γ_0 ^b | q_0 ^b | G_0 (GPa) | G_0' | η_{s0} |
|---|---|-------------------|-----------|--------------------------------|-------------------------|--------------------|----------------|--------|-------------|
| $\text{Mg}_{3.24}\text{Al}_{1.53}\text{Si}_{3.23}\text{O}_{12}$ | 113.4 | 166.5 | 4.7 | 791 | 1 | 1.4 | 91.8 | 1.4 | 1.28 |
| $\text{Mg}_{3.01}\text{Fe}_{0.17}\text{Al}_{1.68}\text{Si}_{3.15}\text{O}_{12}$ | 113.4 | 171.6 | 4.09 | 795 | 1.06 | 1.4 | 92.7 | 1.4 | 1.3 |

^a Calculated via equation (5.7); ^b Fixed to values typical for garnets (Stixrude and Lithgow-Bertelloni, 2011)

The calculated wave velocities are in good agreement with the measured V_P and V_S at high pressures and temperatures (Figure 6.1-1).

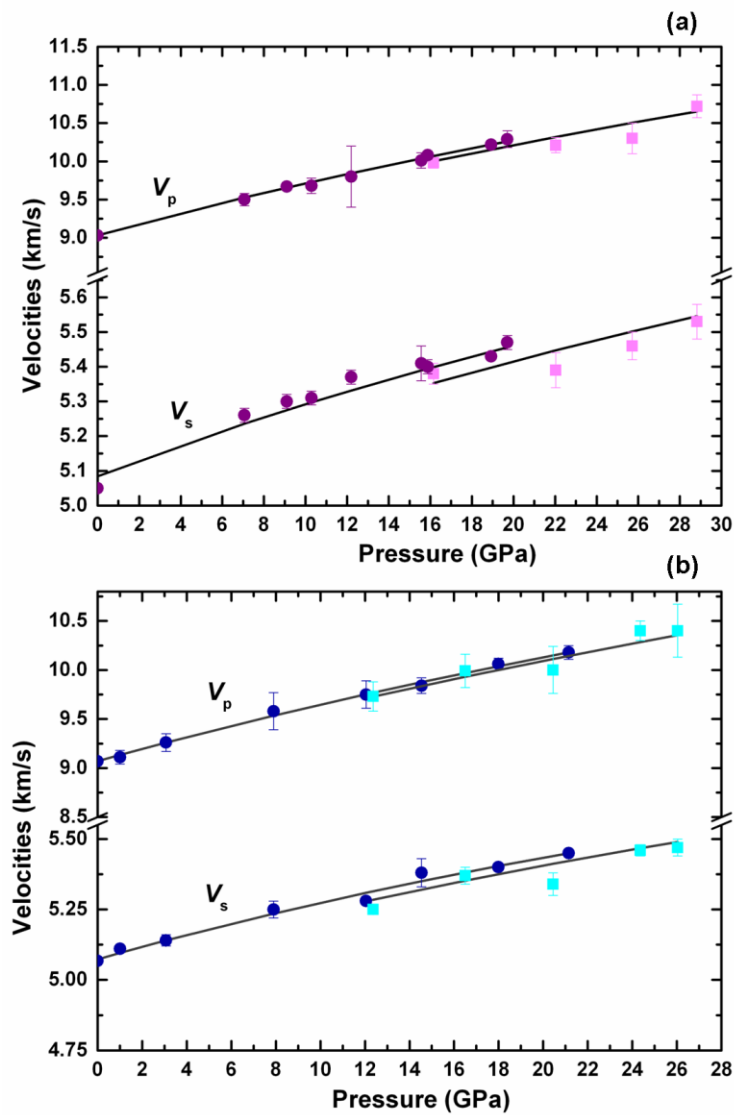


Figure 6.1-1. Compressional and shear wave velocities of (a) Mj sample measured at high pressure at room temperature (purple) and at high pressure and at 558K (magenta) (b) Fe-Mj sample measured at high pressure at room temperature (dark blue) and at high pressure and at 470K (light blue). Solid curves are calculated from the thermo-elastic model parameters given in Table 6.1-1.

6.2 Calculation of elastic properties for majoritic garnets from end member compositions

Due to the partitioning between other phases and potential variations in bulk composition garnets will form complex solid solutions with varying compositions within the upper mantle and transition zone. Different cation substitutions can occur both at the X and Y sites of the garnet structure (see Figure 3.3-6, Section 3.3-2). Within the mantle these chemical variations can be described with respect to the end members pyrope ($\text{Mg}_3\text{Al}_2\text{Si}_3\text{O}_{12}$; Py) and majorite ($\text{Mg}_4\text{Si}_4\text{O}_{12}$; Mj), where Si and Mg cations substitute for Al in the Y sites, in addition to almandine ($\text{Fe}_3\text{Al}_2\text{Si}_3\text{O}_{12}$; Alm) and grossular ($\text{Ca}_3\text{Al}_2\text{Si}_3\text{O}_{12}$; Grs), where Fe and Ca substitute for Mg in the X site, respectively.

The elastic properties of a phase consisting of a solid solution of n end-members in a single mineral phase can be derived through a summation of the individual elastic properties of the corresponding end members (Chantel, 2012):

$$\psi_{ss} = \frac{1}{\sum_{i=1}^n \frac{1}{m_i V_i} \sum_{i=1}^n \frac{m_i V_i}{\psi_i}} \quad (6.13)$$

where ψ_{ss} is the bulk elastic property of interest, ψ_i is the elastic property of component i and V_i and m_i are the volume and mole fraction of component i . This summation assumes that the solid solution is ideal i.e. its properties are a linear function of end members. Although such an assumption is likely incorrect, non-ideal effects can be minimized, as previously described, by refining properties of fictive end members rather than using data on the end members themselves. The actual compositions of the majoritic garnets investigated in this study can be expressed in terms of end-member garnets as $\text{Py}_{76}\text{Mj}_{24}$ and $\text{Py}_{78}\text{Mj}_{16}\text{Alm}_6$ for the iron-free and Fe-bearing samples, respectively. The sound velocity data of these samples can be calculated as a function of pressure as a summation of the elastic properties of the appropriate end members determined according to the formalism reported in Section 6.1 scaled according to their molar proportions. For the refinement, initial values of, V_0 , K_{T_0} , K'_{T_0} , θ_0 , γ_0 , q_0 , G_0 , G'_0 , and η_{S_0} , for the garnet end members were taken from Stixrude and Lithgow-Bertelloni (2011) (Table 6.2-1), however this resulted in poor agreement with the measured values. The Debye temperatures for pyrope and majorite were calculated according to equation (5.7) reported in Chapter 5. Least squares refinement of parameters for the majorite end-member, using the experimental data on the Mj sample, and then on the

almandine end member, using the Fe-Mj data, resulted in the values reported in Table 6.2-1. It was also necessary to refine some terms for pyrope to obtain a good agreement with the experimentally measured values. Note in particular that the refined K'_{T0} for almandine is lower than previously reported (Jiang et al., 2004) for the end member. Values which differ from those reported in the compilation of Stixrude and Lithgow-Bertelloni (2011) are reported in bold in Table 6.2-1.

Table 6.2-1. EoS parameters of garnet components

| Phase | Formula | V_0 (cm ³ /mol) | K_{T0} (GPa) | K'_{T0} | θ_0 (K) | γ_0 | q_0 | G_0 (GPa) | G_0' | η_{s0} |
|-----------|---|---------------------------------|-------------------|------------|------------------------|-------------|------------|----------------|------------|-------------|
| Pyrope | Mg ₃ Al ₂ Si ₃ O ₁₂ | <i>113.08</i> | <i>171</i> | 4.2 | 804^a | <i>1.01</i> | <i>1.4</i> | <i>94</i> | <i>1.4</i> | 1.2 |
| Majorite | Mg ₄ Si ₄ O ₁₂ | 113.97 | 160 | 5.6 | 779^a | <i>0.98</i> | <i>1.5</i> | 86 | <i>1.4</i> | 1.4 |
| Almandine | Fe ₃ Al ₂ Si ₃ O ₁₂ | <i>115.43</i> | 175 | 3.7 | <i>741</i> | <i>1.06</i> | <i>1.4</i> | <i>96</i> | 1.1 | <i>2.1</i> |
| Grossular | Ca ₃ Al ₂ Si ₃ O ₁₂ | <i>125.12</i> | <i>167</i> | <i>3.9</i> | <i>823</i> | <i>1.05</i> | <i>1.9</i> | <i>109</i> | <i>1.2</i> | <i>2.4</i> |

^a Calculated via equation (5.7); values in italics are taken from Stixrude and Lithgow-Bertelloni (2011)

The resulting sound velocities calculated from the modified garnet end member thermodynamic properties are in good agreement with the measured values (Figure 6.2-2), indicating that ideal solid solution behavior is indeed a valid assumption for these garnet solid solutions, once a fictive “cubic” majorite end-member is considered.

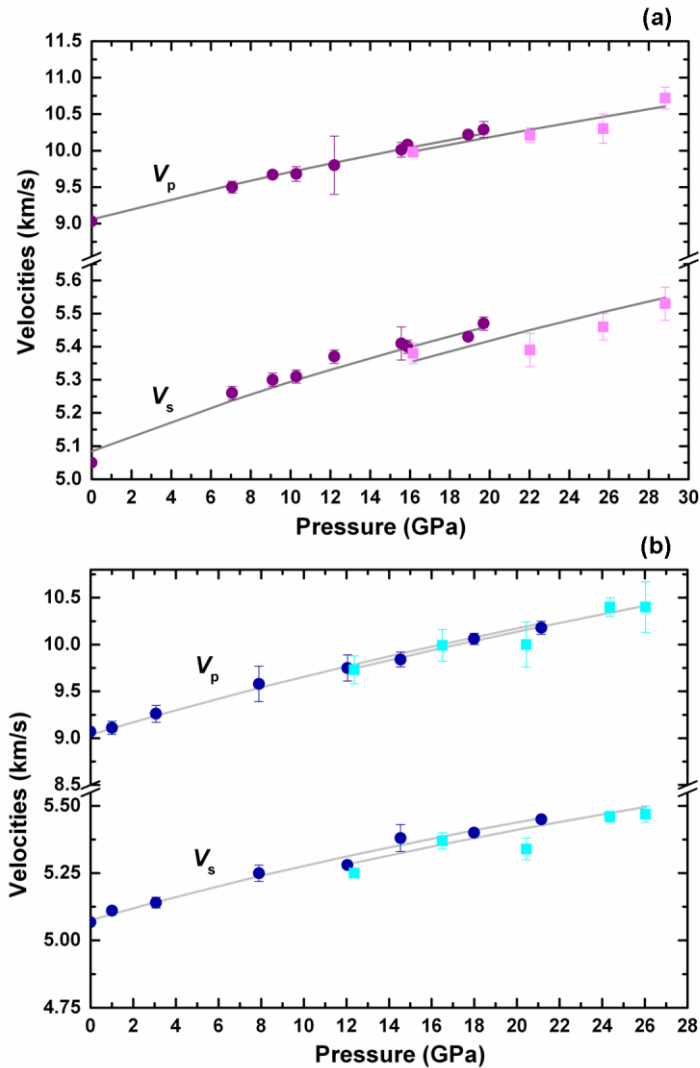


Figure 6.2-2. Compressional and shear wave velocities of (a) $Py_{76}Mj_{24}$ (Mj) measured at high pressure at room temperature (purple) and at high pressure and at 558K (magenta) (b) of $Py_{78}Mj_{16}Al_6$ (Fe-Mj) measured at high pressure at room temperature (dark blue) and at high pressure and at 470K (light blue). Solid curves are calculated from the thermo-elastic model parameters for garnet end members reported in Table 6.2-1.

The sound velocities of Mj and Fe-Mj samples are calculated at different temperatures at 20 GPa using the parameters reported in Table 6.1-1 as well as from the end-member properties reported in Table 6.2-1 in Figure 6.2-3.

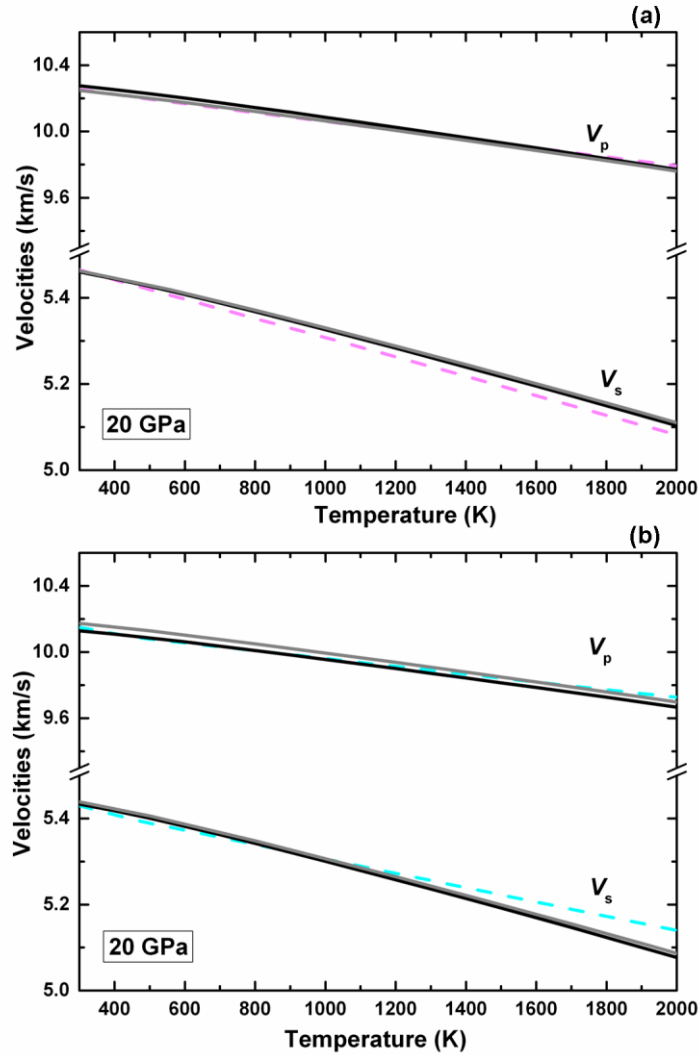


Figure 6.2-3. Variation of sound velocities of (a) Mj and (b) Fe-Mj as a function of temperature at 20 GPa. The solid black lines indicate the velocities derived from the thermo-elastic model parameters given in Table 6.1-1 whereas grey lines correspond to those derived from the parameters reported in Table 6.2-1. Dotted lines are velocities extrapolated using the elastic parameters reported in Chapter 3.

Both approaches result in an identical non-linear behavior for both samples as a function of temperature, whereas they differ from the acoustic velocities extrapolated using the elastic parameters reported in Chapter 3, derived from fitting a high-temperature Birch Murnaghan EoS. The latter in fact display a linear behavior as a function of temperature (Figure 6.2-3), simply due to the bulk and shear moduli being extrapolated with an assumed linear temperature dependence. Extrapolation with a more theoretically justified thermal model yields clear nonlinear dependences.

A nonlinear dependence of acoustic velocities with temperature was reported for a polycrystalline majoritic garnet sample from ultrasonic experiments performed by Irifune et al. (2008) up to 1673 K and ~18 GPa. The authors reported that such behavior was clearly very different from the behavior of majoritic garnet when extrapolated using a linear dependence of elastic moduli with temperature. However, the thermo-elastic model based on the Mie-Grüneisen equation of state with a Debye approximation of the internal energy (Section 6.1) is clearly able to reproduce the non-linear behavior of the sound velocities even when fitted to temperature data collected below 600 K. This is clearly illustrate in Figure 6.2-4, where acoustic velocities for a multi-component garnet identical in composition to that reported by Irifune et al. (2008) ($\text{Py}_{23}\text{Mj}_{50}\text{Al}_6\text{Gr}_{21}$) are calculated using the thermo-elastic model (Table 6.2-1). The calculation was performed at 20 GPa and temperatures up to 2000 K. The resulting shear wave velocity V_s is in excellent agreement with the value reported by Irifune et al. (2008) (Figure 6.2-4), clearly demonstrating the power of extrapolation using a more theoretically justified equation of state.

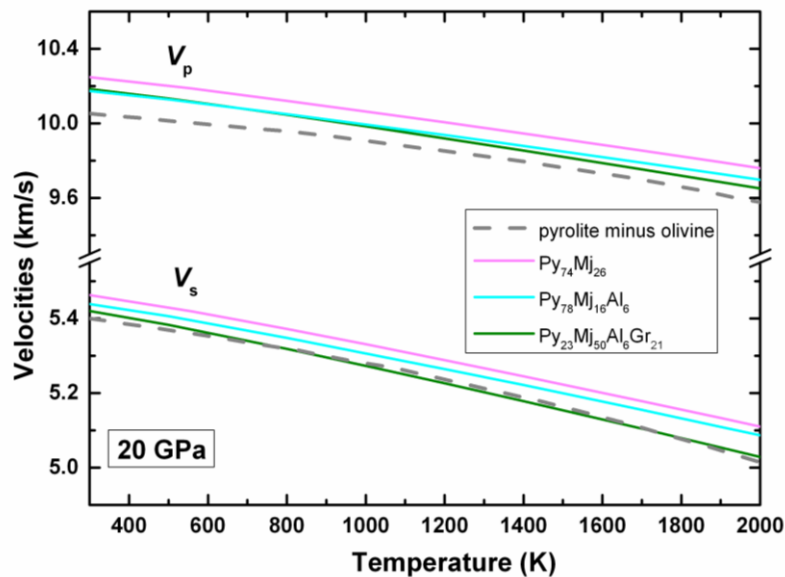


Figure 6.2-4. Variation of sound velocities of different majoritic garnets as a function of temperature at 20 GPa. Solid lines: velocities derived from the thermodynamic parameters of garnet end-members (Table 6.2-1). Dotted lines are velocities reported by Irifune et al. (2008).

Note however, that the compressional velocities determined by Irifune et al. (2008) are smaller than those modelled in this study for the same pyrolite composition garnet. This significant drop, ~2 km/s, between V_p determined for garnets measured in this study and the sample measured by Irifune et al. (2008) is unlikely to be caused by differences in

composition. Although garnets refined in this study do not include a grossular component this was included using literature data (Table 6.2-1) and a recent study indicates relatively small differences in elastic properties when Ca is added to majoritic garnet (Sanchez-Valle et al., 2011). For the compressional velocity data of Irifune et al. (2008) to be correct Ca would have to have a very strong non-linear influence on the garnet solid solution bulk modulus which has not been previously reported (Sanchez-Valle et al. 2011).

6.3 Model for the transition zone and uppermost lower mantle

The elastic properties of garnets and the NAL phase determined in this study (see Tables 5.3-2 and 6.2-1) were used along with additional literature data (summarized in Table 6.3-1) to calculate seismic velocities for pyrolite, harzburgite and MORB bulk compositions at the base of the transition zone and uppermost lower mantle, in the depth range between 480 and 780 km.

Table 6.3-1. Thermo-elastic parameters of mantle components used for calculating the sound wave velocities and densities as a function of pressure and temperature in the transition zone and lower mantle.

| Phase | Formula | V_0 (cm ³ /mol) | K_{T0} (GPa) | K'_{T0} | θ_0 (K) | γ_0 | q_0 | G_0 (GPa) | G_0' | η_{s0} |
|---------------|----------------------------------|---------------------------------|-------------------|-----------|-------------------|------------|-------|----------------|--------|-------------|
| Wadsleyite | Mg ₂ SiO ₄ | 40.52 | 169 | 4.3 | 853 | 1.21 | 2 | 112 | 1.4 | 2.6 |
| Wadsleyite | Fe ₂ SiO ₄ | 42.80 | 169 | 4.3 | 719 | 1.21 | 2 | 72 | 1.4 | 1.1 |
| Ringwoodite | Mg ₂ SiO ₄ | 39.49 | 185 | 4.2 | 891 | 1.11 | 2.4 | 123 | 1.4 | 2.3 |
| Ringwoodite | Fe ₂ SiO ₄ | 41.86 | 213 | 4.2 | 652 | 1.26 | 2.4 | 92 | 1.4 | 1.8 |
| Ca-Perovskite | CaSiO ₃ | 27.45 | 236 | 3.9 | 802 | 1.89 | 0.9 | 157 | 2.2 | 1.3 |
| Stishovite | SiO ₂ | 14.02 | 314 | 3.8 | 1055 | 1.35 | 2.9 | 220 | 1.9 | 4.6 |
| Perovskite | MgSiO ₃ | 24.45 | 250.3 | 4.02 | 901 | 1.44 | 1.4 | 176.8 | 1.75 | 2.6 |
| Perovskite | FeSiO ₃ | 25.40 | 250.3 | 4.02 | 765 | 1.44 | 1.4 | 162.8 | 1.5 | 1.9 |
| Perovskite | FeAlO ₃ | 25.40 | 220 | 4.1 | 765 | 1.44 | 1.4 | 132 | 1.7 | 1.9 |
| Perovskite | AlAlO ₃ | 25.49 | 228 | 4.1 | 886 | 1.44 | 1.4 | 157 | 1.7 | 2.8 |
| Periclase | MgO | 11.24 | 161 | 3.9 | 772 | 1.48 | 1.6 | 130 | 2.3 | 2.3 |
| Wüstite | FeO | 12.26 | 149 | 4.9 | 454 | 1.54 | 1.6 | 47 | 0.7 | 0.6 |

values in italics are taken from Stixrude and Lithgow-Bertelloni (2011) and are in good agreement with recent experimental measurements; values for perovskite are from Boffa Ballaran et al. (2012); Chantel et al. (2012); Frost et al. (2014)

Mineral phase relations and compositions were determined along an adiabat with a potential temperature of 1673 K using a previously described thermodynamic model, (Saikia et al., 2008; Frost, 2003; Frost and Dolejs, 2007; Nakajima et al., 2012), that is based on a range of experimental data on phase relations.

6.3.1 Pyrolite phase relations

Phase relations for the pyrolite bulk composition (Table 1.1-1.) were determined from 480 to 700 km and are reported in Appendix A2. Calculations were not performed at lower pressures due to the absence of sufficient data on the clinopyroxene mineral properties. At 480 km a pyrolite composition is calculated to contain 58.5 vol% wadsleyite and 41.5 vol% majoritic garnet, which equates to 80 mol% $(\text{Mg}_{0.9}\text{Fe}_{0.1})_2\text{SiO}_4$ and 20 mol% $(\text{Py}_{14}\text{Mj}_{56}\text{Al}_8\text{Gr}_{21})$. At approximately 540 km, wadsleyite undergoes a phase transition to ringwoodite over a depth interval of approximately 20 km. Between 480-620 km the garnet composition and proportion remain constant apart from small changes in Fe-Mg partitioning between wadsleyite and ringwoodite. However at 620 km CaSiO_3 perovskite (Ca-Pv) starts to exsolve from garnet, with the volume proportion of Ca-Pv gradually increasing with depth at the expense of the grossular component of garnet (Saikia et al., 2008). As a consequence, the garnet composition loses Ca but also becomes less majoritic (see Appendix A2). The exsolution reaction is inherently non-linear with pressure (Saikia et al., 2008). The gradual increase of Ca-Pv and the consequent compositional variations in garnet are explicitly taken into account by the model. By the base of the transition zone the pyrolite mineralogy comprises 80 mol% ringwoodite $(\text{Mg}_{0.9}\text{Fe}_{0.1})_2\text{SiO}_4$, 17 mol% garnet $(\text{Py}_{34}\text{Mj}_{51}\text{Al}_9\text{Gr}_4)$ and 3 mol% CaSiO_3 perovskite.

At the top of the lower mantle (~23.5 GPa), ringwoodite breaks down to an assemblage of $(\text{Mg,Fe})(\text{Si,Al})\text{O}_3$ perovskite and $(\text{Mg,Fe})\text{O}$ ferropericlasite. As a result the mineralogy comprises 2.8 mol% garnet, 65.2 mol% $(\text{Mg,Fe})(\text{Si,Al})\text{O}_3$ perovskite, 1.3 mol% CaSiO_3 perovskite and 30.7 mol% $(\text{Mg,Fe})\text{O}$. The perovskite composition at the top of the lower mantle is described by the end member proportions 89 mol % MgSiO_3 , 4 mol % FeSiO_3 , 5 mol % FeAlO_3 and 1 mol % AlAlO_3 . With increasing pressure both garnet and $(\text{Mg,Fe})(\text{Si,Al})\text{O}_3$ perovskite become more Al-rich until the complete transformation of garnet to perovskite at 760 km (see Appendix A2).

6.3.2 MORB composition phase relations

In contrast to pyrolite, a MORB composition (Table 1.1-1.) in the mantle transition zone is composed almost entirely of garnet (89 vol%) with additional stishovite (11 vol%), which equates to 50 mol% SiO₂ and 50 mol% (Py₂₄Mj₂₀Al₁₇Gr₃₉). As for pyrolite composition, in the lower transition zone Ca-Pv starts to exsolve from majoritic garnet. Because the Ca content of subducted oceanic crust (MORB) is higher than that of pyrolite, garnet CaSiO₃ saturation should occur at lower pressures, however, this saturation pressure is also a function of the garnet majorite component (Saikia et al., 2008) which is lower in MORB compositions. These two effects act in opposite directions and ensure that the exsolution of CaSiO₃ perovskite from garnet occurs at approximately the same depth for both bulk compositions. With increasing pressure, as CaSiO₃ perovskite exsolves, the garnet also becomes more Al-rich. However, because MORB composition garnets are initially less majoritic, the garnet Al/Si ratio reaches that of pyrope (i.e., Al/Si = 2/3), above 23 GPa. At these conditions the exsolution of Ca-perovskite requires the formation of an additional phase (i.e. the NAL phase) in order to accommodate the excess Al from the breakdown of the Ca₃Al₂Si₃O₁₂ garnet component. As reported by Saikia et al. (2008), the formation of the NAL phase is controlled by the garnet Al/Si ratio, as it should only form at pressures where garnet has obtained the pyrope stoichiometry as a result of Ca-perovskite exsolution. The presence of Na in NAL, however, could stabilize this phase in the presence of garnet with Al contents slightly below 2 formula units, as previously observed (Hirose and Fei, 2002; Litasov and Ohtani, 2005). This effect is not accounted for in the model, but should be minor. The gradual increase of Ca-Pv at the expenses of majoritic garnet and its compositional variations with pressure (see Appendix A2) as well as the formation of the NAL phase (starting from 25 GPa, 697 km) are explicitly considered in this model, seemingly, for the first time.

In the upper part of the lower mantle (720 km) the MORB composition is calculated to comprise 35 mol% garnet (Py₇₀Mj₁Al₂₀Gr₉), 50 mol% stishovite, 2.4 mol% NAL phase and 12.5 mol% CaSiO₃ perovskite. As the transformation into (Mg,Fe)(Al,Si)O₃ perovskite involves only garnet, the stability field of this perovskite is shifted to greater depths with respect to the pyrolite composition. At approximately 766 km the MORB composition comprises 0.9 mol% garnet (Py₇₀Mj₁Al₂₀Gr₉), 60 mol% stishovite, 10.8 mol% NAL phase,

7.6 mol% CaSiO_3 perovskite and 21 mol% $(\text{Mg,Fe})(\text{Al,Si})\text{O}_3$ perovskite. The perovskite composition at these conditions is described by the end member proportions 70 mol % MgSiO_3 and 30 mol % FeAlO_3 .

6.3.3 Harzburgite composition phase relations

Harzburgite phase relations in the transition zone are similar to those of pyrolite, with the main difference being a higher proportion of the $(\text{Fe,Mg})_2\text{SiO}_4$ component. At 480 km the composition is calculated to comprise 81.5 vol% wadsleyite and 18.5 vol% of majoritic garnet, which equates to 92.5 mol% $(\text{Mg}_{0.9}\text{Fe}_{0.1})_2\text{SiO}_4$ and 7.5 mol% $(\text{Mj}_{80}\text{Al}_{12}\text{Gr}_8)$. Phase transformations are similar to those in pyrolite although due to the low Ca content the exsolution of CaSiO_3 is almost insignificant and the low Al content results in a more majorite rich garnet. In the lower mantle, harzburgite is composed of 73 vol% (56.4 mol%) $(\text{Mg,Fe})(\text{Al,Si})\text{O}_3$ perovskite, 25 vol% (43.4 mol%) $(\text{Mg}_{0.87}\text{Fe}_{0.13})$ ferropericlase and 1.4 vol% (0.24 mol%) CaSiO_3 perovskite.

6.3.4 Calculated acoustic velocities compared with reference models

In Figure 6.3-1 V_s and V_p calculated for the three bulk compositions are compared with the seismic reference models PREM and AK135.

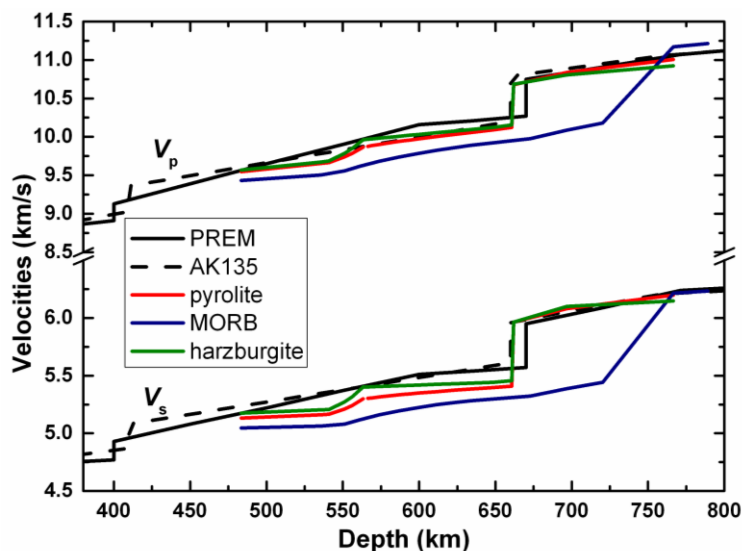


Figure 6.3-1. Sound velocities for pyrolite (red) harzburgite (green) and MORB (blue) compositions in the transition zone and uppermost lower mantle. The solid and dashed black curves show PREM and AK135 seismic reference models, respectively.

While the pyrolite model is in agreement at least with AK135 in terms of V_p , there is a consistent negative deviation for V_s , by ~ 0.2 km/s, between pyrolite and both reference models over the 150 km of the base of the transition zone. Garnet elastic properties are the main reason for this deviation as both ringwoodite and CaSiO_3 -perovskite display velocities which are above both reference models at these conditions. Only garnet brings the bulk velocities below the seismic models. While some deviation from reference models may be expected in detail, on average one would expect negative deviations to be balanced by local positive deviations (Cammarano et al., 2005) if the mineral model is correct. The good agreement between pyrolite and both reference models in the lower mantle means that negative deviations at the base of the transition zone are not balanced by positive deviations in the lower mantle.

Irifune et al. (2008) also proposed that estimated velocities for pyrolite would be lower than reference models at approximately 575 km, but suggested that the subsequent exsolution of CaSiO_3 -rich perovskite from the garnet would alleviate this discrepancy towards the base of the transition zone. Sinogeikin and Bass (2002a) similarly argued that such exsolution would raise the velocity gradient. In this study, the gradual formation of CaSiO_3 -rich perovskite and the compositional variations in garnet were taken into account. A very slight increase in the velocity gradient for the pyrolite model occurs above 570 km due to CaSiO_3 exsolution. Without this exsolution the pyrolite velocities would be similar to the gradient for

harzburgite. Although shear wave properties of CaSiO_3 perovskite are poorly constrained, the G_0 used in the current model (Karki and Crain, 1998) is at the very high limit of recent theoretical studies and is significantly higher than all experimental estimates (Kudo et al., 2012). Therefore it seems unlikely that the V_s for CaSiO_3 perovskite is significantly underestimated, in fact the contrary seems more likely. It would therefore seem that pyrolite along a 1673 K adiabat provides a poor match to seismic reference models at the base of the transition zone.

While other bulk compositions have been proposed for the transition zone, such as piclogite (Bass and Anderson, 1984; Anderson and Bass, 1986) it can be seen that increasing the basaltic component of a composition cannot raise V_s to levels compatible with the reference models. For the MORB composition the exsolution of CaSiO_3 perovskite can be clearly seen to cause an increase in gradient above 550 km. While the resulting gradient is closer to the reference models, the absolute values remain at least 0.3 km/s below both reference models throughout the base of the transition zone.

A number of other effects that could in principal cause differences between mineral and seismic models are also likely to only lower calculated mineral velocities further. Anelastic effects that cause dispersion and potential significant variations of mineral velocities as a function of acoustic wavelength, would only lower velocities of mineral models that accounted for this effect. Similarly the presence of minor defects such as those caused by the presence of dissolved OH^- in minerals should also only lower velocities (Jacobsen, 2006).

If subducted material were to accumulate at the base of the transition zone it is possible that a significant portion of the material in this regions is composed of melt depleted harzburgite. As shown in Figure 6.3-1, however, depleting pyrolite in this way and increasing the component of the $(\text{Fe,Mg})_2\text{SiO}_4$ phase raises velocities but they still fall below the reference models.

One of the few remaining plausible explanations for the deviation between mineral and seismic models at the base of the transition zone would be if the average mantle temperature over this depth interval was below the 1673 K adiabat. While mantle adiabatic temperatures determined from erupted basalt melt compositions vary by approximately $\pm 150^\circ$, (Lee et al., 2009) in order for the pyrolite model to match the seismic model at the base of the transition

zone, it can be estimated that temperatures would need to be 600° lower. This would place mantle temperatures far outside of the range of adiabatic temperature estimates from the surface or from temperature estimates based on the depth of the 410 km discontinuity (Frost, 2008).

Saikia et al. (2008) noted, however, that if the 520 km seismic discontinuity is associated with the wadsleyite to ringwoodite transformation, then it also occurs at a depth that implies lower than expected average mantle temperatures. This can be seen in Figure 6.3-1, where the transformation along a 1673 K adiabat occurs at 550 km, and only if temperatures were ~300 K lower would the transition occur at 520 km. Saikia et al. (2008) proposed that the observation might be explained if subducting slabs stagnate at the base of the transition zone and flatten out to form significant lateral cold heterogeneities. Some tomographic models (e.g. Kárason and van der Hilst, 2000) appear to clearly indicate that such heterogeneities exist. As temperatures in the center of such slabs could be easily 600 K below the average mantle, then they could drag down average mantle temperatures at these depths, if the lateral anomalies were large enough. Furthermore it is possible that a significant proportion of this material will be of near harzburgite composition. It can be estimated that for harzburgite mineral model velocities to match seismic reference models at the base of the transition zone, temperatures would have to be only 200 K below the 1673 K adiabat. If such global horizontal anomalies exist, this average reduction in temperature may be plausible and would be also consistent with the 520 km seismic discontinuity being caused by the wadsleyite to ringwoodite transformation.

A further issue that needs to be investigated is that the mineral akimotoite would be expected to form in both harzburgite and pyrolite compositions if temperatures at the base of the transition zone were several hundred degrees lower than the 1673 K adiabat. The elastic properties of akimotoite are poorly explored and no single crystal data exist on the elastic tensor. Similarly only theoretical calculations exist on the pressure and temperature dependent properties. The shear modulus of akimotoite is expected to be greater than that of garnet but possibly below that of perovskite (Stixrude and Lithgow-Bertelloni, 2011), and its presence may well help to explain the discrepancy in velocities at the base of the transition zone.

6.3.5 Density differences at the base of the transition zone/top of the lower mantle

Density variations of pyrolite, harzburgite, and MORB compositions calculated based on the P - V - T EoS of the different constituent mineral phases and their respective proportions are reported in Figure 6.3-2 along with density profiles from PREM and AK135.

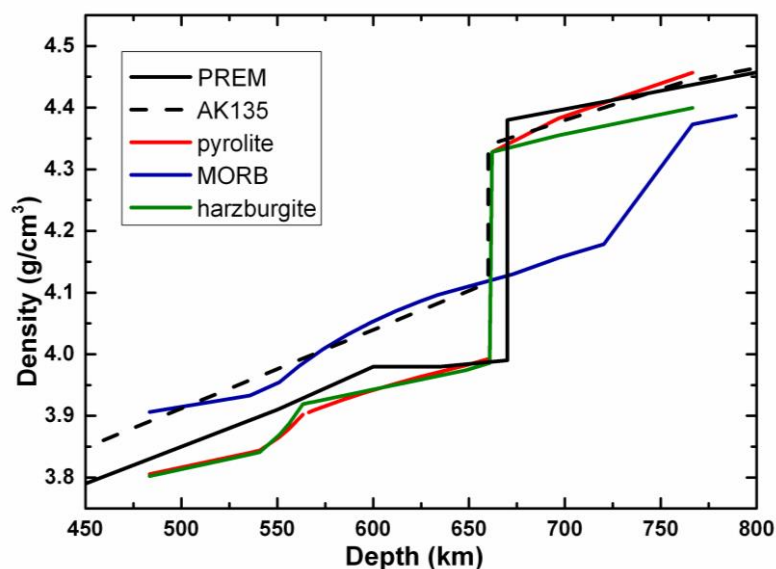


Figure 6.3-2. Density relation as a function of depth for pyrolite (red) harzburgite (green) and MORB (blue) compositions in the transition zone and uppermost lower mantle. The solid and dashed black curves show PREM and AK135 seismic reference models, respectively.

As reported in Chapter 1, the fate of subducted slabs at the 660 km discontinuity has been widely discussed in recent years from both a geophysical and geochemical perspective (e.g. Fukao and Obayashi, 2013). Recent global tomography studies (see Section 1.2) indicate that some slabs penetrate the 660 km boundary into the lower mantle and sink towards the base of the mantle, whereas others slabs appear to be deflected at the boundary, supporting the concept that they encounter significant resistance to entering the lower mantle (e.g. Kárason and van der Hilst, 2000). Numerous studies have focused on the fate of basaltic crust in the deep mantle (see Section 1.1.1). Anderson (1989) and later Irifune and Ringwood (1993), suggested that the basaltic crust becomes less dense than the pyrolitic mantle at the 660 km discontinuity, being thus trapped during subduction to form a “perched eclogite layer”. Recent studies, however, have proposed that MORB remains denser than the average lower mantle and can ultimately reach the core-mantle boundary (Ono et al., 2005; Hirose et al., 2005; Ricolleau et al., 2010). While the slab thermal anomaly is the main driving force for subduction, buoyancy driven by chemical differences may be an important issue in stagnation

and in the ultimate fate of chemical heterogeneities once they have heated up to near average mantle temperatures. If slabs stagnate and then gradually heat up at the base of the transition zone buoyancy forces may lead to advection or result in a global accumulation of certain chemical heterogeneities near 660 km.

The density relations determined in this study (Figure 6.3-2) show that MORB is denser than the reference models throughout the transition zone. If slabs stagnate above 660 km and heat up, this implies that MORB material will have a tendency to remain at the base of the transition zone. It can also be seen that regardless of thermal buoyancy effects, the greater depth of the perovskite transformation in MORB leaves the composition buoyant with respect to the lower mantle. The NAL phase, which forms in MORB at 650 km, does not significantly contribute to an increase in density at this depth.

In the deeper lower mantle at depths below 750 km the MORB composition is less dense than pyrolyte or the reference models. Here the presence of the NAL phase has an important influence on the density as it is the only phase within the MORB composition that lies below the density of the reference models. It is possible that the buoyancy imparted on MORB material in the top of the lower mantle due essentially to the presence of NAL might also cause basaltic material to accumulate there.

6.3.6 Density and velocity changes at the NAL to CF transition

The density of NAL as a function of pressure is compared with other mineral phases in the lower mantle as well as with those of garnets in Figure 6.3-3. As stated above, NAL has a lower density compared to other phases of the lower mantle such as Mg-perovskite and calcium ferrite type aluminum phase (CF).

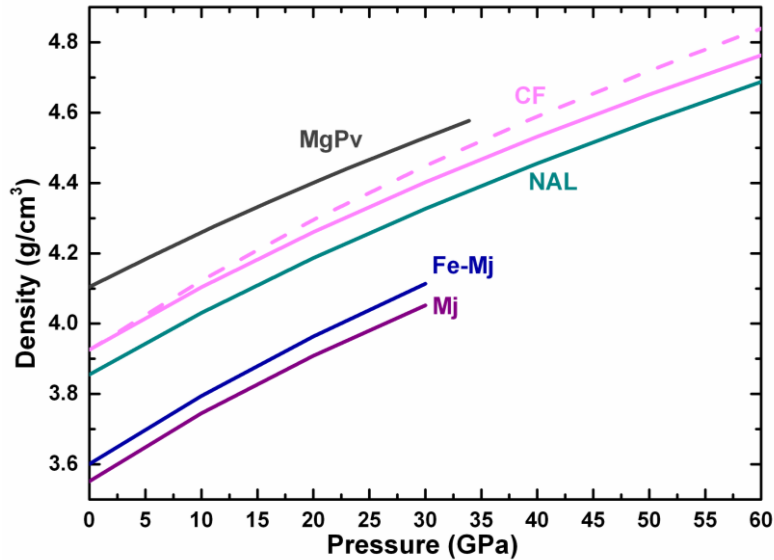


Figure 6.3-3. Density relation as a function of pressure for typical lower mantle minerals. Densities of garnets are also shown for comparison. Data for garnets and NAL phase are taken from the equation of state model described in this study. Data on Mg-perovskite are from Frost et al. (2014). CF data are calculated as described in the text.

NAL and CF phases forming within a MORB composition are generally well described in the compositional range between NaAlSiO_4 - MgAl_2O_4 . NAL is reported to transform to CF at pressures corresponding to ~ 1000 km (~ 40 GPa) (Kawai and Tsuchiya, 2012). Imada et al. (2012) reported a density increase of 2.1 % across the transition from NAL to CF in a system (40% NaAlSiO_4 - 60% MgAl_2O_4). According to Dai et al. (2013) such a phase transition results in a 2.5 % shear wave velocity increase whereas Kawai and Tsuchiya (2012) argued that NAL and CF phases with compositions 33% NaAlSiO_4 - 67% MgAl_2O_4 have comparable shear wave velocities producing less than 1 % velocity difference across the phase transition.

To model the velocity and density changes across the phase transition, a model must be determined to describe the elasticity of the CF phase for a similar bulk composition based on previous theoretical and experimental studies. The composition of the NAL phase determined in this study can be described as 45 mol% NaAlSiO_4 - 55 mol% MgAl_2O_4 . The elastic properties of CF, with the same composition as the NAL phase investigated here, were calculated from NaAlSiO_4 and MgAl_2O_4 end-members according to the procedure described for garnets in sections 6.1 and 6.2.

The elastic parameters for the CF end-members are summarized in Table 6.4-1. The sound velocities of CF were first calculated using the end-member values taken from Stixrude and Lithgow-Bertelloni (2011) reported in italics in Table 6.4-1. To test whether the velocities for CF can be accurately modeled from these end-members, velocities for CF with the composition (33% NaAlSiO₄ - 67% MgAl₂O₄) reported by Kawai and Tsuchiya (2012) were then calculated. The modeled velocities for both CF compositions are reported in Figure 6.3-4 and are compared to the calculated velocities of Kawai and Tsuchiya (2012).

Table 6.4-1. EoS parameters of Ca-Ferrite (CF)

| Phase | Formula | V_0 (cm ³ /mol) | K_{T0} (GPa) | K'_{T0} | θ_0 (K) | γ_0 | q_0 | G_0 (GPa) | G_0' | η_{s0} |
|------------|----------------------|---------------------------------|-------------------|------------|-------------------|-------------|----------|----------------|------------|-------------|
| Ca-ferrite | MgAlAlO ₄ | <i>36.18</i> | <i>211</i> | <i>4.1</i> | <i>838</i> | <i>1.31</i> | <i>1</i> | <i>130</i> | <i>1.8</i> | <i>2.1</i> |
| Ca-ferrite | NaAlSiO ₄ | <i>36.27</i> | 197 | 4.5 | <i>812</i> | <i>1.17</i> | <i>1</i> | 142 | 2.2 | <i>1.6</i> |
| Ca-ferrite | MgAlAlO ₄ | <i>36.18</i> | <i>211</i> | <i>4.1</i> | <i>838</i> | <i>1.31</i> | <i>1</i> | <i>130</i> | <i>1.8</i> | <i>2.1</i> |
| Ca-ferrite | NaAlSiO ₄ | <i>36.27</i> | <i>158</i> | <i>4.3</i> | <i>812</i> | <i>1.17</i> | <i>1</i> | <i>121</i> | <i>2.1</i> | <i>1.6</i> |

values in italics are taken from Stixrude and Lithgow-Bertelloni (2011); other values are from Kawai and Tsuchiya (2010) and Mookherjee (2011)

As shown in Figure 6.3-4, the modeled velocities are significantly lower than those reported by Kawai and Tsuchiya (2012) from theoretical calculations. The sound velocities were then refitted using values for the NaAlSiO₄ end-member reported by Kawai and Tsuchiya (2010) and Mookherjee (2011). In this case, the calculated velocities are in excellent agreement with the calculations Kawai and Tsuchiya (2012) (Figure 6.3-4).

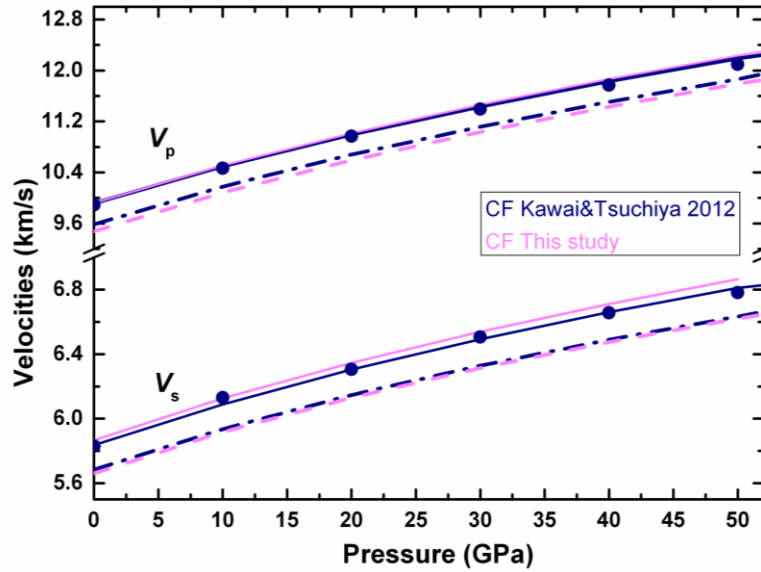


Figure 6.3-4. Compressional and shear wave velocities of CF (33% NaAlSiO_4 - 67% MgAl_2O_4) calculated by Kawai and Tsuchiya (2012) as a function of pressure. Solid curves are velocities calculated from the thermo-elastic parameters from CF end-member reported in Table 6.4-1 using data for NaAlSiO_4 reported by Kawai and Tsuchiya (2010) and Mookherjee (2011). Dashed lines are calculated using data reported in Stixrude and Lithgow-Bertelloni (2011). Blue lines: CF with composition reported by Kawai and Tsuchiya (2012); Magenta: CF with the same composition as the NAL phase determined in this study (55% NaAlSiO_4 - 45% MgAl_2O_4).

The discrepancy between the two models gives rise to different conclusions when considering the density and velocity differences across the transition from NAL to CF. When NAL transforms to CF, the density increase will be larger if one considers the density of CF obtained from Stixrude and Lithgow-Bertelloni (2011) (Figure 6.3-3). However, it is clear that the density of MORB would increase as a result of this transition to values that are much closer to those of pyrolite in the lower mantle, beyond 1000 km. This would likely bring the narrow window where a MORB composition would be less dense in the lower mantle to an end.

If the CF data of Stixrude and Lithgow-Bertelloni (2011) are employed, however, V_p and V_s for CF will be lower than for NAL across the transition (Figure 6.3-5), which seems unlikely. On the other hand the velocities are indistinguishable between the two phases if one uses the data from Kawai and Tsuchiya (2010) and Mookherjee (2011).

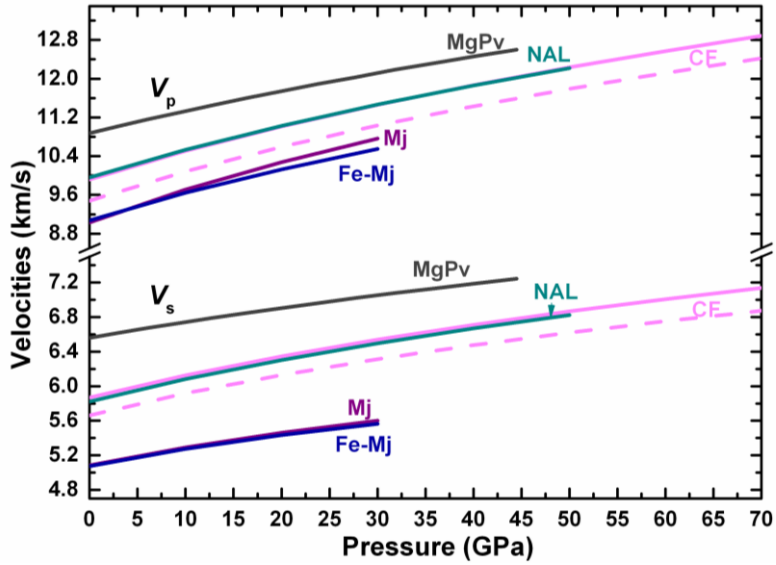


Figure 6.3-5. Variation of the compressional and shear wave velocities as a function of pressure for typical lower mantle minerals. Velocities of garnets are also shown for comparison. Data for garnets and NAL phase are taken from the equation of state model determined in this study. Data on Mg-perovskite are from Frost et al. (2014). CF data are calculated as described in the text.

The density and velocity results obtained in this study, underline the importance of NAL as a transitional phase between garnet and perovskite in the lower mantle. The lower density of this phase may play a role in the buoyancy of subducted slabs and on the density of MORB entering the lower mantle. Therefore, the relative stability of NAL and CF phases are important and any attempt to draw conclusions about the seismic signature of deeply subducted crust must take these phases into account.

7. Conclusions and future perspectives

The work in this thesis comprises an essentially experimental study to determine the single crystal elasticity of aluminium rich mineral phases that form in the transition zone and lower mantle in order to interpret seismic observations in terms of chemistry, mineralogy and temperature. From the results obtained in this study the following conclusions can be drawn:

1. In the past, one of the major obstacles to the study of single crystal elastic properties of high-pressure minerals has been the synthesis of large (at least 50 μm) high-quality single crystals for both Brillouin and X-ray measurements. In this work, an optimal methodology for synthesising high-quality single crystals of majoritic garnets and of a NAL phase has been developed. For each mineral, a fine balance between temperature, pressure and flux concentration has been found. Furthermore results show majoritic garnets produced at 17 GPa from hydrous melts at temperatures of 1900°C contain <20 ppm by weight H_2O .

2. Critical to the success of the project were developments in experimental techniques for measurements of elastic properties at high pressures and high temperatures. In the course of this study, the following developments were achieved:

- Brillouin spectra collected within diamond anvil cells at different pressures, temperatures and orientations display typically different signal to noise ratios, depending on the crystal optical quality, its orientation, as well as on laser focusing, sample alignment and the data collection time. The resolution of such spectra will contribute to the uncertainties in the acoustic velocities used to obtain the elastic constants but the propagation of these uncertainties is generally neglected. In this study a method was developed where an empirical calibration curve was constructed for determining the uncertainty of each Brillouin measurement depending on its signal to noise ratio.
- An electrical heater was designed for the piston-cylinder type DAC and used for high-pressures-high-temperature Brillouin and X-ray measurements.
- Temperatures inside the diamond anvil cell are in general determined using a thermocouple. However, the thermocouple has to be carefully placed close to the sample in order to measure the correct temperature inside the cell. To constrain the temperature inside the pressure chamber without relying uniquely on the

thermocouple, an alternative approach that considers the difference in fluorescence shifts of Sm:YAG and ruby as a sensitive temperature sensors has been used. This technique demonstrated clearly that thermocouple estimates can be easily in error by at least 100 K.

3. One of the major sources of uncertainty in high-pressure elasticity experiments is the pressure determination in the DAC. Internal standard materials for which the physical properties change with pressure are normally employed and loaded together with the sample in the pressure chamber. The novelty of this project has been measuring simultaneously density and sound velocities for the same sample at the same conditions allowing accurate determination of the absolute pressure without having to rely on a secondary pressure scale. This avoids systematic errors due to the use of different pressure calibrations. Significant errors are obvious, particularly in the determinations of the pressure derivative of the bulk modulus, when results obtained using absolute techniques are compared with those determined using secondary standards.

4. Garnet mineral elastic properties are critical since they form major components of both mafic and ultramafic rocks in the upper mantle and transition zone, and are in fact the main mineral host for the mantle's complement of Al_2O_3 and CaO throughout these regions. Interpretations of the seismic results for the transition zone are largely affected by differences in the reported values of the pressure derivatives of elastic moduli of the mineral phases, particularly garnet, that constitute this region. Such discrepancies have an effect on not only absolute velocities, but also density at high pressure.

The elastic properties of single crystals of majoritic garnet ($\text{Mg}_{3.24}\text{Al}_{1.53}\text{Si}_{3.23}\text{O}_{12}$ and $\text{Mg}_{3.01}\text{Fe}_{0.17}\text{Al}_{1.68}\text{Si}_{3.15}\text{O}_{12}$) have been experimentally determined as a function of density, temperature and composition under hydrostatic conditions. High pressure and temperature structural refinements using single-crystal X-ray diffraction data in combination with measurements of acoustic velocities provided fundamental insights into the interatomic forces and compression mechanisms controlling garnet elasticity. The incorporation of Fe in the garnet crystal structure clearly affects the elastic properties, with the Fe bearing sample becoming more compressible at higher pressures. Structural refinements indicate that this is due to the different high-pressure responses of the tetrahedral site, which appear slightly more compressible in the Fe-bearing majoritic garnet.

One of the largest differences compared to previous studies was found to be the value of $(\partial K / \partial P)_T$ for Fe-free majoritic garnet obtained in this study, which is larger than all values reported in the literature. Reasons for this discrepancy may reside not only in the different types of material used in previous studies (i.e. powdered vs single crystals samples), but also in the different pressure calibrants and pressure media chosen.

5. At lower mantle conditions experiments indicate that a MORB bulk composition can contain more than 20% of an aluminium rich phase, the nature of which changes with pressure. The lowest pressure Al-rich phase is referred to as NAL (new aluminum phase). Single-crystals of $\text{Na}_{0.41}[\text{Na}_{0.125}\text{Mg}_{0.79}\text{Al}_{0.085}]_2[\text{Al}_{0.79}\text{Si}_{0.21}]_6\text{O}_{12}$ NAL were synthesized at lower mantle conditions with a composition close to that expected to crystallize in a subducted MORB bulk composition. For the first time single-crystal structure refinements and the full elastic tensor of the NAL phase were determined experimentally. The most remarkable feature of the structural refinement reported in this study is the very large Na displacement parameter at the M3 site, which is elongated along the c axis, suggesting dynamic disorder of the Na atoms in the channels along this direction. This large elongation along the c axis has not been observed before since the only previous study used an isotropic displacement parameter, but may radically influence transport properties.

The measured values of the NAL elastic moduli are lower than those obtained from theoretical calculations. On the other hand, the pressure derivative of the shear modulus obtained in this study $(\partial G / \partial P)_T = 1.92(5)$ is higher than those obtained from theoretical calculations. Such discrepancy between experimental and theoretical values may be due to differences in cation distributions among the crystallographic sites.

The shear velocity and shear modulus obtained in this study are higher than those determined in a previous study by means of Brillouin scattering on a powdered sample in the DAC. This is due to the highly anisotropic behaviour of the NAL phase, which was not correctly averaged in the polycrystalline study. Single-crystal data are clearly more reliable than measurements on polycrystalline samples which can be affected by uncertainties in texture, grain size and stress state. Most importantly, these experiments only provide aggregate properties and, therefore, do not give any information on the anisotropy of the sound velocities nor can they constrain the complete elastic tensor of this low symmetry material.

At pressures corresponding to ~1000 km (~40 GPa), NAL is expected to transform to the calcium ferrite type aluminum phase (CF). Based on the previous experimental study of a polycrystalline sample, this phase transition has been predicted to cause a 2.5 % shear wave

velocity increase. The present results on the high pressure elasticity of the NAL phase, however, bring into question such a conclusion and a negligible bulk change in velocity seems more likely. At pressures of the transition, theoretical calculations found that CF is significantly more anisotropic ($AV_p = 11.1\%$; $AV_s = 22.1\%$) than the NAL phase ($AV_p = 9.8\%$; $AV_s = 13.3\%$). Based on the experimental data obtained in this study, the NAL phase has similar compressional wave anisotropy ($AV_p = 9.7\%$) than reported by theoretical calculations whereas displays a lower (2%) shear wave anisotropy ($AV_s = 11.1\%$). The phase transition from the NAL to CF will thus result in a significant change in elastic anisotropy, particularly in the shear wave. Given sufficient texture in the lower mantle such a transition could produce a weak seismic discontinuity if the lattice preferred orientation of the NAL phase was optimally aligned with seismic ray paths.

6. The experimental data gathered in this study were used to derive parameters for a thermo-elastic model. End-member garnet thermo-elastic properties were fitted using the experimental data on solid solutions. Although the fitted data were only collected up to temperatures 600 K, extrapolation of the thermo-elastic model demonstrated excellent agreement with ultrasonic data for complex garnet V_s measurements up to 1673 K. A thermodynamic model was then used to calculate phase proportions for different bulk compositions, which combined with thermo-elastic parameters could be used to calculate seismic wave velocities for these compositions in the mantle. Using this model V_s , V_p and density for pyrolite, harzburgite and MORB bulk compositions were calculated along a 1673 K adiabat between 480 and 780 km. These models were then compared with seismic reference models to draw the following conclusions:

- At the base of the transition zone V_s values calculated for pyrolite, MORB and harzburgite compositions are significantly below seismic reference models. Harzburgite shows the smallest deviation but model values for V_s are still 0.2 km/s lower than seismic models.
- Garnet is the principal cause of low V_s deviations in the calculated models as it is the only phase with V_s determinations that are consistently below reference models. Consequently the MORB composition, which is mainly comprised of garnet, shows the greatest deviation with reference models.

- The most plausible explanation for the deviation in V_s is that temperatures at the base of the transition zone are lower, on average, than a 1673 K adiabat. For a pyrolite model to match seismic reference models, temperatures would have to be 600 K lower, whereas for harzburgite they would have to be 200 K lower.
- Large lateral low-temperature anomalies due to stagnant slabs flattening out at the base of the transition zone might be able to lower average mantle temperatures when the low temperatures of these anomalies are averaged out in the reference models over the entire lateral extent of the mantle. Such subduction anomalies would be expected to contain a large proportion of harzburgite.
- If temperatures are lower than a 1673 K adiabat experiments have indicated that akimotoite could be a potentially important phase in a harzburgitic and even pyrolite compositions, replacing garnet to some extent. Higher velocities expected for akimotoite may then further help to explain the V_s discrepancy.

7. To test this idea, laboratory data on single-crystal elastic properties of akimotoite at pressures and temperatures of the transition zone are of crucial importance. Experimental measurements on the thermo-elastic properties of akimotoite are limited except for recent theoretical simulations. The next step will be to determine the P - V - T EoS and acoustic velocities of single crystals of akimotoite following the experimental procedures described in this thesis. Because akimotoite is also found (theoretically) to be very anisotropic, single-crystal elasticity measurements will provide not only the full elastic tensor of this low symmetry phase but also insights into the high pressure anisotropic behaviour.

8. The density relations determined in this study show that MORB is denser than pyrolitic mantle at the base of the transition zone but less dense than the surrounding mantle at the top of the lower mantle. The low density of MORB in the lower mantle is due to the presence of the NAL phase, which is the only phase with a density significantly lower than reference model densities at these conditions. This may create a window between the base of the transition zone and top of the lower mantle where MORB-type chemical heterogeneities may accumulate once the thermal subduction anomaly has relaxed.

9. At depths of 520-550 km CaSiO_3 perovskite (Ca-Pv) starts to exsolve from majoritic garnet, with the volume of Ca-Pv gradually increasing with depth at the expense of majorite

garnet. CaSiO_3 perovskite (CaPv) is one of the most important components of the Earth's lower mantle comprising approximately 6% and 23% of the volume of a peridotitic mantle and subducted mid ocean ridge basalt (MORB) slab respectively. Constraining its crystal structure and possible phase transitions at realistic pressure and temperature conditions is of crucial importance for understanding the mineralogy of the lower mantle as well as for the interpretation of seismic observations. Despite its important role for lower mantle properties, very few measurements have been performed on Ca-Pv elasticity and those that have are exclusively on polycrystalline materials with the result that only average properties of the tetragonal structured perovskite have been reported. Furthermore, elasticity data at simultaneous high pressures and temperatures on the cubic structured perovskite are still missing. The major hurdle in measuring the single crystal elastic properties of Ca-Pv is that this phase is unquenchable, and it becomes amorphous at room pressure and temperature. A possible experimental approach would be to synthesize crystals of CaSiO_3 in situ using laser heating in the DAC. As in the multianvil a flux agent would be employed such as CaCO_3 or H_2O . Firstly, polycrystalline CaPv could be synthesized in situ at high pressure using a laser heated diamond anvil cell (DAC). After the synthesis, simultaneous X-ray diffraction and Brillouin scattering measurements at HP and HT would be performed in the DAC equipped with an external resistive heater. This approach would provide new insights into the aggregate elastic properties of the cubic CaPv at lower mantle conditions as well as new constraints on the structural phase transition.

10. Finally, the density and velocity results obtained in this study underline the importance of NAL as a transitional phase in terms of density between garnet and perovskite. The intermediate density of this phase appears to play an important role in the buoyancy of MORB heterogeneities above and below the 660 km discontinuity. The density increase across the phase transition from NAL to the CF phase at approximately 1000 km would likely bring the density of MORB heterogeneities close to those of the ambient lower mantle. Therefore, the relative stability of NAL and CF phases are very important and any attempt to draw conclusions about the seismic signature of deeply subducted crust must account for the relative stability of these two phases. Currently only theoretical calculations have examined the elasticity of the CF phase, which therefore should be complemented with experimental measurements at high pressure and temperature.

Acknowledgments

First of all I would like to thank my supervisors Tiziana Boffa Ballaran and Daniel Frost for their support and patience, and for believing and trusting me during my entire work. Thanks for being such special persons, from the professional point of view but mostly for your humanity. I feel very lucky I have had the opportunity to work with you!

Alex Kurnosov, this entire work would have been *IMPOSSIBLE* without you! Thanks for the incredible help during the course of my PhD with the diamond anvil cell, single crystal X-ray diffraction and Brillouion scattering measurements. Thanks for answering the numerous questions I always had and for assisting me with Mathcad operations. Dyma Trots is also acknowledged for his valuable help.

I acknowledge the support of the Bayerischen Eliteförderungsgesetz (BayEFG) and further funding from the DEEP project and DFG.

I would like to thank all the people at the Bayerisches Geoinstitut for helping me during these years, particularly to the administrative and technical staff for making this place special.

A special thank goes to Hans Keppler, Gerd Steinle-Neumann and Tomoo Katsura for their kind support, especially received two years ago.

Geeth Manthilake and Slava Shcheka are thanked for their assistance with multianvil experiments and Florian Heidelberg for help with the SEM and for translating the summary of this thesis. Many thanks also to Luca Ziberna, Mattia Giannini and Elena Bykova for helping during the visits to APS. Kirill Zhuravlev, Sergey Tkachev and Vitali Prakapenka, are also thanked for their help and for setting up the experiments at APS. Leonid Dubrovinsky is also acknowledged for many suggestions and comments regarding my work. Sergio Speziale, Razvan Caracas and Nathalie Bolfan-Casanova are thanked for their help with calculations and measurements presented in this thesis. Michael Carpenter is also acknowledged for giving me the possibility to visit his lab and for the nice time spent in Cambridge.

Thanks to all my friends at BGI who were always there in these years. Particularly to my office mates Esther and Fabian and to the “girls”, Leyla and Michelle, for supporting me in

the last period of my PhD. Girls, thanks for the numerous lunches and dinners together and for the “*Grey’s anatomy*” nights!

Grazie di cuore a Laura ed Enrico per avermi insegnato e aiutato molto dal punto di vista personale e umano.

Alla mia meravigliosa famiglia per avermi sempre sostenuto e motivato in ogni circostanza e per avermi dato l’opportunità di perseguire i miei studi e sogni.

Il grazie più speciale va alla persona più importante nella mia vita, Davide. Semplicemente grazie per essermi sempre stato vicino, per aver sempre creduto in me soprattutto nei momenti più difficili. Assieme ce l’abbiamo fatta! Grazie di tutto!

References

- Agee, C.B. (1998) Phase transformations and seismic structure in the upper mantle and transition zone. In: Ultrahigh-pressure Mineralogy, Hemley, R.J. (ed), Mineralogical Society of America, Reviews in Mineralogy, 37, 165-203.
- Akaogi, M., Ito, E., and Navrotsky, A. (1989) Olivine modified spinel–spinel transitions in the system $\text{Mg}_2\text{SiO}_4\text{–Fe}_2\text{SiO}_4$: calorimetric measurements, thermochemical calculation, and geophysical application. *Journal of Geophysical Research*, 94, 15671-15685.
- Akaogi, M., Hamada, Y., Suzui, T., Kobayashi, M., and Okada, M. (1999). High pressure transitions in the system $\text{MgAl}_2\text{O}_4\text{–CaAl}_2\text{O}_4$: a new hexagonal aluminous phase with implication for the lower mantle. *Physics of the Earth and Planetary Interiors*, 115, 67-77.
- Anderson, D.L. (1989). *Theory of the Earth*. Blackwell, Boston, 366 pp.
- Anderson, D.L. (2007) *New theory of the Earth*, pp. 384. Cambridge University Press.
- Anderson, D.L., and Bass, J.D. (1986) Transition region of the Earth's upper mantle. *Nature*, 320, 321-328.
- Anderson, O.L., and Isaak, G.G. (1995) Elastic constants of mantle minerals at high temperatures. In *Mineral Physics and Crystallography, a handbook of physical constants*, Ahrens, T.J. ed., pp. 64-97, AGU Publications, Washington DC.
- Anderson, O.L, Isaak, D.G, and Yamamoto, S. (1989) Anharmonicity and the equation of state for gold. *Journal of Applied Physics*, 65, 1534-1543.
- Angel, R.J. (2000) Equations of State. In: *High-temperature and high-pressure crystal chemistry*. Reviews in Mineralogy and Geochemistry, Hazen R.M., and Downs R.T. eds. Mineralogical Society of America and Geochemical Society, Washington. 41, 35-39.
- Angel R.J. (2002) EOSFIT V5.2. Crystallography Laboratory. Department of Geosciences, Virginia Tech, USA.
- Angel, R.J. (2003) Automated profile analysis for single-crystal diffraction data. *Journal of Applied Crystallography*. 36, 295-300.
- Angel, R.J., Finger LW, Hazen, R.M, Kanzaki, M, Weidner, D.J, Liebermann, R.C., and Veblen, D.R. (1989) Structure and twinning of single - crystal MgSiO_3 garnet synthesised at 17 GPa and 1800 °C. *American Mineralogist*, 74, 509-512.

- Angel, R.J., Downs, R.T., and Finger, L.W. (2000) High-temperature and high-pressure diffraction. In: High-temperature and high-pressure crystal chemistry. Reviews in Mineralogy and Geochemistry. Hazen, R.M., and Downs, R.T. eds. Mineralogical Society of America and Geochemical Society, Washington. 41, 559-596.
- Angel, R.J., Bujak M., Zhao J., Gatta G.D., and Jacobsen, S.D. (2007) Effective hydrostatic limits of pressure media for high-pressure crystallographic studies. *Journal of Applied Crystallography*, 40, 26-32.
- Angel, R.J., Jackson, J.M., Reichmann, H.J., and Speziale, S. (2009) Elasticity measurements on minerals: a review. *European Journal of Mineralogy*, 21, 525-550.
- Angel, R.J., and Finger, L.W. (2011) SINGLE: A program to control single crystal diffractometers, *Journal of Applied Crystallography*, 44, 247-251, doi:10.1107/S0021889810042305.
- Armbruster, T., Geiger, C.A., and Lager, G.A. (1992) Single-crystal X-ray structure study of synthetic pyrope almandine garnets at 100 and 293K. *American Mineralogist*, 77, 512-521.
- Baroni, S., de Gironcoli, S., Dal Corso, A., and Giannozzi, P. (2001) Phonons and related crystal properties from density-functional perturbation theory. *Reviews in Modern Physics*, 73, 515-562.
- Bass, J.D. (2007) Mineral physics: techniques for measuring high P/T elasticity. In: *Treatise of Geophysics*. Price, G.D., and Schubert, J. eds. Pp. 269-292.
- Bass, J.D., and Anderson, D.L. (1984) Composition of the upper mantle-geophysical tests of 2 petrological models, *Geophysical Research Letters*, 11, 237-240.
- Bass, J.D., and Kanzaki, M. (1990). Elasticity of a majorite-pyrope solid solution. *Geophysical Research Letters* 17: doi: 10.1029/GL017i011p01989.
- Bass, J.D., and Parise, J.B. (2008). Deep Earth and recent developments in mineral physics. *Elements*, 4, 157-163.
- Bass, J.D., Sinogeikin, S.V., and Li, B. (2008) Elastic properties of minerals: a key for understanding the composition and temperature of Earth's interior. *Elements*, 4, 165-170.
- Bina, C.R., Stein, S., Marton, F.C., and van Ark, E.M. (2001) Implications of slab mineralogy for subduction dynamics. *Physics of the Earth and Planetary Interiors*, 127, 51-66.
- Birch, F. (1947) Finite elastic strain of cubic crystals. *Physical Review*, 71, 809-824.
- Birch, F. (1952) Elasticity and constitution of the Earth's interior. *Journal of Geophysical Research*, 57(2), 277-286.

- Boffa Ballaran, T. (2010) Equations of State and Their Applications in Geosciences. In: High-pressure crystallography NATO Science for peace and security series B: physics and biophysics. Boldyreva, E., and Dera, P. eds. Pp. 135-145.
- Boffa Ballaran, T., Kurnosov, A., Glazyrin, K., Frost, D.J., Merlini, M., Hanfland, M., and Caracas, R. (2012) Effect of chemistry on the compressibility of silicate perovskite in the lower mantle. *Earth and Planetary Science Letters*, 333-334, 181-190.
- Boffa Ballaran, T., Kurnosov, A., and Trots, D. (2013) Single-crystal X-ray diffraction at extreme conditions: a review. *High Pressure Research: An International Journal*, 33(3), 453-465, DOI: 10.1080/08957959.2013.834052
- Cammarano, F., Deuss, A., Goes, S., and Giardini, D. (2005). One-dimensional physical reference models for the upper mantle and transition zone: combining seismic and mineral physics constraints. *Journal of Geophysical Research*, 110, B01306, doi:10.1029/2004JB003272.
- Caracas, R., and Banigan, E.J. (2009) Elasticity and Raman spectra of MgAl_2O_4 spinel from density functional perturbation theory. *Physics of the Earth and Planetary Interiors*, 172, 113-121.
- Caracas, R., and Gonze, X. (2010) Lattice dynamics and thermodynamical properties. In Chaplot, S.L, Mittal, R., and Choudhoury, N. Eds., *Thermodynamical Properties of Solids: Experiment and Modelling*, Ch. 8, 291 - 315, WILEY-VCH Verlag, Weinheim.
- Caracas, R., and Bobocoiu, E. (2011) The WURM project – a freely available web-based repository of computed physical data for minerals. *American Mineralogist*, 96, 437-444.
- Chantel, J. (2012) Measurement of elastic properties of silicates at realistic mantle pressures. PhD. Thesis. University of Bayreuth.
- Chantel, J., Frost, D. J., McCammon, C. A., Jing, Z., and Wang, Y., (2012). Acoustic velocities of pure and iron-bearing magnesium silicate perovskite measured to 25 GPa and 1200K. *Geophysical Research Letters*, doi:10.1029/2012GL053075.
- Chen, G., Cooke, J.A., Gwanmesia, G.D., and Liebermann, R.C. (1999) Elastic wave velocities of $\text{Mg}_3\text{Al}_2\text{Si}_3\text{O}_{12}$ -pyrope garnet to 10 GPa. *American Mineralogist*, 84, 384-388.
- Cohen, M.L. (2007) Quantum alchemy. In E. Keinan and I. Schechter, Eds., *Chemistry for the 21st Century*. Chap. 14, pp. 247-270, Wiley-VCH, Berlin.
- Collier, J.D., Helffrich, G.R., and Wood, B.J. (2001). Seismic discontinuities and subduction zones. *Physics of the Earth and Planetary Interiors*, 127, 35-49.

- Conrad, P.G., Zha, C-S, Mao, H-K, and Hemley, R. J. (1999) The high-pressure, single crystal elasticity of pyrope, grossular and andradite. *American Mineralogist*, 84, 374-383.
- Cottaar, S., Heister, T., Rose, I., and Unterborn, C. (2014). BurnMan: A lower mantle mineral physics toolkit. *Geochemistry, Geophysics, Geosystems*, 15, doi: 10.1002/2013GC005122.
- Cummins, H.Z., and Schoen, P.E. (1972). Linear scattering from thermal fluctuations. In 'Laser handbook', Arecchi, F.T., and Schultz-DuBois, E.O. eds. North Holland Publishing Co., Amsterdam.
- Dai, L., Kudo, Y., Hirose, K., Murakami, M., Asahara, Y., Ozawa, H., Ohishi, Y., and Hirao, N. (2013) Sound velocities of $\text{Na}_{0.4}\text{Mg}_{0.6}\text{Al}_{1.6}\text{O}_4$ NAL and CF phases to 73 GPa determined by Brillouin scattering method. *Physics and Chemistry of Minerals*, 40, 195-201.
- Davies, G.F. (1974). Effective elastic-moduli under hydrostatic stress. 1: quasi-harmonic theory, *Journal of Physics and Chemistry of Solids*, 35(11), 1513-1520.
- Dobson, D.P., and Jacobsen, S.D. (2004) The flux growth of magnesium silicate perovskite single crystals. *American Mineralogist*, 89, 807-811.
- Dubrovinskaia, N., and Dubrovinsky, L. (2003) Whole-cell heater for the diamond anvil cell. *Review of Scientific Instruments*, 74, 3433-3437.
- Duffy, T.S. (2014) Crystallography's journey to the deep Earth. *Nature*, 506, 427-429.
- Duffy, T.S., and Anderson, D.L. (1989) Seismic velocities in mantle minerals and the mineralogy of the upper mantle. *Journal of Geophysical Research* 94(B2), 1895-1912.
- Duffy, T.S., and Wang, Y. (1998). Pressure-volume-temperature equations of state. In: *Ultrahigh-pressure mineralogy: physics and chemistry of the Earth's deep interior*, MSA Reviews in Mineralogy. Hemley, R.J. ed. 37, 425-457.
- Dziewonski, A.M., and Anderson, D.L. (1981). Preliminary reference Earth model. *Physics of the Earth and Planetary Interiors*, 25, 297-356.
- Every, A.G. (1980) General closed-form expressions for acoustic waves in elastically anisotropic solids. *Physical Review B*, 22, 1746-1760.
- Farrugia, L.J. (1999) WinGX suite for small-molecule single-crystal crystallography. *Journal of Applied Crystallography*, 32, 837-838.
- Fei, Y. (1995) Thermal expansion. In *Mineral Physical and Crystallography, a handbook of physical constants*, Ahrens, T.J. ed., pp. 64-97, AGU Publications, Washington DC.

- Fei, Y., Li, J., Hirose, K., Minarik, W., Van Orman, J., Sanloup, C., van Westrenen, W., Komabayashi, T., and Funakoshi, K. (2004) A critical evaluation of pressure scales at high temperatures by in situ X-ray diffraction measurements. *Physics of the Earth and Planetary Interiors*, 143-144, 515-526.
- Fei, Y., Ricolleau, A., Frank, M., Mibe, K., Shen, G., and Prakapenka, V. (2007) Toward an internally consistent pressure scale. *Proceedings of the National Academy of Sciences*, 104(22): 9182-9186.
- Frost, D.J. (2003) The structure and sharpness of $(\text{Mg,Fe})_2\text{SiO}_4$ phase transformations in the transition zone. *Earth and Planetary Science Letters*, 216, 313-318.
- Frost, D.J. (2008). The upper mantle and transition zone. *Elements*, 4(3), 171-176.
- Frost, D.J., and Dolejš, D. (2007) Experimental determination of the effect of H_2O on the 410 km discontinuity. *Earth and Planetary Science Letters*, 256(1-2), 182-195.
- Frost, D.J., Poe, B.T., Tronnes, R.G., Liebske, C., Duba, A., and Rubie, D.C. (2004) A new large-volume multianvil system. *Physics of the Earth and Planetary Interiors*. 143-144, 507-514.
- Frost, D.J., Kurnosov, A., Boffa Ballaran, T., Pamato, M., and Chantel, J. (2014) Elasticity measurements on magnesium silicate perovskite and the chemical composition of the lower mantle. *Goldschmidt Abstract* 742.
- Fukao, Y., and Obayashi, M. (2013) Subducted slabs stagnant above, penetrating through, and trapped below the 660 km discontinuity. *Journal of Geophysical Research Solid Earth*, 118, 5920-5938, doi:10.1002/2013JB010466.
- Ganguli, J., Freed, A.M., and Saxena, S.K. (2009). Density profiles of oceanic slabs and surrounding mantle: integrated thermodynamic and thermal modeling, and implications for the fate of slabs at the 660 km discontinuity. *Physics of the Earth and Planetary Interiors*, 172, 257-267.
- Gasparik, T., Tripathi, A., and Parise, J.B. (2000) Structure of a new Al-rich phase, $[\text{K,Na}]_{0.9}[\text{Mg, Fe}]_2[\text{Mg, Fe, Al, Si}]_6\text{O}_{12}$, synthesized at 24 GPa. *American Mineralogist*, 85, 613-618.
- Gonze, X., Beuken, J.-M., Caracas, R., Detraux, F., Fuchs, M., Rignanese, G.-M., Sindic, L., Verstraete, M., Zerah, G., Jollet, F., Torrent, M., Roy, A., Mikami, M., Ghosez, Ph., Raty, J.-Y., and Allan, D.C. (2002) First-principle computation of material properties the ABINIT software project. *Computational Materials Science*, 25, 478-492. [<http://www.abinit.org>]

- Gonze, X., Rignanese, G.-M., and Caracas, R. (2005) First-principles studies of the lattice dynamics of crystals, and related properties. *Zeitschrift für Kristallographie*, 220, 458-472.
- Gonze, X., Amadon, B., Anglade, P.-M., Beuken, J.-M., Bottin, F., Boulanger, P., Bruneval, F., Caliste, D., Caracas, R., Côté, M., Deutsch, T., Genovesi, L., Ghosez, Ph., Giantomassi, M., Goedecker, S., Hamann, D.R., Hermet, P., Jollet, F., Jomard, G., Leroux, S., Mancini, M., Mazevet, S., Oliveira, M.J.T., Onida, G., Pouillon, Y., Rangel, T., Rignanese, G.-M., Sangalli, D., Shaltaf, R., Torrent, M., Verstraete, M.J., Zerah, G., and Zwanziger, J.W. (2009) ABINIT: First-principles approach to material and nanosystem properties. *Computer Physics Communications*, 180, 2582-2615.
- Guignot, N., and Andraut, D. (2004) Equations of state of Na-K-Al host phases and implications for MORB density in the lower mantle. *Physics of the Earth and Planetary Interiors*, 143-144, 107-128.
- Gwanmesia, G.D., Chen, G., and Liebermann, R.C. (1998) Sound velocities in MgSiO₃-garnet to 9 GPa at room temperature. *Geophysical Research Letters*, 25, 4553-4556.
- Gwanmesia, G.D., Zhang, J., Darling, K., Kung, J., Li, B., Wang, L., Neuville, D., and Liebermann, R.C. (2006). Elasticity of polycrystalline pyrope (Mg₃Al₂Si₃O₁₂) to 9 GPa and 1000 °C. *Physics of the Earth and Planetary Interiors*, 155, 179-190.
- Gwanmesia, G.D., Wang, L., Triplett, R., and Liebermann, R.C. (2009) Pressure and temperature dependence of the elasticity of pyrope–majorite [Py₆₀Mj₄₀ and Py₅₀Mj₅₀] garnets solid solution measured by ultrasonic interferometry technique. *Physics of the Earth and Planetary Interiors*, 174, 105-112.
- Hamann, D., Wu, X., Rabe, K.M., and Vanderbilt, D. (2005). Metric tensor formulation of strain in density-functional perturbation theory. *Physical Review B*, 71, 035117.
- Hazen, R.M. and Downs, R.T. (2000). High-pressure and high-temperature crystal chemistry. *Reviews in Mineralogy and Geochemistry*. Mineralogical Society of America and Geochemical Society, Washington. 41.
- Hazen, R.M., Downs, R.T., Conrad, P.G., Finger, L.W., and Gasparik, T. (1994) Comparative compressibilities of majorite-type garnets. *Physics and Chemistry of Minerals* 21, 344-349.
- Heinz, D.L., and Jeanloz, R. (1984) The equation of state of the gold calibration standard. *Journal of Applied Physics*, 55, 885-893.
- Hellfrich, G.R., and Wood, B.J. (2001) The Earth's mantle. *Nature*, 412, 501-507.

- Hess, H.H. (1962) History of Ocean Basins. Petrologic studies: A Volume to Honor A. F. Buddington, Engel, A.E.J., James H.L., and Leonard B.F. eds. New York, Geological Society of America. pp. 599-620
- Hill, R. (1952) The elastic behaviour of a crystalline aggregate. Proceedings of the Physical Society, London, Section A, 65, 349-354.
- Hirose, K. and Fei, Y. (2002) Subsolvus and melting phase relations of basaltic composition in the uppermost lower mantle. *Geochimica Cosmochimica Acta*, 66, 2099-2108.
- Hirose, K., Fei, Y., Ma, Y., and Mao, H-K. (1999). The fate of subducted basaltic crust in the Earth's lower mantle. *Nature*, 397, 53-56.
- Hirose, K., Takafuji, N., Sata, N., and Ohishi, Y. (2005) Phase transition and density of subducted MORB crust in the lower mantle. *Earth and Planetary Science Letters*, 237, 239-251.
- Hoffmann, A.W. (1997) Mantle geochemistry: the message from oceanic volcanism. *Nature*, 385, 219-229.
- Hoffmann, A.W., and White, W.M. (1982). Mantle plumes from ancient oceanic crust. *Earth and Planetary Science Letters*, 57, 421-436.
- Holmes, N.C., Moriarty, J.A, Gathers, G.R, and Nellis, W.J (1989) The equation of state of platinum to 660 GPa (6.6 Mbar). *Journal of Applied Physics*, 66, 2962-2967.
- Holzappel, C., Rubie, D.C., Frost, D.J., and Langenhorst, F. (2005) Fe-Mg interdiffusion in (Mg,Fe)SiO₃ perovskite and lower mantle reequilibration. *Science*, 309, 1707-1710.
- Imada, S., Hirose, K., and Ohishi, Y. (2011) Stabilities of NAL and Ca-ferrite-type phases on the join NaAlSiO₄-MgAl₂O₄ at high pressure. *Physics and Chemistry of Minerals*, 38, 557-560.
- Imada, S., Hirose, K., Komabayashi, T., Suzuki, T., and Ohishi, Y. (2012) Compression of Na_{0.4}Mg_{0.6}Al_{1.6}Si_{0.4}O₄ NAL and Ca-ferrite-type phases. *Physics and Chemistry of Minerals*, 39, 525-530.
- Irifune, T. (1993) Phase transformations in the Earth's mantle and subducting slabs: Implications for their compositions, seismic velocity and density structures and dynamics. *The Island Arc*, 2, 55-71.
- Irifune, T., and Ringwood, A.E. (1987) Phase transformations in a harzburgite composition to 26 GPa: implications for dynamical behaviour of the subducting slab. *Earth and Planetary Science Letters*, 86, 365-376.

- Irifune, T., and Ringwood, A.E. (1993) Phase transformations in subducted ocean crust and buoyancy relationships at depths of 600-800 km in the mantle. *Earth and Planetary Science Letters*, 117, 101-110.
- Irifune, T., Koizumi, T., and Ando, J. (1996) An experimental study of the garnet-perovskite transformation in the system $\text{MgSiO}_3\text{-Mg}_3\text{Al}_2\text{Si}_3\text{O}_{12}$. *Physics of the Earth and Planetary Interiors*, 96, 147-157.
- Irifune, T., and Tsuchiya, T. (2007) Mineralogy of the Earth - Phase transitions and mineralogy of the lower mantle. In: *Treatise on Geophysics 2*, Price, D. ed. Pp: 33-62. Elsevier.
- Irifune, T., Higo, Y., Inoue, T., Kono, Y., Ohfuji, H., and Funakoshi, K. (2008) Sound velocities of majorite garnet and the composition of the mantle transition region. *Nature*, 451, 814-817.
- Ita, J., and Stixrude, L. (1992) Petrology, elasticity, and composition of the mantle transition zone. *Journal of Geophysical Research*. 97(B5), 6849-6866.
- Ito, E. (2007). Theory and practice - Multianvil cells and high-pressure experimental methods. In: *Treatise on Geophysics 2*, Price, D. ed. Pp: 197-230. Elsevier.
- Ito, E., and Weidner, D.J. (1986) Crystal growth of MgSiO_3 perovskite. *Geophysical Research Letters*, 13, 464-466.
- Jacobsen, S.D. (2006) Effect of water on the equation of state of nominally anhydrous minerals. In: *Water in nominally anhydrous minerals*, Keppler, H., and Smyth, J.R. (Eds), *Reviews in Mineralogy and Geochemistry*, 62, Geochemical Society Mineralogical Society of America.
- Jacobsen, S.D., Holl, C.M, Adams, K.A., Fischer, R.A., Martin, E.S., Bina, C.R., Lin, J.F., Prakapenka, V.B., Kubo, A., and Dera, P. (2008) Compression of single-crystal magnesium oxide to 118 GPa and a ruby pressure gauge for helium pressure media. *American Mineralogist*, 93, 1823-1828.
- Jiang, F.M., Speziale, S., and Duffy, T.S. (2004) Single-crystal elasticity of grossular- and almandine-rich garnets to 11 GPa by Brillouin scattering. *Journal of Geophysical Research*, 109 (B10), p. B10210.
- Kantor, I., Prakapenka, V. Kantor, A., Dera, P., Kurnosov, A., Sinogeikin, S., Dubrovinskaia, N., and Dubrovinsky, L. (2012) BX90: A new diamond anvil cell design for X-ray diffraction and optical measurements. *Review of Scientific Instruments*, 83, 125102; doi: 10.1063/1.4768541.

- Kárason, H., and Van der Hilst, R.D. (2000). Constraints on mantle convection from seismic tomography. In: *The History and Dynamics of Global Plate Motion*, Richards, M.R., Gordon, R., and Van der Hilst, R.D. eds. Geophysical Monograph. 121, 277-288.
- Karki, B.B., and Crain, J. (1998). First-principles determination of elastic properties of CaSiO_3 perovskite at lower mantle pressures. *Geophysical Research Letters*, 25(14), 2741-2744.
- Karki, B.B., Stixrude, L., and Wentzcovitch, R.M. (2001). High-pressure elastic properties of major materials of Earth's mantle from first principles. *Reviews of Geophysics*, 39, 507-534.
- Kato, T., and Kumazawa, M. (1985) Garnet phase of MgSiO_3 filling the pyroxene-ilmenite gap at very high temperature. *Nature*, 316, 803-805.
- Kawai, K., and Tsuchiya, T. (2010) Ab initio investigation of high-pressure phase relation and elasticity in the $\text{NaAlSi}_2\text{O}_6$ system. *Geophysical Research Letters*, 37, L17302, doi:10.1029/2012GL044310.
- Kawai, K., and Tsuchiya, T. (2012) Phase stability and elastic properties of the NAL and CF phases in the $\text{NaMg}_2\text{Al}_5\text{SiO}_{12}$ system from first principles. *American Mineralogist*, 97, 305-314.
- Kawai, N., and Endo, S. (1970) The generation of ultrahigh hydrostatic pressure by a split sphere apparatus. *Review of Scientific Instruments*, 41, 425-428.
- Kennett, B.L.N., Engdahl, E.R., and Buland, R. (1995) Constraints on seismic velocities in the Earth from travel times. *Geophysical Journal International*, 122, 108-124.
- Keppler, H., and Frost, D.J. (2005) Introduction to minerals under extreme conditions. In: *Mineral behaviour at extreme conditions*. Miletich, R. Ed. *EMU Notes in Mineralogy*, 7, 1-30.
- Keppler, H., Wiedenbeck, M., and Shcheka, S.S. (2003) Carbon solubility in olivine and the mode of carbon storage in the Earth's mantle. *Nature*, 424, 414-416.
- Kesson, S.E., Fitz Gerald, J.D., and Shelley, J.M. (1994) Mineral chemistry and density of subducted basaltic crust at lower-mantle pressures. *Nature*, 372, 767-769.
- Kesson, S.E., Fitz Gerald, J.D., and Shelley, J.M. (1998) Mineralogy and dynamics of a pyrolite lower mantle. *Nature*, 393, 252-255.
- King, H.E., and Finger, L. (1979) Diffracted beam crystal centering and its application to high pressure crystallography. *Journal of Applied Crystallography*. 12, 374-378.
- Kohn, W., and Sham, L.J. (1965) Self-consistent equations including exchange and correlation effects. *Physical Reviews*, 140, A1133-A1138.

- Kojitani, H., Iwabuchi, T., Kobayashi, M., Miura, H., and Akaogi, M. (2011) Structure refinement of high-pressure hexagonal aluminous phases $K_{1.00}Mg_{2.00}Al_{4.80}Si_{1.15}O_{12}$ and $Na_{1.04}Mg_{1.88}Al_{4.64}Si_{1.32}O_{12}$. *American Mineralogist*, 96, 1248-1253.
- Kudo, Y., Hirose, K., Murakami, M., Asahara, Y., Ozawa, H., Ohishi, Y., and Hirao, N. (2012) Sound velocities measurements of $CaSiO_3$ perovskite to 133 GPa and implications for lowermost mantle seismic anomalies. *Earth and Planetary Science Letters*, 1-7, 349-350.
- Kurnosov, A., Kantor, I., Boffa Ballaran, T., Lindhardt, S., Dubrovinsky, L., Kuznetsov, A., and Zehnder, B.H. (2008) A novel gas-loading system for mechanically closing of various types of diamond anvil cells. *Review of Scientific Instruments*, 79, 045110.
- Lee, C.T.A., Luffi, P., Plank, T., Dalton, H.A., and Leeman, W.P. (2009). Constraints on the depths and temperatures of basaltic magma generation on Earth and other terrestrial planets. *Earth and Planetary Science Letters*, 279, 20-33.
- Ledbetter, H.M. (1973) Estimation of Debye temperatures by averaging elastic coefficients. *Journal of Applied Physics*, 44(4), 1451-1454.
- Li, B., and Liebermann, R.C. (2007) Indoor seismology by probing the Earth's interior by using sound velocity measurements at high pressures and temperatures. *Proceedings of the National Academy of Sciences*, 104, 9145-9150.
- Liebermann, R.C. (2011) Multi-anvil, high pressure apparatus: a half-century of development and progress. *High Pressure Research: An International Journal*, 31, 493-532.
- Litasov, K.D., and Ohtani, E., (2005). Phase relations in hydrous MORB at 18-28GPa: implications for heterogeneity of the lower mantle. *Physics of the Earth and Planetary Interiors*, 150, 239-263.
- Litasov, K., Ohtani, E., Suzuki, A., and Kawazoe, T. (2004) Absence of density crossover between basalt and peridotite in the cold slabs passing through 660 km discontinuity. *Geophysical Research Letters*, 31, L24607, doi:10.1029/2004GL021306.
- Liu, J., Chen, G., Gwanmesia, G.D., and Liebermann, R.C. (2000). Elastic wave velocities of pyrope–majorite garnets ($Py_{62}Mj_{38}$ and $Py_{50}Mj_{50}$) to 9 GPa. *Physics of the Earth and Planetary Interiors*, 120, 153-163.
- Lu, C., Mao, Z., Lin, J-F., Zhuravlev, K.K., Tkachev, S.N., and Prakapenka, V.B. (2013) Elasticity of single-crystal iron-bearing pyrope up to 20 GPa and 750 K. *Earth and Planetary Science Letters* 361, 134-142.
- Mainprice, D. (1990) An efficient Fortran program to calculate seismic anisotropy from the lattice preferred orientation of minerals. *Computers & Geosciences*, 16, 385-393.

- Mainprice, D. (2007). Seismic anisotropy of the deep Earth from a mineral and rock physics perspective. In: *Treatise on Geophysics 2*. Schubert, G. ed. pp: 437-492.
- Mao, H.K., Xu, J., and Bell, P.M. (1986) Calibration of the ruby pressure gauge to 800 kbar under quasi-hydrostatic conditions. *Journal of Geophysical Research*, 91 (B), 4673-4676.
- Martin, R.M. (2003) *Electronic structure. Basic theory and practical methods*. Cambridge University Press. 596 pp.
- Meister, R., and Peselnick, L. (1966) Variational method of determining effective moduli of polycrystals with tetragonal symmetry. *Journal of Applied Physics*, 37, 4121-4125.
- Merli, M., Callegari, A., Cannillo, E., Caucia, F., Leona, M., Oberti, R., and Ungaretti, L. (1995) Crystal-chemical complexity in natural garnets: structural constraints on chemical variability. *European Journal of Mineralogy*, 7, 1239-1249.
- Miletich, R., Allan, D.R., and Kuhs, W.F. (2000) High-pressure single-crystal techniques. In: *High-temperature and high-pressure crystal chemistry. Reviews in Mineralogy and Geochemistry*. Hazen, R.M., and Downs, R.T. Eds. Mineralogical Society of America and Geochemical Society, Washington. 41, 445-519.
- Miletich, R., Hejny, C., Krauss, G., and Ullrich, A. (2005) Diffraction techniques: Shedding light on structural changes at extreme conditions. In: *Mineral behaviour at extreme conditions*. Miletich, R. Ed. *EMU Notes in Mineralogy*, 7, 281-388.
- Miyajima, N., Fujino, K., Funamori, N., Kondo, T., and Yagi, T. (1999) Garnet-perovskite transformation under conditions of the Earth's lower mantle: an analytical electron microscopy study. *Physics of the Earth and Planetary Interiors*, 116, 117-131.
- Miyajima, N., Yagi, T., Hirose, K., Kondo, T., Fujino, K., and Miura, H. (2001) Potential host phase of aluminum and potassium in the Earth's lower mantle. *American Mineralogist*, 86, 740-746.
- Miura, H., Hamada, Y., Suzuki, T., Akaogi, M., Miyajima, N., and Fujino, K. (2000) Crystal structure of $\text{CaMg}_2\text{Al}_6\text{O}_{12}$, a new Al-rich high pressure form. *American Mineralogist*, 85, 1799-1803.
- Monkhorst, H.J., and Pack, J.D. (1976) Special points for Brillouin-zone integrations. *Physical Reviews B*, 13, 5188-5192.
- Mookherjee, M. (2011) Mid-mantle anisotropy: Elasticity of aluminous phases in subducted MORB. *Geophysical Research Letters*, 38, L14302, doi:10.1029/2011GL047923.
- Mookherjee, M., Karki, B.B., Stixrude, L., and Lithgow-Bertelloni, C. (2012) Energetics, equation of state, and elasticity of NAL phase: Potential host for alkali and aluminum

- in the lower mantle. *Geophysical Research Letters*, 39, L19306, doi:10.1029/2012GL053682.
- Morgan, W.J. (1968) Rises, Trenches, Great Faults, and Crustal Block. *Journal of Geophysical Research*, 6, 1959-1982.
- Murakami, M., Hirose, K., Kawamura, K., Sata, N., and Ohishi, Y. (2004) Post-perovskite phase transition in MgSiO_3 . *Science*, 304, 855-858.
- Murakami, M., Sinogeikin, S.V., Litasov, K., Ohtani, E., and Bass, J.D. (2008) Single-crystal elasticity of iron-bearing majorite to 26 GPa: Implications for seismic velocity structure of the mantle transition zone. *Earth and Planetary Science Letters* 274, 339-345.
- Nakajima, Y., Frost, D.J., and Rubie, D.C. (2012) Ferrous iron partitioning between magnesium silicate perovskite and ferropericlaase and the composition of perovskite in the Earth's lower mantle. *Journal of Geophysical Research-Solid Earth*, 117, B08201.
- Nakatsuka, A., Shimokawa, M., Nakayama, N., Ohtaka, O., Arima, H., Okube, M., and Yoshiasa, A. (2011) Static disorders of atoms and experimental determination of Debye temperature in pyrope: Low- and high-temperature single-crystal X-ray diffraction study. *American Mineralogist*, 84, 374-383.
- Nye, J.F. (1985). *Physical properties of crystals: their representation by tensors and matrices*. Oxford Science Publications, 322 pp.
- Ohtani, E., Kagawa, N., and Fujino, K. (1991) Stability of majorite $(\text{Mg,Fe})\text{SiO}_3$ at high pressures and at 1800 °C. *Earth and Planetary Science Letters*, 102, 158-166.
- O'Neill, B., Bass, J.D., Rossman, G.R., Geiger, C.A., and Langer, K. (1991) Elastic properties of pyrope. *Physics and Chemistry of Minerals*, 17, 617-621.
- Ono, A., Akaogi, M., Kojitani, H., Yamashita, K., and Kobayashi, M. (2009) High-pressure phase relations and thermodynamic properties of hexagonal aluminous phase and calcium-ferrite phase in the systems $\text{NaAlSiO}_4\text{-MgAl}_2\text{O}_4$ and $\text{CaAl}_2\text{O}_4\text{-MgAl}_2\text{O}_4$. *Physics of the Earth and Planetary Interiors*, 174, 39-49.
- Ono, S., Ito, E., and Katsura, T. (2001). Mineralogy of subducted basaltic crust (MORB) from 25 to 37 GPa, and chemical heterogeneity of the lower mantle. *Earth and Planetary Science Letters*, 190, 57-63.
- Ono, S., Hirose, K., Isshiki, M., Mibe, K., and Saito, Y. (2002) Equation of state of hexagonal aluminous phase in basaltic composition to 63 GPa at 300 K. *Physics and Chemistry of Minerals*, 29, 527-531.

- Ono, S., Ohishi, Y., Isshiki, M. and Watanuki, T. (2005). In situ X-ray observations of phase assemblages in peridotite and basalt compositions at lower mantle conditions: Implications for density of subducted oceanic plate. *Journal of Geophysical Research*, 110: doi: 10.1029/2004JB003196.
- Oxford Diffraction (2006) CrysAlis Software system, Version 171.35.19. Oxford Diffraction Ltd., Xcalibur CCD system.
- Pamato, M.G., Kurnosov, A., Boffa Ballaran, T., Trots, D.M., Caracas, R., Frost, D.J. (2014) Hexagonal $\text{Na}_{0.41}[\text{Na}_{0.125}\text{Mg}_{0.79}\text{Al}_{0.085}]_2[\text{Al}_{0.79}\text{Si}_{0.21}]_6\text{O}_{12}$ (NAL phase): Crystal structure refinement and elasticity. *American Mineralogist*, 99, 1562-1569.
- Paterson, M.S. (1982) The determination of hydroxyl by infrared absorption in quartz, silicate glasses and similar materials. *Bulletin de Mineralogie*, 105, 20-29.
- Payne, M.C., Teter, M.P., Allan, D.C., Arias, T.A., and Joannopoulos, J.D. (1992) Iterative minimization techniques for ab initio total-energy calculations: molecular dynamics and conjugate gradients. *Reviews of Modern Physics*, 64, 1045-1097.
- Peselnick, L., and Meister, R. (1965) Variational methods of determining effective moduli of polycrystals: (A) hexagonal symmetry, (B) trigonal symmetry. *Journal of Applied Physics*, 36, 2879-2884.
- Perrillat, J.-P., Ricolleau, A., Daniel, I., Fiquet, G., Mezouar, M., Guignot, N., and Cardon, H. (2006). Phase transformations of subducted basaltic crust in the upmost lower mantle. *Physics of the Earth and Planetary Interiors*, 157, 139-149.
- Piermarini, G.J., Block, S., Barnett, J.D., and Forman, R.A. (1975) Calibration of the R1 ruby fluorescence line to 195 kbar. *Journal of Applied Physics*, 46, 2774-2780.
- Poirier, J.-P. (2000) *Introduction to the Physics of the Earth Interior*. Second edition, Cambridge University Press, Cambridge. 312 pp.
- Ralph R.L., and Finger L.W. (1982) A computer program for refinement of crystal orientation matrix and lattice constants from diffractometer data with lattice symmetry constraints. *Journal of Applied Crystallography*, 15, 537-539.
- Reed, S.J.B. (2005). *Electron Microprobe analyses and Scanning Electron Microscopy in Geology*. Cambridge University press, 189 pp.
- Rekhi, S., Dubrovinsky, L., and Saxena, S.K. (1999) Temperature-induced ruby fluorescence shifts up to a pressure of 15 GPa in an externally heated diamond anvil cell. *High Temperatures- High Pressures*, 31, 299-305.
- Reuss, A. (1929). Berechnung der Fließgrenze von Mischkristallen aufgrund der Konstanten des Einkristalls. *Zeit. Angew. Math. Mech*, 9, 49-58.

- Ricolleau, A., Fiquet, G., Addad, A., Menguy, N., Vanni, C., Perrillat, J.-P., Daniel, I., Cardon, H., and Guignot, N., (2008). Analytical transmission electron microscopy study of a natural MORB sample assemblage transformed at high pressure and high temperature. *American Mineralogist*, 93, 144-153.
- Ricolleau, A., Perrillat, J.-P., Fiquet, G., Daniel, I., Matas, J., Addad, A., Menguy, N., Cardon, H., Mezouar, M., and Guignot, N., (2010). Phase relations and equation of state of a natural MORB: implications for the density profile of subducted oceanic crust in the Earth's lower mantle. *Journal of Geophysical Research*, 115, B08202, doi:10.1029/2009JB006709.
- Rigden, S.M., Gwanmesia, G.D., and Liebermann, R.C. (1994) Elastic wave velocities of a pyrope-majorite garnet to 3 GPa. *Physics of the Earth and Planetary Interiors*, 86, 35-44.
- Ringwood, A.E. (1967) Pyroxene-garnet transition in the Earth's mantle. *Earth and Planetary Science Letters* 2, 255-263.
- Ringwood, A.E. (1975) Composition and petrology of the Earth's mantle. McGraw-Hill, New York, p. 618.
- Ringwood, A.E. (1976) Phase transformations in descending plates: implications for mantle dynamics and differentiation. In: *The geophysics of the pacific ocean basin and its margin* (Sutton, G.H., Manghnani, M.H., Moberly, R., and Mcafee, E.U.). 19, 391–398.
- Ringwood, A.E. (1982) Phase Transformations and differentiation in subducted lithosphere: implications for mantle dynamics, basalt petrogenesis, and crustal evolution. *The journal of Geology*. 90(6), 611–643.
- Rivers, M., Prakapenka, V.B., Kubo, A., Pullins, C., Holl, C.M., and Jacobsen, S.D. (2008) The COMPRES/GSECARS gas-loading system for diamond anvil cells at the Advanced Photon Source. *High Pressure Research*, 28(3), 273–292.
- Robie, R.A., and Edwards, J.L. (1966) Some Debye temperatures from single crystal elastic constant data, *Journal of Applied Physics*, 37, 2659–2663, dx.doi.org/10.1063/1.1782100.
- Rubie, D.C., and Ross II, C.R. (1994) Kinetics of the olivine–spinel transformation in subducting lithosphere: experimental constraints and implications for deep slab processes. *Physics of the Earth and Planetary Interiors*, 86, 223-241.

- Saikia, A., Frost, D.J., and Rubie, D.C. (2008) Splitting of the 520-kilometer seismic discontinuity and chemical heterogeneity in the mantle. *Science*, 319(5869), 1515-1518.
- Sanchez-Valle, C., Wang, J., and Rohrbach, A. (2011) Sound velocities of calcium-bearing majorite to high pressure and the seismic gradients in the transition zone. American Geophysical Union, Fall Meeting 2011, abstract #DI31B-2187.
- Sandercock, J.R. (1982) Trends in Brillouin scattering studies of opaque materials supported films, and central modes. In *Topics in Applied Physics 51*, Cardona, M., and Guntherodt, G. pp. 173-206, Springer-Verlag, New York.
- Sanehira, T., Irifune, T., Shinmei, T., Brunet, F., Funakoshi, K., and Nozawa, A. (2006) In-situ X-ray diffraction study of an aluminous phase in MORB under lower mantle conditions. *Physics and Chemistry of Minerals*, 33, 28-34.
- Seifert, F. (2004) From crust to core and back. *Geomaterials research at Bayerisches Geoinstitut*. Druckerei Heinz Neubert GmbH, Bayreuth. 72 pp.
- Shatskiy, A., Fukui, H., Matsuzaki, T., Shinoda, K., Yoneda, A., Yamazaki, D., Ito, E., and Katsura, T. (2007) Growth of large (1 mm) MgSiO_3 perovskite single crystals: A thermal gradient method at ultrahigh pressure. *American Mineralogist*, 92, 1744-1749.
- Sheldrick, G.M. (2008) A short history of SHELX. *Acta Crystallographica*, A64, 112-122.
- Shen, G., Prakapenka, V.B., Eng, P.J., Rivers, M.L., and Sutton, S.R. (2005) Facilities for High Pressure Research with the Diamond Anvil Cell at GSECARS. *Journal of Synchrotron Radiation*, 12, 642-649.
- Shim, S.H., Duffy, T.S, and Takemura, K. (2002) Equation of state of gold and its application to the phase boundaries near 660 km depth in Earth's mantle. *Earth and Planetary Science Letters*, 203, 729-739
- Shinmei, T., Sanehira, T., Yamazaki, D., Inoue, T., Irifune, T., Funakoshi, K., and Nozawa, A. (2005) High-temperature and high-pressure equation of state for the hexagonal phase in the system $\text{NaAlSiO}_4\text{-MgAl}_2\text{O}_4$. *Physics and Chemistry of Minerals*, 32, 594-602.
- Sinogeikin, S.V., and Bass, J.D. (2000) Single-crystal elasticity of pyrope and MgO to 20 GPa by Brillouin scattering in the diamond anvil cell. *Physics of the Earth and Planetary Interiors*, 120, 43-62.

- Sinogeikin, S.V., and Bass, J.D. (2002a) Elasticity of Majorite and a Majorite-Pyrope solid solution to high pressure: implications for the transition zone. *Geophysical Research Letters*, 29(2), 1017, 10.1029/2001GL013937.
- Sinogeikin, S.V., and Bass, J.D. (2002b) Elasticity of Pyrope and majorite-pyrope solid solutions to high temperatures. *Earth and Planetary Science Letters*, 203, 549-555.
- Sinogeikin, S.V., Bass, J.D., Prakapenka, V., Lakshtanov, D.L., Shen, G., Sanches-Valle, C., and Rivers, M. (2006) A Brillouin spectrometer interfaced with synchrotron X-radiation for simultaneous x-ray density and acoustic velocity measurements. *Review of Scientific Instruments*, 77, 103905.
- Stixrude, L., and Lithgow-Bertelloni, C. (2005a). Thermodynamics of mantle minerals – I. Physical properties. *Geophysical Journal International*, 162, 610-632, doi: 10.1111/j.1365-246X.2005.02642.x.
- Stixrude, L., and Lithgow-Bertelloni, C., (2005b) Mineralogy and elasticity of the oceanic upper mantle: origin of the low-velocity zone. *Journal of Geophysical Research*, 110(B3), B03204, doi:10.1029/2004JB002965.
- Stixrude, L., and Lithgow-Bertelloni, C. (2011). Thermodynamics of mantle minerals – II. Phase equilibria. *Geophysical Journal International*, 184, 1180-1213, doi: 10.1111/j.1365-246X.2010.04890.x.
- Stixrude, L., and Lithgow-Bertelloni, C. (2012). Geophysics of chemical heterogeneity in the mantle. *Annual Reviews of Earth and Planetary Sciences*, 40, 569-595, doi: 10.1146/annurev.earth.36.031207.124244.
- Tetzlaff, M., and Schmeling, H. (2000). The influence of olivine metastability on deep subduction of oceanic lithosphere. *Physics of the Earth and Planetary Interiors*, 120, 29-38.
- Thomsen, L. (1972) The fourth-order anharmonic theory: elasticity and stability. *Journal of Physics and Chemistry of Solids*, 33, 363-378.
- Trampert, J., Deschamps, F., Resovsky, J., and Yeun, D. (2004). Probabilistic tomography maps chemical heterogeneities throughout the lower mantle. *Science*, 306, 853-856.
- Trots, D.M., Kurnosov, A., Vasylechko, L., Berkowski, M., Boffa Ballaran, T., and Frost, D.J. (2011) Elasticity and equation of state of $\text{Li}_2\text{B}_4\text{O}_7$. *Physics and Chemistry of Minerals*, 38(7), 561-567.
- Trots, D.M., Kurnosov, A., Boffa Ballaran, T., Tkachev, S., Zhuravlev, K., Prakapenka, V., Berkowski, M., and Frost, D.J. (2013). The Sm:YAG primary fluorescence pressure scale. *Journal of Geophysical Research: Solid Earth*. 118, doi:10.1002/2013JB010519.

- Tsuchiya, T. (2003) First-principles prediction of the P-V-T equation of state of gold and the 660-km discontinuity in Earth's mantle. *Journal of Geophysical Research*, 108, 2462, doi:2410.1029/2003JB002446.
- van der Hilst, R.D. (2004) Changing views on Earth's deep mantle. *Science*, 306, 817-818.
- van der Hilst, R.D., Widiyantoro, S., Creager, K.C., and McSweeney, T. (1998) Deep subduction and aspherical variations in P-wave speed at the base of Earth's mantle. In: observational and theoretical constraints on the core mantle boundary region, Gurnis, M., Wysession, M.E., Knittle, E., and Buffett, B.A. eds. *Geodyn. Ser.* 28, 5-20.
- van Mierlo, W.L., Langenhorst, F., Frost, D.J., and Rubie, D.C. (2013). Stagnation of subducting slabs in the transition zone due to slow diffusion in majoritic garnet. *Nature Geoscience*. 6, 400-403.
- Vanpeteghem, C.B., Ohtani, E., Litasov, K., Kondo, T., Watanuki, T., Isshiki, M., and Takemura, K. (2003) The compressibility of hexagonal Al-rich NAL phase: similarities and differences with calcium ferrite-type (CF) phase with implications for the lower mantle. *Physics of the Earth and Planetary Interiors*, 138, 223-230.
- Veithen, M., Gonze, X., and Ghosez, Ph. (2005) Non-linear optical susceptibilities, Raman efficiencies and electrooptic tensors from first-principles density functional perturbation theory. *Physical Review B*, 71, 125107.
- Voigt, W. (1928). *Lehrbuch der Kristallphysik*, Teubner, Berlin.
- Walter, M.J. (2004). Melt extraction and compositional variability in mantle lithosphere. In: *Treatise of geochemistry*, vol 2, The mantle and the core. Carlson, R.W. ed. Pp: 363-394.
- Walter, M.J., Kohn, S.C., Araujo, D., Bulanova, G.P., Smith, C.B., Gaillou, E., Wang, J., Steele, A., and Shirey, S.B. (2011) Deep mantle cycling of oceanic crust: evidence from diamonds and their mineral inclusions. *Science*, 334, 54-57.
- Wang, Y., Gasparik, T., and Liebermann, R.C. (1993) Modulated microstructure in synthetic majorite. *American Mineralogist*, 78, 1165-1173.
- Wang, Z., and Ji, S. (2001) Elasticity of six polycrystalline silicate garnets at pressure up to 3.0 GPa. *American Mineralogist*, 86, 1209-1218.
- Watt, J.P. (1979) Hashin-Shtrikman bounds on the effective elastic moduli of polycrystals with orthorhombic symmetry. *Journal of Applied Physics*, 50, 6290-6295.
- Watt, J.P. (1980) Hashin-Shtrikman bounds on the effective elastic moduli of polycrystals with monoclinic symmetry. *Journal of Applied Physics*, 51, 1520-1524.

- Watt, J.P. (1986) Hashin-Shtrikman bounds on the effective elastic moduli of polycrystals with trigonal (3,3) and tetragonal (4,4,m) symmetry. *Journal of Applied Physics*, 60, 3120-3124.
- Watt, J.P., and Peselnick, L. (1980) Clarification of the Hashin-Shtrikman bounds on the effective elastic moduli of polycrystals with hexagonal, trigonal, and tetragonal symmetries. *Journal of Applied Physics*, 51, 1525-1531.
- Watt, J.P., Davies, G.F., and O'Connell, R.J. (1976) The elastic properties of composite materials. *Review of Geophysics*, 14, 541-563.
- Weidner, D.J., and Ito, E. (1987) Mineral physics constraints on uniform mantle composition. In: *High-Pressure Research in Mineral Physics (The Akimoto Volume)*, Manghni, M.H., and Syono, Y. eds., Terra Scientific Publishing Co., Tokyo/American Geophysical Union, Washington, D.C., pp. 439-446.
- Whitfield, C.H., Brody, E.M, and Bassett, W.A. (1976) Elastic moduli of NaCl by Brillouin scattering at high pressure in a diamond anvil cell. *Review of Scientific Instruments*, 47, 942, doi:10.1063/1.1134778.
- Wilson, T. (1962) Cabot Fault, An Appalachian Equivalent of the San Andreas and Great Glen Faults and some Implications for Continental Displacement. *Nature*, 195, 135-138.
- Xu, W., Lithgow-Bertelloni, C., Stixrude, L., and Ritsema, J. (2008) The effect of bulk composition and temperature on mantle seismic structure. *Earth and Planetary Science Letters*, 275, 70-79.
- Yagi, T., Akaogi, M., Shimomura, O., Tamai, H., and Akimoto, S. (1987) High pressure and high temperature equation of state of majorite. In: *High Pressure Research in Mineral Physics*, Geophysical Monograph series, Manghani, M.H, Syono, Y. eds., 39, 141-147, AGU.
- Zha, C.S., Mao, H.K., and Hemley, R.J. (2000) Elasticity of MgO and a primary pressure scale to 55 GPa. *Proceedings of the National Academy of Sciences*, 27, 13494-13499.
- Zhang, L., Ahsbahs, H., and Kutoglu, A. (1998) Hydrostatic compression and crystal structure of pyrope to 33 GPa. *Physics and Chemistry of Minerals* 25, 301-307.
- Zhang, L., Ahsbahs, H., Kutoglu, A., and Geiger, C.A. (1999) Single-crystal hydrostatic compression of synthetic pyrope, almandine, spessartine, grossular and andradite garnets at high pressures. *Physics and Chemistry of Minerals* 27, 52-58.

Appendix A1

Brillouin spectra collected using diamond anvil cell at different pressures and orientations have typically different signal to noise ratio, depending on the crystal optical quality and its orientation, as well as on laser focusing, sample alignment and time of collection. This results in different uncertainties on the V_s and V_p values which are then fit together to obtain the elastic constant of the material. Ideally, one should weight any data point according to its uncertainty, however since estimating the error of a single measurement is a time consuming task, normally the fitting of the V_s and V_p data are done with unit weights as done for spectra collected in air and therefore with much better quality. In order to weight properly our fitting (not only for this project, but also for any measurement done using the Brillouin system at the BGI) we have estimated the uncertainty of a single measurement by measuring of the same Brillouin signal with a given signal to noise ratio many times and we have repeated such procedure for different signal to noise ratio. We have been therefore able to calculate the standard deviations of these repeated measurements which give their precision. By plotting the standard deviations so obtained versus the signal to noise ratio of the set of measurements we obtained a "calibration" (Figure A1) which gives the uncertainty in m/s of a values obtained from a single spectrum with a given signal to noise ratio of In our case – a precision of single measurement of velocity with given signal to noise ratio.

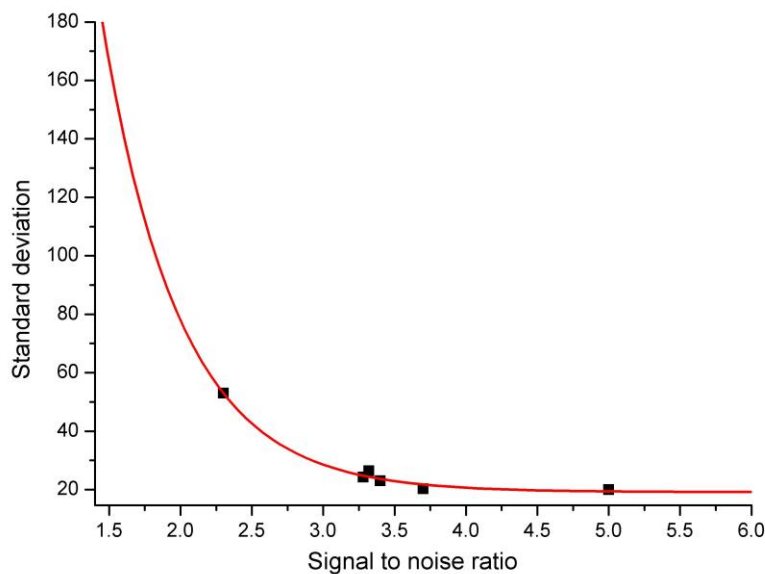


Figure A1. Calibration curve showing the exponential increase of the uncertainty of a Brillouin peak as its signal to noise ratio decreases.

Appendix A2

Table A.2-1. Mole fraction of Mg and Fe in Wadsleyite and Ringwoodite as a function of depth in a pyrolite

| Depth (km) | Wadsleyite | | Ringwoodite | |
|------------|-------------|-------------|-------------|-------------|
| | Mg_2SiO_4 | Fe_2SiO_4 | Mg_2SiO_4 | Fe_2SiO_4 |
| 542 | 0.8936 | 0.0989 | 0.0064 | 0.0011 |
| 549 | 0.6821 | 0.0668 | 0.2179 | 0.0332 |
| 551 | 0.5905 | 0.0551 | 0.3095 | 0.0449 |
| 554 | 0.4902 | 0.0434 | 0.4098 | 0.0566 |
| 556 | 0.3799 | 0.0319 | 0.5201 | 0.0681 |
| 563 | 0.0030 | 0.0002 | 0.8970 | 0.0998 |

Table A.2-2. Mole fraction of the different garnet end-members as a function of depth in pyrolite.

| Depth (km) | $Mg_3Al_2Si_3O_{12}$ | $Mg_4Si_4O_{12}$ | $Fe_3Al_2Si_3O_{12}$ | $Ca_3Al_2Si_3O_{12}$ | Mol |
|------------|----------------------|------------------|----------------------|----------------------|--------------------|
| | | | | | fraction of garnet |
| 566 | 0.1554 | 0.5555 | 0.0839 | 0.2059 | 0.1986 |
| 569 | 0.1654 | 0.5529 | 0.0843 | 0.1977 | 0.1972 |
| 574 | 0.1859 | 0.5466 | 0.0855 | 0.1825 | 0.1946 |
| 584 | 0.2206 | 0.5363 | 0.0875 | 0.1560 | 0.1902 |
| 589 | 0.2355 | 0.5320 | 0.0883 | 0.1443 | 0.1884 |
| 594 | 0.2502 | 0.5274 | 0.0892 | 0.1336 | 0.1867 |
| 599 | 0.2629 | 0.5237 | 0.0900 | 0.1237 | 0.1852 |
| 612 | 0.2917 | 0.5149 | 0.0916 | 0.1023 | 0.1819 |
| 624 | 0.3144 | 0.5083 | 0.0929 | 0.0849 | 0.1794 |
| 649 | 0.3785 | 0.4751 | 0.0937 | 0.0594 | 0.1758 |
| 661 | 0.3422 | 0.5084 | 0.0944 | 0.0410 | 0.1731 |

Table A.2-3. Mole fraction of the different perovskite and periclase end-members as a function of depth in pyrolite.

| Depth (km) | Perovskite | | | | Periclase | Wüstite |
|------------|------------|-----------|-----------|-----------|-----------|---------|
| | $MgSiO_3$ | $FeSiO_3$ | $FeAlO_3$ | $FeAlO_3$ | MgO | FeO |
| 662 | 0.8939 | 0.0430 | 0.0500 | 0.0130 | 0.860 | 0.140 |
| 697 | 0.8968 | 0.0320 | 0.0638 | 0.0075 | 0.848 | 0.137 |
| 766 | 0.8692 | 0.0560 | 0.0482 | 0.0265 | 0.871 | 0.129 |

Table A.2-4. Mole fraction of the different garnet end-members as a function of depth in MORB.

| Depth (km) | $Mg_3Al_2Si_3O_{12}$ | $Mg_4Si_4O_{12}$ | $Fe_3Al_2Si_3O_{12}$ | $Ca_3Al_2Si_3O_{12}$ | Mol fraction of garnet |
|------------|----------------------|------------------|----------------------|----------------------|------------------------|
| 551 | 0.2499 | 0.1970 | 0.1677 | 0.3848 | 0.4977 |
| 561 | 0.3137 | 0.1646 | 0.1744 | 0.3466 | 0.4784 |
| 574 | 0.3821 | 0.1299 | 0.1817 | 0.3056 | 0.4593 |
| 587 | 0.4395 | 0.1008 | 0.1877 | 0.2712 | 0.4445 |
| 599 | 0.4873 | 0.0766 | 0.1928 | 0.2425 | 0.4328 |
| 612 | 0.5268 | 0.0566 | 0.1970 | 0.2189 | 0.4236 |
| 624 | 0.5588 | 0.0404 | 0.2004 | 0.1998 | 0.4165 |
| 634 | 0.5794 | 0.0299 | 0.2026 | 0.1874 | 0.4120 |
| 673 | 0.6205 | 0.0066 | 0.2048 | 0.1671 | 0.4043 |
| 697 | 0.6626 | 0.0066 | 0.2048 | 0.1239 | 0.3743 |
| 720 | 0.6980 | 0.0066 | 0.2048 | 0.0885 | 0.3507 |

Table A.2-5. Mole fraction of Mg and Fe in Wadsleyite and Ringwoodite as a function of depth in harzburgite

| Depth (km) | Wadsleyite | | Ringwoodite | |
|------------|-------------|-------------|-------------|-------------|
| | Mg_2SiO_4 | Fe_2SiO_4 | Mg_2SiO_4 | Fe_2SiO_4 |
| 542 | 0.8936 | 0.0989 | 0.0064 | 0.0011 |
| 549 | 0.6821 | 0.0668 | 0.2179 | 0.0332 |
| 551 | 0.5905 | 0.0551 | 0.3095 | 0.0449 |
| 554 | 0.4902 | 0.0434 | 0.4098 | 0.0566 |
| 556 | 0.3799 | 0.0319 | 0.5201 | 0.0681 |
| 563 | 0.0030 | 0.0002 | 0.8970 | 0.0998 |

Table A.2-6 Mole fraction of the different perovskite and periclase end-members as a function of depth in harzburgite.

| Depth (km) | Perovskite | | | Periclase | Wüstite |
|------------|------------|-----------|-----------|-----------|---------|
| | $MgSiO_3$ | $FeSiO_3$ | $FeAlO_3$ | | |
| 662 | 0.9283 | 0.0594 | - | 0.860 | 0.140 |
| 697 | 0.9283 | 0.0594 | - | 0.871 | 0.129 |
| 766 | 0.9283 | 0.0594 | - | 0.871 | 0.129 |

(Eidesstattliche) Versicherungen und Erklärungen

(§ 8 S. 2 Nr. 6 PromO)

Hiermit erkläre ich mich damit einverstanden, dass die elektronische Fassung meiner Dissertation unter Wahrung meiner Urheberrechte und des Datenschutzes einer gesonderten Überprüfung hinsichtlich der eigenständigen Anfertigung der Dissertation unterzogen werden kann.

(§ 8 S. 2 Nr. 8 PromO)

Hiermit erkläre ich eidesstattlich, dass ich die Dissertation selbständig verfasst und keine anderen als die von mir angegebenen Quellen und Hilfsmittel benutzt habe.

(§ 8 S. 2 Nr. 9 PromO)

Ich habe die Dissertation nicht bereits zur Erlangung eines akademischen Grades anderweitig eingereicht und habe auch nicht bereits diese oder eine gleichartige Doktorprüfung endgültig nicht bestanden.

(§ 8 S. 2 Nr. 10 PromO)

Hiermit erkläre ich, dass ich keine Hilfe von gewerbliche Promotionsberatern bzw. -vermittlern in Anspruch genommen habe und auch künftig nicht nehmen werde.

Bayreuth, July 30th, 2014

.....
Ort, Datum, Unterschrift

